Hana Uršič Nemevšek

STRUCTURAL AND ELECTRICAL PROPERTIES OF 0.65PMN–0.35PT THICK FILMS ON DIFFERENT SUBSTRATES

Doctoral Dissertation

STRUKTURNA IN ELEKTRIČNA KARAKTERIZACIJA 0.65PMN–0.35PT DEBELIH PLASTI NA RAZLIČNIH PODLAGAH

Doktorska disertacija

Supervisor: Prof. Dr. Marija Kosec

Co-Supervisor: Asst. Prof. Dr. Marko Hrovat

April 2010

MEDNARODNA PODIPLOMSKA ŠOLA JOŽEFA STEFANA
JOŽEF STEFAN INTERNATIONAL POSTGRADUATE SCHOOL
Ljubljana, Slovenia

Index

Abstract ..... **V**

Povzetek ..... **VII**

Abbreviations ..... **IX**

1 Introduction **1**

1.1 Dielectric, piezoelectric and ferroelectric materials 1

1.1.1 Dielectrics 1

1.1.2 Piezoelectrics 1

1.1.3 Electrostrictive effect 3

1.1.4 Pyroelectrics, ferroelectrics and relaxors 3

1.2 Piezoelectric and ferroelectric ceramics and films 5

1.2.1 Ceramics 5

1.2.1.1 Crystal structure 5

1.2.1.2 Ferroelectric properties of the ceramics 6

1.2.2 Ferroelectric and piezoelectric thick films 8

1.2.2.1 Processing of the thick films 8

1.2.2.2 Residual stresses in the films 8

1.2.2.3 Dielectric, ferroelectric and piezoelectric properties of the films 10

1.2.2.4 Influence of stresses on the properties of thin films 11

1.2.3 Applications of piezoelectric ceramics and films 12

1.3 Properties of (1-x)Pb($Mg_{1/3}Nb_{2/3}$)O_3–x$PbTiO_3$ (PMN–PT) 14

1.3.1 Phase composition of the PMN–PT material 14

1.3.2 Dielectric, piezoelectric and ferroelectric properties of the PMN–PT composition on the morphotropic phase boundary (MPB) 16

1.3.3 The 0.65PMN–0.35PT thick films 18

2 Aims and Hypothesis **19**

3 Materials and Methods **21**

3.1 Sample preparation 21

3.1.1 Preparation of the 0.65PMN–0.35PT films on different substrates 21

3.1.2 Preparation of the 0.65PMN–0.35PT bulk ceramics 24

3.1.3 Preparation of the 0.65PMN–0.35PT/Pt actuators 25

3.2 Characterization 29

3.2.1 Structural characterization 29

3.2.1.1 Granulometry 29

3.2.1.2 X-ray diffraction analysis 29

3.2.1.3 Scanning electron microscopy with energy-dispersive X-ray analysis (EDXS) 30

3.2.1.4 Transmission electron microscopy with EDXS 30

3.2.1.5 Density 30

3.2.1.6 Median grain size and porosity 30

3.2.2 Mechanical characterization 31

3.2.2.1 Determination of Young's moduli 31

3.2.2.2 The coefficient of thermal expansion (TEC) by dilatometer 31

3.2.3 Electrical characterization 32

3.2.3.1 Dielectric and ferroelectric measurements 32

3.2.3.2 Poling 33

3.2.3.3 Measurements of coupling coefficients of bulk ceramics 34
3.2.3.4 Measurements of the piezoelectric coefficient with the Berlincourt piezometer 35
3.2.3.5 Measurement of the displacement versus the electric field for the 0.65PMN–0.35PT films 36
3.2.3.6 Measurement of displacement versus electric field for 0.65PMN–0.35PT/Pt actuators 36
3.3 Finite element modelling 38

4 Results and Discussion 39
4.1 Properties of 0.65PMN – 0.35PT powder 39
4.2 Properties of the 0.65PMN – 0.35PT bulk ceramics fired at 1200°C 41
4.2.1 Structural properties of the 0.65PMN–0.35PT bulk ceramics fired at 1200°C 41
4.2.2 Electrical properties of the 0.65PMN–0.35PT bulk ceramics fired at 1200°C 43
4.2.3 Correlation between the structural and electrical properties of the 0.65PMN–0.35PT bulk ceramics fired at 1200°C 47
4.3 Influence of the substrate materials on the structural and electrical properties of the 0.65PMN–0.35PT thick films 51
4.3.1 Influence of the substrate materials on the microstructural properties of the 0.65PMN–0.35PT thick films 51
4.3.1.1 Thicknesses of the 0.65PMN–0.35PT films 51
4.3.1.2 Microstructures of the 0.65PMN–0.35PT thick films 53
4.3.1.3 Chemical composition of the 0.65PMN–0.35PT thick film 59
4.3.1.4 Phase composition of the 0.65PMN–0.35PT films at room temperature 66
4.3.1.5 Phase composition of the 0.65PMN–0.35PT bulk ceramics fired at 950°C at room temperture 70
4.3.1.6. Temperature dependence of the phase composition of 0.65PMN–0.35PT films 72
4.3.1. 7 Influence of the film thickness on the phase composition of the 0.65PMN–0.35PT films 77
4.3.1.8. Young's modulus of the 0.65PMN–0.35PT film and bulk ceramics 82
4.3.2 Influence of the substrate materials on the electrical properties of the 0.65PMN–0.35PT thick films 85
4.3.2.1 Dielectric properties of the 0.65PMN–0.35PT thick films 85
4.3.2.2 Piezoelectric properties of the 0.65PMN–0.35PT thick films 87
4.3.2.3 Ferroelectric properties of the 0.65PMN–0.35PT thick films 88
4.3.3 Discussion on the influence of the substrate materials on the structural and electrical properties of the 0.65PMN–0.35PT films 90
4.4 Realization of the 0.65PMN–0.35PT/Pt actuators 94
4.4.1 Electrostrictive effect in the 0.65PMN–0.35PT thick films 94
4.4.2 Preparation procedure and microstructures of the 0.65PMN–0.35PT/Pt actuators 97
4.4.3 Functional characterization of the 0.65PMN–0.35PT/Pt actuators 98
4.4.4 The linear finite elements model of the actuator's displacement 100

5 Conclusions 103

Acknowledgements 107

References 109

Index of Figures 117

Index of Tables 123

Publications from the Disertation 125

COBISS 127

Abstract

A starting powder with the nominal composition $0.65Pb(Mg_{1/3}Nb_{2/3})O_3–0.35PbTiO_3$ (0.65PMN–0.35PT), which corresponds to the morphotropic phase boundary (MPB) composition, was prepared by mechanochemical activation followed by attritor milling and low-temperature calcination at 700°C. It had a narrow particle size distribution with the median particle size equal to 0.3 μm. From the synthesized powder dense bulk ceramics of 98% of theoretical density were prepared by firing at 1200°C for 2 hours. The influence of the poling electric field on the electromechanical properties and the phase composition of 0.65PMN–0.35PT ceramics was studied. The phase ratio of the monoclinic Pm to the tetragonal P4mm phases is changed by the application of a poling electric field and the extent of this change is dependent on the value of the electric field. This phenomenon was not yet reported for 0.65PMN–0.35PT ceramics. The piezoelectric coefficient and the coupling coefficients are the highest for ceramics poled at electric fields between 2 kV/mm and 3.5 kV/mm. This corresponds to largest amount of monoclinic Pm phase in ceramics.

Thick films with the composition of 0.65PMN–0.35PT were made by screen-printing and firing of the paste prepared from an organic vehicle and pre-reacted powder. The films were fired for 2 hours at 950°C on alumina (Al_2O_3), platinum (Pt), 0.65PMN–0.35PT and aluminium nitride (AlN) substrates. Alumina and platinum substrates have a higher temperature expansion coefficient (TEC) than 0.65PMN–0.35PT films, aluminium nitride substrates have a lower TEC, and the TEC of 0.65PMN–0.35PT substrates is the same as the TEC of the films. Under identical processing conditions the microstructures, phase compositions, dielectric, ferroelectric and piezoelectric properties strongly depend on the choice of the substrate material. If the thick films are after firing and cooling under compressive stresses, i.e, films on substrates with higher TEC, films are dense with grain sizes 1.7 μm on alumina substrates and 1.2 μm on platinum substrates. The X-ray analyses and Rietveld refinements showed the coexistence of monoclinic and tetragonal phases. Dielectric constants were 3400 and 2000, piezoelectric coefficients d_{33}^{eff} were 180 pC/N and 140 pC/N and remanent polarizations were 22 $\mu C/cm^2$ and 27 $\mu C/cm^2$ for films on Al_2O_3 and Pt substrates, respectively. The electrical properties of films on Al_2O_3 and Pt substrates and also the coexistence of tetragonal and monoclinic phases are comparable to results obtained on densly sintered bulk ceramics. The exception is the lower piezoelectric constant of films, which is partly due to the clamping of the films on rigid substrates. Films fired and cooled on substrates with lower TEC (AlN) or with the same TEC (0.65PMN–0.35PT) were porous with grain sizes below or equal to 0.5 μm. In this case we presume that the tensile stresses were relaxed during cooling and the characteristics are therefore similar for films on AlN as for stress free films on 0.65PMN–0.35PT substrates. For these films the X-ray analyses and Rietveld refinements showed the monoclinic phase. The dielectric constants were 700 and 300, piezoelectric coefficients d_{33}^{eff} were 105 pC/N and 30 pC/N and remanent polarizations were 8 $\mu C/cm^2$ and 3 $\mu C/cm^2$ for films on 0.65PMN–0.35PT and AlN substrates, respectively, which is a consequence of the porous structure. These results indicate that substrates strongly influence the densification and microstructural characteristics of thick films and, consequently, the structural and electrical properties.

The electrostrictive effect in 0.65PMN–0.35PT films on alumina substrates was measured. The electrostrctive coefficient M_{33} of 0.65PMN–0.35PT thick films on alumina substrates was high, i.e., $7.6 \cdot 10^{-16}$ m^2/V^2. Due to high electrostriction of thick 0.65PMN–0.35PT films, we decided to prepare the 0.65PMN–0.35PT thick-film actuators.

A novel approach to preparing large-displacement "substrate-free" 0.65PMN–0.35PT/Pt actuators was developed. After screen printing and firing the 0.65PMN–0.35PT/Pt composites were peeled off from the alumina substrates. The normalized displacements of 55 μm/cm were achieved for actuators with dimensions of 1.8 cm × 2.5 mm × 65 μm, which is 5–10 times higher in comparison with the normalized displacements of bulk PMN–PT or thick-film $Pb(Zr,Ti)O_3$ (PZT) actuators.

Povzetek

Začetni prah s kompozicijo na morphotropni fazni meji $0{,}65Pb(Mg_{1/3}Nb_{2/3})O_3–0{,}35PbTiO_3$ (0,65PMN–0,35PT) smo pripravili z mehanokemijsko aktivacijo, kateri je sledilo mletje v atritorskem mlinu in nizkotemperaturno kalciniranje pri 700°C. Porazdelitev velikosti delcev prahu je ozka z mediano 0,3 μm. Iz sintetiziranega 0,65PMN–0,35PT prahu smo pripravili keramiko z žganjem pri 1200°C, 2 uri. Gostota keramike je bila 98% teoretične vrednosti. Raziskovali smo vpliv električnega polja na fazno sestavo in na elektromehanske lastnosti 0,65PMN–0,35PT keramike. Ugotovili smo, da lahko razmerje monoklinske Pm in tetragonalne P4mm faze spreminjamo z električnim poljem. Pri keramiki, polarizirani z električnim poljem med 2–3,5 kV/mm, je najvišja vsebnost monoklinske faze o čemer pri keramiki s to sestavo doslej še ni bilo poročano. Tudi piezoelektrični koeficient d_{33} in sklopitvena koeficienta k_p in k_t sta najvišja za keramiko, polarizirano z električnim poljem med 2–3,5 kV/mm.

0,65PMN–0,35PT debele plasti smo pripravili s sitotiskom paste iz organskega nosilca in 0,65PMN–0,35PT prahu. Plasti so bile žgane 2 uri pri 950°C na korundni (Al_2O_3), platinasti (Pt), 0,65PMN–0,35PT in aluminij nitridni (AlN) podlagi. Korundna in platinska podlaga imata višji temperaturni razteznostni koeficient kot 0,65PMN–0,35PT plast, aluminij nitridna podlaga ima manjšega, 0,65PMN–0,35PT podlaga pa ima temperaturni razteznostni koeficient enak kot plast. Mikrostruktura, fazna sestava, dielektrične, piezoelektrične in feroelektrične lastnosti so močno odvisne od materiala, iz katerega je podlaga. Če je 0,65PMN–0,35PT plast po segrevanju in ohlajanju pod tlačno napetostjo, to so plasti na podlagah z višjim razteznostnim koeficientom, so plasti goste s povprečno velikostjo zrn 1,7 μm na korundni podlagi in 1,2 μm na platinski podlagi. Rentgenska in Rietveldova analiza sta pokazali soobstoj monoklinske in tetragonalne faze kot v primeru volumenske keramike sintrane pri 1200°C. Za plasti na korundni in platinski podlagi sta bili dielektrični konstanti 3400 in 2000, piezoelektrična koeficienta d_{33}^{eff} 180 pC/N in 140 pC/N, remanentni polarizaciji pa 22 μC/cm^2 in 27 μC/cm^2. Električne lastnosti plasti na Al_2O_3 in Pt podlagah in tudi soobstoj tetragonalne in monoklinske faze so primerljivi z rezultati dobljenimi za gosto volumensko keramiko. Izjema je nizek piezoelektrični koeficient plasti, ki je delno posledica pripetosti plasti na podlago. Plasti na podlagah z razteznostnim koeficientom manjšim (AlN podlage) ali enakim (0,65PMN–0,35PT podlage) od koeficenta plasti, so bile porozne ter so imele povprečno velikost zrn manjšo ali enako 0,5 μm. V tem primeru so zaradi porozne strukture natezne napetosti na AlN podlagah verjetno popustile tako, da niso vplivale na lastnosti plasti. Za plasti na 0,65PMN–0,35PT in na AlN podlagah sta rentgenska in Rietveldova analiza pokazali monoklinsko fazo. Plasti na obeh podlagah so imele dielektrično konstanto 700 in 300, piezoelektrični koeficient d_{33}^{eff} 105 pC/N in 30 pC/N, remanentno polarizacijo pa 8 μC/cm^2 in 3 μC/cm^2, kar je posledica porozne strukture. Ti rezultati nakazujejo, da podlage močno vlivajo na zgoščevanje in mikrostrukturo plasti ter posledično na strukturne in električne lastnosti plasti.

Izmerili smo elektrostrikcijski pojav v 0,65PMN–0,35PT debelih plasteh na korundnih podlagah. Elektrostrikcijski koeficient M_{33} plasti na korundnih podlagah je visok, t.j. $7{,}6 \cdot 10^{-16}$ m^2/V^2. Zaradi visokega elektrostrikcijskega pojava v 0,65PMN–0,35PT plasteh, smo jih uporabili za pripravo 0,65PMN–0,35PT debeloplastnih aktuatorjev.

Razvili smo nov postopek priprave 0,65PMN–0,35PT/Pt aktuatorja z velikim odmikom. 0,65PMN–0,35PT/Pt kompozit smo odstranili iz podlage. Dosegli smo velike normalizirane odmike aktuatorja, t. j. 55 μm/cm za aktuatorje velikosti 1,8 cm × 2,5 mm × 65 μm. Ti normalizirani odmiki so zelo visoki v primerjavi z objavljenimi normaliziranimi odmiki volumenskih PMN–PT aktuatorjev ali debeloplastnih $Pb(Zr,Ti)O_3$ (PZT) aktuatorjev na korundnih podlagah.

Abbreviations

Acronyms

0.65PMN–0.35PT	=	$0.65Pb(Mg_{1/3}Nb_{2/3})O_3–0.35PbTiO_3$
AFM	=	atomic force microscope
CCD	=	charge coupled device
EDXS	=	energy-dispersive X-ray analysis
FC	=	field cooled
FE	=	finite element
FE-SEM	=	field emission scanning electron microscope
LT	=	low temperature
MEMS	=	micro electro mechanical systems
MPB	=	morphotropic phase boundary
PFM	=	piezo force microscope
PLZT	=	$(Pb,La)(Zr,Ti)O_3$
PMN	=	$Pb(Mg_{1/3}Nb_{2/3})O_3$
PMN–PT	=	$(1–x)Pb(Mg_{1/3}Nb_{2/3})O_3–xPbTiO_3$
PT	=	$PbTiO_3$
PZ	=	$PbZrO_3$
PZT	=	$Pb(Zr,Ti)O_3$
SEM	=	scanning electron microscope
TEC	=	thermal expansion coefficient
TEM	=	transmission electron microscope
ZFC	=	zero field cooled
ZFH	=	zero field heated

Symbols

α	=	TEC
ε	=	dielectric permittivity (dielectric constant)
ε_o	=	dielectric permittivity in vacuum
ν	=	Poisson`s ratio
σ	=	stress
χ	=	dielectric susceptibility
c	=	elastic stiffness constants
C	=	capacitance
d	=	piezoelectric coefficient
d_{50}	=	median particle size determined by laser granulometry
$\vec{D}$	=	dielectric displacement
$\vec{E}$	=	electric field
E_c	=	coercive field
f_a	=	antiresonance frequency
f_r	=	resonance frequency
F(h)	=	load – displacement curve
Gof	=	factor of validity of the profile, called goodness of the fit
k_p	=	radial coupling coefficient
k_t	=	thickness coupling coefficient
M	=	electrostrictive coefficient

$\vec{P}$	=	electrical polarization
P_r	=	remanent polarization
R	=	reliability factor of the X-ray profile
R_M	=	reliability factor for the monoclinic phase
R_T	=	reliability factor for the tetragonal phase
s	=	elastic compliance
S	=	strain
T	=	temperature
T_c	=	Curie temperature
tg δ	=	dielectric losses
Y	=	Young`s modulus

1 Introduction

1.1 Dielectric, piezoelectric and ferroelectric materials

1.1.1 Dielectrics

A dielectric is a nonconducting material, which can be polarized by the application of an electric field $\vec{E}$. The surface charge density, which is induced in the material by the application of the electric field, is given by the dielectric displacement vector $\vec{D}$ with the components D_i:

$$D_i = \varepsilon_0 E_i + P_i \qquad (1)$$

where $\varepsilon_0 = 8.85 \cdot 10^{-12}$ (As/Vm) is the dielectric permittivity of vacuum, and $\vec{P}$ is electrical polarization. The equation (1) can be written as:

$$D_i = \varepsilon_0 E_i + P_i = \varepsilon_0 E_i + \varepsilon_0 \chi_{ij} E_j = \varepsilon_0 \varepsilon_{ij} E_j \qquad (2)$$

where χ_{ij} is the component of the dielectric susceptibility tensor and ε_{ij} is the component of the dielectric tensor (or dielectric permittivity tensor) of the material [1, 2]. The relation is valid only for linear materials or in a linear limit for nonlinear materials and, in general, P_i depends on higher-order terms of the electric field.

1.1.2 Piezoelectrics

Piezoelectricity is the property of some materials to develop a dipole moment when a mechanical stress is exerted on them [1]. This effect is called the direct piezoelectric effect. In other words, the dielectric materials are referred to as the piezoelectric materials, if they can be polarized, in addition to an electric field, by application of mechanical stress. In piezoelectric materials, an inverse piezoelectric effect is also observed. The inverse piezoelectric effect is an effect when an external electric field applied to an piezoelectric material produces a deformation of the material. In Fig. 1 the direct and inverse piezoelectric effects are shown schematically.

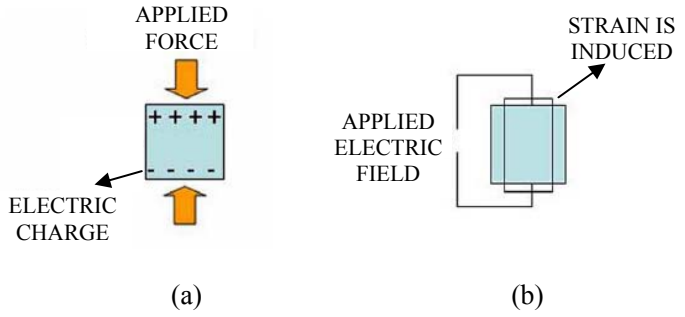

Figure 1: The direct piezoelectric effect (a) and the inverse piezoelectric effect (b).

The basic equations in tensor form that describe these two effects in regard to the electric and elastic properties are

$$D_i = d_{ijk}\sigma_{jk} + \varepsilon_{ij}^{\sigma} E_j, \qquad (3)$$

$$S_{ij} = s_{ijkl}^{E}\sigma_{kl} + d_{kij}E_k, \qquad (4)$$

where
i, j, k = 1, 2, 3 (Note, we use Einstein summation convention: when a letter suffix occurs twice in the same term, summation with respect to that suffix is to be automatically understood.)
D_i is a component of dielectric displacement vector (As/m^2),
σ_{ij} is a component of second-rank stress tensor (N/m^2),
E_i is a component of electric field vector (V/m),
S_{ij} is a component of second-rank strain tensor,
d_{ijk} is a component of third rank piezoelectric tensor (As/N or C/N for direct effect and m/V for inverse effect),
s_{ijkl}^{E} is a component of fourth rank elastic compliance tensor (m^2/N) under constant electric field,
$\varepsilon_{ij}^{\sigma}$ is a component of dielectric tensor (As/Vm) under constant stress.

The matrix notation is more common. The basic equations in matrix form that describe these two effects in regard to electric and elastic properties are:

$$D_i = d_{im}\sigma_m + \varepsilon_{ij}^{\sigma} E_j, \qquad (5)$$

$$S_m = s_{mn}^{E}\sigma_n + d_{im}E_i, \qquad (6)$$

where i, j = 1, 2, 3 and m, n = 1,... 6 [1, 2]. The piezoelectric coefficients of material in matrix form are written as d_{im}. The direction of positive polarization usually coincides with z-axis of a rectangular system of x, y, and z-axes. Direction x, y, or z is represented by the subscript 1, 2, or 3, as it is shown in Fig. 2.

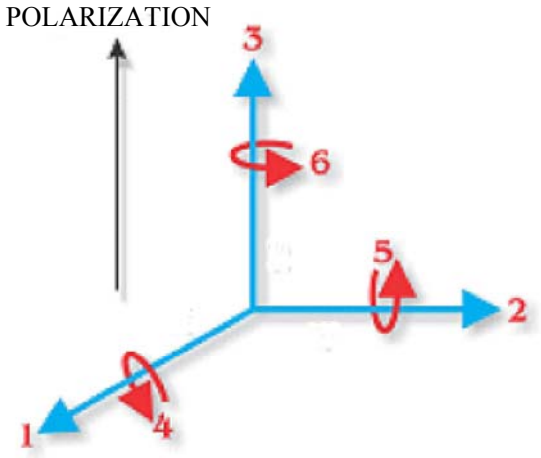

Figure 2: Coordinate system used in the thesis. The direction of polarization is marked [3]. Numbers 4, 5 and 6 represents directions of shear stresses.

For example: d_{33} means the induced polarization in direction 3 (parallel to the direction in which the element is polarized) per unit stress applied in direction 3 or the induced strain in direction 3 per unit of electric field applied in direction 3 [3].

1.1.3 Electrostrictive effect

In general, the electrostriction is defined as the quadratic coupling between the strain developed in a material and the applied electric field,

$$S_{ij} = M_{ijmn} E_m E_n. \quad (7)$$

Here, S_{ij} is the component of strain tensor, E_m and E_n are the components of the electric field vector (V/m), and M_{ijmn} (m^2/V^2) is the component of fourth-rank electrostrictive tensor [4]. The Einstein summation convention is used. Electrostriction can also be expressed by the equivalent relation

$$S_{ij} = Q_{ijkl} P_k P_l, \quad (8)$$

where S_{ij} is the component of strain tensor, Q_{ijkl} is the component of electrostrictive tensor (m^4/C^2), and P_i is the component of electrical polarization [5]. The electrostrictive coefficients M_{ijmn} and Q_{ijmn} can be written in matrix form as M_{kl} and Q_{kl}, respectively.

1.1.4 Pyroelectrics, ferroelectrics and relaxors

Pyroelectrics are materials that are permanently polarized within a given temperature range. Unlike the more general piezoelectric classes that produce a polarization under stress, the pyroelectrics develop the polarization spontaneously and form permanent dipoles in the structure [6]. A subgroup of the spontaneously polarized pyroelectrics is a group of materials known as ferroelectrics. Similar to pyroelectrics, materials in this group possess spontaneous dipoles. However, unlike pyroelectrics, these dipoles are reversible by an application of the electric field lower than the electric field, which induce dielectric breakdown of the material. The two conditions necessary for the materials to be classified as a ferroelectric are: the existence of spontaneous polarization and a demonstrated reorienting of the polarization [1].Various ferroelectric materials are single crystals, ceramics, polymers and ceramic-polymer composite [7]. Most ferroelectric materials undergo a structural phase-transition from a high-temperature non-ferroelectric, called the paraelectric phase into a low-temperature ferroelectric phase [1]. The temperature of the phase-transition is called the Curie temperature T_c at which the dielectric constant ε has strong anomaly (Figure 3).

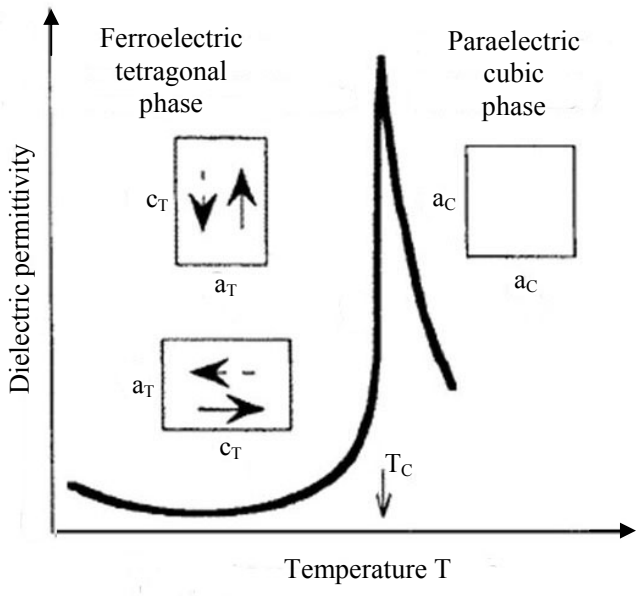

Figure 3: Illustration of the changes in the dielectric constant ε of a ferroelectric material, which transforms from a paraelectric cubic phase into a ferroelectric tetragonal phase, versus temperature T. The arrows show possible directions of the spontaneous polarization (the unit-cell is represented by a square in the cubic phase and rectangle in the tetragonal phase) [1].

For example the T_c of $Pb(Zr_{0.52}Ti_{0.48})O_3$ materials is 386°C [8]. Some ferroelectrics, e.g. $BaTiO_3$, undergo several phase transitions in ferroelectric phases. Only the transition temperature of the phase transformation from paraelectric phase into the first ferroelectric phase is called the Curie temperature [1]. Polymers have a low Curie temperature and the degradation of the properties starts at low temperatures (70–100°C). On the other hand, the Curie temperature T_c of ceramics is changing with the variation of the ceramic's composition.
The Curie temperature can be higher than 1000°C, for this reason the ferroelectric ceramic elements can be used in high-temperature applications [7–9].

While in ferroelectric materials the dielectric constant has a sharp, frequency independent maximum at the temperature T_c, in relaxor materials the temperature of the dielectric constant maximum is frequency dependent. In Fig. 4 [10] the temperature at which the dielectric constant reaches the maximum T_{max} increase with the increasing frequency for relaxor $Pb(Mg_{1/3}Nb_{2/3})O_3$ (PMN) crystal.

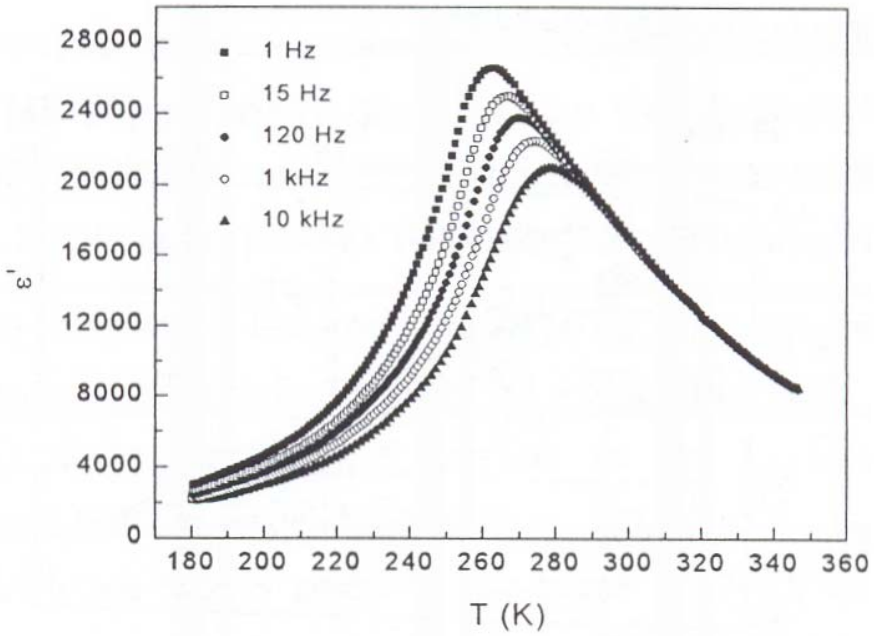

Figure 4: Temperature dependence of dielectric constant **ε** measured at different frequencies for the relaxor $Pb(Mg_{1/3}Nb_{2/3})O_3$ (PMN) crystal [10].

1.2 Piezoelectric and ferroelectric ceramics and films

In the previous section we reported the general properties of dielectric, pyroelectric, piezoelectric and relaxor materials. The basic principles and characteristics of ferroelectric materials including single crystals, ceramics and polymers were also reported. In this section the properties of polycrystalline ferroelectric ceramics and films are discussed.

1.2.1 Ceramics

1.2.1.1 Crystal structure

The most common piezoelectric ceramics have a perovskite crystal structure ABO_3. An example of the perovskite crystal structure is shown in Fig. 5. Each unit-cell consists of a small, tetravalent ion, for example zirconium or titanium, in a lattice of large, divalent metal, like lead or barium, and O^{2-} ions [3]. In Fig. 5 (a) the non-piezoelectric paraelectric cubic lattice with a symmetric arrangement of positive and negative charges is shown. Noncentro-symmetry is a necessary condition for piezoelectricity to exist. In Fig. 5 (b) the piezoelectric tetragonal lattice with the electrical dipole moment is shown [3].

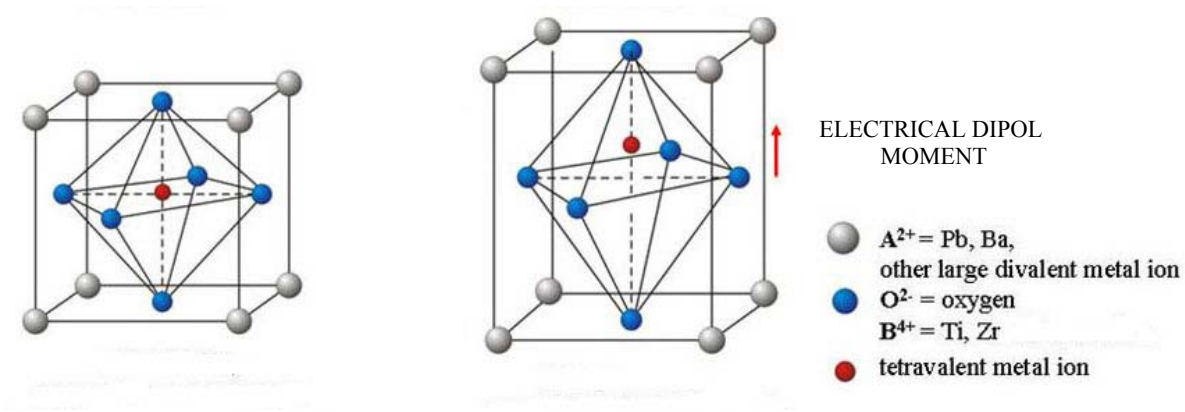

a) b)

Figure 5: An example of perovskite crystal structure: a) cubic lattice, symmetric arrangement of positive and negative charges, temperature above Curie point, b) tetragonal lattice, crystal has electrical dipole, temperature below Curie point [3].

Perovskite unit-cells of cubic, rhombohedral, tetragonal, orthorhombic and monoclinic phases are shown in Fig. 6. The cubic cell (Fig. 6a) has three crystallographic axes that are equal in length ($a = b = c$) and perpendicular to each other ($\alpha = \beta = \gamma = 90°$). The rhombohedral cell is similar to a cube, which has been stretched in on direction as it is shown with red arrows in Fig. 6b. The sides of the cell $a = b = c$ and angles $\alpha = \beta = \gamma$ are equal, however the angles are different from 90°. A tetragonal cell (Fig. 6c) is simple cubic, which is stretched along its *c* axis to form a rectangular prism ($a = b$, c, $\alpha = \beta = \gamma = 90°$). The orthorhombic cell, which is shown in Fig. 6d, has three perpendicular axes with unequal lengths ($a \neq b \neq c$, $\alpha = \beta = \gamma = 90°$). The monoclinic cell also has three unequal axes, as shown in Fig. 6e. The a and c axes are inclined toward each other at an oblique angle, and the b axis is perpendicular to a and c [11].

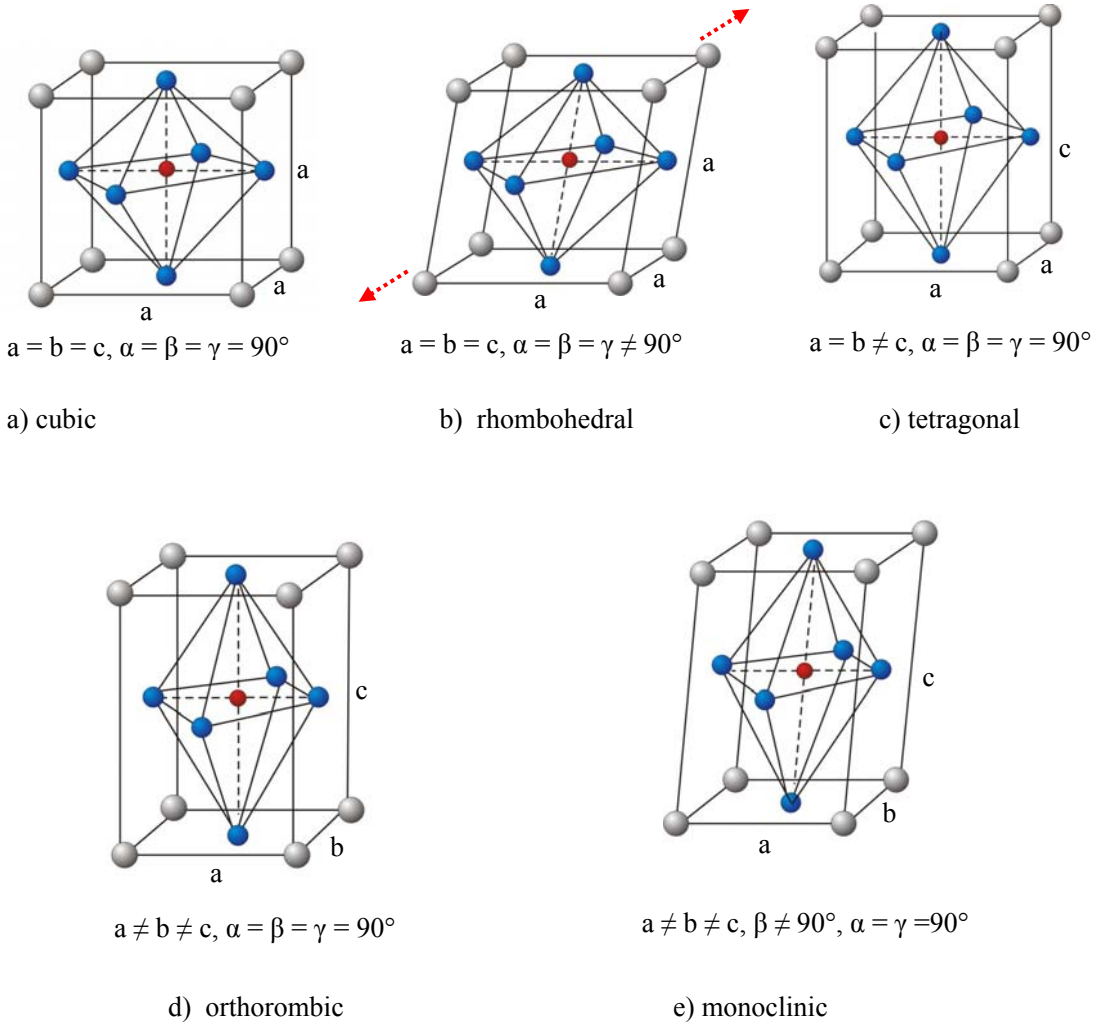

Figure 6: Perovskite unit-cells of a) cubic, b) rombohedral, c) tetragonal, d) orthorhombic and e) monoclinic phases.

1.2.1.2 Ferroelectric properties of the ceramics

The dipole moments are differently oriented among different ceramics grains, or even among different regions within a single grain. The regions with the dipole moments with the same orientation are called domains. Because the domains are randomly oriented, the ceramics have no overall polarization (Fig. 7a) [3]. The ceramics are poled, when they are exposed to a strong DC electric field. In this process, the spontaneous polarization directions are reoriented by an external electric field in the direction of the field (Fig. 7b). When the electric field is removed most of the dipoles are locked into this configuration of the near alignment (Fig. 7c). This gives the material a permanent polarization called the remanent polarization P_r. The electric field that brings the mean polarization down to zero is referred to as the coercive electric field E_c. The ferroelectric materials exhibit a hysteresis curve for the polarization versus the electric field (Fig. 8).

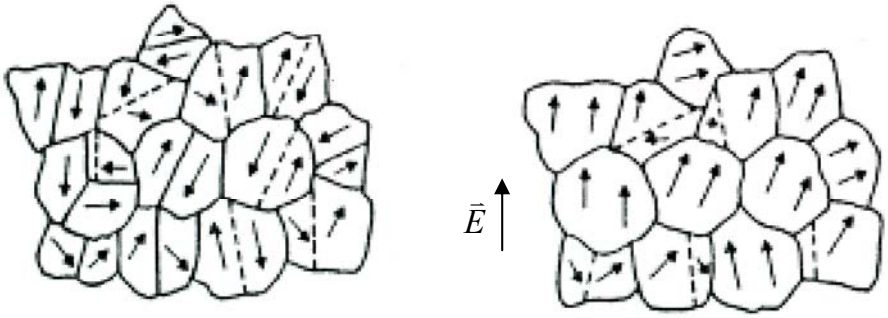

a) b)

Figure 7: Poling of piezoelectric ceramics: a) The unpoled ceramics. Each grain contains a number of domains and the net polarization is zero. b) After poling the domains are oriented with a net polarization along the direction of the applied field [12].

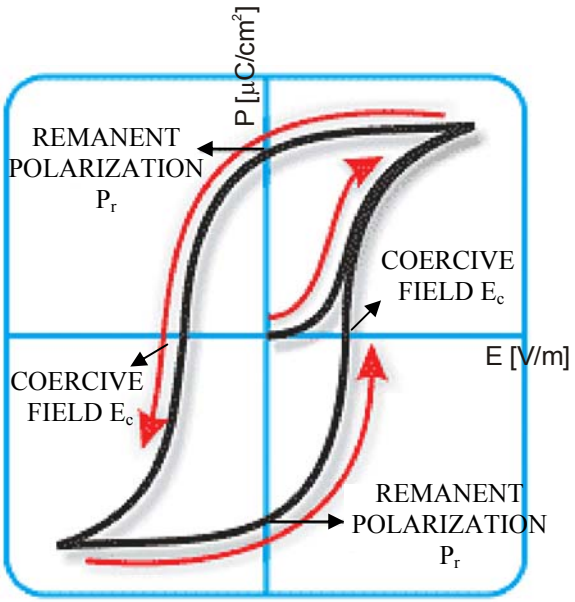

Figure 8: Hysteresis curve of ferroelectric ceramics [3].

1.2.2 Ferroelectric and piezoelectric thick films

1.2.2.1 Processing of the thick films

In recent years ceramics films have attracted much attention due to the need for miniaturization of the electronic components. A lot of literature exists about thin films (usually less than 1 µm thick), while for the thick films (usually thicker than 10 µm) not much has been done. Ceramic thick films are mostly made by the screen printing of ceramic ink and subsequent firing. The screen printing process is a process where the paste is forced through the open areas of the screen on to the surface of the substrate [13, 14]. The paste is applied to the upper surface of the screen and a squeegee is traversed across the pattern area [13]. In Fig. 9 the screen printing procedure is shown schematically.

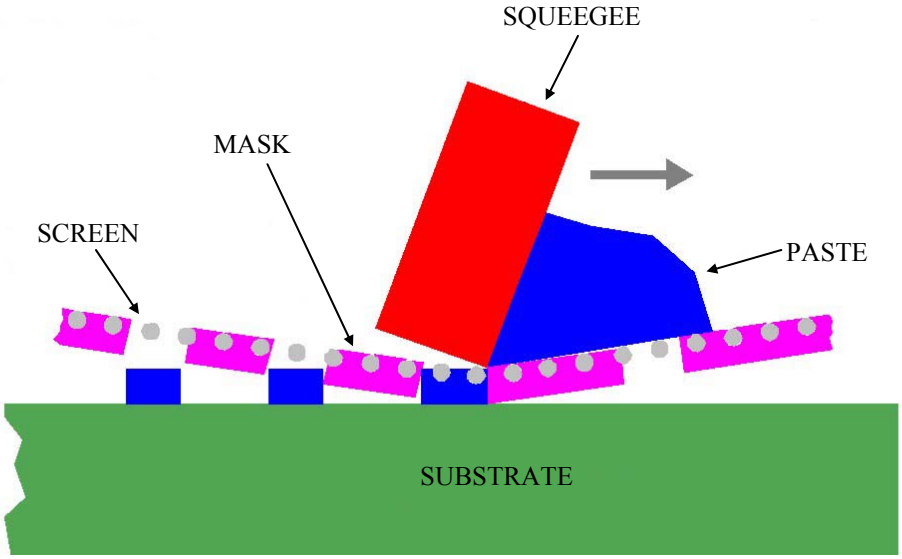

Figure 9: The scheme of the screen printing procedure.

While thin films are prepared at temperatures of a few hundred degree Celsius, ceramic thick films are fired typically at much higher temperatures around 1000°C. This could lead to interactions between films and substrates [15–18], and changes of stochiometry due to the sublimation of oxides, e.g.: PbO, which could strongly influence structural and electrical characteristics.

1.2.2.2 Residual stresses in the films

Internal stresses are stresses that remain after the original cause for their existence (external forces, heat gradient, etc.) has been removed. These stresses are also called residual stresses [19, 20]. The films on substrates prepared at elevated temperatures and cooled to room temperatures will be thermally stressed, due to the thermal mismatch between the film and the substrate [19, 21, 22]. In Fig. 10 the cooling stresses in the substrate-film system are shown. In this example the linear thermal expansion coefficient (TEC) of the substrate is higher than the TEC of the film.

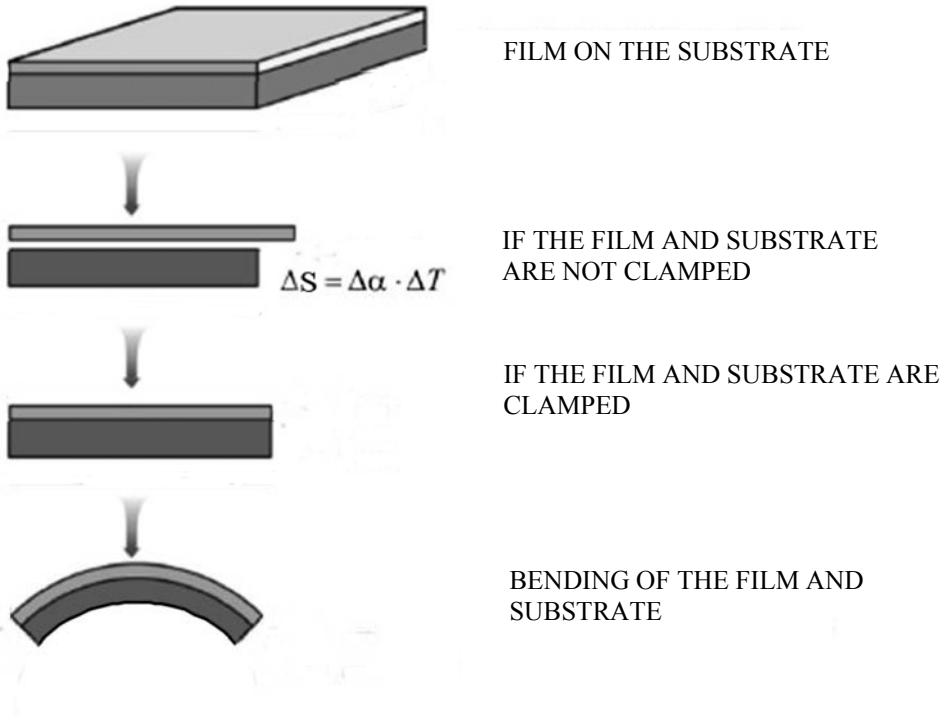

Figure 10: Cooling stresses in the substrate-film system: ΔS is difference in deformation between substrate and film, Δα is difference in TEC of substrate and film, ΔT is a difference in temperature [19, 23].

The basic equation for the thermal stress in films is [19]

$$\sigma_f(T) = (\alpha_s - \alpha_f)(T_2 - T_1)Y_f/(1 - \nu_f), \qquad (9)$$

where
α_s is a TEC of the substrate (K^{-1}),
α_f is a TEC of the film (K^{-1}),
T_2-T_1 = ΔT is a difference in temperature (K),
Y_f is Young`s modulus of the film (N/m^2),
ν_f is Poisson`s ratio of the film.

A film prepared at elevated temperature will be residually compressed when measured at room temperature if $\alpha_s > \alpha_f$. In the opposite case, if $\alpha_s < \alpha_f$, the film will be under residual tension. In Fig. 11 the bending of the film under compression and tension is illustrated [19].

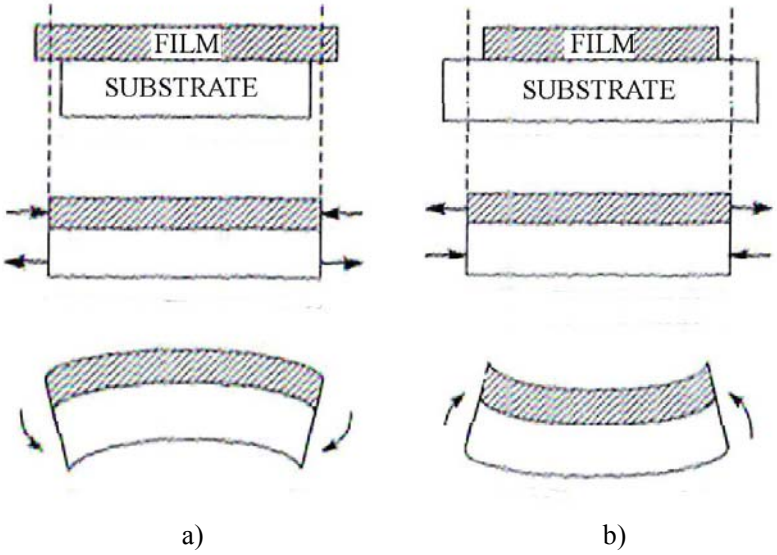

Figure 11: Film under a) compressive and b) tensile residual stress [19].

In the case when the film is residually compressed, the substrate shrinks more than the film. Due to the clamping of the film to the substrate, a compromise has to be made; the substrate is not allowed to contract fully and is, therefore, placed in tension, and the film hindered from shrinking, is consequently forced into compression [19]. Large residual stresses in films can lead to cracking of the films.

1.2.2.3 Dielectric, ferroelectric and piezoelectric properties of the films

The differences of the dielectric, piezoelectric and ferroelectric properties of films and bulk ceramics have been widely studied [1, 24–26]. For the dielectric, ferroelectric and piezoelectric properties the film should be placed between the bottom and top electrode. In Fig. 12 a schematic illustration of a film on a substrate and a rectangular system of 1, 2, and 3-axes is shown.

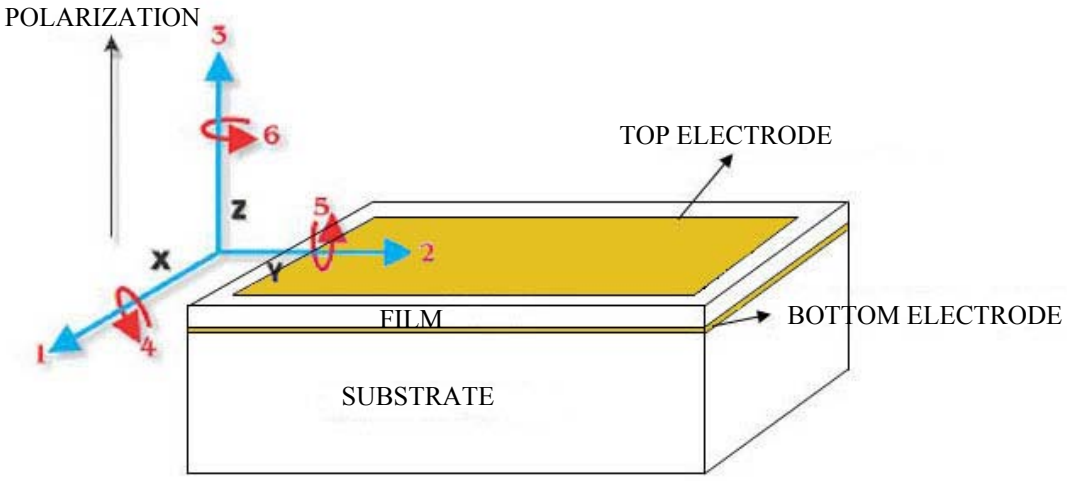

Figure 12: Illustration of the film on the substrate and a rectangular system of 1, 2, and 3-axes. The direction of polarization coincides with axis 3.

The ε of thin films is generally lower than for bulk ceramics. Also, the ferroelectric properties for films are different than for bulk ceramics or single crystals with the same composition. The hysteresis loop of films may be affected by many factors including the thickness of the film, the mechanical stresses, the preparation conditions, the thermal treatment and the presence of charge defects [1, 27]. The piezoelectric coefficients of films and bulk ceramics or single crystals with the same composition are also different. The most important difference between piezoelectric films and bulk piezoelectrics is the clamping of the

films by the substrate, which results in a reduction of the macroscopically measured d_{33} [24, 25, 28, 29]. Namely, the ratio D_3/σ_3 does not represent the piezoelectric coefficient d_{33} of the free sample, but an effective piezoelectric coefficient

$$d_{33}^{eff} = d_{33} - 2d_{31}\frac{\frac{\nu_s}{Y_s} + s_{13}^E}{(s_{11}^E + s_{12}^E)}, \qquad (10)$$

where
d_{33} and d_{31} are the piezoelectric coefficients (C/N or m/V),
s^E_{13}, s^E_{11}, s^E_{12} are the elastic compliance coefficients at constant electric field (m^2/N),
ν_s is Poisson`s ratio of the substrate,
Y_s is Young`s modulus of the substrate (N/m^2).

Since for most materials $d_{31} < 0$, $s_{13} < 0$ and d_{31} is relatively large, the measured coefficient in films is lower than in unclamped materials ($d_{33}^{effective} < d_{33}$).

1.2.2.4 Influence of stresses on the properties of thin films

The electrical properties of thin $BaTiO_3$ films under stresses can change dramatically in comparison to the unstressed films [27]. The influence of the residual stress on the electrical and structural properties of $Pb(Zr,Ti)O_3$ (PZT) thin films were reported [30–34]. In ref. [30] the thermodynamic formalism based on the Landau-Devonshire`s phenomenological theory predicts the enhanced thermodynamic stability of the tetragonal phase under a two-dimensional compressive stress. In Fig. 13 the computed phase diagram of the PZT system under compressive stress is shown, where it is seen that a compressive stress of -50 MPa shifts the morphotropic phase boundary (MPB) toward the rhombohedral phase and force PZT films to be in the tetragonal phase [30]. In other words, the same composition, which shows rombohedral phase at zero stress, shows tetragonal phase under compressive stress.

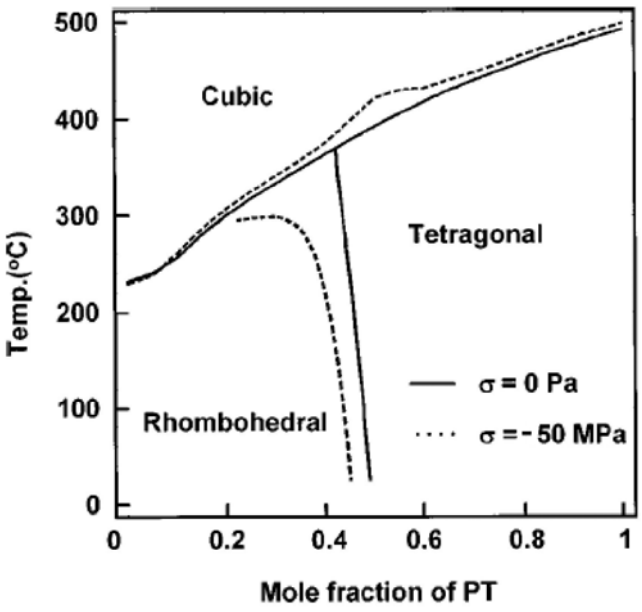

Figure 13: The computed phase diagram of $PbZrO_3$–$PbTiO_3$ (PZ–PT) system, showing the effect of two-dimensional compressive stress on the shift of the MPB [30].

In ref. [30] the PZT films (Zr/Ti = 52/48) were also prepared on MgO substrates. The thermal expansion coefficient $\alpha_s = 13.3 \cdot 10^{-6}$/K of the MgO substrate is larger than $\alpha_f = 9 \cdot 10^{-6}$/K of PZT film, therefore the films were under compressive stress. As suggested in ref. [30], this compressive stress enhances the tetragonal phase in PZT films on a MgO substrate. Also in ref. [31] in PZT thin films on MgO substrates the MPB moves toward the Zr-rich composition due to the residual stress. In ref. [32] the residual stress in the PZT thin films strongly affects the measured electrical properties of the films, while

the MBP shifts to the $PbZrO_3$-rich composition upon compressive residual stress. In ref. [33, 34] it is also predicted from Landau-Devonshire theory that compressive stress shifts the MPB toward the $PbZrO_3$-rich composition and enhanced thermodynamic stability of the tetragonal phase, however for tensile stress in PZT films it is predicted that it also shifts the MPB to the $PbZrO_3$-rich composition and in addition it makes a new ferroelectric orthorhombic phase stable [33].

1.2.3 Applications of piezoelectric ceramics and films

Piezoelectric ceramics can be hundreds of times more sensitive to mechanical or electrical input than natural materials, for example quartz, and the dimensions, shape and composition of a ceramic can be formed as it is required for a desired specific purpose [3], as it is shown in Fig. 14 [35]. Piezoelectric ceramics are used in a wide range of sensors, actuators and micro-electro mechanical devices (MEMS). These devices are used in expanding fields, such as: microelectronic, medical applications (e.g. ultrasonic medical diagnostic and therapy) and industry (e.g. automotive industry, sports industry) [1].

Figure 14: Varity of piezoelectric bulk parts [35].

Thick-film technology is used to produce electronic devices such as hybrid integrated circuits, sensors and actuators. In Fig. 15 an example of the versatility of thick-film technology is shown, i.e., hybrid integrated circuits, sensors and actuators. The manufacture of such devices typically involves the deposition of several layers onto an electrically insulating substrate using a screen printing process [25, 36].

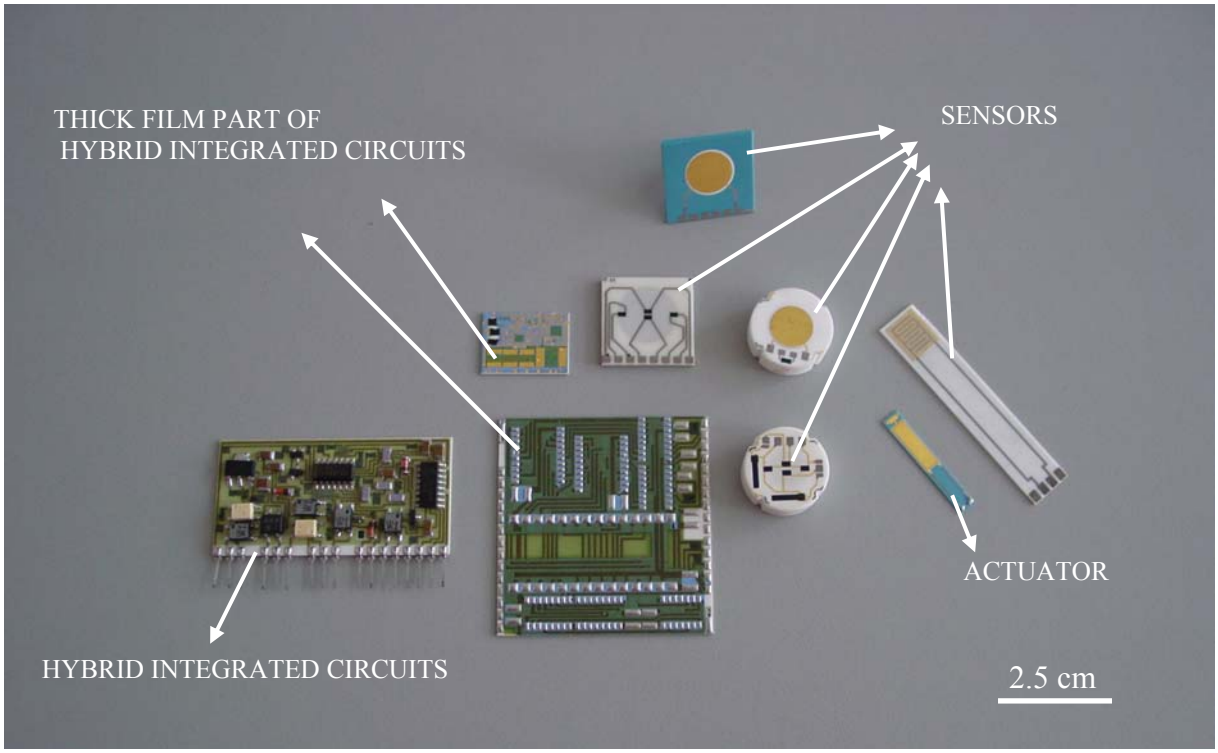

Figure 15: Example of the versatility of thick-film technology: the hybrid integrated circuits, sensors and actuators produced at Institute Jožef Stefan, Electronic Ceramics Department.

Piezoelectric actuators have simple structures, compact sizes, quick responses and they can be positioned precisely, meaning they can be used in many applications such as micro-positioners, miniature ultra sonic motors, and adaptive mechanical dampers [37–40]. In an optical system, for example, an actuator can move a mirror or another optical switch. In mechanical systems, a unimorph or bimorph actuator can activate a suitable mechanical device [41]. Bimorph bender actuators are employed for applications that require a large displacement output, i.e., fluid control devices [37, 39], the cooling of micro-electronic components [42], robotic systems [39], swing CCD (charge-coupled device) mechanisms [37, 43], etc. In Fig. 16 a schematic view, a photograph and a picture of a computational simulation of bending for PZT bimorph bender actuator is shown [44].

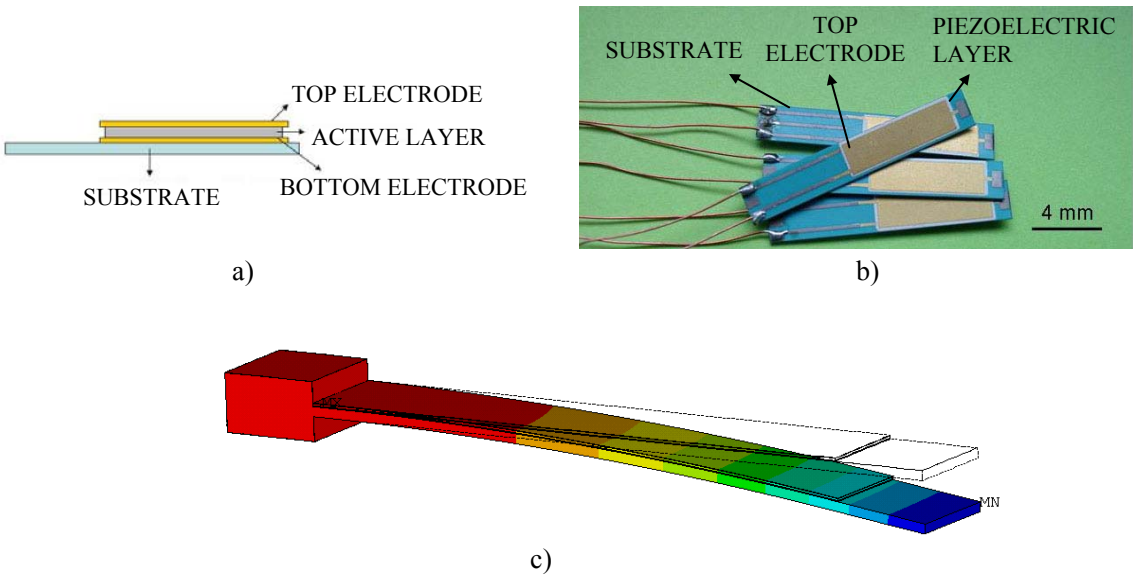

Figure 16: a) Schematic view, b) photograph [44] and c) picture of computational simulation of bending [44] for PZT bimorph bender actuator.

1.3 Properties of (1-x)Pb($Mg_{1/3}Nb_{2/3}$)O_3–x$PbTiO_3$ (PMN–PT)

1.3.1 Phase composition of the PMN–PT material

The phase diagram of the (1-x)Pb($Mg_{1/3}Nb_{2/3}$)O_3–x$PbTiO_3$ (PMN–PT) solid solution is shown in Fig. 17. The elementary cell of PMN–PT material has the cubic Pm-3m perovskite ABO_3 structure. Lead (Pb^{2+}) ions are in the A sides and niobium (Nb^{5+}) ions, magnesium (Mg^{2+}) ions or titanium (Ti^{4+}) ions are in the B sides of the perovskite unit-cell. Below the temperature T_c the crystal structure of PMN–PT material can be tetragonal P4mm, monoclinic Pm and Cm or rombohedral R3m.

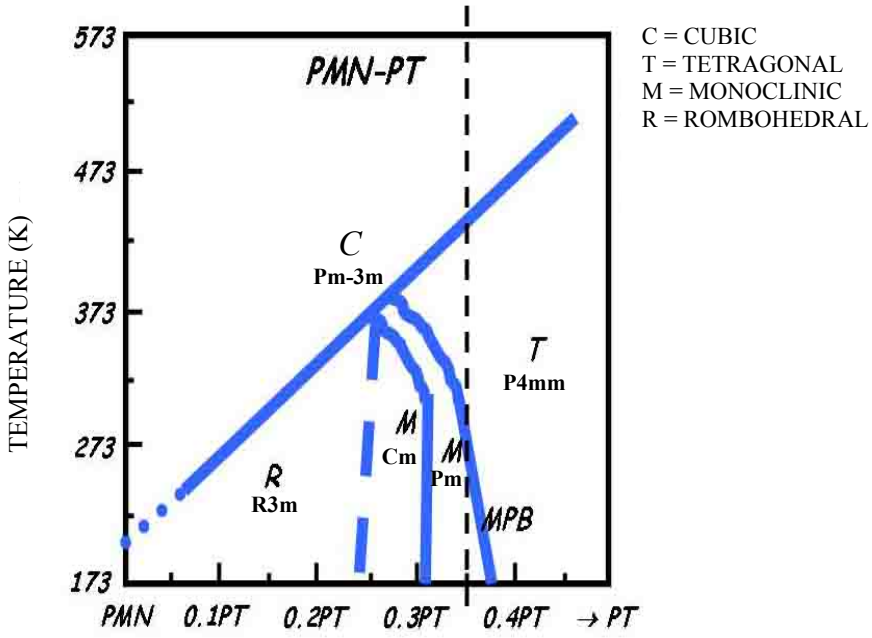

Figure 17: Phase diagram of PMN–PT material [45].

Before 2001, it was believed that in the PMN–PT solid solution the MPB at x ≈ 0.35 separating the rhombohedral from the tetragonal phases [46–48]. In 2001 it was confirmed [49] that the composition of 0.66PMN–0.34PT and 0.65PMN–0.35PT consists of monoclinic phase with the space group Pm and tetragonal phase with the space group P4mm, respectively. The following year also a Pm monoclinic phase for the case of 0.65PMN–0.35PT at room temperature was reported [50]. The Pm space group for the PMN–PT MPB composition was confirmed with X-ray studies at various temperatures [51]. This was in contrast to an earlier study by the same authors that found a monoclinic Cm space group in poled 0.65PMN–0.35PT single crystals [52]. Later results [53–56] showed the coexistence of the monoclinic Pm and the tetragonal P4mm phases at room temperature for bulk 0.65PMN–0.35PT ceramics. In ref. [53] the authors reported around 60% of tetragonal P4mm phase and 40% of monoclinic Pm phase for the 0.65PMN–0.35PT composition. The molar fractions of different phases versus the composition for PMN–PT ceramics are shown in Fig. 18 (a). In Fig. 18 (b) the lattice parameters for the majority phases versus the composition of PMN–PT are shown [53]. In contrast to this in ref. [54] reported 0.65PMN–0.35PT the ceramics monoclinic Pm phase is in coexistence with a minor amount of tetragonal P4mm phase and that the phase ratio depends on the grain size. For 0.65PMN–0.35PT ceramics with the grain size of 4 μm, the phase ratio is 89% of monoclinic Pm phase and 11% of tetragonal P4mm phase, while for the 0.65PMN–0.35PT ceramics with the grain size of 0.15 μm, the phase ratio is 95% of monoclinic Pm phase and 5% of tetragonal P4mm phase [54].

The later reports [55] also describe the high-temperature phase transition between ferroelectric phase and high-temperature relaxor state for 0.8PMN-0.2PT and 0.7PMN-0.3PT ceramics. High-temperature relaxor states were reported for PMN-PT ceramics up to 0.5PMN-0.5PT [56].

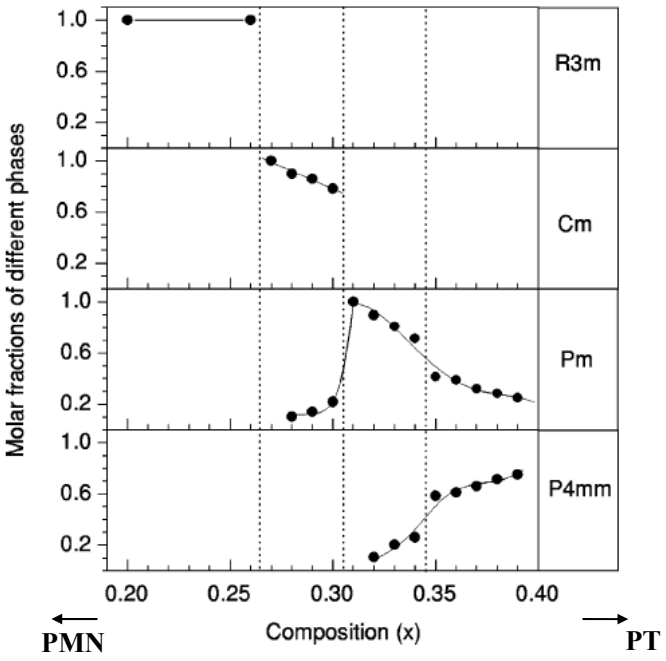

a)

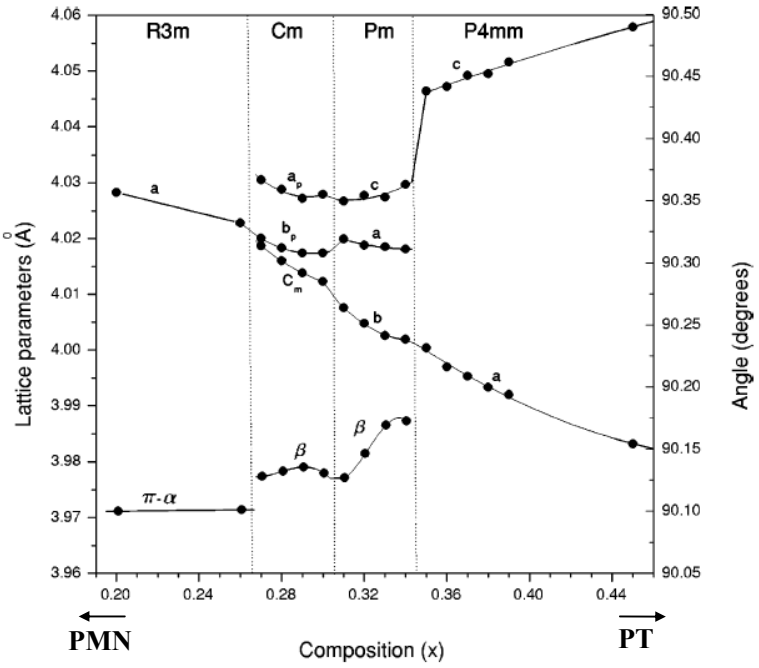

b)

Figure 18: a) The molar fractions of different phases versus the composition for PMN–PT ceramics and b) lattice parameters for the majority phases versus composition of PMN–PT ceramics [53].

1.3.2 Dielectric, piezoelectric and ferroelectric properties of the PMN–PT composition on the morphotropic phase boundary (MPB)

The 0.65PMN–0.35PT composition on MPB has always been the subject of special interest, because it exhibits good piezoelectric properties and a high dielectric constant ε [45, 46, 48, 53]. In the literature different values for ε of 0.65PMN–0.35PT ceramics are reported [48, 53, 57]. The values of ε measured at 1 kHz for non-poled 0.65PMN–0.35PT ceramics varied from 1500 to 6350 [48, 53, 54, 58–60]. The values are dependent on the preparation conditions, the porosity and the average grain size.

In comparison with PMN (x = 0) [61–63], which exhibit relaxor behaviour (Fig. 4), the composition 0.65PMN–0.35PT shows ferroelectric hysteresis [54, 57] and ferroelectric behaviour, i.e., the phase-transition temperature is independent of the frequency of the applied electric field [43, 47, 57] (Fig. 19 a). However, when the average grain size decreases to the submicron range and approaching the nanoscale, the relaxor type behaviour is observed [54] (Fig. 19 b). For submicron-structured 0.65PMN-0.35PT ceramic the relaxor type behaviour was observed down to room temperature [54]. The decrease in grain size also causes a strong decrease of the electrical polarization as it is shown in Fig. 20. The grain size effect was also studied by Carreaud et al. for PMN [64], 0.8PMN-0.2PT [65] and 0.65PMN-0.35PT [64] ceramics.

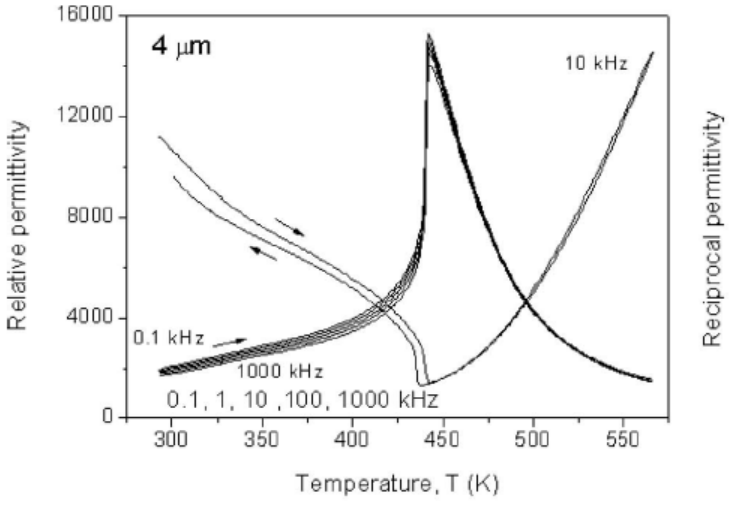

a)

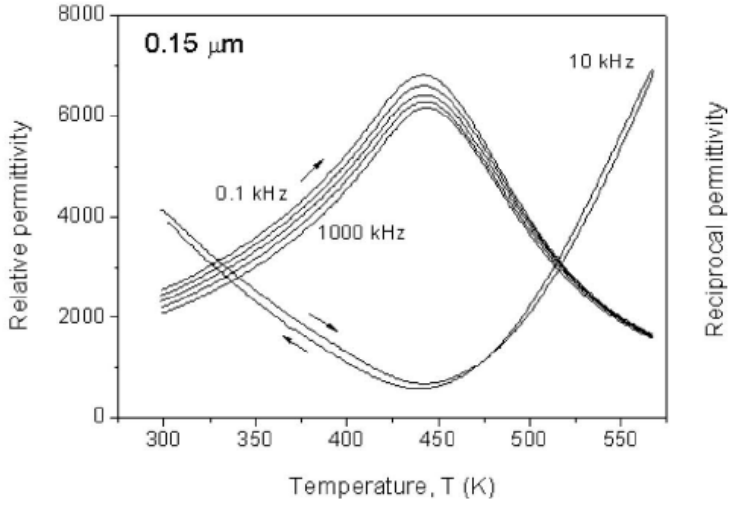

b)

Figure 19: The dielectric constant ε versus temperature for 0.65PMN–0.35PT ceramics with the average grain size of a) 4 μm and b) 0.15 μm [54].

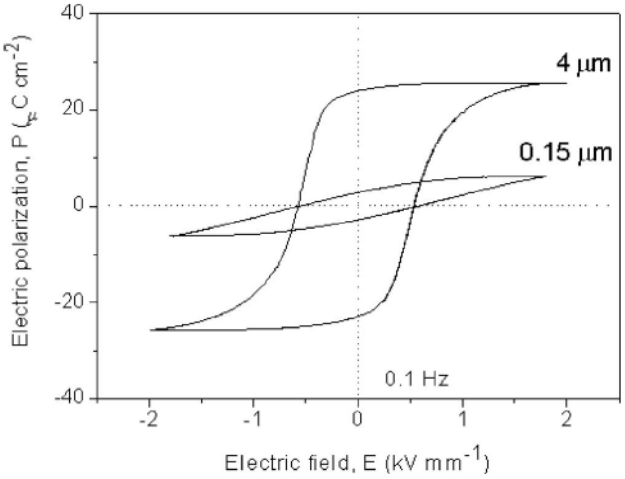

Figure 20: The hysteresis loop measured at 0.1 Hz for 0.65PMN–0.35PT ceramics with the average grain size of 4 μm and 0.15 μm [54].

The values for the piezoelectric coefficients d_{33} of bulk 0.65PMN–0.35PT ceramics in the open literature are from 525 pC/N to 710 pC/N [6, 48, 57, 59, 60]. In ref. [52] the highest d_{33} = 610 pC/N ± 5 pC/N was measured for 0.65PMN–0.35PT ceramics, which were poled at 1 kV/mm. For the 0.65PMN–0.35PT ceramics poled at 3 kV/mm, d_{33} of 525 pC/N and 709 pC/N are reported in ref. [54] and [60], respectively. For the 0.65PMN–0.35PT ceramics poled at 2 kV/mm the value of d_{33} is 700 pC/N [48]. In the same reference the coupling coefficients k_p and k_t for 0.65PMN–0.35PT ceramics are 0.61 and 0.44, respectively. For comparison the d_{33} of PZT, $BaTiO_3$ and $(K,Na)NbO_3$ ceramics are 590 pC/N [6], 190 pC/N [6, 9] and 160 pC/N [9, 66], respectively. The processing conditions, dielectric, piezoelectric, electromechanical and ferroelectric properties of 0.65PMN–0.35 PT ceramics obtained by different groups are collected in Table 1.

Table 1: The processing conditions, dielectric, piezoelectric, ferroelectric properties and coupling coefficients of 0.65PMN–0.35 PT ceramics obtained by different authors. Notation: ε-dielectric constant, d_{33}-piezoelectric coefficient P_r remanent polarization, E_c coercitive field and k_p, k_t coupling coefficients.

Literature	**The processing conditions**	**ε** (frequency)	**d_{33} (pC/N)**	**P_r (μC/cm²)**	**E_c (kV/cm)**	**k_p**	**k_t**
Alguero et al. [54], [57]	mechanochemical sint. T_{firing} 1200°C, 1 hour	~2000 (1kHz)	525	24	5	/	/
Leite et al. [58]	the columbite method hot-pressed T_{firing} 1150°C, 5 hours	~ 4000 (1kHz)	/	33.1 12.3*	4.3 3.3*	/	/
Kelly et al. [48]	the columbite method T_{firing} 1250°C, 1.5 hour	5229 (1 kHz)	700	/	/	0.61	0.44
Xia et al. [60]	T_{firing} 1200°C, 2 hours	4000 (1 kHz)	709	/	/	/	/
Koo et al. [59]	the columbite method T_{firing} 1200–1250 °C, 5 hours	6350 (1 kHz)	610	/	/	/	/
Singh et al. [53]	the columbite method T_{firing} 1260°C, 2 hours	3000 (1 kHz)	/	/	/	/	/
Noblanc et al. [47]	the columbite method T_{firing} 1260°C, time not given	4000 (10 kHz)	/	/	/	/	/
Carreaud et al. [64]	mechanochemical sint. T_{firing} 1200°C, 2.5 hours	1400** (100 kHz)	/	/	/	/	/

/not given, *hot pressed, ** submicron grain size

1.3.3 The 0.65PMN–0.35PT thick films

Just a few articles were reported previously about 0.65PMN–0.35PT thick films [67–71]. The 0.65PMN–0.35PT thick films were prepared by a screen-printing procedure on an Al_2O_3 (alumina) or Si/SiO_2 substrate [67–70]. The influence of the sintering temperature, time and the amount of PbO-containing packing powder were studied [67, 70]. In Fig. 21 the X-ray diagram of 0.65PMN–0.35PT films on alumina substrates sintered at 850°C, 900°C, 950°C [67] and 1184°C [68] are shown. As we can see in Fig. 21, the X-ray spectra are changing with the sintering temperature, i.e., the peak (200) is splitting at the temperature higher than 900°C.

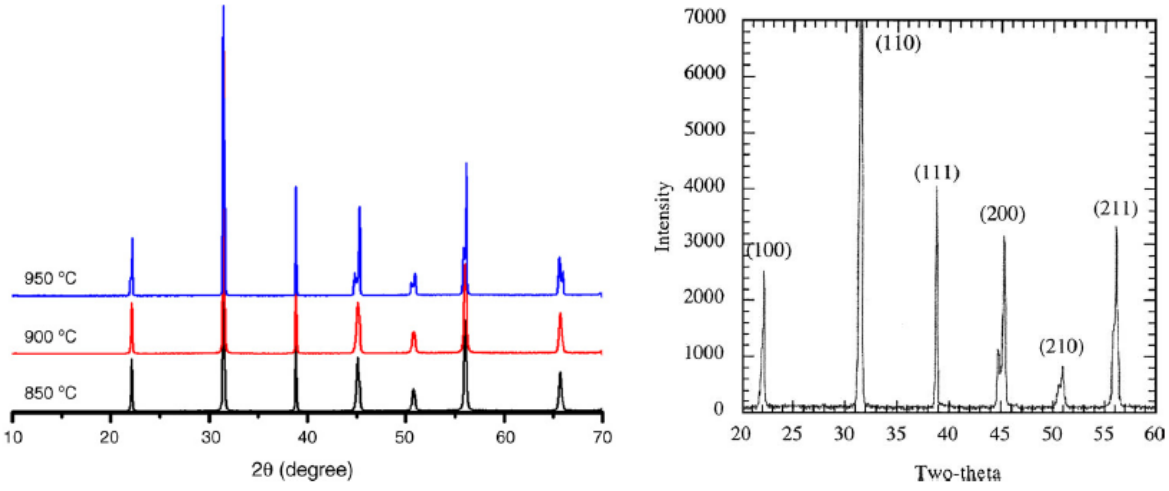

Figure 21: The X-ray diagram of 0.65PMN–0.35PT films on alumina substrates sintered at a) 850°C, 900°C, 950°C [67] and b) 1184°C [68].

The dielectric, ferroelectric and piezoelectric properties of 0.65PMN–0.35PT thick films on alumina substrates were reported [67–70]. Reported values of ε for the 0.65PMN–0.35PT thick films on alumina substrates measured at 1 kHz are 3600–5000 [67–70]. Remanent polarization P_r and coercitive field E_c of the 0.65PMN–0.35PT films on alumina substrates fired at 950°C are 26 μC/cm^2 and 5.7 kV/cm. The piezoelectric coefficient d_{33}^{eff} for 0.65PMN–0.35PT thick films on alumina substrates was determined to be 140–180 pC/N [67, 68, 70]. The dielectric, piezoelectric and ferroelectric properties of 0.65PMN–0.35 PT thick films obtained by different authors are collected in Table 2.

Table 2: Dielectric, piezoelectric, ferroelectric properties of 0.65PMN–0.35 PT thick films obtained by different authors. Notation: ε dielectric constant, d_{33}^{eff} piezoelectric coefficient, P_r remanent polarization and E_c coercitive field.

Literature	**Substrate**	**T_{firing}** (°C)	**ε** (at 1 kHz)	**d_{33}^{eff}** (pC/N)	**P_r** (μC/cm^2)	**E_c** (kV/cm)
Gentile et al. [68]	alumina	1184	5000	180	15.6	6.7
Gentile et al. [69]	alumina silicon	910 890	3800 2200	/	/	/
Kosec et al. [67]	alumina	950	4100	170	26	5.7
Kuščer et al. [70]	alumina	950	3600	140	/	/

/not given

2 Aims and Hypothesis

The solid solutions $xPb(Mg_{1/3}Nb_{2/3})O_3–(1–x)PbTiO_3$ with a morphotropic phase boundary (MPB) composition around $x \approx 0.35$ are a subject of interest, because they exhibit good piezoelectric properties and a high dielectric constant. While there are several publications about bulk ceramics and thin films there are only few reports in the literature about 0.65PMN–0.35PT thick films [67–70]. The major difference between either thin or thick films and bulk ceramics is that films are clamped to rigid substrates.

The aim of the present work was to study the influence of the substrate materials on the structural and electrical properties of 0.65PMN–0.35PT thick films. We assumed that the substrates on which the thick films are clamped can significantly influence the properties of 0.65PMN–0.35PT films, either through interface reactions between the film and substrate or through stresses due to the different temperature expansion coefficients (TEC) between the films and substrates. Also, as already reported for 0.65PMN–0.35PT bulk ceramics, the grain size considerably effects the structural and electrical characteristics [54].

Our hypothesis was that the grain size [54] as well as the mechanical stresses, by analogy with $Pb(Zr,Ti)O_3$ (PZT) thin films [30–33], influence the phase composition of MPB in 0.65PMN–0.35PT thick films. To evaluate these hypothesis thick films were prepared on different kinds of substrates. Two types of substrates with a TEC higher than the TEC of 0.65PMN–0.35PT films, i.e., polycrystalline alumina substrates and metal platinum substrates, one type of substrates with a lower TEC, i.e., AlN substrates and one type made from the material of the same composition as the films. The X-ray analysis was used to determine the phase compositions of the films. The phase ratios were calculated by Rietveld refinements. The microstructures were investigated by scanning electron microscopy and analyzed by energy dispersive X-ray analysis. Young`s modulus was measured by the nanoindentation technique. Electrical characteristic, i.e., dielectric constants vs. temperature, piezoelectric coefficients and ferroelectric hysteresis loops were studied. The correlations between the structural, microstructural and electrical characteristics were obtained. To obtain the optimal poling fields for the 0.65PMN–0.35PT material the influence of the poling field on the structural and electrical properties of densely sintered bulk ceramics was studied.

To compare the structural and electrical properties of films with the stress-free bulk ceramics the 0.65PMN–0.35PT ceramics were sintered under the same conditions (sintering time and temperature) as the films. The microstructure, the phase composition, the Young's modulus and dielectric characteristics were evaluated and the results were compared with those of thick films.

The electrostrctive effect was measured for films on alumina substrates and relatively high values were obtained. Therefore we decided to use thick films as active layers for the actuators. One of the aims was to make the "substrate-free" 0.65PMN–0.35PT/Pt actuator with large displacements. This was realized with thick-film layers on thin free-standing platinum electrodes. Finite element models were used to calculate the bending vs. applied electric field. Results of calculations were compared with the experimental results.

3 Materials and Methods

3.1 Sample preparation

3.1.1 Preparation of the 0.65PMN–0.35PT films on different substrates

The 0.65PMN–0.35PT material was prepared by mechanochemical synthesis using PbO (99.9%, Aldrich), MgO (98%, Aldrich), TiO_2 (99.8%, Alfa Aesar) and Nb_2O_5 (99.9%, Aldrich). A mixture of PbO, MgO, TiO_2 and Nb_2O_5 in the molar ratio corresponds to the stoichiometry of $0.65Pb(Mg_{1/3}Nb_{2/3})O_3$–$0.35PbTiO_3$ (0.65PMN–0.35PT) with 2 mol% excess of PbO. An excess amount of PbO was added for two reasons: to advance the sintering with the formation of a liquid phase rich in PbO and to replace the PbO lost from the PMN–PT during the sintering [70-72]. PbO can evaporate during sintering due to its low melting point (888°C) and high vapour pressure [71]. Mechanochemical synthesis of PMN–PT is published in ref. [73].

The mixture of oxides was high-energy milled in a planetary mill (Retsch, Model PM 400). After mechanochemical synthesis the powder was milled in an attritor mill at 800 rpm for 4 hours in isopropanol, and then dried and sieved using a polyethylene sieve with a 0.5-mm opening. The powder was heated to 700°C for 1 hour.

For thick-film structures the alumina (Al_2O_3), platinum (Pt), 0.65PMN–0.35PT and aluminium nitride (AlN) substrates were used. The alumina substrates were prepared by slip casting from Alcoa A-16 and sintering at 1700°C for 4 hours. Pt substrates were obtained from Zlatarna Celje (Pt 999). 0.65PMN–0.35PT substrates were prepared by pressing the 0.65PMN–0.35PT powder isostatically with the 300 MPa and sintered in a double alumina vessel in 0.65PMN–0.36PT packing powder at 1200°C for 2 hours. AlN substrates (AlunitR) were made by CeramTec. The substrate dimensions are summarized in Table 3.

Table 3: The thickness, shape, dimensions and producer of the Al_2O_3, Pt, 0.65PMN–0.35PT and AlN substrates.

substrate	thickness (mm)	shape	dimensions of the plane	producer
Al_2O_3	3	square	30 x 30 mm^2	Electronic Ceramics Department, JSI
Pt	2	round	2r = 10 mm	Zlatarna Celje
0.65PMN–0.35PT	1.5	round	2r = 12 mm	Electronic Ceramics Department, JSI
AlN	0.64	square	16 x 16 mm^2	CeramTec

The $PbZr_{0.53}Ti_{0.47}O_3$ barrier layer was interposed between an active structure and an Al_2O_3 substrate, as was suggested in ref. [15–17] for the $(Pb,La)(Zr,Ti)O_3$ thick films on Al_2O_3 substrates. The purpose of the $PbZr_{0.53}Ti_{0.47}O_3$ barrier layer was to improve the adhesion between the Pt electrode and the Al_2O_3 substrate and prevent interactions between the 0.65PMN–0.35PT layer and the Al_2O_3 substrate. The $PbZr_{0.53}Ti_{0.47}O_3$ powder with 6 mol% excess of PbO used for preparation of the barrier layers was prepared by mixed-oxide synthesis at 900°C for 1 hour using PbO (99.9%, Aldrich), ZrO_2 (99%, Tosoh), and TiO_2 (99.8%, Alfa Aesar). The $PbZr_{0.53}Ti_{0.47}O_3$ paste for screen printing was prepared from prereacted powders and an organic vehicle, i.e., alpha-terpineol 2-2-butoxy-ethoxy-ethyl acetate and ethyl cellulose in the ratio 60/25/15. The $PbZr_{0.53}Ti_{0.47}O_3$ barrier layer was printed on an alumina substrate. After printing the $PbZr_{0.53}Ti_{0.47}O_3$ layer on the alumina substrate the samples were heated to 500°C for 1 hour to remove the organic compounds

from the $PbZr_{0.53}Ti_{0.47}O_3$ and then sintered at 1100°C for 2 hours. The thickness of the $PbZr_{0.53}Ti_{0.47}O_3$ barrier after firing was around 10 μm.

A platinum paste (Ferro 6412), which was used as a bottom electrode, was printed and fired at 1200°C for 1 hour on 0.65PMN–0.35PT and AlN substrates or on a $PbZr_{0.53}Ti_{0.47}O_3$ barrier layer on the alumina substrate. The thickness of the Pt electrode after firing was around 15 μm. The Pt paste was not screen printed on the Pt substrate, because the Pt substrate itself is conductive.

The 0.65PMN–0.35PT paste was prepared from powders synthesized as described above and an organic vehicle, i.e., alpha-terpineol 2-2-butoxy-ethoxy-ethyl acetate and ethyl cellulose in the ratio 60/25/15. The 0.65PMN–0.35PT paste was printed with intermediate drying at 150°C after each printing step. In Fig. 22 the manual screen printer is shown.

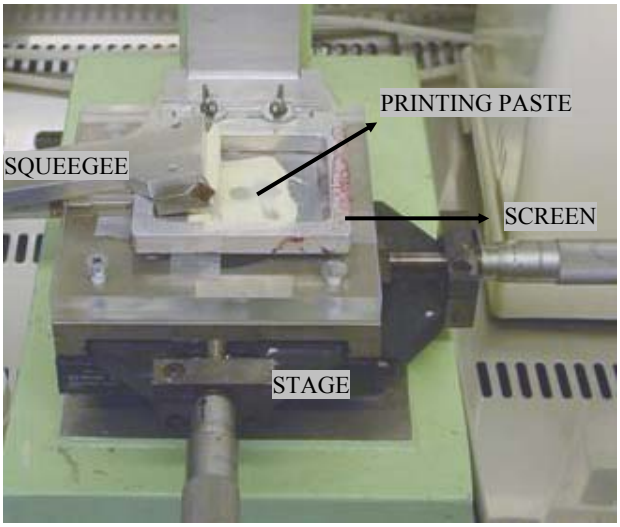

Figure 22: Photograph of the manual screen printer in the laboratory.

The printed samples were then heated for 1 hour to 500°C to evaporate and burn out the organic compounds from the paste. After that the samples were sintered at 950°C for 2 hours in a lead-oxide-rich atmosphere. The heating and cooling rate was 3°C/min. The controlled atmosphere was achieved with the addition of the packing powder with the composition of $PbZrO_3$ with 2 mol% excess of PbO [70]. The sintering vessel and the arrangement of the packing powder during sintering are shown in Fig. 23.

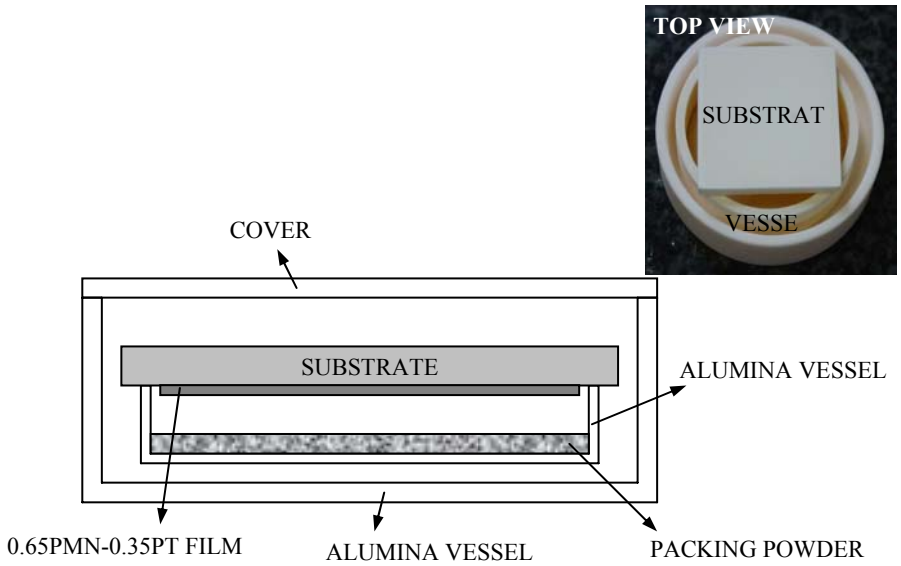

Figure 23: The sintering vessels and the arrangement of packing powder during the sintering of the 0.65PMN–0.35PT films.

For the electrical measurements, the top gold electrodes were deposited by sputtering (5PASCAL SRL). The diameters of the electrodes were 1.5 mm or 3 mm and the thickness of the top electrodes was around 100 nm. The thicknesses of the fired films were measured with the profilometer (Form Talysurf Series 2, Taylor-Hobson Ltd., Leicester, G. B.). For films prepared by two printed, dried and fired layers on Al_2O_3, Pt, 0.65PMN–0.35PT and AlN substrates the thicknesses were 21 µm, 20 µm, 26 µm and 34 µm, respectively. In Fig. 24 the scheme of the cross-sections of the 0.65PMN–0.35PT films on the Al_2O_3 substrate with the interposed $PbZr_{0.53}Ti_{0.47}O_3$ barrier layer and on Pt, 0.65PMN–0.35PT and AlN substrates are shown schematically. In Fig. 25 the top view photographs of the 0.65PMN–0.35PT films are shown.

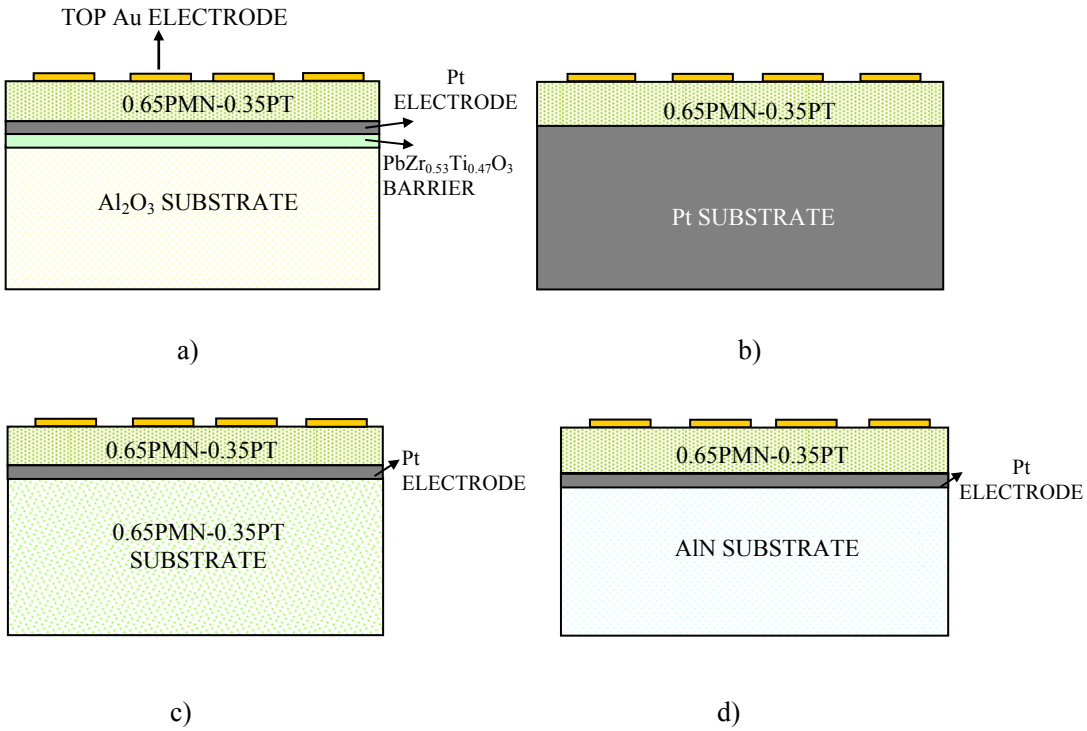

Figure 24: The schemes of the cross-sections of the 0.65PMN–0.35PT films on a) Al_2O_3, b) Pt, c) 0.65PMN–0.35PT and d) AlN substrates.

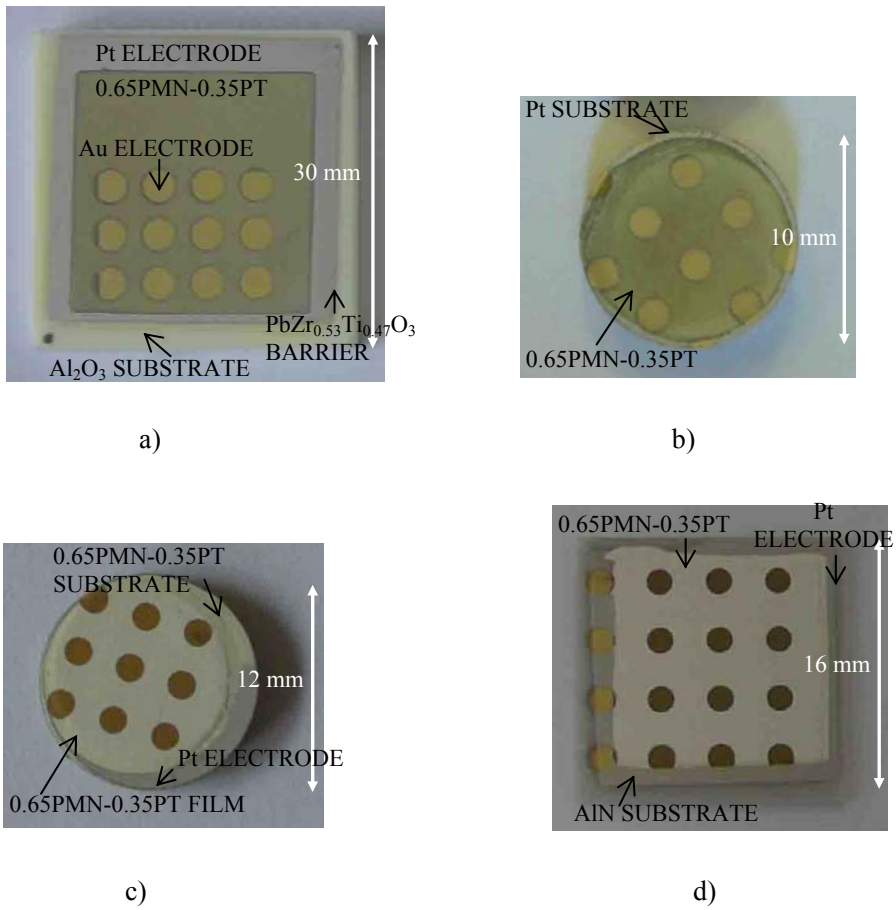

Figure 25: The 0.65PMN–0.35PT films on a) Al_2O_3, b) Pt, c) 0.65PMN–0.35PT and d) AlN substrates.

3.1.2 Preparation of the 0.65PMN–0.35PT bulk ceramics

The 0.65PMN–0.35PT bulk ceramics were prepared from the powder prepared in the same way as it is explained in section 3.1.1. The powders were pressed in a steel mould with 500 kg/cm^2. The compacts were then pressed isostatically with 300 MPa and sintered in a double alumina vessel in 0.65PMN–0.35PT packing powder at 950°C for 2 hours. This low temperature of the firing was chosen to have the same sintering conditions for bulk ceramics as for 0.65PMN–0.35PT films. The thicknesses and the diameters of the pellets were 0.8 mm and 6 mm, respectively.

The 0.65PMN–0.35PT bulk ceramics fired at 1200°C for 2 hours were also prepared. The firing temperatures for this composition are over 1100°C [58]. These ceramics were sintered from the powder, which was prepared by the same procedure as previous one (section 3.1.1), but without excess of PbO. The reason for this was a preliminary study [74], which shows that density, dielectric constant ε, coupling coefficient k_p and remanent polarization P_r of 0.65PMN–0.35PT ceramics sintered from powder with 2 mol% excess of PbO are lower as for ceramics sintered from powder without excess of PbO. The powders were pressed in a steel mould with 500 kg/cm^2. The powder compacts were then pressed isostatically with 300 MPa and sintered in a double alumina vessel at 1200°C for 2 hours.

The arrangement of the packing powder during sintering is shown in Fig. 26a. The heating and cooling rate was 3°C/min. After sintering the pellets were cut, polished and annealed at 600°C for 1 hour with a cooling rate of 1°C/min. The pellets had a diameter of 6 mm and were 0.6 mm thick. For the electrical measurements, the gold electrodes, 5 mm in diameter, were deposited by sputtering. In Fig. 26b the photograph of the 0.65PMN–0.35PT bulk sample is shown.

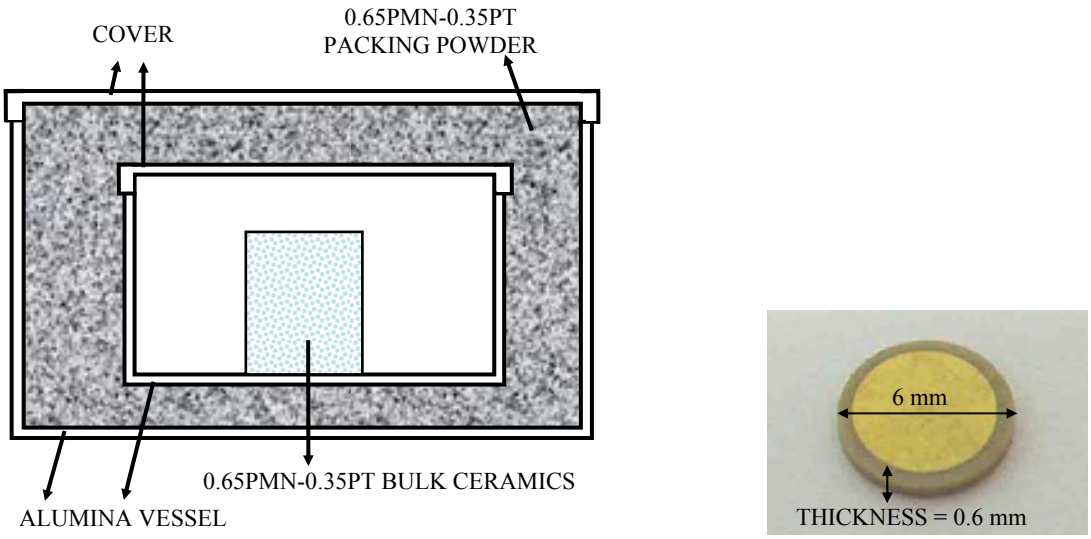

Figure 26: a) The arrangement for sintering of the 0.65PMN–0.35PT bulk ceramics and b) the photograph of the 0.65PMN–0.35PT ceramics after cutting, polishing and after deposition of the electrodes. Thickness of the pellets and diameter of the pellets are 0.6 mm and 6 mm, respectively.

3.1.3 Preparation of the 0.65PMN–0.35PT/Pt actuators

The 0.65PMN–0.35PT/Pt actuators were prepared with a new procedure, which we developed. In the preparation procedure of the high bending actuator it is important to prepare the actuator on the thin substrate. For this reason we developed a new approach to prepare a 0.65PMN–0.35PT actuator clamped only on thin Pt support. The 0.65PMN–0.35PT/Pt actuators were, at the end of the procedure, removed from the thick alumina substrates. This was possible to realize due to the bad adhesion between the platinum electrode and the alumina substrate [15, 16].

For the films on the alumina substrates, the bad adhesion among the bottom platinum electrodes and alumina substrates was observed. The same phenomena was observed for other lead-containing perovskite, i.e., $(Pb,La)(Zr,Ti)O_3$ (PLZT) [15-17]. The 0.65PMN–0.35PT film with the Pt electrode (the 0.65PMN–0.35PT/Pt composite) peeled off from the alumina substrates after firing. On the Pt, 0.65PMN–0.35PT and AlN substrates, the bad adhesion among the film-electrode and the substrate was not observed.

The micrograph of the surface of the alumina substrate after the peeling off of the 0.65PMN–0.35PT/Pt composite is shown in Fig. 27. The inset in Fig. 27 shows the photograph of the alumina substrate after peeling off of the 0.65PMN–0.35PT/Pt composite.

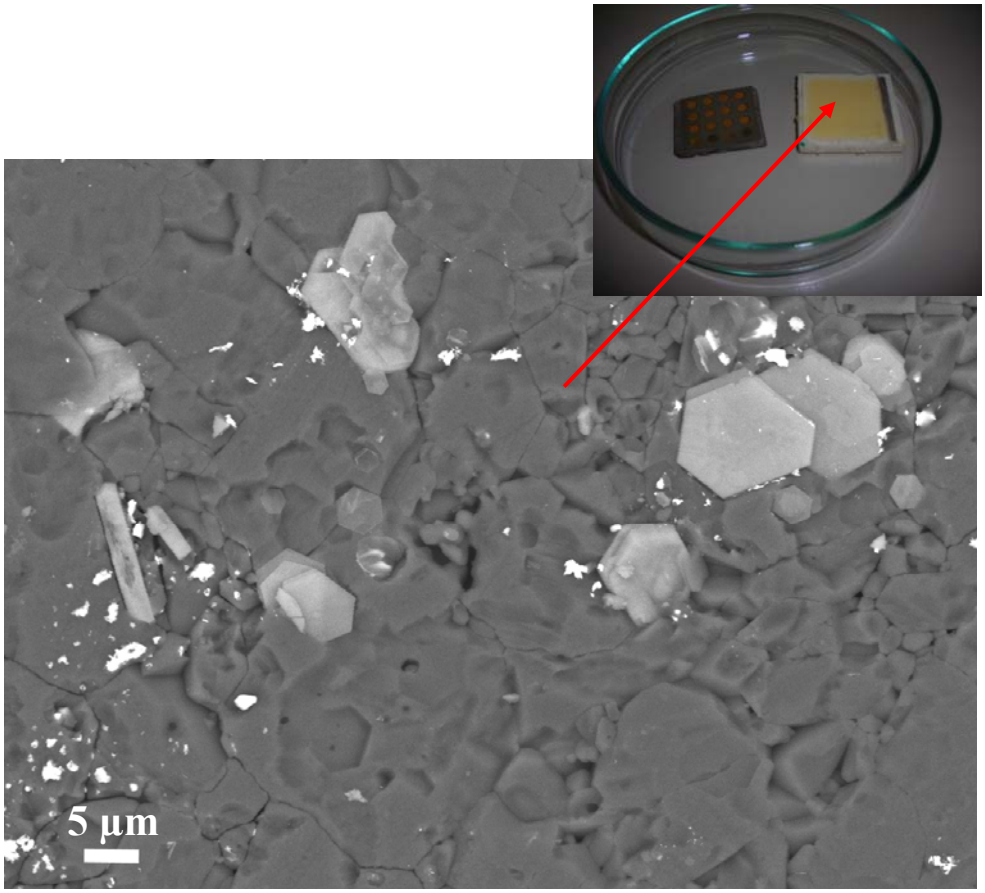

Figure 27: Microstructure of the surface of the alumina substrate after the peeling off of the 0.65PMN–0.35PT/Pt composite. Inset shows the photograph of the alumina substrate after peeling off of the 0.65PMN–0.35PT/Pt composite. The yellow colour of the substrates shown in the inset is due to the reaction between PbO from the film and alumina substrates.

Light hexagonal grains are clearly visible in the Fig. 27. The EDXS analysis of these light hexagonal grains on the surface of the alumina substrate showed a strong peak of Al as well as peaks of Pb (Fig. 28). Similar crystals were identified at the interface Al_2O_3-Pt on the (Pb,La)(Ti,Zr)O_3 (PLZT) thick films on a Pt-coated alumina substrate [15-17]. This also suggests that in the case of 0.65PMN–0.35PT films on alumina the light phase is β-alumina with the approximate formula $PbAl_{12}O_{19}$. The crystals are formed due to the diffusion of PbO from the 0.65PMN–0.35PT layer through the pores in Pt electrode, to the surface of the alumina substrate during the firing. The β-alumina crystals presumably "pushed off" the Pt electrodes together with 0.65PMN–0.35PT layer during the firing cycle.

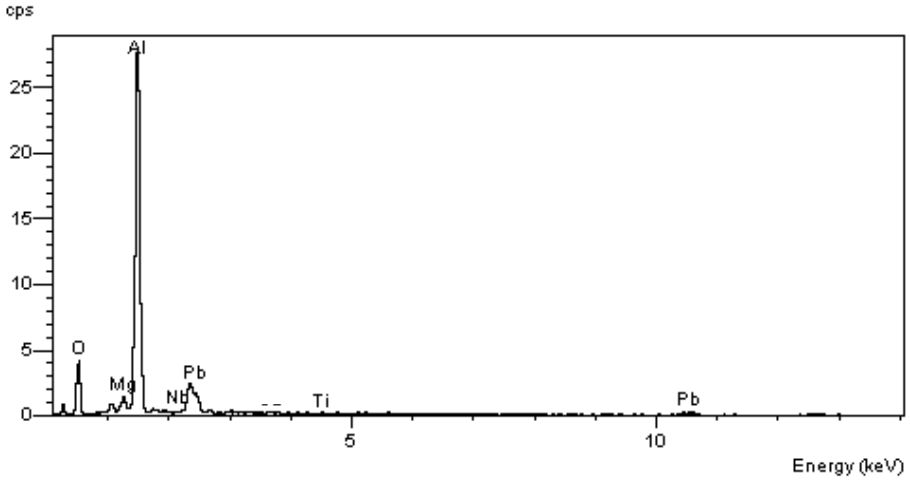

Figure 28: EDXS analysis of the white crystals on the surface of Al_2O_3 substrate, beside strong peaks of Al, peaks of Pb are also detected.

To confirm the above mentioned hypothesis the samples without Pt electrodes were also prepared. The 0.65PMN–0.35PT films were screen-printed directly onto the alumina substrates and fired under the same conditions. As expected, the β-alumina crystals formed, as is shown in Fig. 29.

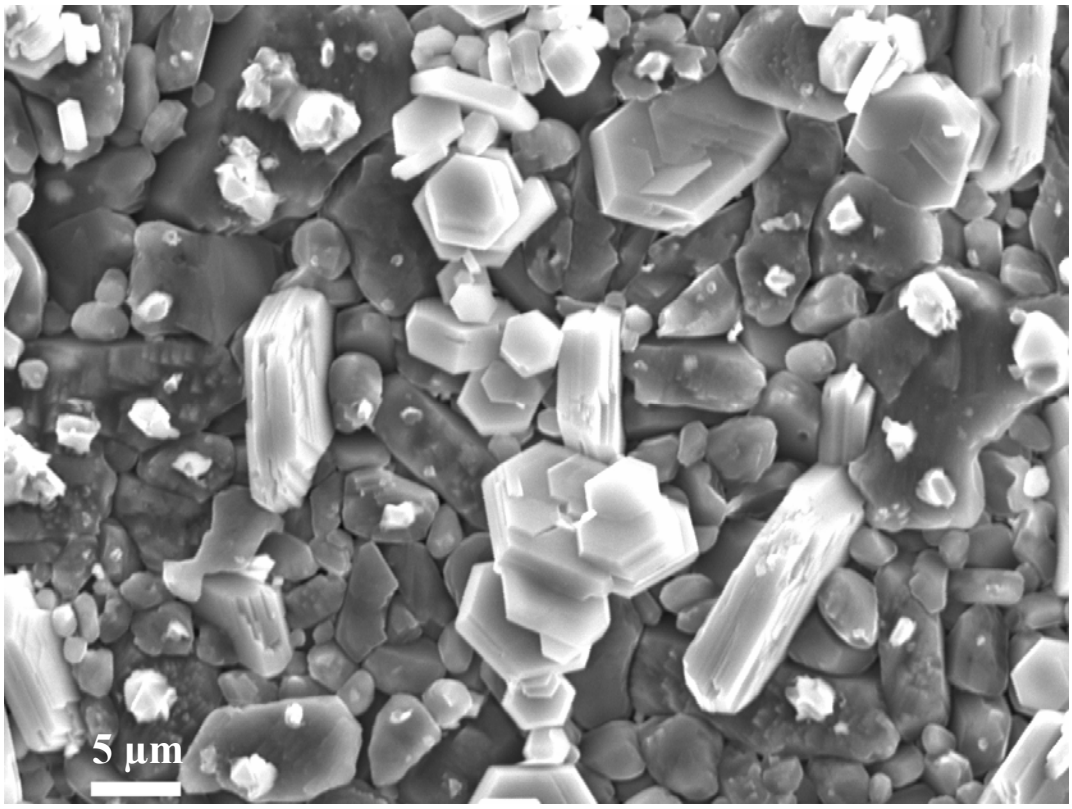

Figure 29: Microstructure of the surface of the alumina substrate after firing the 0.65PMN–0.35PT film at 950°C for 2 hours. The lighter hexagonal grains are PbO-stabilised β-alumina on the surface of darker alumina substrates.

A platinum paste (Ferro 6412), which was used as a bottom electrode, was printed two times and fired at 1200°C for 1 hour on an alumina substrate. The thickness of the Pt electrode after firing was around 15 µm. Eight 0.65PMN–0.35PT layers were screen printed and fired for 2 hours at 950°C, as explained in section 3.1.1. The films thicknesses after sintering were 50 µm. The masks for sputtering were made from pasteboard and fixed with the scotch tape to the surface of the 0.65PMN–0.35PT films. The top gold electrodes were deposited by sputtering (5PASCAL SRL). In Fig. 30 the cross-section of the 0.65PMN–0.35PT films on alumina substrates prepared for the 0.65PMN–0.35PT/Pt bimorph actuator realization is shown schematically.

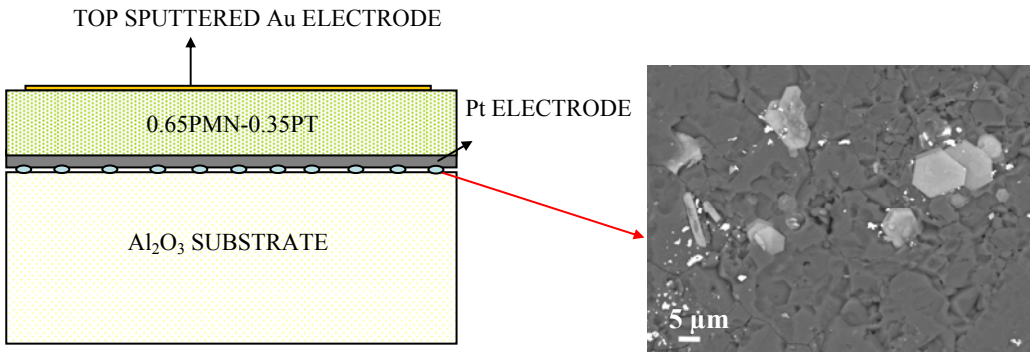

Figure 30: The scheme of the cross-section of the 0.65PMN–0.35PT films on alumina substrates prepared for the 0.65PMN–0.35PT/Pt bimorph actuator realization. Inset: Microstructure of the surface of the alumina substrate after the peeling off of the 0.65PMN–0.35PT/Pt composite. β-alumina crystals are visible.

The 0.65PMN–0.35PT thick films were then peeled off from the substrates together with the Pt

electrodes. The 0.65PMN–0.35PT thick film and the bottom Pt electrode were used for the realisation of the bimorph actuators. In Fig. 31 the four steps for realising the actuators are presented schematically. In the first step the 0.65PMN–0.35PT film structures were prepared. In the second step the alumina supports were glued on the top of the 0.65PMN–0.35PT layers. In the third step the 0.65PMN–0.35PT/Pt composites that were glued on the alumina supports were removed from the alumina substrates. In the fourth, and final, step the alumina supports were removed. The glue was dissolved in acetone and the 0.65PMN–0.35PT/Pt actuators were then ready for testing.

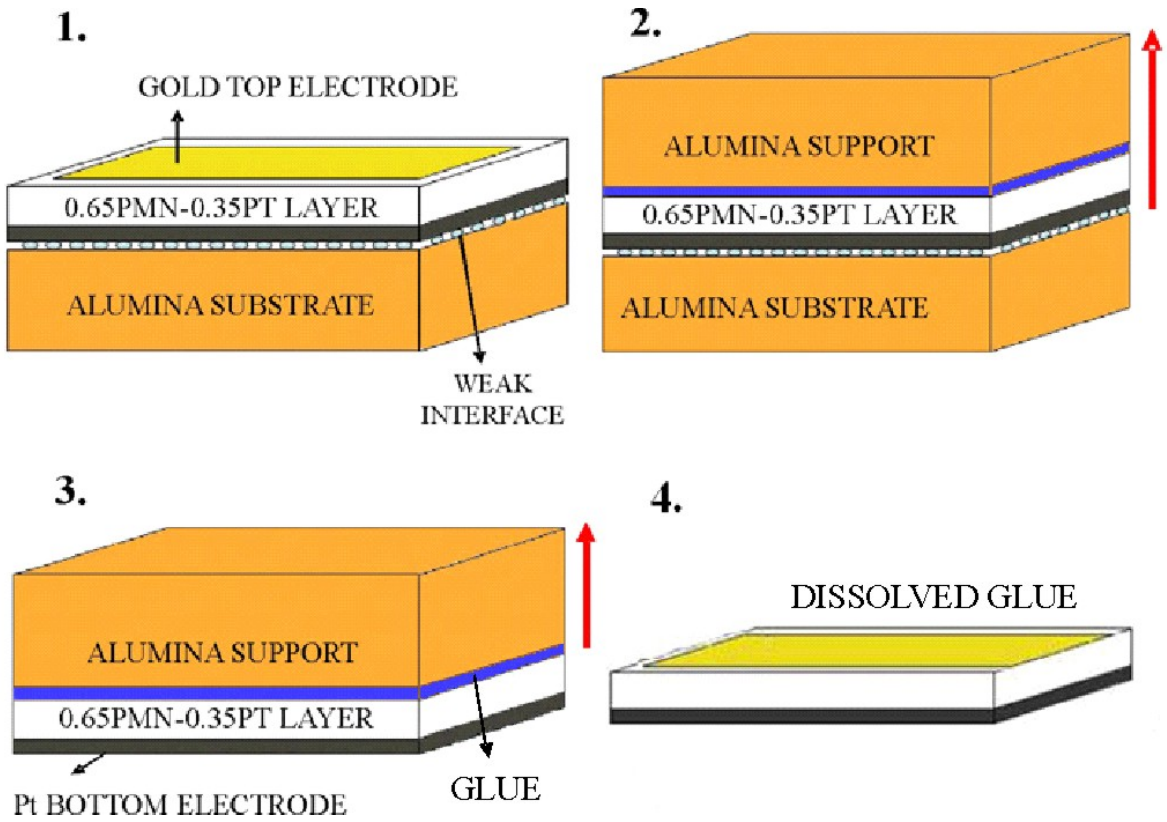

Figure 31: A schematic view of the actuator's realization in four steps.

The dimensions of the actuator's 0.65PMN–0.35PT layers were 1.8 cm × 2.5 mm × 50 µm. In Fig. 32 the scheme of the cross-section and the photograph of the top view of the 0.65PMN–0.35PT/Pt bimorph actuator are shown.

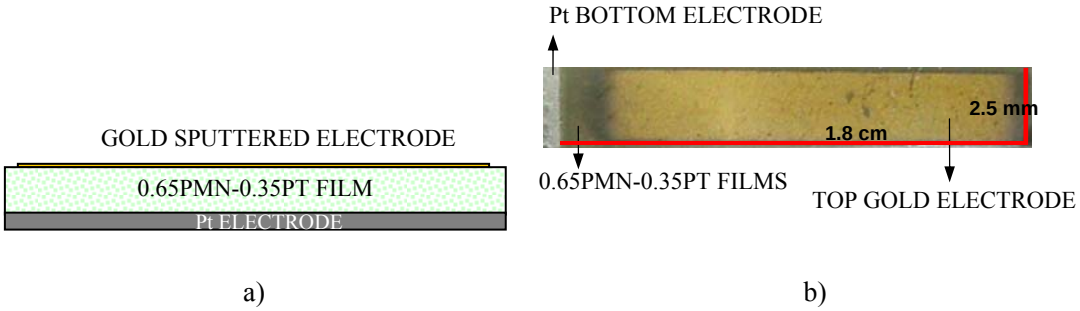

Figure 32: a) The scheme of the cross-section and b) the photograph of the top view of the 0.65PMN–0.35PT/Pt bimorph actuators.

3.2 Characterization

3.2.1 Structural characterization

3.2.1.1 Granulometry

The size of the particles in the starting 0.65PMN–0.35PT powder prepared by the mechanochemical synthesis and heated at 700°C for 1 hour was determined by a light-scattering technique using a Microtrac S3500 Series Particle Size Analyzer instrument. All the measurements were performed in isopropanol. The results were derived from the area particle size distribution. The most common parameter used is the median particle size d_{50}, where the area of all particles smaller than d_{50} accounts for 50% of the area of all the particles.

3.2.1.2 X-ray diffraction analysis

The 0.65PMN–0.35PT powder was analyzed at room temperature by X-ray diffraction analyses with a Philips PW 1710 X-ray diffractometer using Cu-K_α radiation (wavelength 1.3922 Å). The X-ray spectra were measured from $2\theta = 5°$ to $2\theta = 85°$ using a step of 0.016° and a dwell of 100 seconds per step.

The 0.65PMN–0.35PT films on Al_2O_3, Pt, 0.65PMN–0.35PT and AlN substrates and non-poled and ceramics poled with different poling fields were analyzed at room temperature by X-ray diffraction analyses with a Panalytical XPert Pro HTK diffractometer using Cu-K_α radiation. The X-ray spectra were measured from $2\theta = 10°$ to $2\theta = 70°$ using a step of 0.033° and a dwell of 1 second per step. The X-ray diffraction measurements of the poled ceramics were performed through the sputtered gold electrode.

The X-ray diffractions of the 0.65PMN–0.35PT films were also measured with an X-ray diffractometer (made in Laboratory Structure, Ecole Polytechnic, Paris) using Cu-K_β radiation (wavelength 1.54051 Å) at different temperatures: from -173°C to 127°C using a step of 20°C and from 127°C to 200°C using a step of 10°C. The X-ray diffractions were measured within three intervals: from $2\theta = 39.75°$ to $2\theta = 41.25°$, from $2\theta = 58.00°$ to $2\theta = 59.5°$ and from $2\theta = 73.00°$ to $2\theta = 74.3°$ using a step of 0.01°.

The phase composition was determined with a Rietveld analysis of the diagrams, using the software Jana2006 [75]. Structure refinement using the Rietveld method [76, 77] consists of the simulation of the entire diagram, bringing the peak position, intensity and profile as close to the experimental ones as possible by changing the unit-cell parameters and the atomic positions. The reliability factors R_{Wall} (noted as R) of the profile are used to estimate the relevance of the results. The reliability factors are different for each phase. For example, R_M is the reliability factor for the monoclinic phase and R_T is the reliability factor for the tetragonal phase of the Rietveld analysis. The factor Gof is the factor of validity of the profile, called the goodness of fit. In the ideal case the goodness of the fit is 1, which means that the experimental error of the diffraction diagram is equal to an error made by calculation.

We used the starting unit-cell parameters and atomic positions of the PMN–PT material from a former Rietveld study made by Singh et al. [53]. In the case of poled ceramics the presence of the sputtered-gold upper electrodes decrease the general quality of the data. The atomic positions proposed by Singh et al. were not modified. The background, the shift, the unit-cell parameters, the profile parameters, the phase ratio and the preferential orientation were refined to obtain the lowest reliability factors.

3.2.1.3 Scanning electron microscopy with energy-dispersive X-ray analysis (EDXS)

The powder morphology was analyzed using field-emission scanning electron microscopy (FE-SEM, Supra 35 VP, Carl Zeiss). The powders were dispersed in acetone under ultrasound, and a few drops were spread on highly oriented pyrolytic graphite substrates.

For the microstructural and compositional analyses of the 0.65PMN–0.35PT films and bulk ceramics a scanning electron microscope (SEM) A JEOL JSM 5800 equipped with Link ISIS 300, Oxford Instruments energy-dispersive X-ray analyser (EDXS) at 20 kV was used. The semi-quantitative standard-less compositional analyses were performed. For the analysis of cross-sections of the films and bulks the samples were cut, mounted in epoxy in a cross-sectional orientation and polished using standard metallographic techniques. Prior to analysis in the SEM, the samples were coated with carbon to provide electrical conductivity and to avoid charging. The EDXS micro-analyses were made either in a "point" (note that the analysed area/volume is more than 1 μm x 1 μm^2 = 1 μm^3) or over an area ("over the window"). The dimensions of the analysed areas will be stated for all results. For the micrograph of the 0.65PMN–0.35PT film on the AlN substrate and the bulk ceramics fired at 950°C the FE-SEM, Supra 35 VP, Carl Zeiss was used at 5 kV.

3.2.1.4 Transmission electron microscopy with EDXS

For the transmission electron microscope TEM (JEM 2010F) observation, the cross-sections "sandwich" type of preparation technique was employed. Two pieces of layer structure (head to head) were first glued together with highly dispersed epoxy glue and afterwards glued into the alumina tube. After the hardening of the glue, the tube was cut into 500-μm-thick disks with a wire–saw. The disks were then ground mechanically to approximately 100 μm and dimpled from one side so that the middle part of the disk achieved a thickness of approximately 25 μm. Finally, an ion-milling procedure with 3.8-keV argon ions was applied. The areas adjacent of the specimen hole were used for the TEM observation. The EDXS analyses of nano-regions were performed by Link ISIS 300, Oxford Instruments at 200 kV.

3.2.1.5 Density

The density of the sintered ceramics [g/cm^3] was determined by measuring the mass and dimensions using the equation:

$$\rho = \frac{m}{V} = \frac{m}{\frac{\pi \cdot d^2}{4} \cdot h}, \qquad (11)$$

where

m.....mass [g]
d……..diameter [cm]
h……. thickness [cm]
V……..volume [cm^3]

The theoretical density of the 0.65PMN–0.35PT material was calculated from the cell parameters, obtained from X-ray diffraction, and using the stoichiometric composition.

3.2.1.6 Median grain size and porosity

For the grain size estimation the polished cross-sections of the samples were thermally etched. The temperature of the thermal etching was 50°C below the sintering temperature of the samples. The bulk 0.65PMN–0.35PT ceramics fired at 1200°C were thermally etched at 1150°C for 20 minutes in the PbO-rich atmosphere. The 0.65PMN–0.35PT films were thermally etched at 900°C for 20 minutes. After

thermal etching the SEM micrographs of the samples were made. Due to the low density of the 0.65PMN–0.35PT films on the AlN substrate and the bulk fired at 950°C the grain sizes for these samples were determined from the micrographs of the surface and the micrographs of the fracture surface, respectively. The estimated grain sizes of the films of different thicknesses (section 4.3.1.7) were determined from the surface micrographs. The grains were copied to the transparent foil and the image was digitalized. Feret's diameter (d_F) was used to get a median value of the grain size using microscopic measurements. The digitalized image was analyzed by the program UTHSCSA image Tool (UTHSCSA Image Tool Version 3.00, 2002) [78]. Note that the median grain size calculated from the SEM cross-section micrograph is in fact the value obtained from the measurement performed on the 2D cut and therefore smaller than the actual median grain size. However, the calculated values are later in the text called the median grain sizes of the particles.

For the estimation of the porosity, the cross-sections of the samples were polished. The SEM micrographs of the samples were made. The porosity was then copied to the transparent foil and the image was digitalized. The area of the pores was analysed by the program UTHSCSA image Tool (UTHSCSA Image Tool Version 3.00, 2002).

3.2.2 Mechanical characterization

3.2.2.1 Determination of Young's moduli

The Young's moduli Y of the 0.65PMN–0.35PT films were measured by the nanoindentation technique (ASTM Standard C 1161-90). The measurements of the indentation modulus were conducted using a Fisherscope H100C [79]. The important advantage of this technique is that it is a local measurement and only small volumes of the material are needed. For the measurements the most important requirement is that the film must be thick enough to avoid the influence of the substrate [44, 80].

The diamond Vickers tip was used. A load of 1 N was applied to press the indenter into the surface of the samples at different positions on the surface. In the standard for measurements [81] it is reported that the results should not be affected by the presence of an interface. The test piece thickness should be 10 x the indentation depth or 3 x the indentation diameter. The maximum indentation depths were less than 5 μm (the film thickness was 50 μm), which fulfils the first condition. The second condition was also fulfilled for bulk ceramics fired at 1200°C and 950°C. The technological process for the preparation of the crack-free films allowed the maximum thickness of 110 μm. Therefore, we assumed that the comparisons between the results obtained for different films are still reliable. The load 1 N was chosen to exclude the contribution of the surface roughness to the measured value.

The Young's moduli Y_{33} were calculated from the equation:

$$Y = \frac{Y_{MEASURED}}{(1-\nu^2)}\ , \qquad (12)$$

where $Y_{MEASURED}$ is a measured value determined by the nanoindentation technique and ν is the Poisson's ratio of the material [82]. The assumption was made that the Poisson's ratio of the 0.65PMN–0.35PT films was the same as the Poisson's ratio for the bulk PMN ceramics from the ref. [83], i.e., ν = 0.3. On every sample seven measurements were made and the results were averaged.

3.2.2.2 The coefficient of thermal expansion (TEC) by dilatometer

The thermal expansion coefficient (TEC) of the sintered bulk 0.65PMN–0.35PT was determined using a dilatometer (Netzsch DIL 402EP). Samples were in the form of test cylinders with diameters 2r = 7.5 mm and lengths d = 27 mm. The measurements of the sample expansion versus the temperatures were made in the temperature range from 30–490 °C at temperature intervals of 10°C.

3.2.3 Electrical characterization

3.2.3.1 Dielectric and ferroelectric measurements

The capacitance (C) and dielectric losses (tg δ) were measured by a HP 4284 A Precision LCR Meter at several frequencies and the dielectric constants (ε) were calculated from the capacitance measurements. The dielectric constants (ε) and the dielectric losses (tg δ) vs. temperature were determined in the temperature range from -130°C to 300°C. The measurements from -130°C to 70°C, were made in a vacuum chamber. The measurements from 70°C to 300°C were made in a furnace in air. The measurements were made using a step 1°C.

The ferroelectric hysteresis loops were measured by an Aixact TF Analyser 2000 and the high voltage amplifier TREK 609E-6 at frequencies 50 Hz. An external sinusoidal AC voltage was applied between the top and bottom electrodes of the measured samples. The remanent polarization P_r and the coercive field E_c were determined from measured hysteresis loops. In Fig. 33a the setup for measuring the ferroelectric hysteresis loops is shown. Fig. 33b shows the micro-manipulator stage with the thick-film sample.

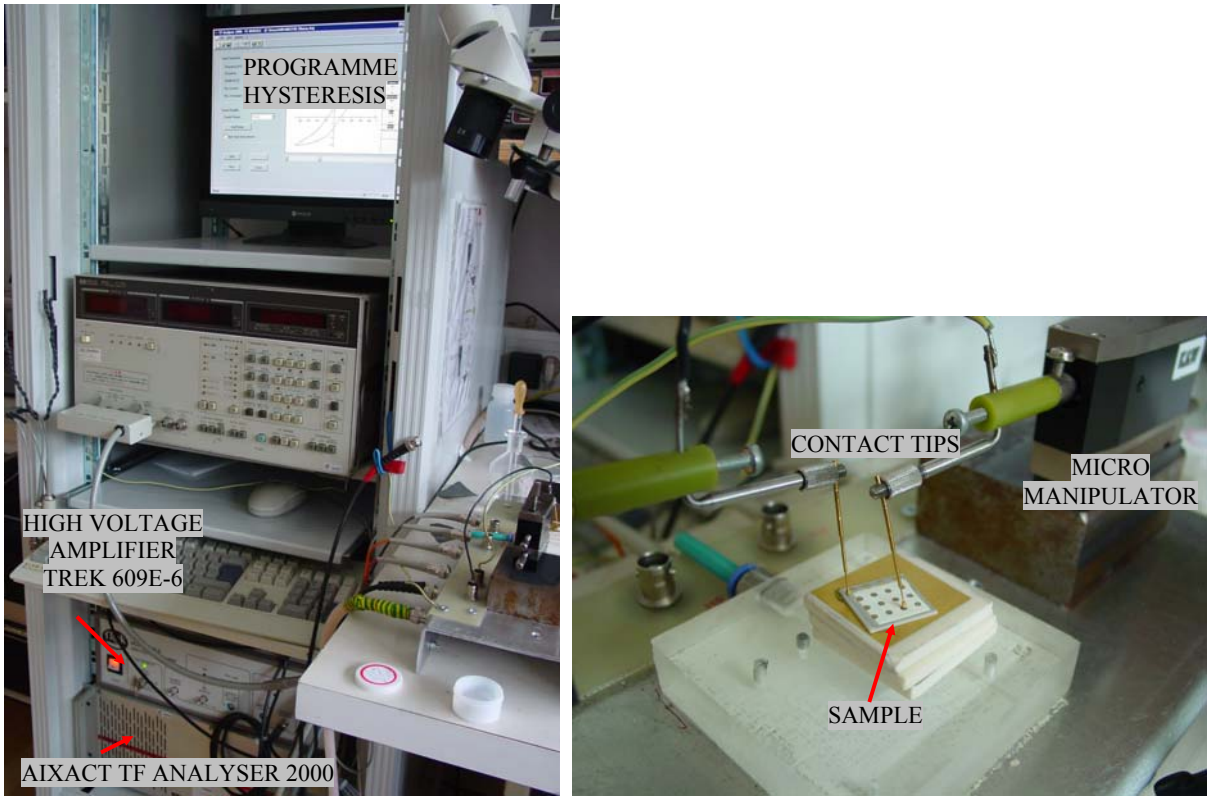

a) b)

Figure 33: a) The setup for measuring the ferroelectric hysteresis loops; an Aixact TF Analyser 2000, high voltage amplifier TREK 609E-6 and computer. b) Micro manipulator stage with the thick-film sample.

3.2.3.2 Poling

An external DC voltage was applied between the top and bottom electrodes of the samples with a high-voltage supply KEITHLEY MODEL 248. The samples were placed in silicon oil and heated to 160°C. In Fig. 34 the photograph of the poling setup is shown. The inset shows the 0.65PMN–0.35P thick-film sample placed on the poling stage between the contact tips.

a) b)

Figure 34: a) The poling setup; high voltage supply KEITHLEY MODEL 248. b) 0.65PMN–0.35P thick-film sample placed on the poling stage between contact tips.

The poling fields of 2.5 kV/mm and 3.5 kV/mm are the most common poling fields reported in the literature for 0.65PMN–0.35PT bulk ceramics and thick films [54, 57, 60, 68, 71]. However, in the literature no systematic study of the poling fields for 0.65PMN–0.35PT ceramics or films was made. Due to this the 0.65PMN–0.35PT bulk ceramics were poled with electric fields of 0.5 kV/mm to 4.5 kV/mm at 160°C for 5 minutes and then cooled in the same bias field, i.e., the field cooling (FC) run, with the intention to find the most proper poling field. After the systematic study of the poling conditions, 0.65PMN–0.35PT thick films were poled with an electric field of 2.5 kV/mm at 160°C for 5 minutes and then FC. The poled samples were aged for 24 hours. The 0.65PMN–0.35PT/Pt actuators were poled with an electric field of 2.5 kV/mm at 160°C for 5 minutes and then FC before being peeled off the substrate. After removal from the substrates, the actuators were aged for 24 hours.

3.2.3.3 Measurements of coupling coefficients of bulk ceramics

The coupling coefficients k_p and k_t of the poled ceramics were determined with the resonance method [84]. The impedance for the bulk 0.65PMN–0.35PT ceramics was measured from the frequencies of the applied field 1 Hz - 10 MHz with the BODE 100 Omicron Lab, which is shown in Fig. 35.

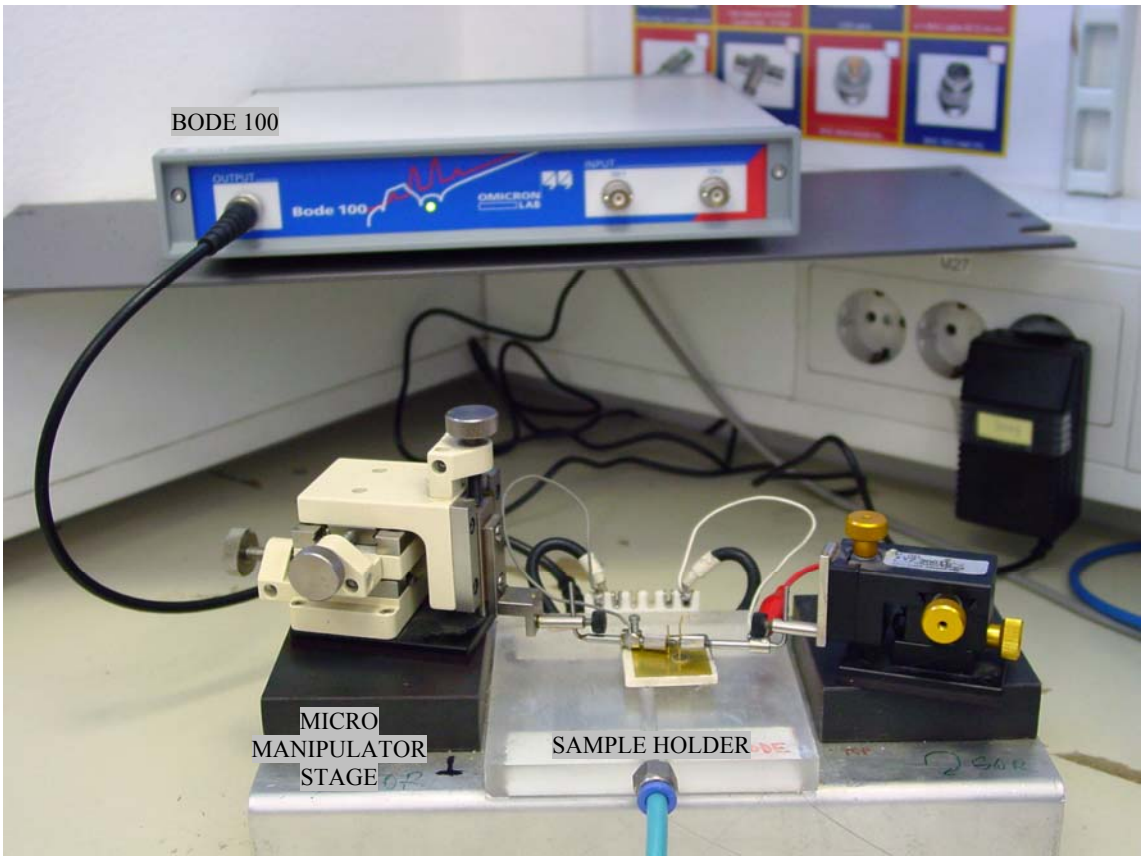

a)

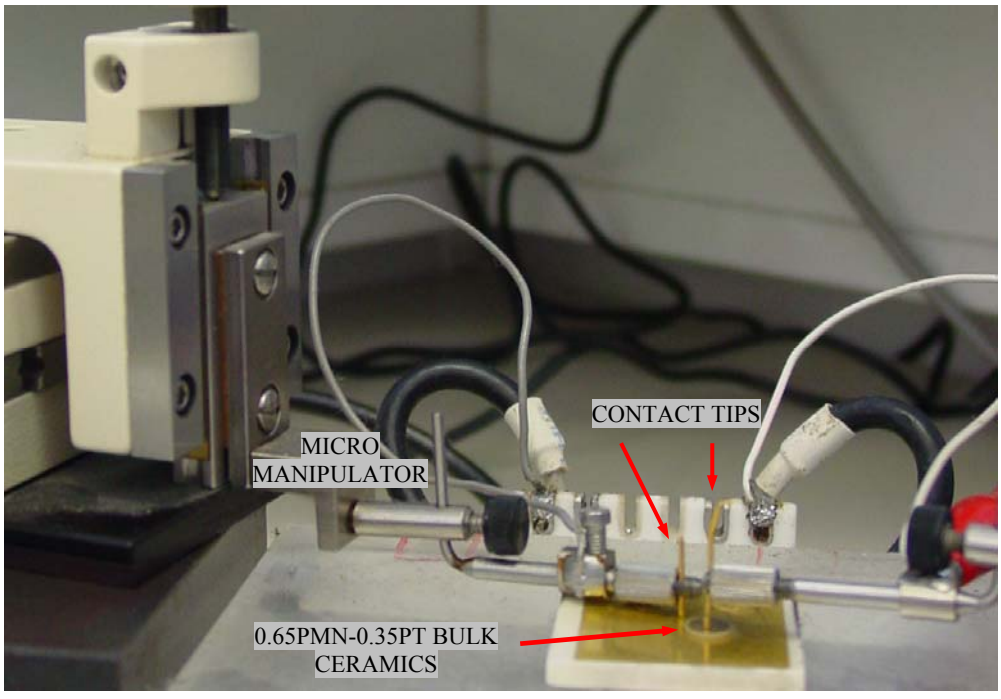

b)

Figure 35: a) The resonance measurement setup; BODE 100 Omicron Lab device and the micro manipulator stage and the sample holder. b) Micro manipulators, contact tips and the 0.65PMN–0.35PT bulk ceramic sample.

The frequencies at the maximum (antiresonance frequency f_a) and minimum (resonance frequency f_r) of the impedance were determined with the programme BODE ANALYZER. Before the measurements the BODE 100 was calibrated with a load resistance of 50.72 Ω. The coupling coefficients k_p and k_t were calculated from the equations:

$$k_p = \sqrt{[2.51 \cdot (\frac{f_a - f_r}{f_a}) - (\frac{f_a - f_r}{f_a})^2]} \qquad (13)$$

$$k_t = \sqrt{\frac{\pi}{2} \cdot \frac{f_r}{f_a} \operatorname{ctg}[\frac{\pi}{2} \cdot \frac{f_r}{f_a}]} \qquad (14)$$

3.2.3.4 Measurements of the piezoelectric coefficient with the Berlincourt piezometer

The piezoelectric constants d_{33} of the 0.65PMN–0.35PT poled ceramics were measured with a Berlincourt piezometer (Take Control PM10, Birmingham, UK [85]). The oscillation frequency of the force head was 50 Hz. In Fig. 36 (a) the Berlincourt Take Control piezometer is shown. Fig. 33 (b) shows the bulk 0.65PMN–0.35PT ceramic placed in the force head of piezometer.

The d_{33}^{eff} measurements for the 0.65PMN–0.35PT poled thick films were also performed with the Berlincourt piezometer. Although the dimensions of the measured thick films were not according to the IEEE standard [84] the measured d_{33}^{eff} values were comparable with the values obtained by other methods; Photonic Sensor and AFM. The thick films were measured in such a way that the active part of the force head was placed on the top electrode and the bottom electrode was connected with the wire to the other part of the force head, as is shown in Fig. 36 (b).

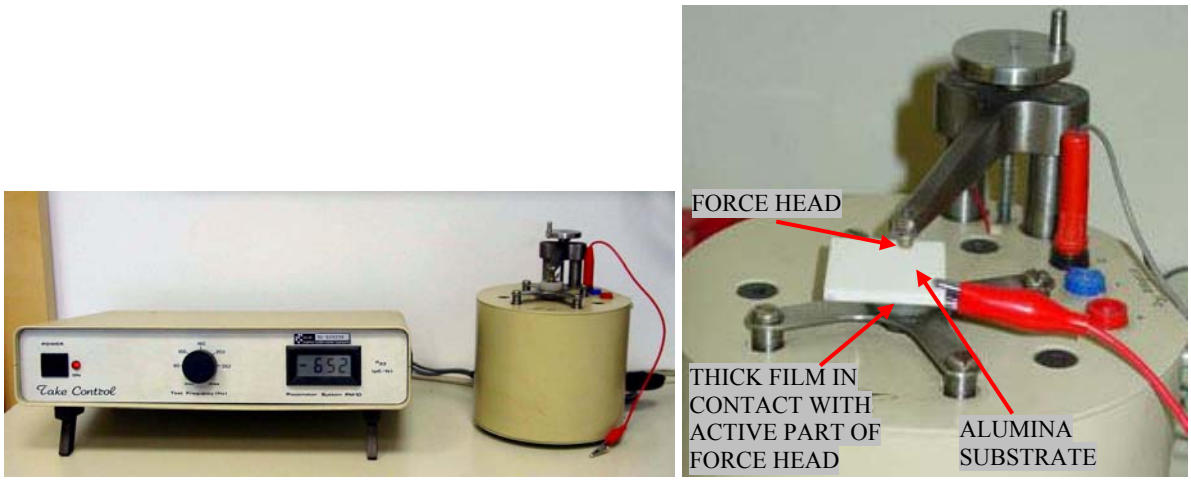

a) b)

Figure 36: a) The Berlincourt Take Controle Piezometer PM10. b) 0.65PMN–0.35PT thick film on alumina substrate placed in the force head of piezometer during measurements of d_{33}^{eff}.

3.2.3.5 Measurement of the displacement versus the electric field for the 0.65PMN–0.35PT films

Measurements by Photonic sensor

The measurements of the displacements vs. the applied electric fields of 0.65PMN–0.35PT thick films were made by the Photonic Sensor MTI 2000. A robust housing was holding the thick-film sample and the Photonic Sensor probe in place in order to limit the vibrations. The function generator Stanford Research Systems DS 360 and the high-voltage DC amplifier TREK 609C-6 were used for generation of the signal. Only unipolar external electric fields were applied in the direction of the polarization of the sample to avoid depoling. The frequency and the amplitude of the sinusoidal signal were 1.1 Hz and 50 V, respectively. The readout on the Photonic Sensor gave the displacements, which were observed in the oscilloscope Tektronix TDS 410. Data were then captured by a computer running a suitable LabView program [86]. The measurements were repeated more than 8 times and the average value was taken.

Measurements by atomic force microscope (AFM)

The displacements vs. the applied electric fields of the 0.65PMN–0.35PT thick films were measured with the AFM. Conductive, doped, silicon AFM tips (Nanosensors) with a nominal spring constant of 0.1 N/m were used. The native oxide layer was removed from the tips in diluted HF acid and the electrical contact was made with a silver conductive paste. The measurements were made using a commercial Nanoscope III (Digital Instruments) AFM. The AFM was used in the force-spectroscopy mode, and during the experiments the tip was in contact with the sample at a constant force. Since the AFM tip and the sample were in hard contact, the measured displacements of the tip represent the displacement of the sample. For the measurements of the piezoelectric coefficient d_{33}^{eff} an external AC quadratic signal (squared wave) with a frequency of 5 Hz was applied between the top and bottom electrodes (with the AFM tip on the top electrode) of the poled thick films at applied forces 300 nN. For the measurements of electrostriction an external AC sinusoidal voltage with the frequency of 200 Hz was applied between the AFM tip and the embedded Pt electrodes, inducing oscillations of the previously not poled 0.65PMN–0.35PT thick films. The amplitudes of the applied signals were from 15 V to 50 V at an applied force of 80 nN. The measurements at the sinusoidal electric voltage with the amplitude of 50 V were performed at applied forces of 80 nN, 200 nN and 300 nN to examine the force dependence of the samples' displacements.

3.2.3.6 Measurement of displacement versus electric field for 0.65PMN–0.35PT/Pt actuators

The displacements of the 0.65PMN–0.35PT/Pt actuators versus the applied electric fields were measured with the Viking optical profiler system (Solarius Development) using the non-contact white light Nobis sensor based on confocal chromatic technology. In Fig. 37 the measurement setup is shown. The external electric field was applied between the top and bottom electrodes using the function generator Hewlett Packet 33120A and the high-voltage amplifier Kepco BOP 1000M. One end of the actuator (3 mm from the edge of the actuator, Fig. 37) was placed on the conductive substrate, where the electrical contact with the bottom electrode was achieved. The top electrode was connected in one point with the contact tip as it is shown in the inset in Fig. 37. The measurements were performed at the end of the actuator's cantilever.

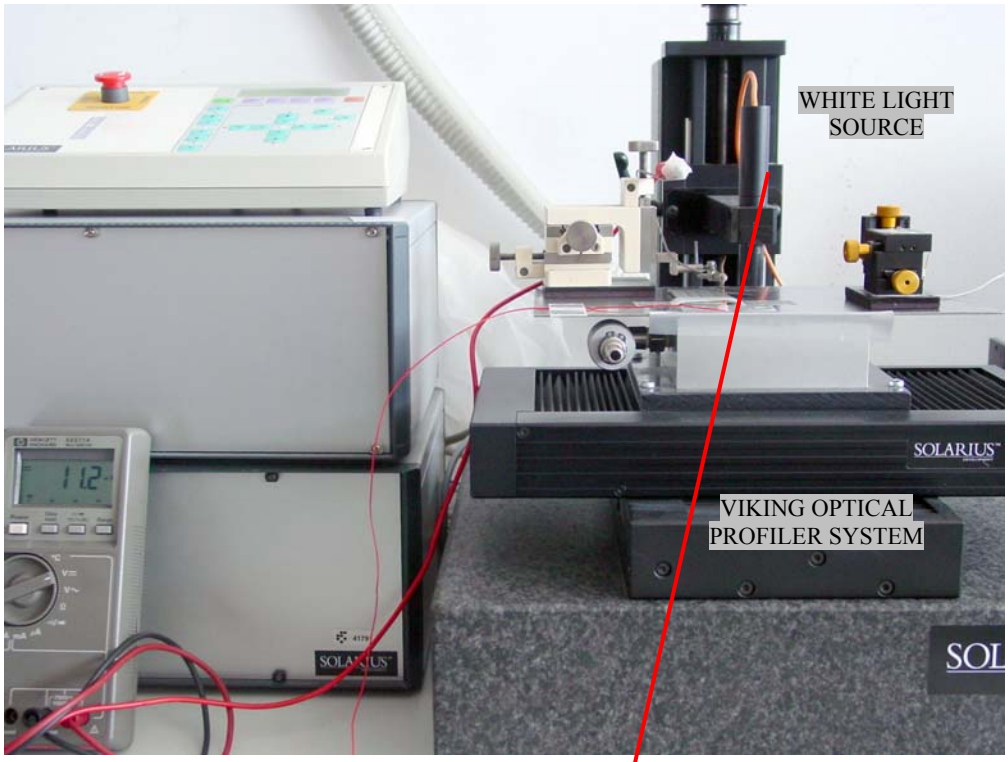

a)

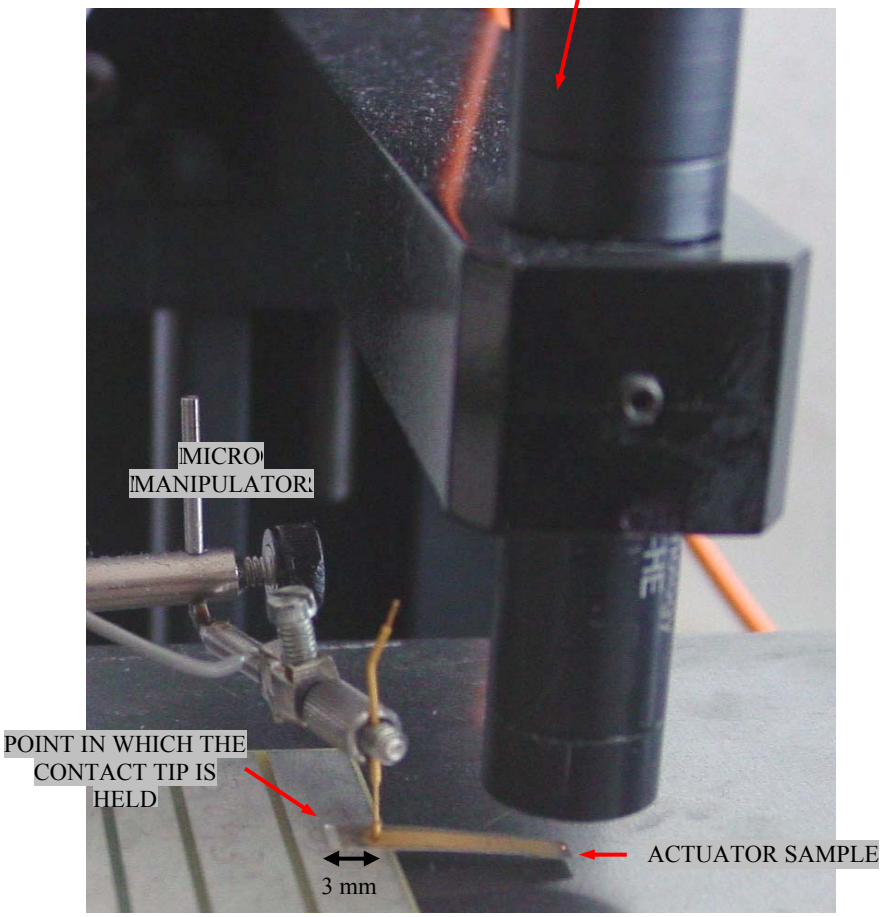

b)

Figure 37: a) The measurement setup for measuring the displacements of the 0.65PMN–0.35PT/Pt actuators vs. the applied electric field with the Viking optical profiler system (Solarius Development). b) The actuator during measurement. The external electric field was applied between the top and bottom electrodes. The 3 mm long bottom part of the actuator was placed on the conductive step. The top electrode was connected with the contact tip. The measurements were performed at the end of the actuator's cantilever.

3.3 Finite element modelling

The finite element (FE) analyses were made for the 0.65PMN–0.35PT/Pt actuator's displacements versus the applied electric fields. The FE models were built using the piezo-capabilities of ANSYS/multiphysics. The geometry was meshed with 8-nodes 3-D coupled-field solid elements (SOLID5), which have large deflection capabilities [87]. The dimensions of the 0.65PMN–0.35PT layer were 18 mm x 3 mm x 50 µm. In the models a half symmetry was used, i.e., 18 mm x 1.5 mm x 50 µm, as is shown in Fig. 38. The thickness of the 0.65PMN–0.35PT layer was 50 µm and the thickness of the Pt electrode was 15 µm. The z = 0 was defined between the 0.65PMN–0.35PT layer and Pt electrode.

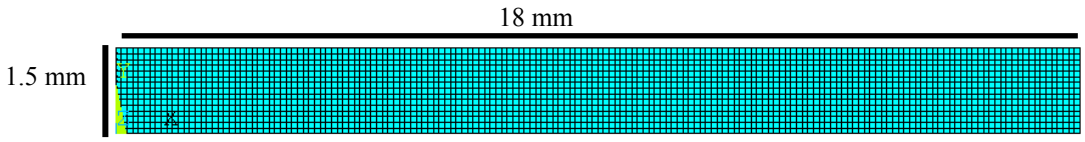

Figure 38: Top view of 0.65PMN–0.35PT layer geometry (half symmetry) used in FE models.

The FE model boundary conditions are shown in Fig. 39. The boundary conditions were chosen to be similar to the experimental conditions (section 3.2.3.6). In the models we fixed one point in the middle of the actuator, which corresponds in the experiment to a point in which the contact tip was held (Fig. 37). The fixed point is shown in Fig. 39 at the edge of the structure, due to the half symmetry, which was taken. Also, the rectangular area with dimensions 1 mm x 1.5 mm and 2 mm away from the actuator edge was fixed. This area corresponds in the experiment to the 3 mm step on which the sample was placed (Fig. 37).

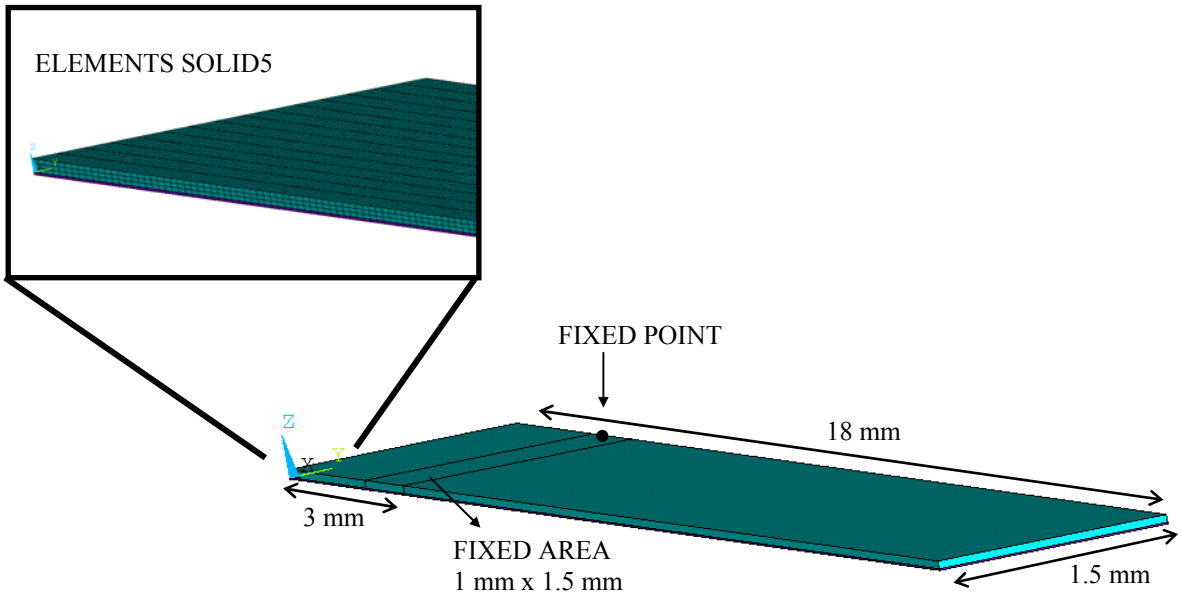

Figure 39: The geometry of the actuator and the boundary conditions (fixed point and fixed area) used in the FE model are shown.

The semi-static analyses of the actuators for different electrical loads were performed. In the models the voltages were applied directly to the surface of the Pt electrodes and the 0.65PMN–0.35PT films. The tip displacement in the z direction at different voltages, i.e., 0.5 V, 1 V, 2 V, 3 V, 4 V, 5 V, 7 V, 10 V, 15 V and 20 V were calculated.

4 Results and Discussion

4.1 Properties of 0.65PMN – 0.35PT powder

The particle size distribution of the starting 0.65PMN–0.35PT powder prepared by mechanochemical synthesis and heated at 700°C for 1 hour determined by laser granulometry is shown in Fig. 40. The cumulative curve is also shown.

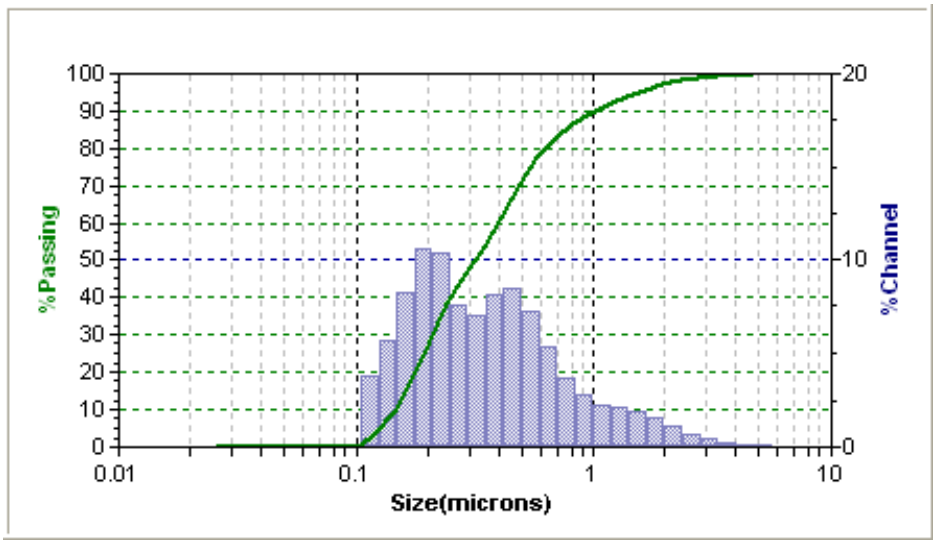

Figure 40: The particle size distribution of the 0.65PMN–0.35PT powder. The green line is the cumulative curve.

The particle size distribution is narrow with the median particle size d_{50} equal to 0.32 µm. The largest particles have diameters around 5 µm. The FE-SEM micrograph of the submicron particles, which are in majority (around 90%) are shown in Fig. 41a. Only 10% of particles are larger than 1 µm and the micrograph of these particles is shown in Fig. 41b.

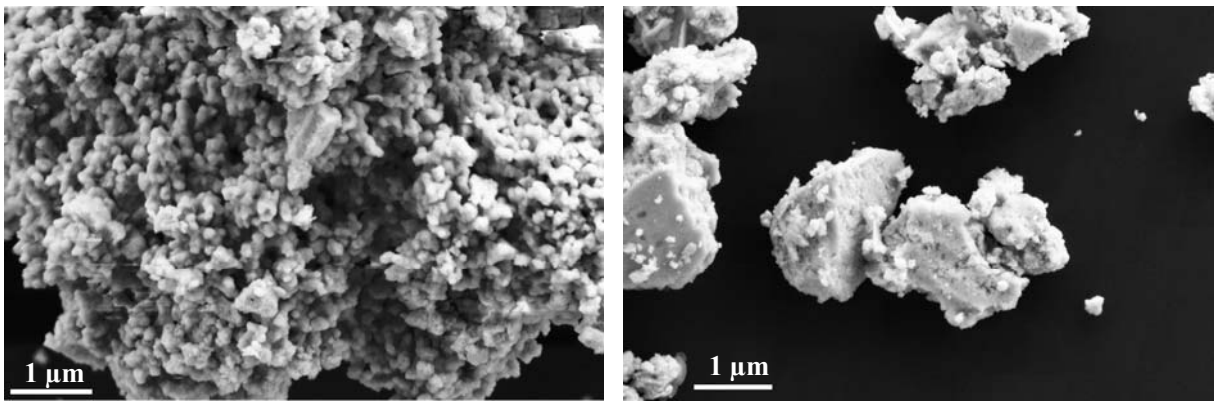

a) b)

Figure 41: The FE-SEM micrographs of the a) submicron particles and b) particles larger than 1 µm.

In Fig. 42 the X-ray diffraction diagram of 0.65PMN–0.35PT mechanochemically synthesized powder after calcination at 700°C is shown. The chemical homogeneity of this powder is confirmed to be

high according to ref. [88]. The regions from 2θ = 36° to 2θ = 48° of measured X-ray diffraction diagram for 0.65PMN–0.35PT powder and profile matching for monoclinic Pm, tetragonal P4mm and cubic Pm-3m phases are shown in Fig. 43. Peaks correspond to the families of planes (111) at around 2θ = 38° and (200) at around 2θ = 45°. The measurements are shown by dots and the calculated curve is shown by the line. The curves of the difference between the measurement and calculation are shown at the bottom of the diagrams. The particles of the mechanochemical synthesised powder are small (Fig. 40, d_{50} equal to 0.32 µm) resulting in broad peaks, which is also reported in ref. [74]. The peaks are also asymmetric with a broadening at small angles, which can results from a particle surface relaxation [89]. The goodness of fit (Gof) is best for the monoclinic phase Pm, i.e., 1.18, worse for tetragonal phase P4mm, i.e., 1.26 and the worst for cubic phase Pm-3m, i.e., 1.33. We can conclude that the starting powder is not cubic. Note that it is hard to distinguish between the monoclinic Pm and tetragonal P4mm phases. However, these results and the results for the bulk ceramics fired at 950°C (section 4.3.1.6) indicate that the starting powder is presumably mainly monoclinic Pm.

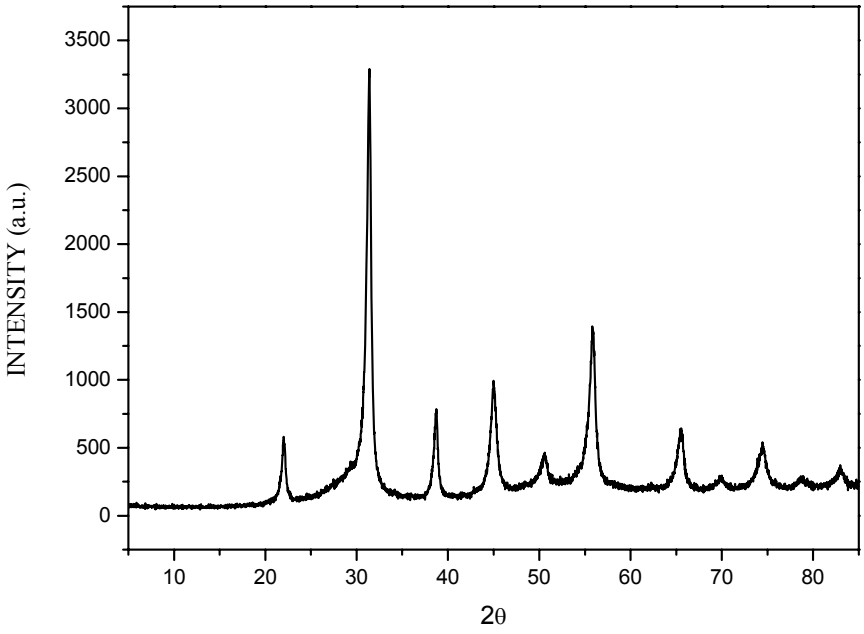

Figure 42: The X-ray diagram of the 0.65PMN–0.35PT powder.

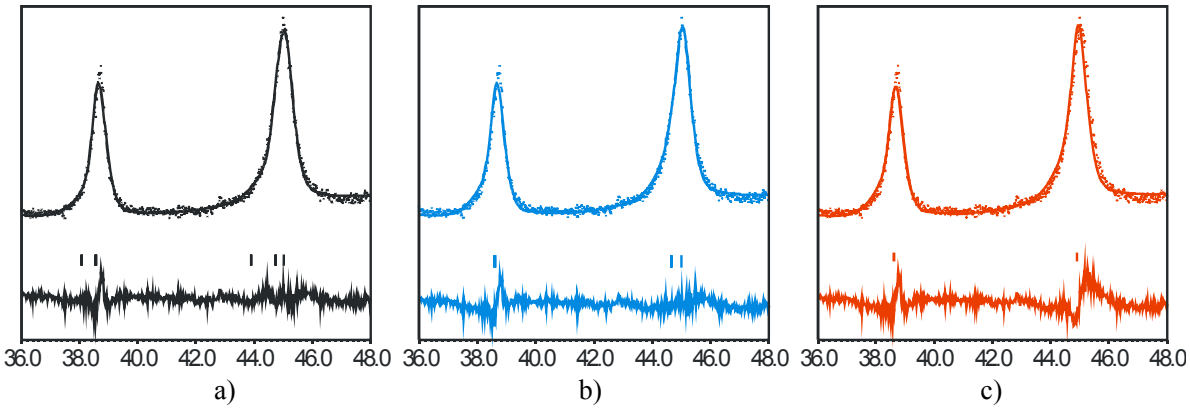

Figure 43: The measured (dot), calculated (line) and difference (bottom) curve of the 0.65PMN–0.35PT powder. The regions from 2θ = 36° to 2θ = 48° of measured X-ray diffraction for the 0.65PMN–0.35PT powder and profile matching for a) monoclinic Pm, b) tetragonal P4mm and c) cubic Pm-3m phases. Peaks correspond to the families of planes (111) at around 2θ = 38° and (200) at around 2θ = 45°. The thick marks correspond to the positions of the peaks for (111) and (200) families of planes.

4.2 Properties of the 0.65PMN – 0.35PT bulk ceramics fired at 1200°C

As the data in the literature (Table 1) on dielectric, piezoelectric and ferroelectric characteristics of the 0.65PMN–0.35PT ceramics prepared under similar conditions differ, we prepared and characterized 0.65PMN–0.35PT ceramics fired at 1200°C for 2 hours. The purpose of this work was to prepare stress-free dense ceramics with good structural and electrical properties for a comparison with thick films of the same composition. Later in the text the structural and electrical properties of 0.65PMN–0.35PT films are compared with the properties of dense bulk ceramics fired at 1200°C. The second purpose of the preparation of 0.65PMN–0.35PT bulk ceramics fired at 1200°C was to make a systematic study of the poling procedure for the 0.65PMN–0.35PT material with intention to find the best poling conditions for the 0.65PMN–0.35PT material.

4.2.1 Structural properties of the 0.65PMN–0.35PT bulk ceramics fired at 1200°C

The measured density of the ceramics was 7.98 g/cm^3, that is 98% of theoretical density. The calculated theoretical value was 8.13 g/cm^3, which is in agreement with the reported value for $Pb(Mg_{0.333}Nb_{0.667})O_3$, i.e., 8.13 g/cm^3 [90]. The obtained high density is due to highly chemical homogenous mechanochemically synthesized powder with the median particle size equal to 0.3 μm.

The SEM microstructure of the polished and thermally etched cross-section for the 0.65PMN–0.35PT bulk ceramics fired at 1200°C are shown in Figs. 44 and 45, respectively, where it is seen that the ceramics are well sintered. The holes in Figs. 44 are the pulled out grains during polishing. The median grain size is 1.1 μm ± 0.5 μm.

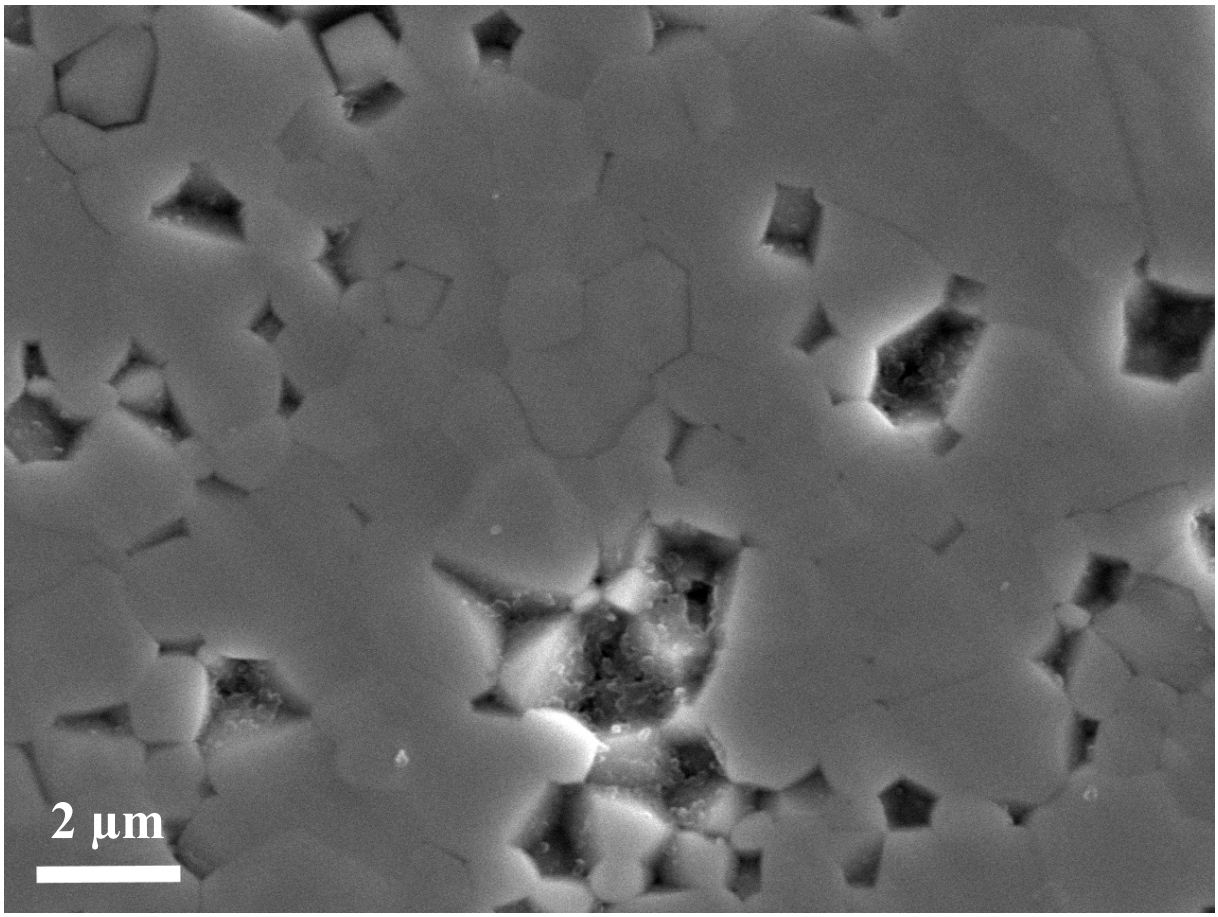

Figure 44: The SEM micrographs of polished cross-section for the bulk 0.65PMN–0.35PT ceramics fired at 1200°C for 2 hours.

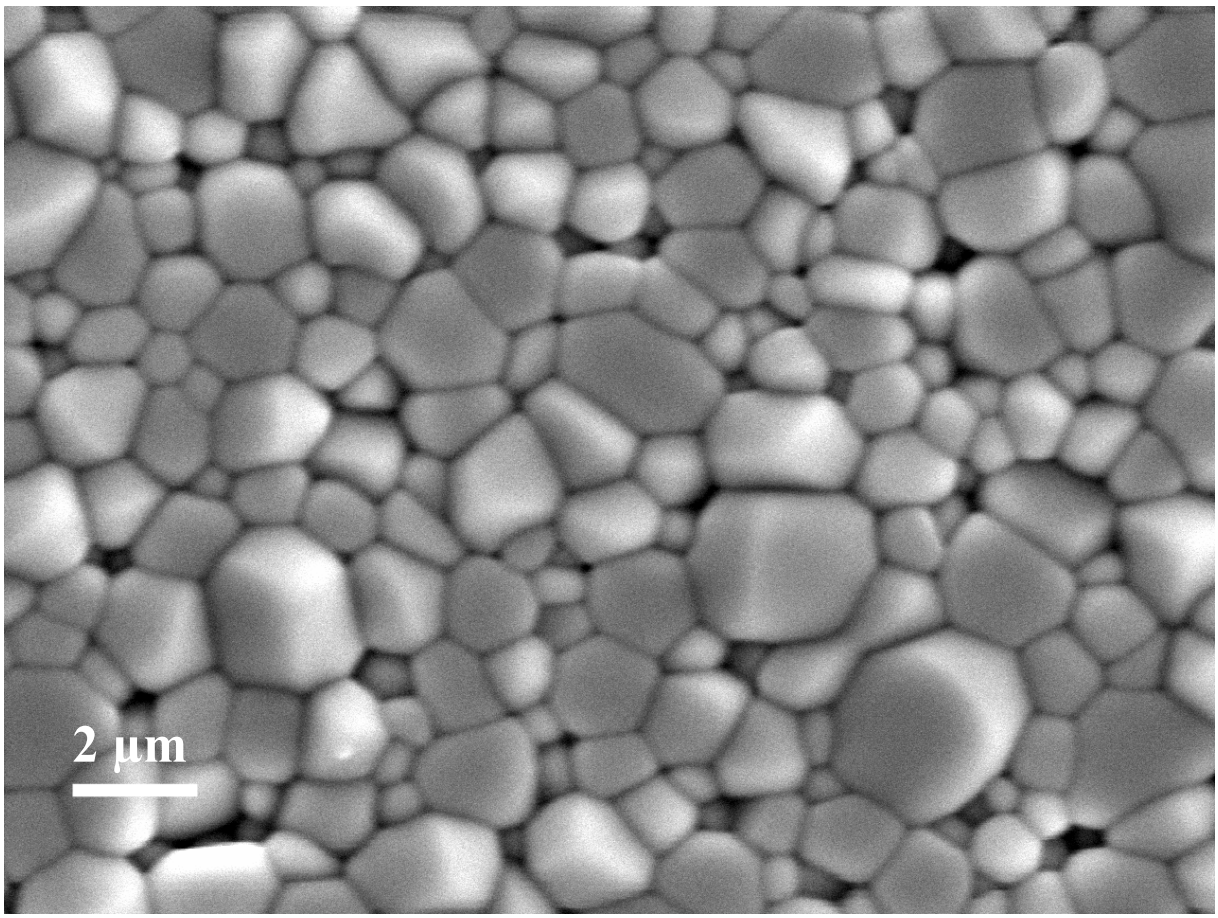

Figure 45: The SEM micrographs of thermally etched cross-section for the bulk 0.65PMN–0.35PT ceramics fired at 1200°C for 2 hours.

The EDXS "point" analyses of the 0.65PMN–0.35PT bulk ceramics were performed in 23 spots. The results and the standard deviation of the analyses for the 0.65PMN–0.35PT bulk ceramics are summarized in Table 4. For EDXS analyses, which were performed at 20 kV, the Mg(K), Ti(K), Nb(L), Pb(M) series were used. The oxygen was calculated by difference to hundred percent. The average results of the analyses differ from the expected values for the 0.65PMN–0.35PT material, i.e., 4.3% of Mg, 7% of Ti, 8.7% of Nb, 20% of Pb and 60% of oxygen. All the results of the analyses slightly overestimate the concentration of Nb and underestimate the concentration of Mg and Pb, due to overlapping of the peak series Pb(M)/Nb(L).

Table 4: The average EDXS "point" analysis made in 23 spots (atomic percents), the standard deviation and the maximum and minimum determined values of the 0.65PMN–0.35PT bulk ceramic fired at 1200°C for 2 hours.

	Mg (%)	**Ti (%)**	**Nb (%)**	**Pb (%)**	**O (%)**
bulk ceramic					
Average	3.5	7.3	9.6	18.7	60.9
Standard deviation	0.5	0.4	0.3	0.5	
Maximal value	4.6	8.4	10.2	19.9	
Minimal value	2.6	6.5	8.8	18.1	

The X-ray diagram of the non-poled 0.65PMN–0.35PT ceramics is shown in Fig. 46. The families of planes are given in brackets. No extra diffraction peaks that might correspond to the pyrochlore or PbO phases were detected. The Rietveld analysis of the X-ray data of the 0.65PMN–0.35PT bulk fired at 1200°C for 2 hours shows the coexistence of the monoclinic Pm and the tetragonal P4mm phases. The inset in Fig. 46 shows the convolution of the (002) and (200) tetragonal peaks and the (002), (200), (020) monoclinic peaks. The approximate peak positions of the tetragonal (grey) and the monoclinic (black) phases are marked with dash lines.

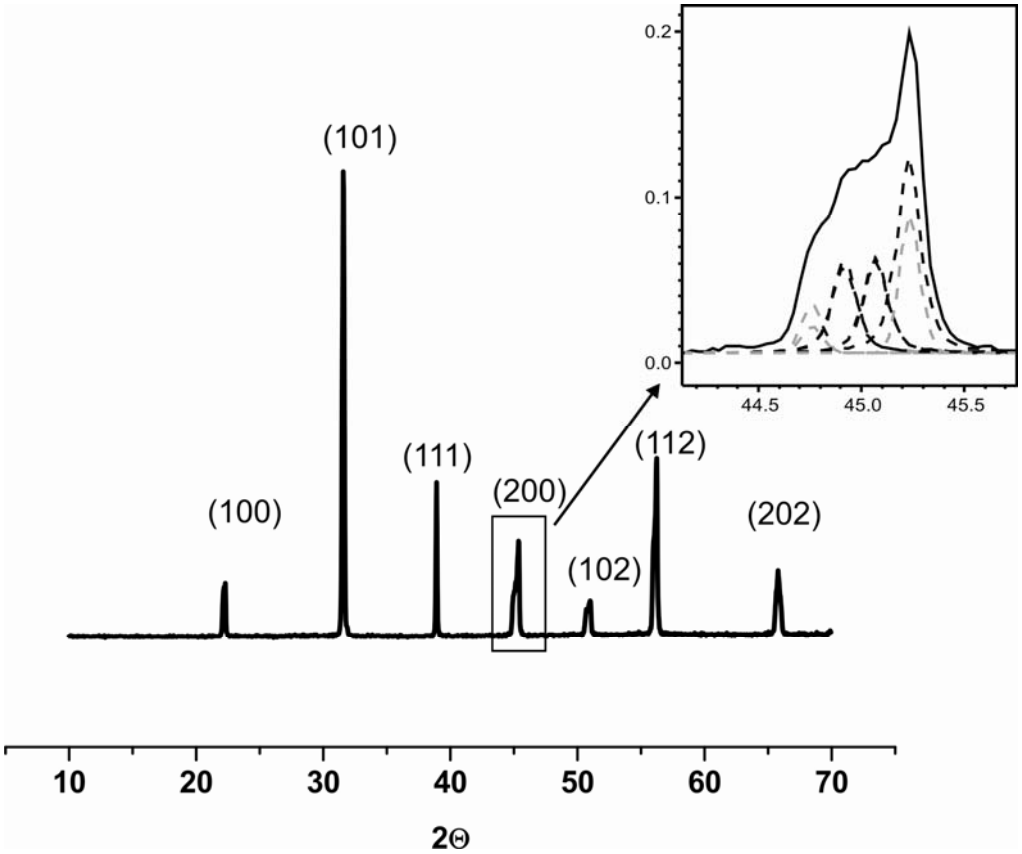

Figure 46: The X-ray diagram of the non-poled 0.65PMN–0.35PT ceramics fired at 1200°C for 2 hours. The families of planes are given in brackets. The inset shows the convolution of the (002) and (200) tetragonal peaks and the (002), (200), (020) monoclinic peaks. The approximate peak positions of the tetragonal (grey) and monoclinic (black) phases are marked with dashed lines.

The coexistence of the monoclinic and tetragonal phases in 0.65PMN–0.35PT ceramics was reported before in the literature [54, 57, 64]. The determined monoclinic-to-tetragonal ratio in percentage for bulk 0.65PMN–0.35PT ceramics fired at 1200°C for 2 hours was 86% of monoclinic Pm and 14% of tetragonal P4mm phases, which is in close agreement with the previously reported results, i.e., 89% of monoclinic Pm and 11% of tetragonal P4mm phases [54]. The X-ray diagram reveals no preferential orientation of the unit-cells, and attempts to add some orientation decreased the quality of the refinement. The cell parameters are a = b = 4.0037(2) Å, c = 4.0442(3) Å and V_T = 64.827(5) Å^3, for the tetragonal phase and a = 4.0178(2) Å, b = 4.0042(2) Å, c = 4.0308(2) Å, β = 90.147(4)° and V_M = 64.848(5) Å^3 for the the monoclinic phase. The values are in close agreement with the cell parameters obtained for ceramics with the compositions near 0.65PMN–0.35PT; a = b = 4.0004(2) Å, c = 4.0464(1) Å for P4mm tetragonal phase and a = 4.0174(2) Å, b = 4.0019(2) Å, c = 4.0289(2) Å, β = 90.177(3)° for Pm monoclinic phase [53].

4.2.2 Electrical properties of the 0.65PMN–0.35PT bulk ceramics fired at 1200°C

The temperature dependence of the dielectric constant ε and the dielectric losses tg δ, measured at 1 kHz, 10 kHz and 100 kHz, for non-poled 0.65PMN–0.35PT ceramics is presented in Fig. 47, where the tetragonal-to-high-temperature relaxor state transition peak is clearly evident. The ε at room temperature is 3600 and 3400 at 1 kHz and 100 kHz, respectively. The values are in agreement with the literature [58, 60], i.e., 4000 at 1 kHz (Table 1). The maximum value of ε is approximately ε_{max} = 56.500 at the temperature T_{max} = 172°C and a frequency of 100 kHz. No dependence of T_{max} on the frequency was observed. In ref. [58] it is reported that for 0.65PMN-0.35PT ceramics annealed 5 hours the ε_{max} measured at 1 kHz is 34.100 at T_{max} = 172°C.

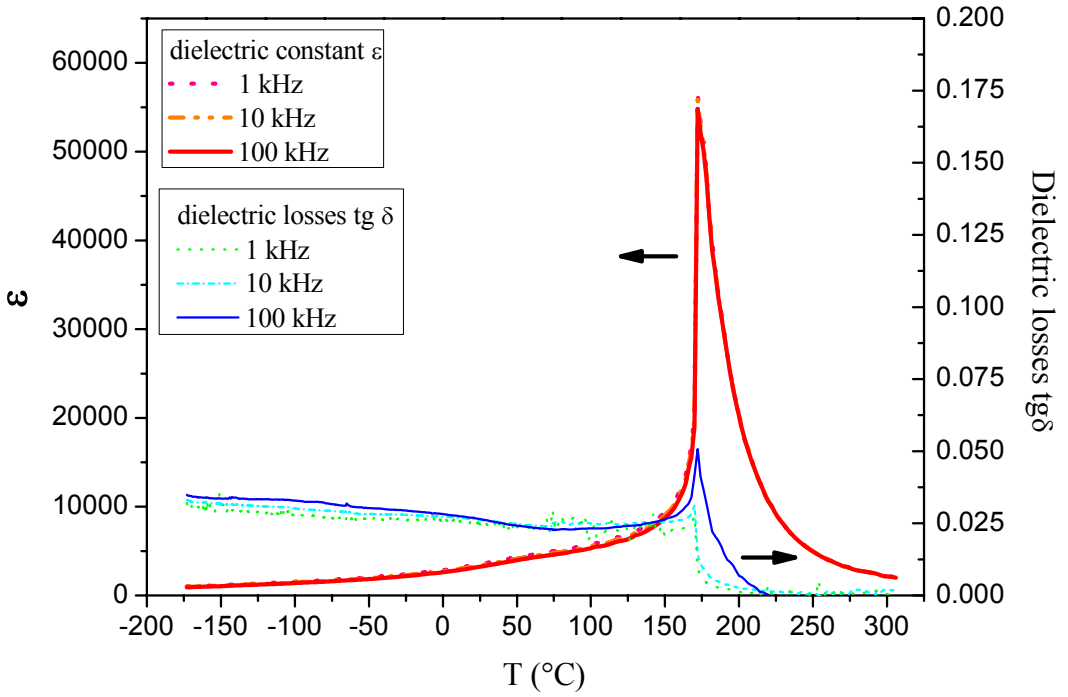

Figure 47: Dielectric constant ε and dielectric losses tg δ vs. temperature at frequencies of 1 kHz, 10 kHz and 100 kHz for non-poled 0.65PMN–0.35PT bulk ceramics fired at 1200°C.

The ferroelectric hysteresis loops of the 0.65PMN–0.35PT ceramics fired at 1200°C for 2 hours were measured. As seen in Fig. 48, the remanent polarization P_r and coercitive fields E_c are 33 μC/cm^2 and 6 kV/cm, respectively. The measurements are in close agreement with the P_r and E_c for bulk 0.65PMN–0.35PT ceramics from ref. [58], i.e., 33.1 μC/cm^2 and 4.3 kV/cm, respectively.

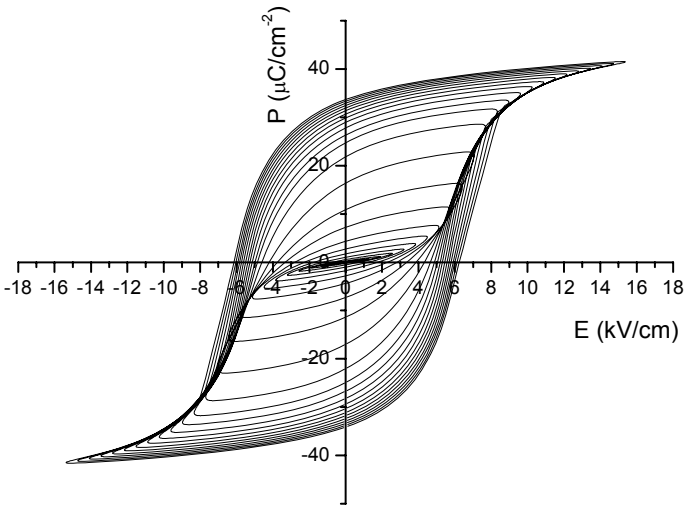

Figure 48: The ferroelectric hysteresis loops of the 0.65PMN–0.35PT ceramics fired at 1200°C for 2 hours.

The ceramics were poled with a DC electric field of 0.5 kV/mm – 4.5 kV/mm at 160°C for 5 minutes, field cooled (FC), and then aged for 24 hours, as is explained in section 3.2.3.2 The piezoelectric coefficient d_{33} and the coupling coefficients k_p and k_t were measured. The part of measurement of impedance vs. frequency (i.e. from 700 kHz to 1250 kHz), which represents the radial vibrations of the samples, for 0.65PMN–0.35PT ceramics poled with an el. field of 4 kV/mm is shown in Fig. 49. The antiresonance f_a and resonance f_r frequencies are marked.

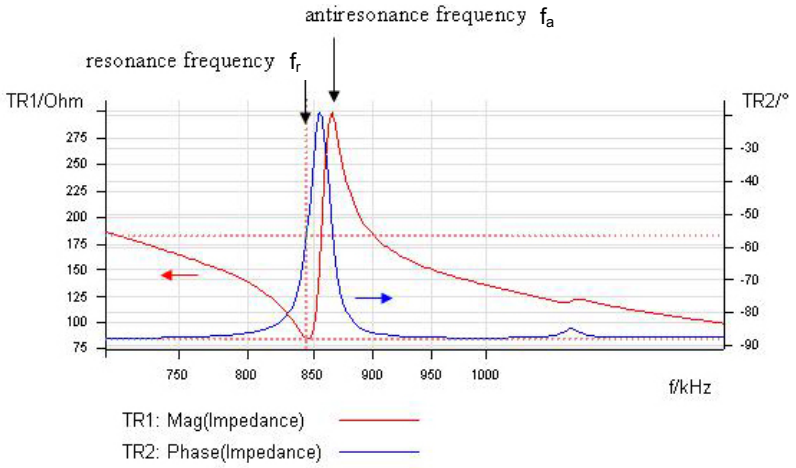

Figure 49: The measurement of impedance, i.e., magnitude (red) and phase (blue) vs. frequency of applied el. field for 0.65PMN–0.35PT ceramics poled with 4 kV/mm. Antiresonance f_a and resonance f_r frequencies are marked. The crossed dotted lines show the position of determined f_r.

The piezoelectric coefficient d_{33} and the coupling coefficients k_p and k_t are summarized in Table 5. In Fig. 50 the piezoelectric coefficient d_{33} and the coupling coefficients k_p and k_t versus the poling field are shown. For 0.65PMN–0.35PT ceramics poled at 0.5 kV/mm, the d_{33} was 628 pC/N ± 4 pC/N, and it increased with the poling field up to 2 kV/mm. The highest d_{33}, around 660 pC/N, was measured for the samples poled at electric fields between 2 kV/mm and 3.5 kV/mm. For the samples poled at poling fields higher than 3.5 kV/mm, i.e., 4 kV/mm and 4.5 kV/mm, the d_{33} was lower, i.e., 642 pC/N ± 4 pC/N. Similar behaviour was observed for k_p and k_t versus the poling electric field. The lowest values of k_p and k_t, i.e., 0.67 and 0.5, respectively, were measured at an electric field of 0.5 kV/mm. The k_p and k_t increased with the increasing poling field up to 2 kV/mm. The highest k_p and k_t were measured for the 0.65PMN–0.35PT ceramics poled between 2 kV/mm and 3.5 kV/mm. When the poling field was higher than 3.5 kV/mm, i.e., 4 kV/mm and 4.5 kV/mm, the k_p and k_t decreased.

The results show that the highest values of d_{33}, k_p and k_t were obtained for the poling fields between 2 kV/mm and 3.5 kV/mm, and these can be referred to as the optimum poling conditions for the 0.65PMN–0.35PT ceramics poled at 160°C for 5 minutes and then field cooled (FC). In Fig. 50 the rectangle shows the area of the optimum poling conditions. The differences between the highest and the lowest measured k_p and k_t were as high as 13% and 10%, respectively (Table 5).

Table 5: The piezoelectric coefficient d_{33} and the coupling coefficients k_p and k_t measured for the 0.65PMN–0.35PT ceramics poled at different poling fields.

Poling field (kV/mm)	**d_{33} (pC/N)**	**k_p**	**k_t**
0.5	628	0.67	0.5
1	640	0.73	0.53
1.5	654	0.75	0.53
2	660	0.76	0.54
2.5	663	0.76	0.55
3	664	0.77	0.54
3.5	664	0.76	0.55
4	640	0.75	0.54
4.5	642	0.75	0.53

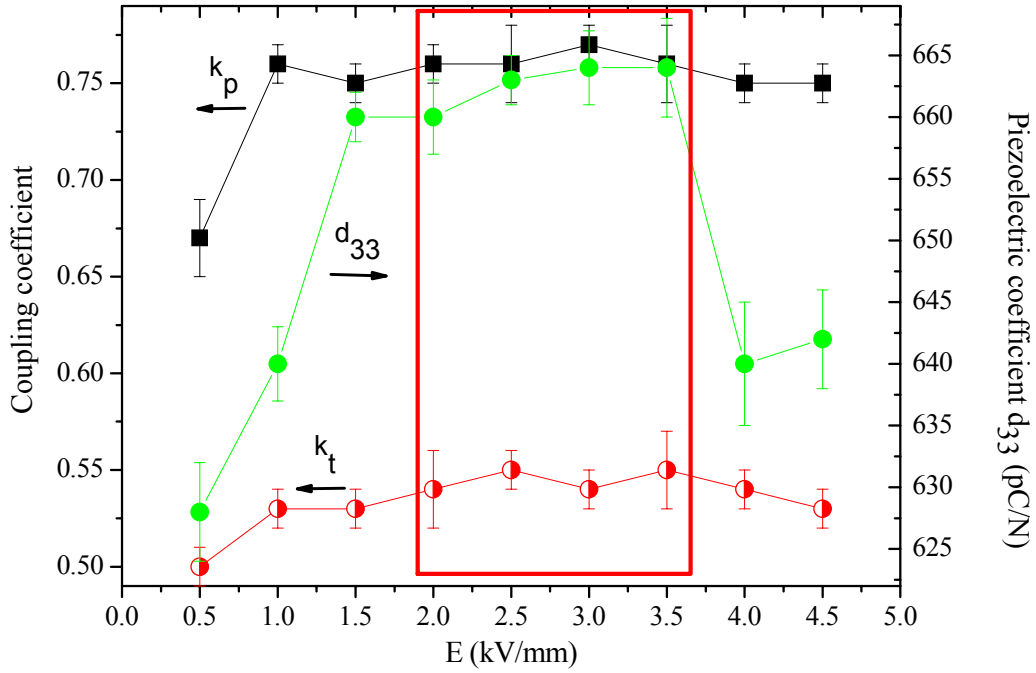

Figure 50: The piezoelectric coefficient d_{33} and the coupling coefficients k_p and k_t vs. poling field. The rectangle shows the area of the optimum poling conditions. The line between the measured values is just a guide to the eye.

In the open literature (Table 1) the values for d_{33} are different due to the different preparation procedure of the samples and also due to the various poling conditions. The poling electric field in the literature varies from 0.7 kV/mm–1 kV/mm [59] to 2 and 3.5 kV/mm [48, 54, 57, 60]. The piezoelectric coefficient d_{33} of 0.65PMN–0.35PT ceramics poled at 0.7 kV/mm was 610 pC/N ± 5 pC/N [59], which is in close agreement with our value 628 pC/N ± 4 pC/N poled at 0.5 kV/mm. The 0.65PMN–0.35PT ceramics poled at 2 kV/mm [48] or 3 kV/mm [60] have a piezoelectric coefficient d_{33} 700 pC/N and 709 pC/N, respectively. These values are also in close agreement with our measurements at 2 kV/mm–3 kV/mm, i.e., around 660 pC/N. However, the measured coupling coefficients k_p and k_t, i.e., 0.76 and 0.54, are higher than reported in ref. [48] for the ceramics poled with 2 kV/mm, i.e., 0.61 and 0.44, respectively.

4.2.3 Correlation between the structural and electrical properties of the 0.65PMN–0.35PT bulk ceramics fired at 1200°C

The X-ray diagram of the family of (200) peaks for the 0.65PMN–0.35PT ceramics poled with a DC electric field from 0.5 kV/mm to 4.5 kV/mm is shown in Fig. 51.

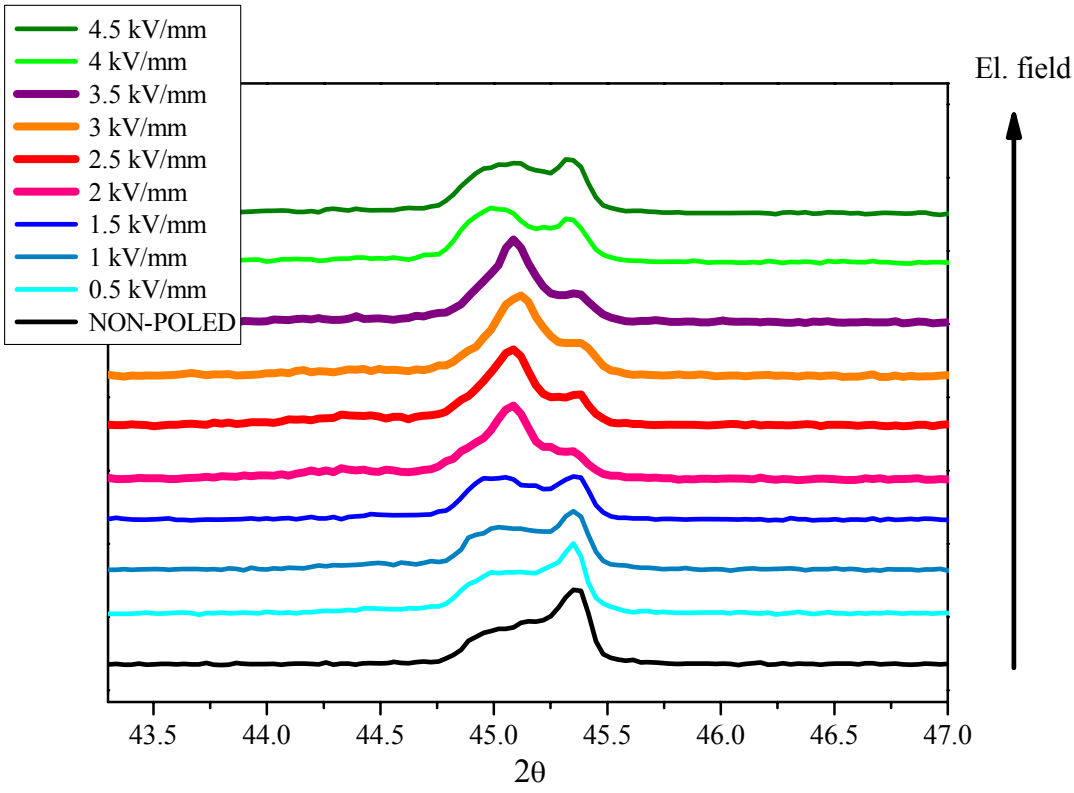

Figure 51: The X-ray diffraction diagram of the family of (200) peaks for the poled 0.65PMN–0.35PT ceramics. The X-ray diagram of the non-poled material is added for comparison. The black arrow indicates the increase in the poling electric field from 0 kV/mm to 4.5 kV/mm in steps of 0.5 kV/mm.

The X-ray diagrams of the poled bulk ceramics were measured. It is clear that the X-ray diagram of the 0.65PMN–0.35PT samples changes with the poling electric field. Three main types of X-ray diagrams are presented in Fig. 51: for the non-poled ceramics, for the ceramics poled between 2 kV/mm and 3.5 kV/mm, and for ceramics poled at 4.5 kV/mm.

In Table 6 the calculated phase ratio (monoclinic-to-tetragonal), the reliability factors, for the monoclinic R_M and tetragonal R_T phases, and the goodness of the fit for the profile, Gof of the Rietveld analyses for the X-ray data are reported for the non-poled 0.65PMN–0.35PT ceramics and the 0.65PMN–0.35PT ceramics poled at 2.5 kV/mm and 4.5 kV/mm.

Table 6: Phase ratio in percentage, reliability factors R, for the monoclinic Pm (R_M) and tetragonal P4mm (R_T) phases and the goodness of the fit for the profile Gof, of the Rietveld analyses for the X-ray data of the non-poled and poled 0.65PMN–0.35PT ceramics. The calculated uncertainty for the percentage of phases is less than 1%.

POLING	**Phase ratio in percentage (monoclinic Pm : tetragonal P4mm)**	**R_M**	**R_T**	**Gof**
NON-POLED	86% : 14%	3.86	4.71	1.31
POLED 2.5 kV/mm	99% : 1%	4.11	5.74	1.28
POLED 4.5 kV/mm	95% : 5%	3.89	4.31	1.09

The values of the reliability factors and the goodness of fit are acceptable, taking into account the fixed atomic positions, the quality of the X-ray measurement and the presence of the additional peaks from the gold electrodes. The measured, calculated and difference curves obtained from the Rietveld refinements of the three samples are presented in Fig. 52.

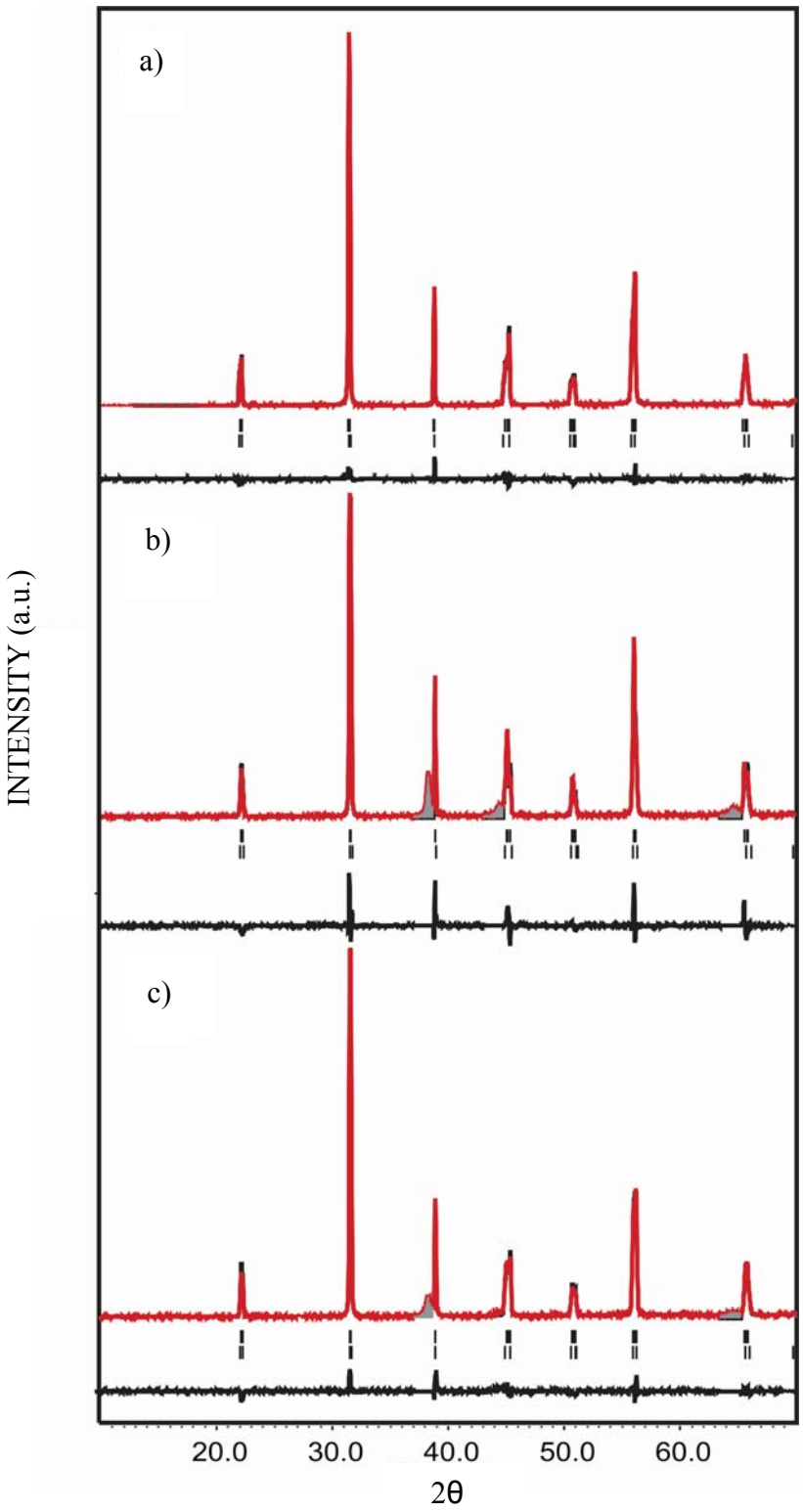

Figure 52: Final observed, calculated and difference plots of the X-ray diffraction Rietveld refinement for a) a non-poled sample and samples poled at b) 2.5 kV/mm and c) 4.5 kV/mm. The top mark corresponds to the tetragonal phase and the bottom ones to the monoclinic. The positions corresponding to the gold (the grey shadows) were excluded from the refinement.

As with the non-poled ceramics, the Rietveld analyses of the X-ray diffraction data of the 0.65PMN–0.35PT poled at 2.5 kV/mm and 4.5 kV/mm show the coexistence of the monoclinic Pm and tetragonal P4mm phases. There is a clear increase in the amount of monoclinic phase for the sample poled at 2.5 kV/mm, which contains 99% of the monoclinic Pm and 1% of the tetragonal P4mm phases. However, the tetragonal phase cannot be neglected due to the existence of shoulders in the diffraction peaks corresponding to this phase. At 4.5 kV/mm, the amount of monoclinic phase decreases, the ceramics contain 95% of the monoclinic Pm and 5% of the tetragonal P4mm phases. In both poled samples, the addition of a slight (001) preferential orientation for the tetragonal phase improved the quality of the refinement, but this was not the case for the monoclinic phase. In other words, some domains were reoriented with the application of the electric fields.

The evolution of the beta angle of the monoclinic phase showed a decrease for the sample poled at 2.5 kV/mm with a value very close to 90°. An attempt was made to refine the X-ray diagram using an orthorhombic phase instead of the monoclinic one; however, the results obtained show a worse fit than when using the monoclinic one.

These results show that the monoclinic-to-tetragonal ratio can be changed with the application of an electric field and that it is dependent on the strength of the electric field. It can be seen from the results that for non-poled 0.65PMN–0.35PT ceramics and ceramics poled at 4.5 kV/mm the amount of tetragonal phase is not negligible; however, in the case of the ceramics poled at 2.5 kV/mm, the major phase is clearly monoclinic, with only a small amount of tetragonal phase present. The X-ray diffraction diagram for the 0.65PMN–0.35PT ceramics poled at an electric field between 2 kV/mm and 3.5 kV/mm look the same; therefore, we can conclude that for 0.65PMN–0.35PT ceramics poled at these fields the major phase is also monoclinic. These electric fields coincide with the electric fields at which the highest piezoelectric d_{33} and coupling coefficients k_p and k_t were obtained, i.e., at 2–3.5 kV/mm. From the results we can suppose that one of the reasons for the differences between the d_{33}, k_p and k_t of the 0.65PMN–0.35PT ceramics poled at 2–3.5 kV/mm and those at higher or lower electric fields could be that the ratios between the monoclinic Pm and the tetragonal P4mm phases are different. In the 0.65PMN–0.35PT ceramics poled at electric fields between 2 kV/mm and 3.5 kV/mm the monoclinic phase is favoured in comparison to the non-poled samples.

The dielectric constants ε vs. the temperatures measured at 100 kHz for non-poled ceramics and ceramics poled at 1.5 kV/mm, 2.5 kV/mm, 3 kV/mm and 4.5 kV/mm are shown in Fig. 53. The data were collected during a zero-field-heated/field cooled (ZFH/FC) run, in order to have the same conditions as during the X-ray diffraction measurement. Here, the low-temperature (LT) phase-transition peak observed between the monoclinic and tetragonal phases is clearly evident. The LT phase-transition peak is broad, and the estimated peak transition temperature is between 50°C and 80°C, which is in agreement with the data reported in the literature. Alguero et al. reported that the mechanical and electro-mechanical properties of 0.655PMN–0.345PT reflect an LT phase-transition at 40–70°C [91], while the data ε(T) reported in ref. [60] show that the LT phase-transition peak for non-poled 0.65PMN–0.35 PT ceramics is around 50–80°C.

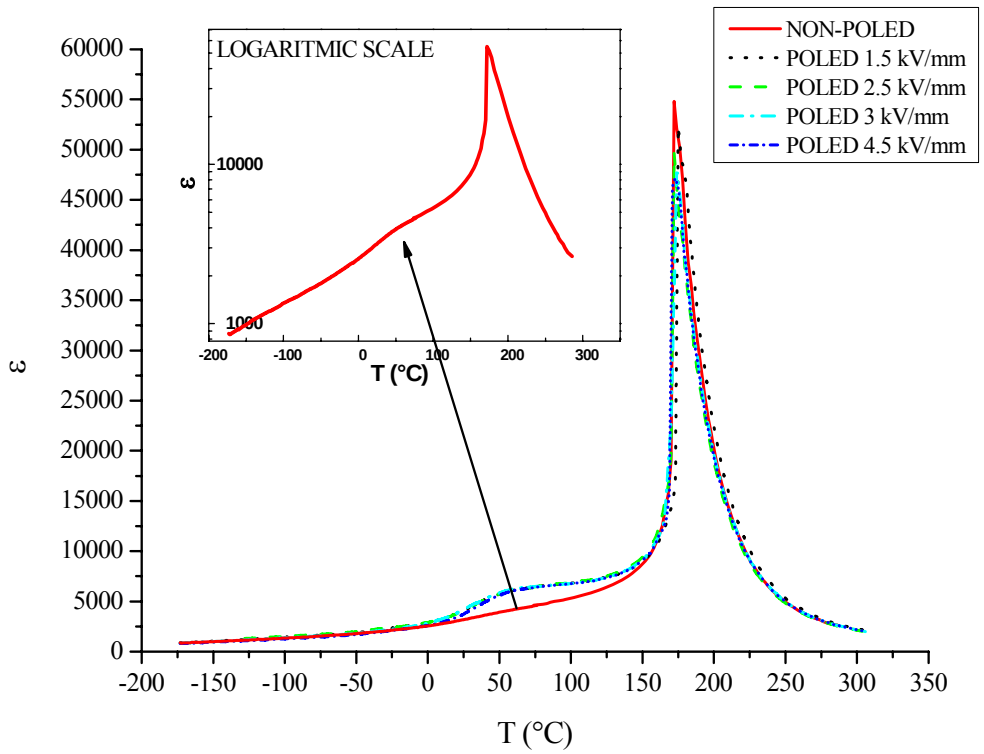

Figure 53: The dielectric constant ε vs. temperature at 100 kHz for the non-poled and poled 0.65PMN–0.35PT ceramics. The inset shows the data obtained for the non-poled sample on a logarithmic scale.

The conformation that the LT phase-transition peak detected during the ZFH/FC run is in fact due to the poling is that during an additional zero-field-cooled (ZFC) run (when the samples are depoled due to a high T) the data are again identical to those detected during the first non-poled run.

For the non-poled 0.65PMN–0.35PT ceramics, the LT phase-transition peak from the monoclinic Pm to tetragonal P4mm phase is less distinctive than for the poled ceramics. However, it is present, as shown in the inset of Fig. 53, which shows the data on a logarithmic scale. The LT phase-transition peak for the poled 0.65PMN–0.35PT ceramics is more distinctive. The same results have been reported for single crystals with the composition around 0.7PMN–0.3PT in the direction <001> [92, 93]. The LT transition peak is distinctive for poled samples and less distinctive for the non-poled samples.

The field induced phases were previously reported by many authors in PMN–PT crystals for compositions x = 0.25 - 0.32 [92, 94 - 99] as well as in similar systems, for example in PZN–PT crystals for the compositions x = 0.05 - 0.08 [97, 98, 100, 101]. For example, for <011> oriented PMN–PT and PZN–PT crystals the poling field induces an orthorhombic ferroelectric phase [92, 94, 95, 100]. In ref. [98] the pseudorhombohedral to tetragonal polarization rotation path is disscused over the orthorhombic and also monoclinic phases. Our results showed that for poled 0.65PMN–0.35PT ceramics no additional orthorhombic phase was observed, neither with X-ray nor with dielectric measurements.

Not much work was done on how the electric field influences the phase composition in 0.65PMN–0.35PT ceramics. In ref. [102] it is reported that for poled 0.65PMN–0.35PT material prepared by tape casting there is a distinctive third peak in addition to the tetragonal ones in the X-ray measurement of the family of (200) peaks, which was not observed in the virgin sample. They explain that the result implies that poling not only switched the *a*-domains in *c*-domains, but also induced some phase transformation [102]. Our results showed that for 0.65PMN–0.35PT ceramics the monoclinic-to-tetragonal ratio can be changed by the application of an electric field and that for the 0.65PMN–0.35PT ceramics poled with the field of 2.5 kV/mm the phase composition is almost pure monoclinic. Moreover, the ratio of the monoclinic-to-tetragonal phase in poled ceramics depends on the electric field strength. Note that at higher poling fields no cracks in the ceramics were observed.

4.3 Influence of the substrate materials on the structural and electrical properties of the 0.65PMN– 0.35PT thick films

The 0.65PMN–0.35PT films on the Al_2O_3, Pt, 0.65PMN–0.35PT and AlN substrates were prepared and characterized. The influence of the substrate materials on the structural and electrical properties of the 0.65PMN–0.35PT thick films was studied. In this part of the thesis the characteristics of the 0.65PMN–0.35PT bulk ceramics fired at the same temperature and time, i.e., 950°C, 2 hours are added for comparison. The results are also compared with the results for the 0.65PMN–0.35PT bulk ceramics fired at 1200°C for 2 hours, which are shown in section 4.2.

4.3.1 Influence of the substrate materials on the microstructural properties of the 0.65PMN–0.35PT thick films

4.3.1.1 Thicknesses of the 0.65PMN–0.35PT films

The 0.65PMN–0.35PT films with different thicknesses were prepared. The thickness of 0.65PMN–0.35PT films after sintering depends on the number of the screen-printed steps. The thickness of the 0.65PMN–0.35PT films on alumina substrates after firing vs. number of screen printed layers is shown in Fig. 54. As expected the thickness is increasing in proportion to the number of printed layers. Films prepared with more than 16 layers cracked.

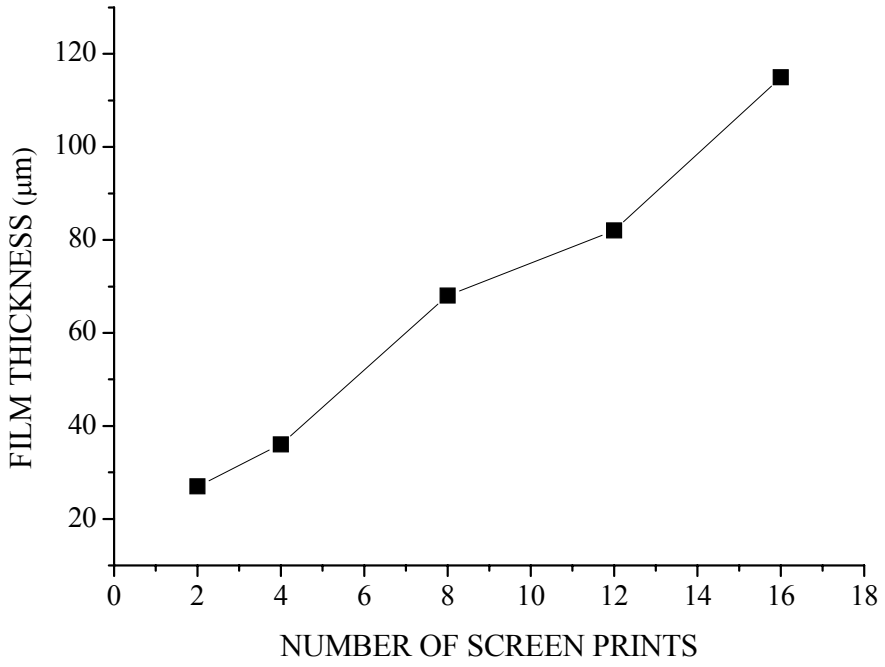

Figure 54: The thickness of the 0.65PMN–0.35PT films on alumina substrates after firing vs. number of screen printed layers. The line between the measured values is just a guide to the eye.

The thickness of 0.65PMN–0.35PT films with the same number of printed layers prepared at the same firing and cooling conditions differs with the choice of the substrates. For films prepared by two printed, dried and fired layers on Al_2O_3, Pt, 0.65PMN–0.35PT and AlN substrates the thicknesses were 21 µm, 20 µm, 26 µm and 34 µm, respectively. This is graphically shown in Fig. 55. The error of the measurement is around ±1 µm. Films on 0.65PMN–0.35PT and AlN substrates are thicker than the films on Al_2O_3 and Pt substrates due to the lower sintering density of the films on these substrates (next section).

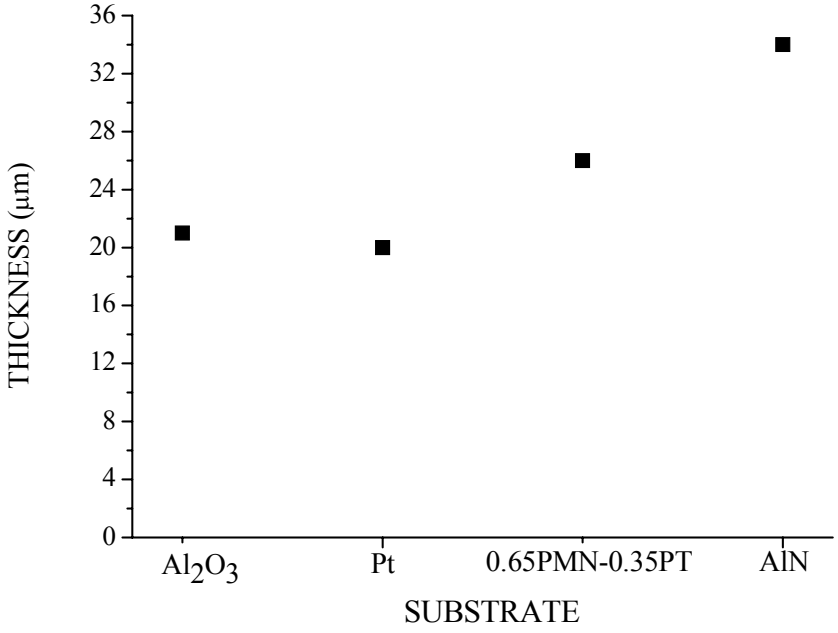

Figure 55: The thickness of the 0.65PMN–0.35PT films on Al_2O_3, Pt, 0.65PMN–0.35PT and AlN after firing. Two layers of 0.65PMN–0.35PT paste were printed in all cases.

The thickess of the 0.65PMN-0.35PT films on Al_2O_3, Pt, 0.65PMN–0.35PT and AlN were measured after screen printing (before sintering) and also after sintering at 950°C for 2 hours. The ratio between the thickness after sintering / the thickness after screen printing for films on Al_2O_3 and Pt substrates was around 40% and 50%, respectively. For films on 0.65PMN–0.35PT and AlN substrates this ratio was 30% and a few %, respectively.

4.3.1.2 Microstructures of the 0.65PMN–0.35PT thick films

The 0.65PMN–0.35PT films were screen printed, dried and heated to 500°C for 1 hour to burn out the organic vehicle. The micrograph of the surface of these films is shown in Fig. 56**.** The structure shows 0.65PMN–0.35PT grains with sub-micron dimensions as seen in the particle size distribution (Fig. 37).

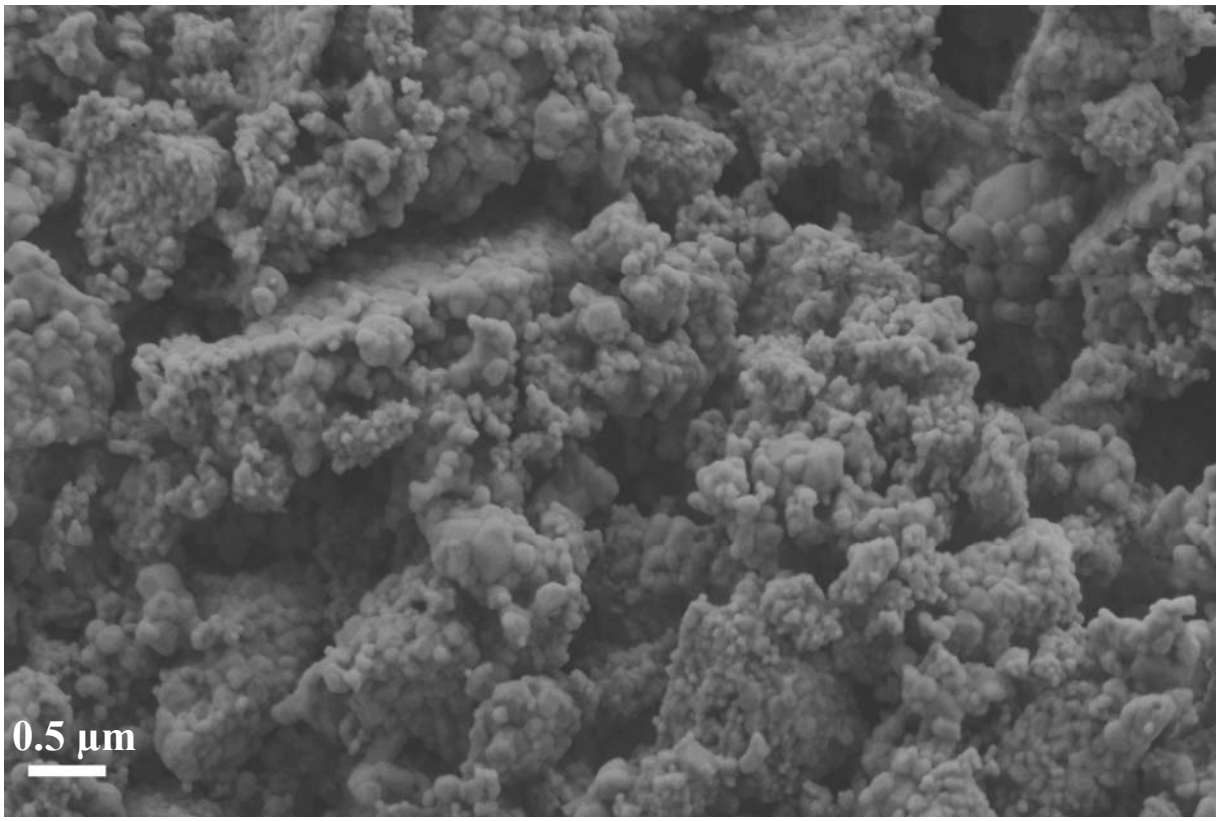

Figure 56: The micrograph of the surface of a 0.65PMN–0.35PT thick film that was screen printed, dried and heated to 500°C.

The micrographs of the surfaces of 0.65PMN–0.35PT films prepared with two printed layers, fired at 950^{o}C for 2 hours on Al_2O_3, Pt, 0.65PMN–0.35PT and AlN substrates are shown in Figs. 57 a, b and Fig. 58 a, b, respectively. The thicknesses of films were 21 µm, 20 µm, 26 µm and 34 µm, respectively. The films on the alumina and platinum substrates are dense. Significant grain growth is observed. The grain size is 1.7 µm ± 0.6 µm for the films on the alumina substrates and 1.2 µm ± 0.3 µm for the films on the platinum substrates. The grains are a few times larger than the grains of the un-fired 0.65PMN–0.35PT powder. Microstructures of the films on the 0.65PMN–0.35PT and AlN substrates consist of large pores and small grains, i.e., 0.5 µm ± 0.2 µm and 0.3 µm ± 0.1 µm, respectively. However, the grains are sintered together and the grain boundaries can be observed. Due to the small grain size of the film on the AlN substrate the micrograph of this film was performed by FE-SEM (Fig. 58 b).

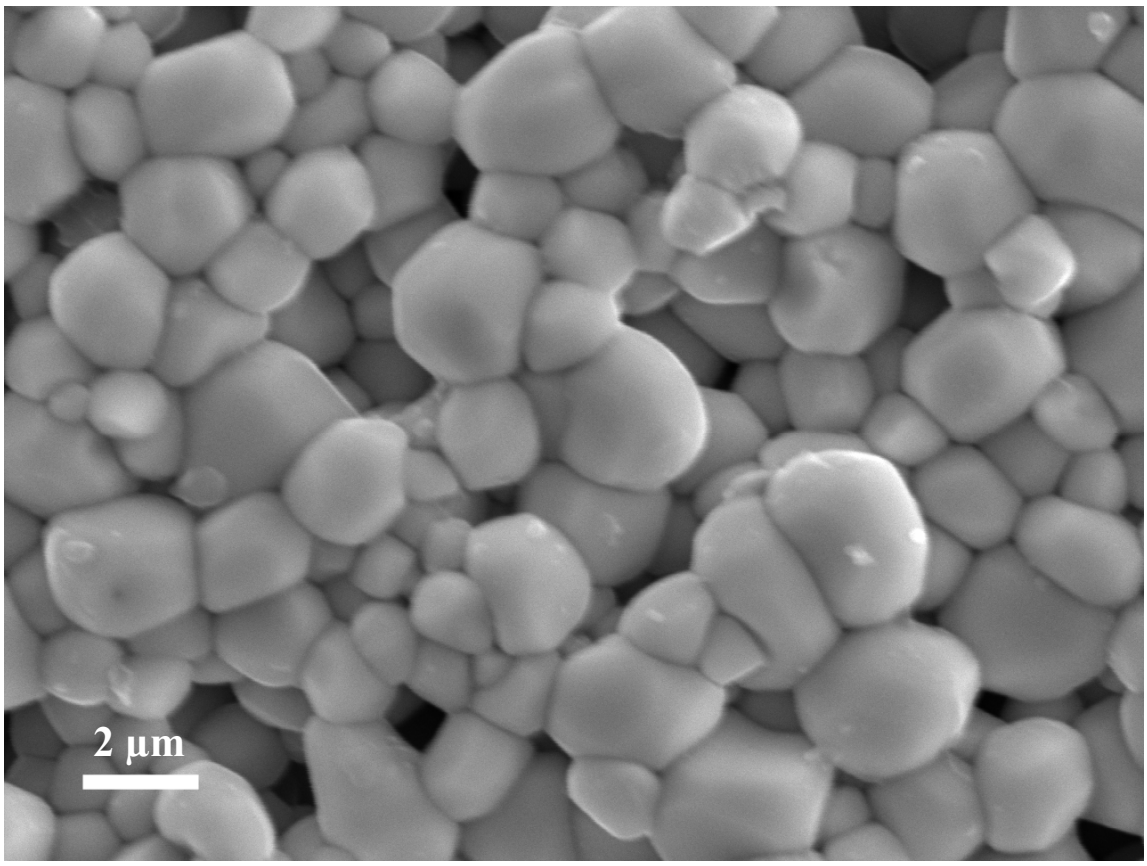

a)

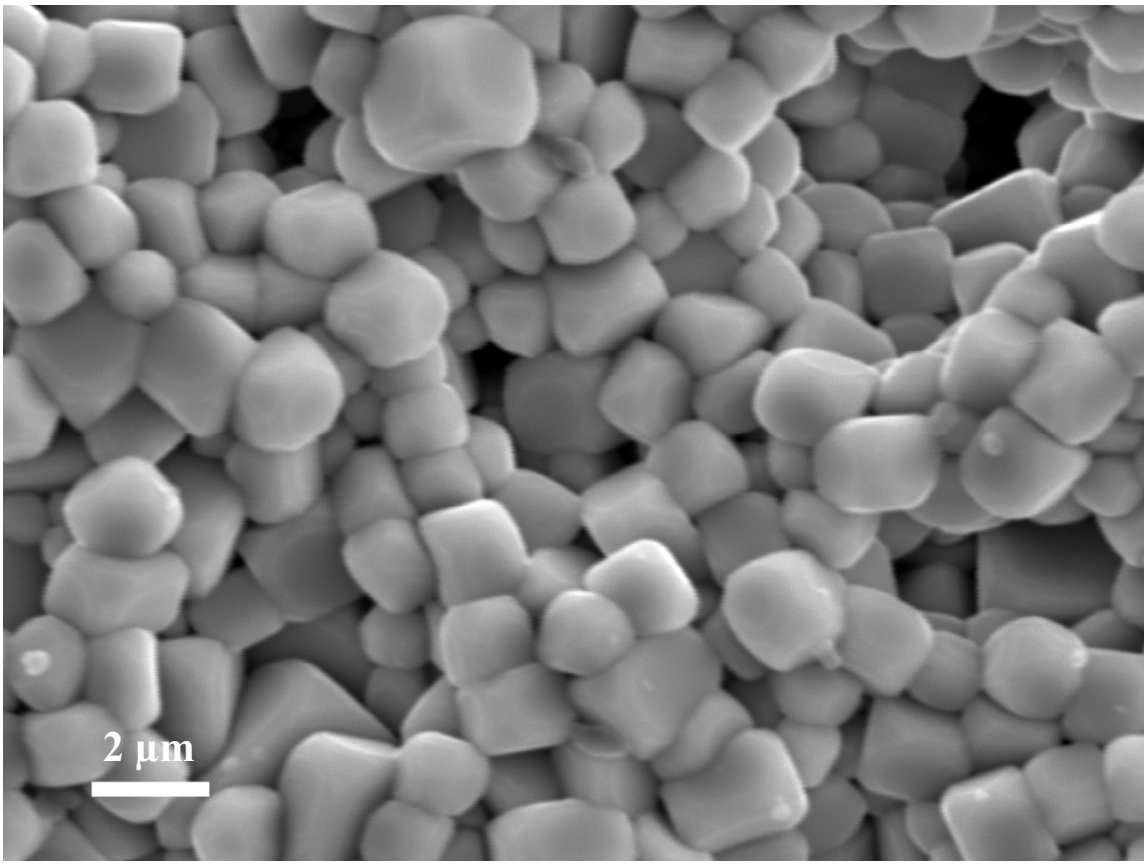

b)

Figure 57: The SEM micrographs of the surface of 0.65PMN–0.35PT thick films on a) Al_2O_3, b) Pt substrates.

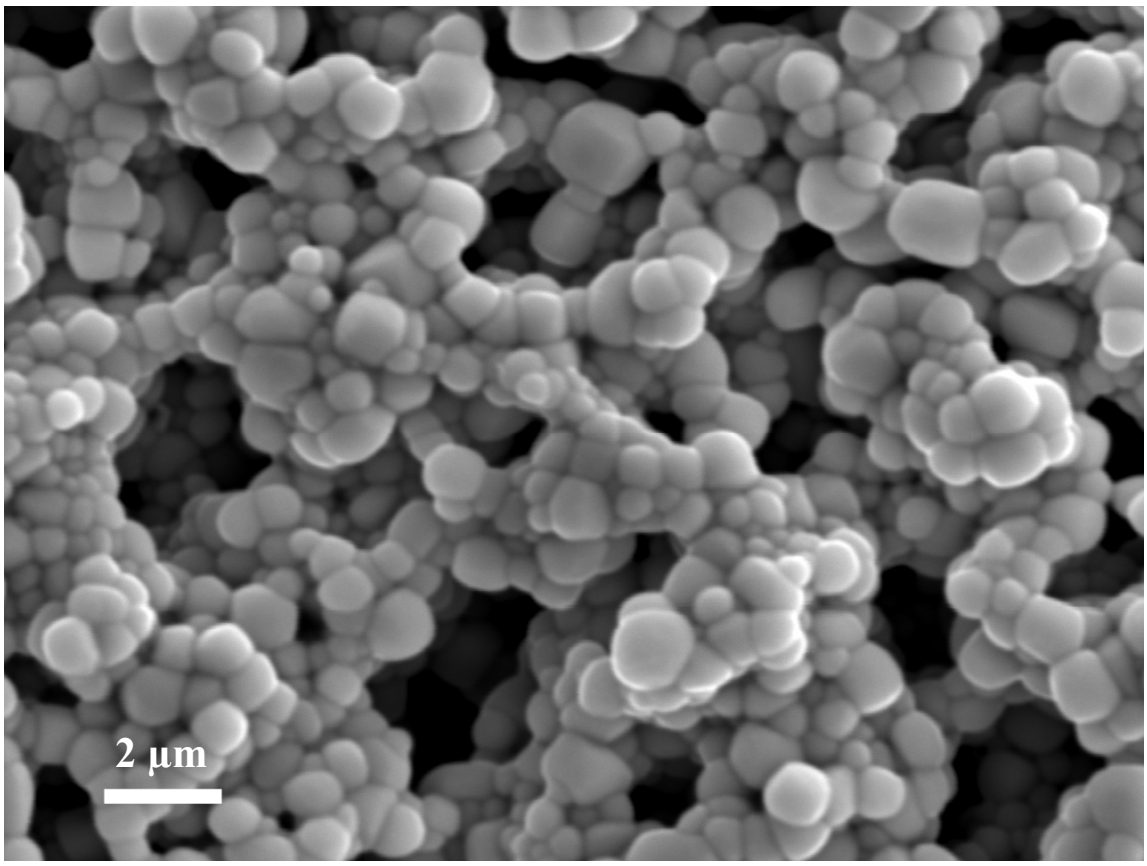

a)

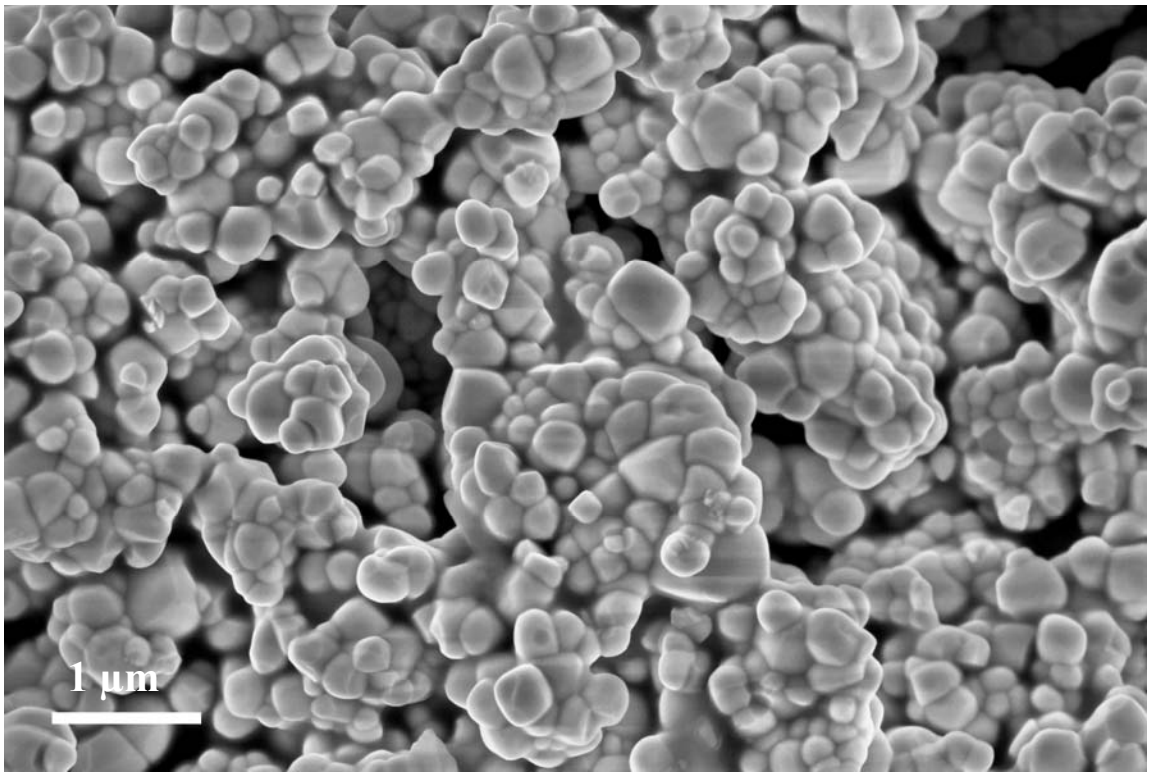

b)

Figure 58: a) The SEM micrographs of the surface of 0.65PMN–0.35PT thick films on 0.65PMN–0.35PT and b) the FE-SEM micrographs of the surface of 0.65PMN–0.35PT thick films on AlN substrates.

In Fig. 59 the fracture cross-section of the bulk 0.65PMN–0.35PT ceramics fired at 950°C is shown. The median grain size is 0.3 µm ± 0.1 µm. The ceramics are porous as the temperature 950°C is low compared to the temperatures over 1100°C usually used for sintering of bulk 0.65PMN–0.35PT ceramics [58]. The firing temperature of 950°C was chosen to have the same sintering conditions for the bulk ceramics as for 0.65PMN–0.35PT films. The measured density of the bulk 0.65PMN–0.35PT ceramics fired at 950°C is $\rho = 5.80$ g/cm^3, which is 71% of the theoretical density.

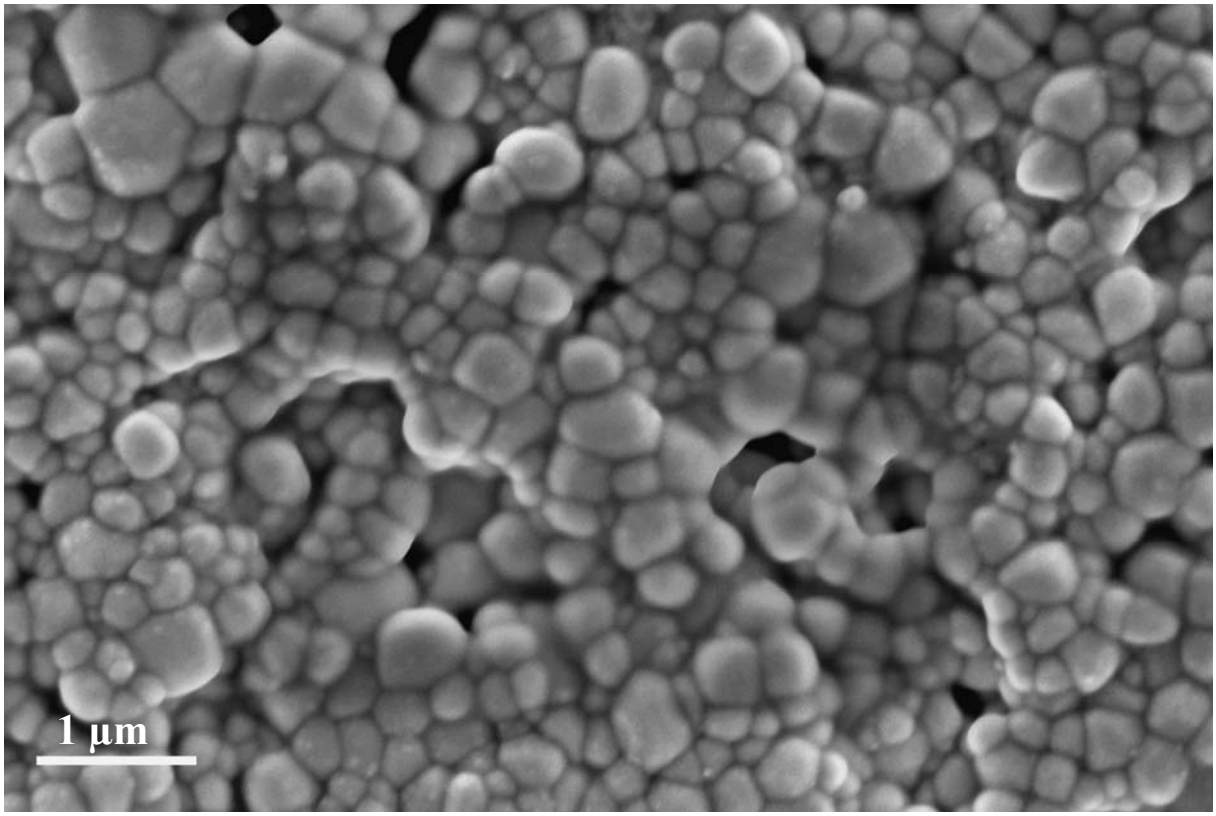

Figure 59: The FE-SEM micrographs of fracture for bulk 0.65PMN–0.35PT ceramics fired at 950°C.

The polished cross-sections of the 0.65PMN–0.35PT films on the Al_2O_3, Pt, 0.65PMN–0.35PT and AlN substrates are shown in Figs. 60a, b and 61 c and d, respectively. The films on the alumina and platinum substrates are dense. The microstructures of the films on the 0.65PMN–0.35PT and AlN substrates are porous. This is in good agreement with the microstructures of the surfaces of the films fired on the same substrates.

To summarise the 0.65PMN-0.35PT thick films on the Al_2O_3 or Pt substrates are dense and significant grain growth is observed. The median grain size of these films is larger than 1 µm, i.e., 1.7 µm for films on Al_2O_3 and 1.2 µm for films on Pt substrates, as in the case of 0.65PMN-0.35PT bulk ceramics sintered at 1200°C (section 4.2.1). The thickness of the films printed two times is around 20 µm. The films on 0.65PMN-0.35PT and AlN substrates are porous with a median grain size smaller than 1 µm, i.e., 0.5 µm and 0.3 µm, respectively, which is comparable with the 0.65PMN-0.35PT bulk ceramics sintered at 950°C. The thickness of the films printed two times is 26 µm and 34 µm, respectively. However, the grains are sintered together and grain boundaries can be observed.

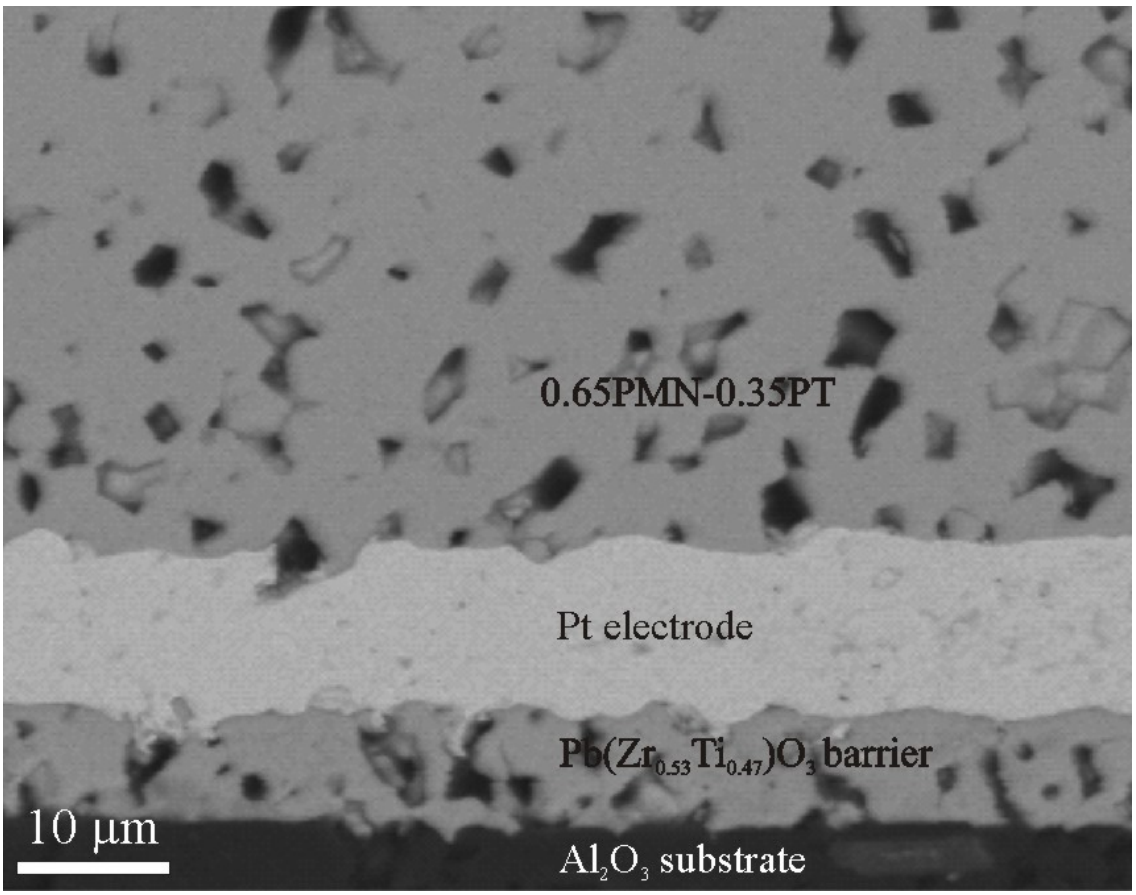

a)

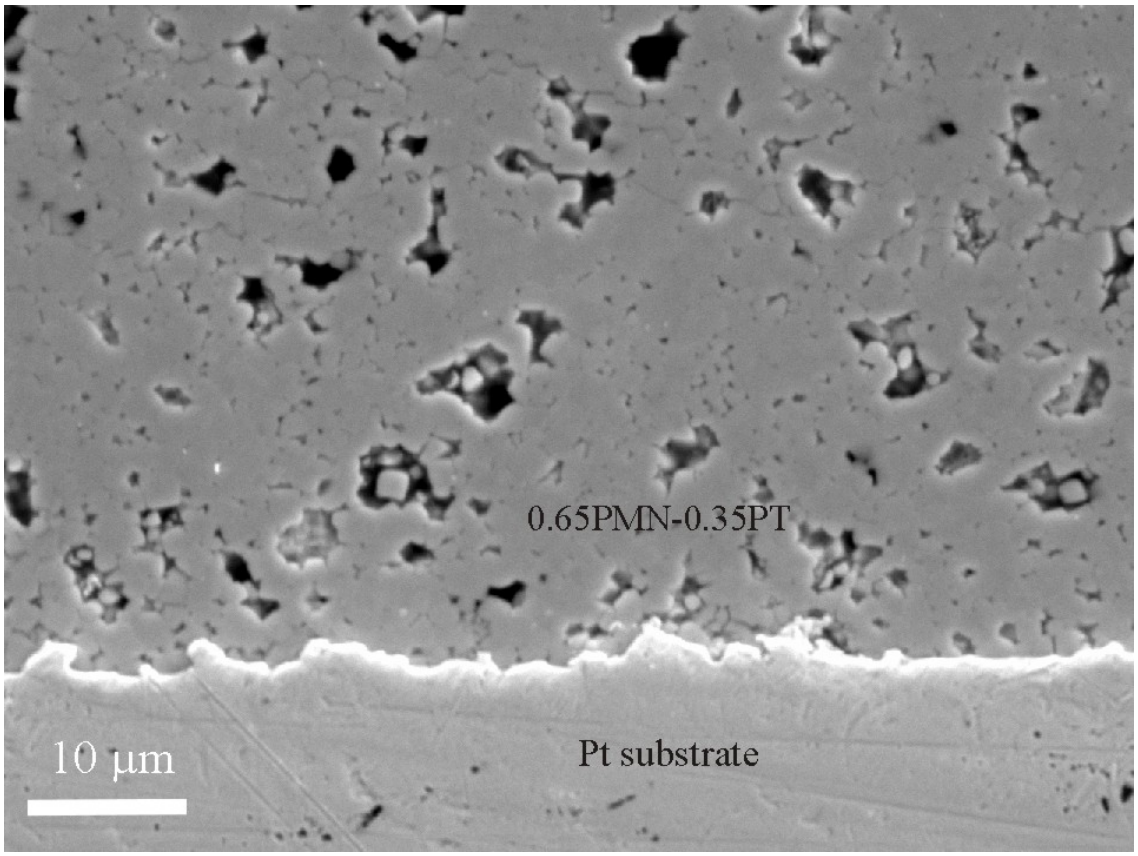

b)

Figure 60: SEM micrographs of the cross-section of the 0.65PMN–0.35PT thick films on a) Al_2O_3 and b) Pt substrates.

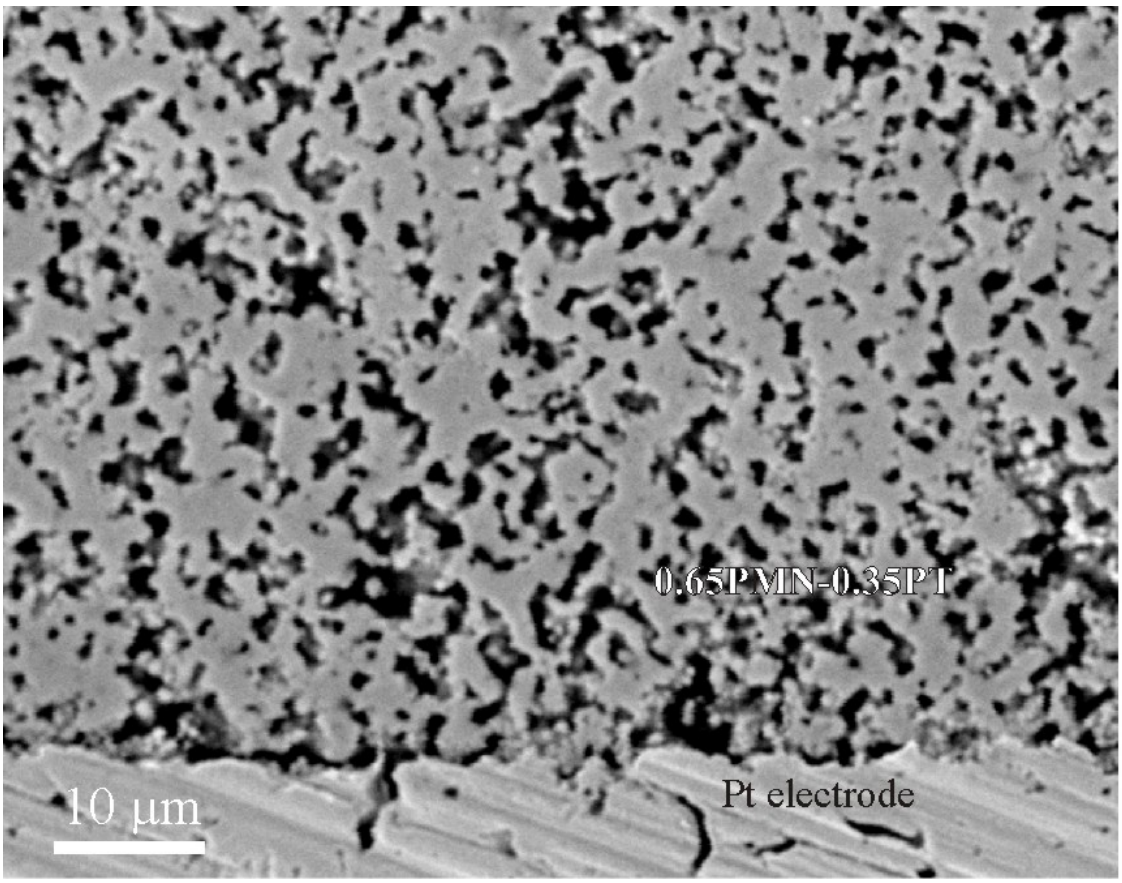

a)

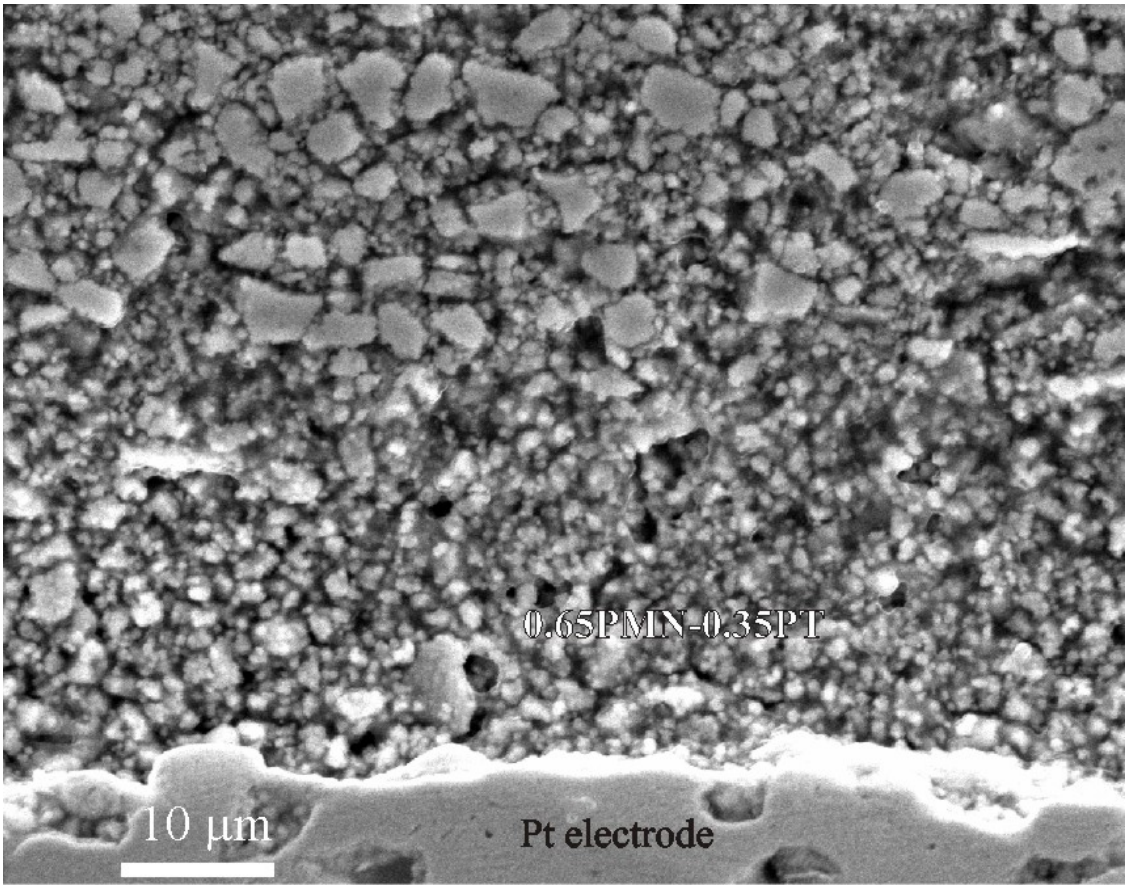

b)

Figure 61: SEM micrographs of the cross-section of the 0.65PMN–0.35PT thick films on a) 0.65PMN–0.35PT and b) AlN substrates.

4.3.1.3 Chemical composition of the 0.65PMN–0.35PT thick film

Pt substrates were considered as the most inert and therefore no significant reactions between the films and the substrates would be obtained. For this reason the films on Pt substrates were chosen for the detailed EDXS analysis of possible composition variations vs. thicknesses. The "point" analyses were performed in 23 spots on the cross-section microstructure from 0.65PMN–0.35PT/Pt interface to around 30 μm distance from the interface. For the "reference" material, dense bulk ceramics with the same composition as the films and prepared from the same powder was used. The ceramics were fired at 1200°C for 2 hours. The "point" analyses of the 0.65PMN–0.35PT bulk ceramics were also performed in 23 spots. The results and the standard deviation of the analyses for the 0.65PMN–0.35PT thick film and bulk are summarized in Table 7. Data for bulk ceramics are from Table 4. The oxygen was calculated by difference to a hundred percent. The averaged composition of the films on the Pt substrates is in agreement with the composition of the bulk ceramics within the measurement error.

Table 7: The average EDXS "point" analysis made in 23 spots (atomic percents), the standard deviation and the maximum and minimum determined values of the 0.65PMN–0.35PT thick film on the Pt substrate in comparison with the 0.65PMN–0.35PT bulk ceramic fired at 1200°C for 2 hours.

	Mg (%)	Ti (%)	Nb (%)	Pb (%)	O (%)
bulk ceramic					
Average	3.5	7.3	9.6	18.7	60.9
Standard deviation	0.5	0.4	0.3	0.5	
Maximal value	4.6	8.4	10.2	19.9	
Minimal value	2.6	6.5	8.8	18.1	
thick film					
Average	3.2	7.5	9.6	18.8	61.0
Standard deviation	0.2	0.3	0.3	0.3	
Maximal value	3.5	8.0	10.0	19.3	
Minimal value	2.6	7.1	9.2	18.1	

To evaluate the possible differences in the composition versus the distance from the substrate, the films were divided in 3 layers, i.e., the bottom layer near Pt substrate, the middle layer and the top layer. Every layer was around 10 μm thick and around 8 "point" measurements were made in each layer. The results and the standard deviation of the "point" analyses for the bottom, the middle and the top layers are summarized in Table 8. No difference in composition among the layers could be observed within the measurement error.

Table 8: The EDXS average "point" analysis made for the bottom, the middle and the top layers (atomic percents), standard deviation and the maximum and the minimum determined values.

	Mg (%)	Ti (%)	Nb (%)	Pb (%)	O (%)
top layer					
Average	3.2	7.6	9.7	18.5	61.0
Standard deviation	0.3	0.2	0.2	0.3	
Maximal value	3.5	7.9	9.8	18.9	
Minimal value	2.6	7.3	9.3	18.1	
middle layer					
Average	3.2	7.4	9.7	18.7	61.0
Standard deviation	0.2	0.2	0.2	0.3	
Maximal value	3.4	8.0	9.7	19.3	
Minimal value	2.9	7.4	9.2	18.4	
bottom layer					
Average	3.1	7.7	9.4	18.9	60.9
Standard deviation	0.2	0.2	0.2	0.3	
Maximal value	3.4	8.0	9.7	19.3	
Minimal value	2.9	7.4	9.2	18.4	

In addition to the examination of the composition vs. thickness of the films on the Pt substrates, five EDXS area analyses were performed over the film cross-section as shown in Fig. 62. Analyses were made over the areas of 7 μm x 7 μm. The results are summarized in Table 9. Again, no significant difference among the results of the analyses could be observed.

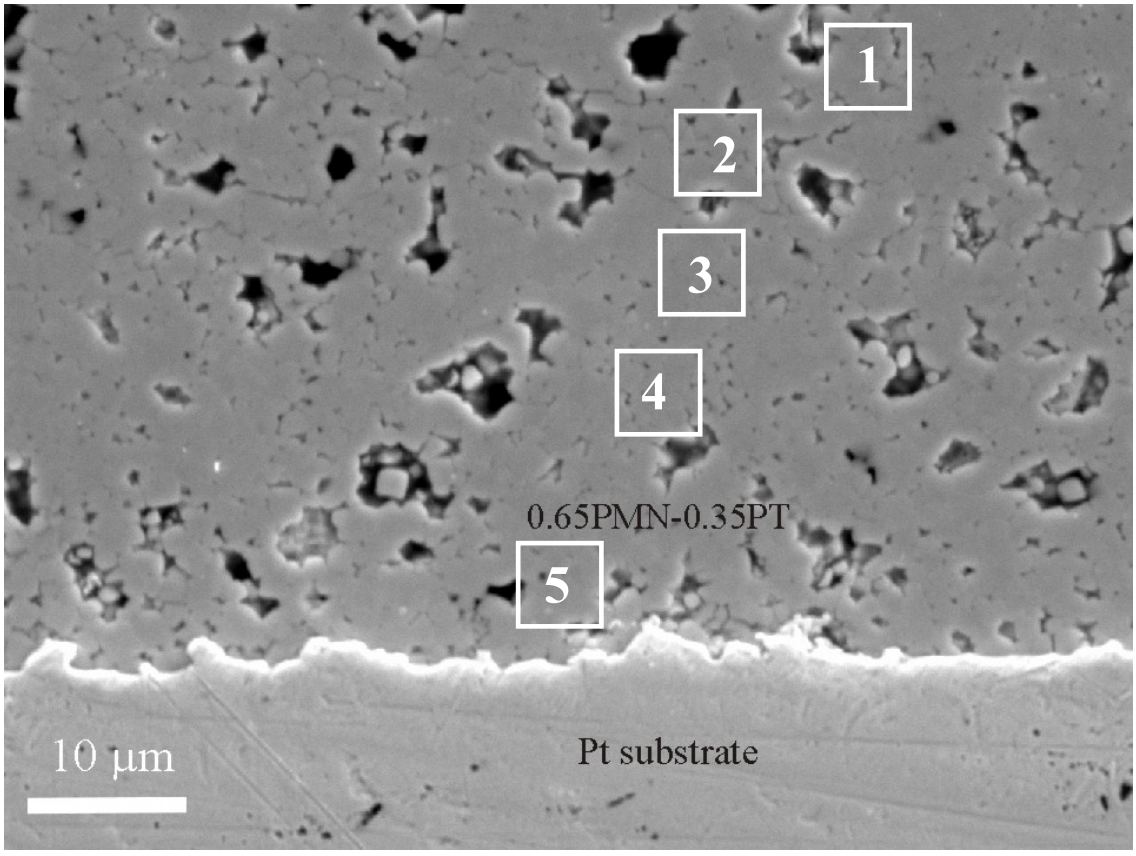

Figure 62: The cross-section of the 0.65PMN–0.35PT thick film on the Pt substrate. The positions of EDXS area analyses (area 7 μm x 7 μm) on the 0.65PMN–0.35PT thick-film cross-section.

Table 9: Area EDXS analyses for the 0.65PMN–0.35PT thick film on the Pt substrate cross-section (atomic percents) shown in Fig. 62.

Number of area analysis	Mg (%)	Ti (%)	Nb (%)	Pb (%)	O (%)
1	3.4	7.1	9.4	19.6	60.6
2	3.4	7.3	9.4	19.1	60.7
3	3.4	7.2	9.5	19.2	60.7
4	3.5	7.2	9.6	18.9	60.8
5	3.4	7.2	9.6	19.1	60.8

The 0.65PMN–0.35PT film/Pt substrate interface was investigated by TEM. The microstructure is shown in Fig. 63. The EDXS analyses were performed in the points marked with the numbers 1 and 2. The analysis performed in the 0.65PMN–0.35PT thick film (marked with number 1) showed the presence of the Pb, Mg, Nb, Ti and O elements, as expected (Fig. 64). However, the analysis made in point 2 showed the "strong" peaks of the Pb and Pt elements (Fig. 65), which indicates the existence of the Pb-Pt alloy layer at the interface between the film and the Pt substrate. In both spectra peaks of Cu and Cr are also present. These peaks are due to the holder on which the sample was placed. The Pb-Pt alloy layer is around 30 nm thick (Fig. 63). The thickness is much less than the thickness of the thick 0.65PMN–0.35PT film, therefore it is presumed that the influence of this phase on the characteristics of the thick films is negligible. The similar layers were observed by Mandeljc et al. [103] at the interface of the PZT and the Pt electrode in PZT thin films deposited on a platinised silicon substrate.

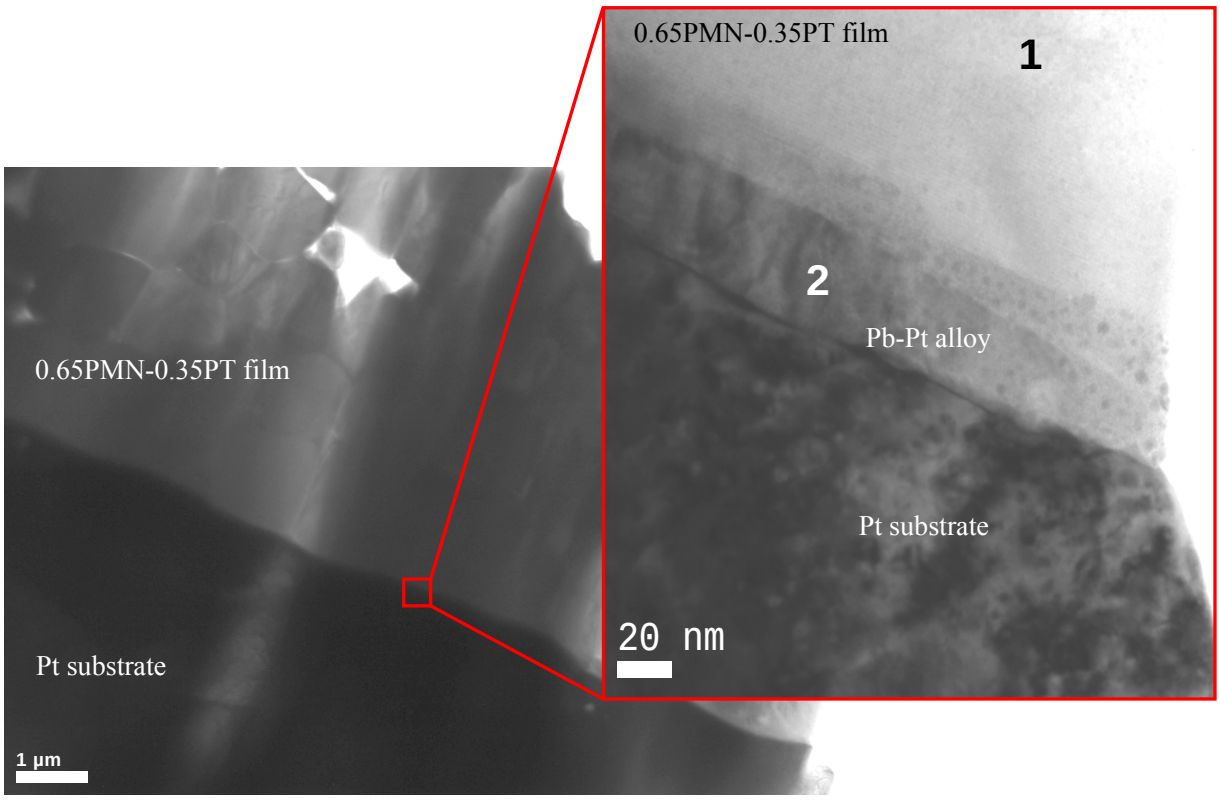

Figure 63: The microstructure of the 0.65PMN–0.35PT film – Pt substrate junction. The EDXS analyses were performed in the "points" marked with the numbers 1 and 2.

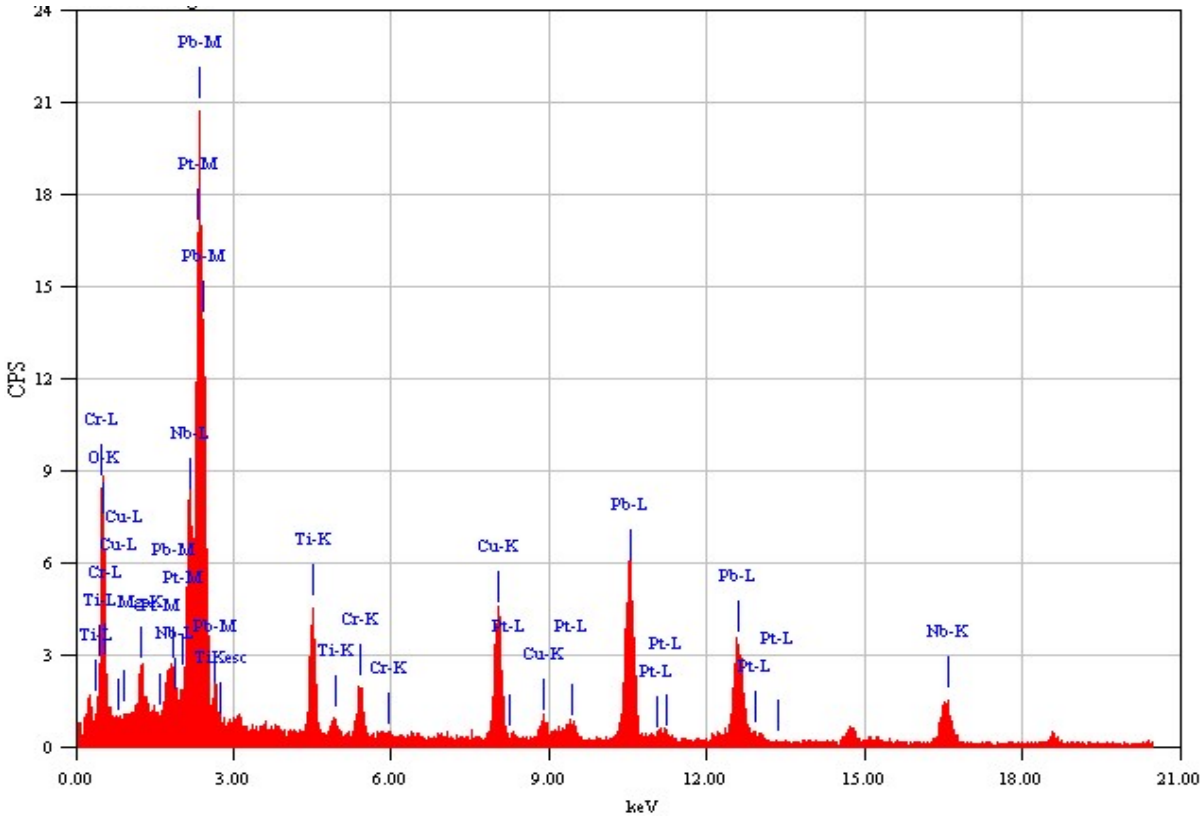

Figure 64: EDXS analysis of the point marked in Fig. 63 with number 1.

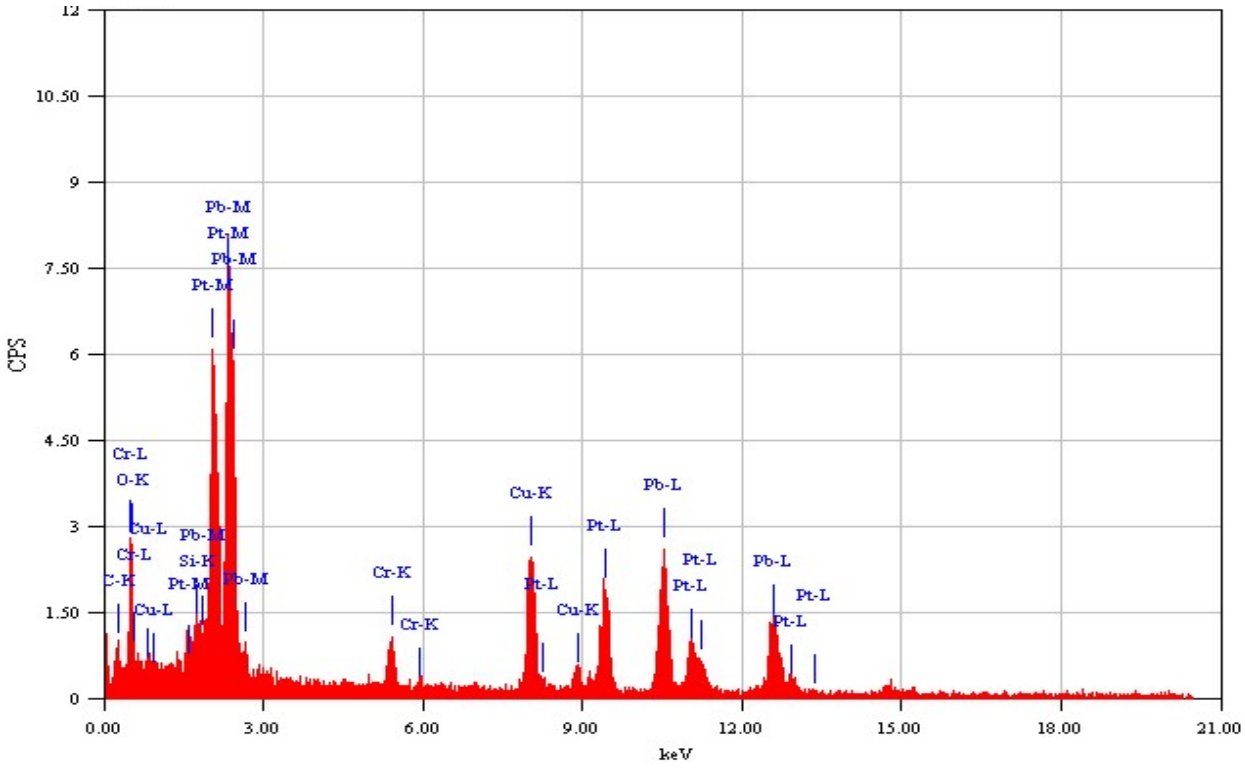

Figure 65: EDXS analysis of the point marked in Fig. 63 with number 2.

The overall analysis of the 0.65PMN–0.35PT films on the Pt substrate showed that thick-film layers are homogenous. Some interactions among the films and the Pt substrates were detected, i.e., the formation of very thin Pb-Pt alloy layers at the interface. However, the Pb-Pt layer is much to thin to influence the properties of the 0.65PMN–0.35PT films with the thickness of a few tens of μm.

To examine the composition vs. thickness for films on other substrates, five EDXS area analyses over the cross-sections of the films on the Al_2O_3, 0.65PMN–0.35PT and AlN substrates were performed. Analyses were made over the areas 7 μm x 7 μm.

The cross-sections of the 0.65PMN–0.35PT thick films on the Al_2O_3, 0.65PMN–0.35PT and AlN substrates are shown in Figs. 66, 67, and 68, respectively. The positions of the analyses are marked with the numbers from 1 to 5. The results are summarized in Tables 10, 11 and 12 for the films on the Al_2O_3, 0.65PMN–0.35PT and AlN, respectively. The obtained results of the analyses performed on the films on the different substrates are inside the standard deviation estimated for the bulk material, which was used as the reference material (see Table 7).

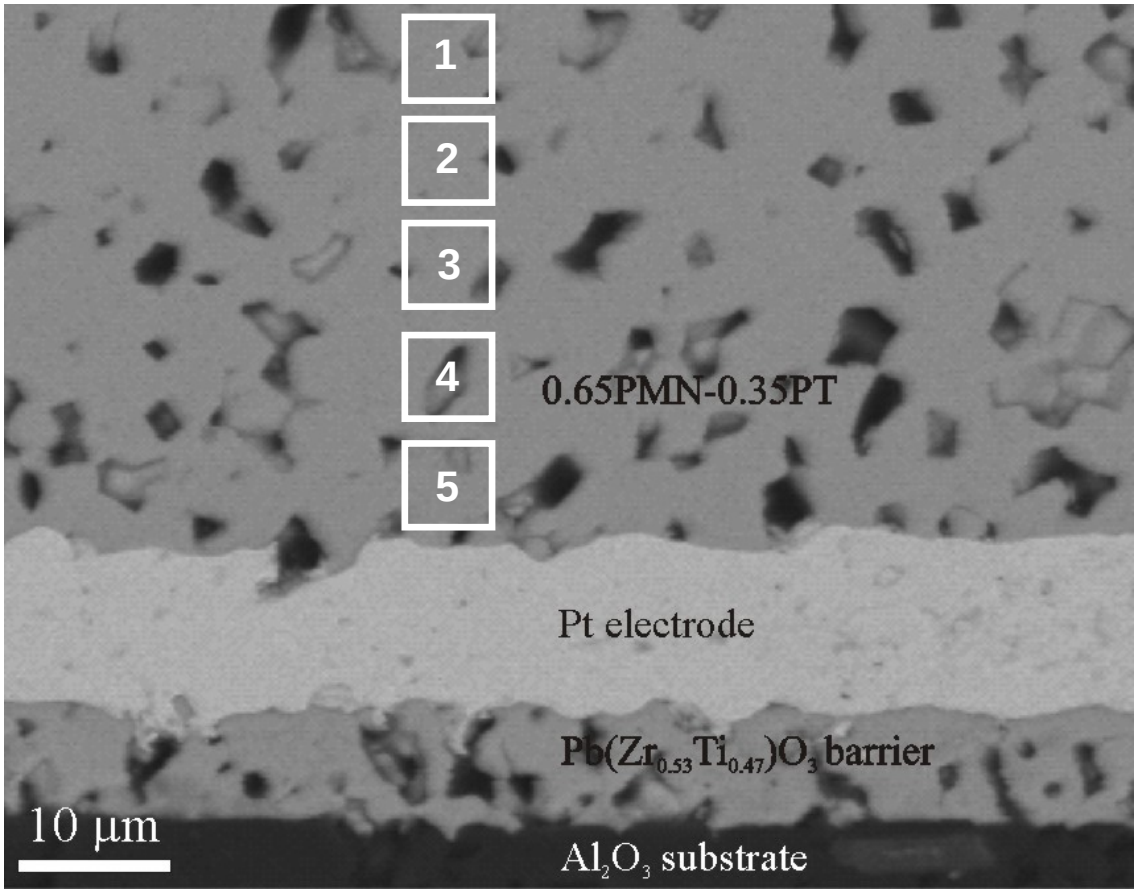

Figure 66: The cross-section of the 0.65PMN–0.35PT thick film on the alumina substrate. The positions of EDXS area analyses (window 7 μm x 7 μm) on the 0.65PMN–0.35PT thick-film cross-section are marked with the white squares and numbers from 1 to 5.

Table 10: Area EDXS analyses for the 0.65PMN–0.35PT thick film on the alumina substrate cross-section (atomic percents) shown in Fig. 66.

Number of area analysis	Mg (%)	Ti (%)	Nb (%)	Pb (%)	O (%)
1	3.8	7.0	9.4	19.2	60.6
2	3.7	7.2	9.5	18.9	60.7
3	3.2	7.6	9.5	18.7	60.9
4	3.1	7.4	9.5	19.1	60.8
5	3.8	7.2	9.3	19.2	60.6

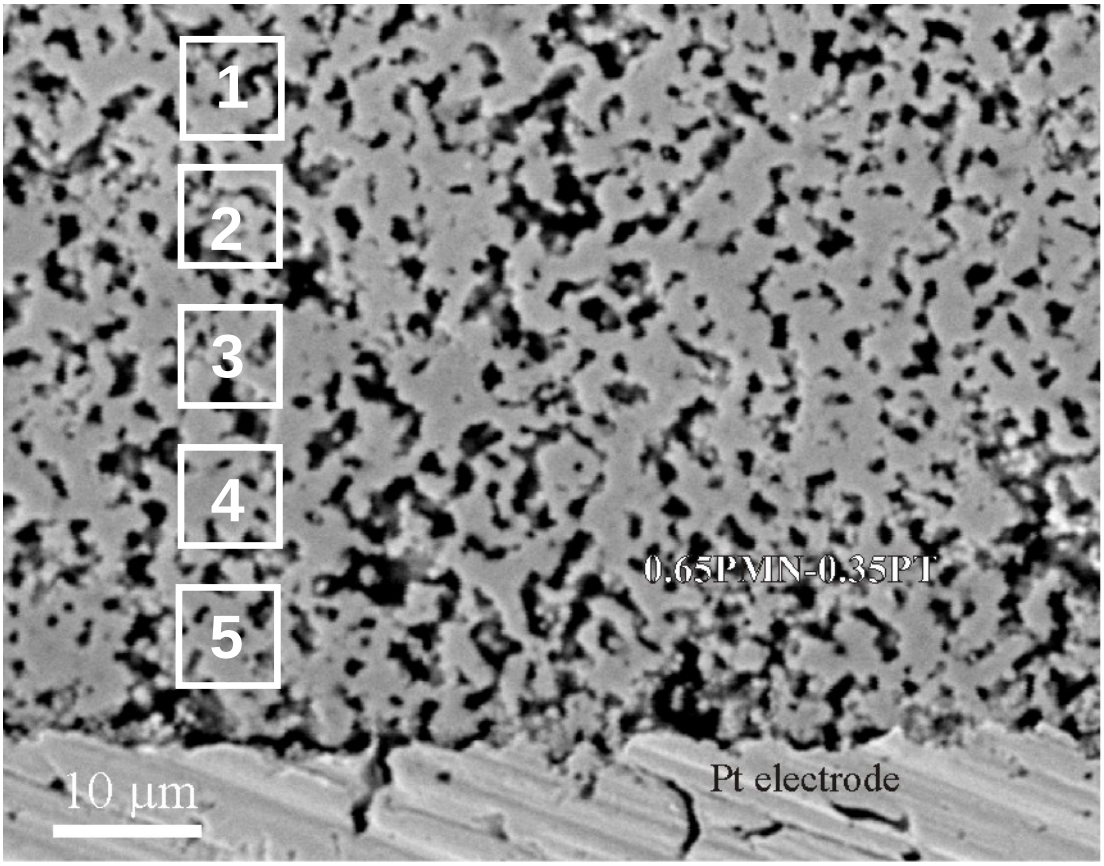

Figure 67: The cross-section of the 0.65PMN–0.35PT thick film on the 0.65PMN–0.35PT substrate. The positions of the EDXS area analyses (window 7 µm x 7 µm) on the 0.65PMN–0.35PT thick-film cross-section are marked with the white squares and numbers from 1 to 5.

Table 11: Area EDXS analyses for the 0.65PMN–0.35PT thick film on the 0.65PMN–0.35PT substrates cross-section (atomic percents) shown in Fig. 67.

Number of area analysis	Mg (%)	Ti (%)	Nb (%)	Pb (%)	O (%)
1	3.2	7.3	9.8	18.8	61.0
2	3.4	7.2	9.7	18.7	60.9
3	3.3	7.3	9.7	18.8	60.9
4	3.3	7.3	9.7	18.7	61.0
5	3.4	7.3	9.8	18.5	60.8

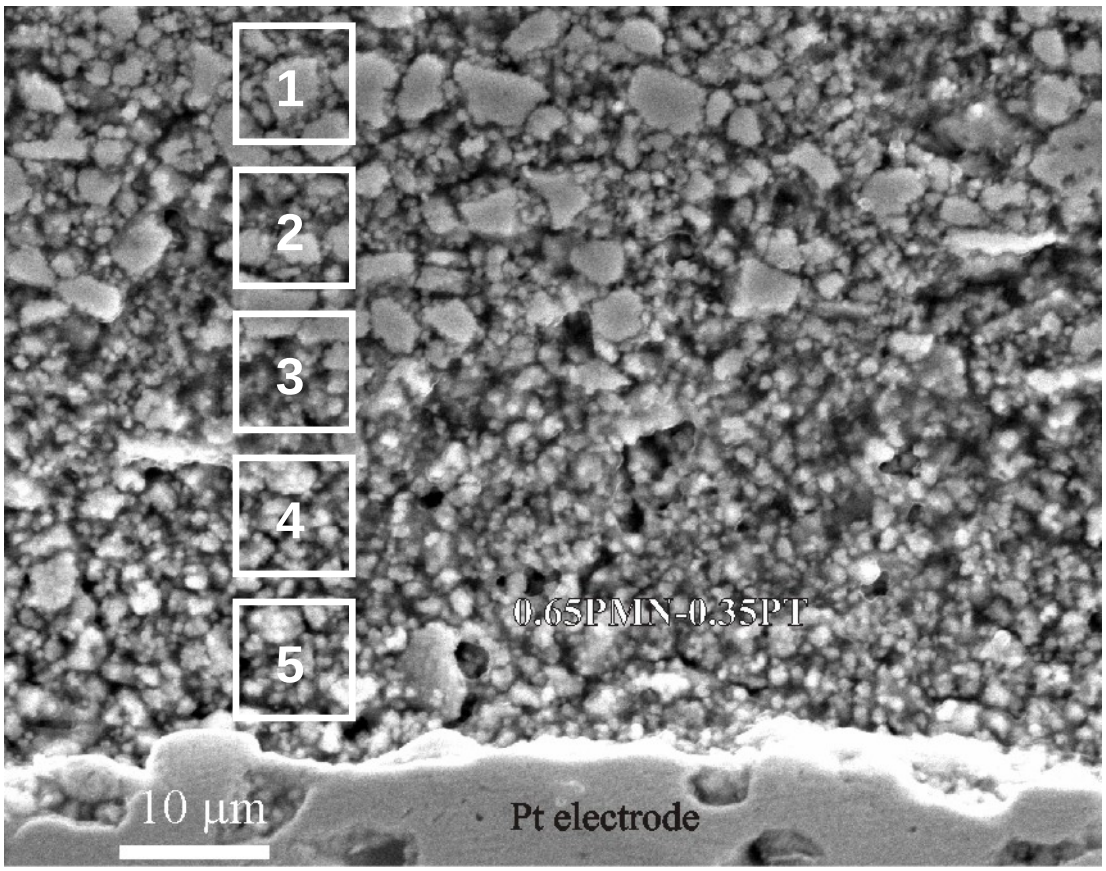

Figure 68: The cross-section of the 0.65PMN–0.35PT thick film on the AlN substrate. The positions of EDXS area analyses (window 7 µm x 7 µm) on the 0.65PMN–0.35PT thick-film cross-section are marked with the white squares and numbers from 1 to 5.

Table 12: Area EDXS analyses for the 0.65PMN–0.35PT thick film on the AlN substrates cross-section (atomic percents) shown in Fig. 68.

Number of area analysis	Mg (%)	Ti (%)	Nb (%)	Pb (%)	O (%)
1	3.1	7.6	9.7	18.6	61.1
2	3.0	7.7	9.5	18.7	61.0
3	3.1	7.4	9.7	18.7	61.0
4	3.2	7.5	9.6	18.7	61.0
5	3.3	7.4	9.5	19.0	60.8

4.3.1.4 Phase composition of the 0.65PMN–0.35PT films at room temperature

The X-ray diffraction diagrams of the 0.65PMN–0.35PT films printed twice on the Al_2O_3, Pt, 0.65PMN–0.35PT and AlN substrates were measured. The thicknesses of the films were 21 μm, 20 μm, 26 μm and 34 μm, respectively, and are shown in Fig. 55. No diffraction peaks that might correspond to the pyrochlore or PbO phases were detected. In Fig. 69 the diffraction diagram of the film on the alumina substrate is shown. The inset shows the de-convolution of the (002) and (200) tetragonal peaks (grey) and the (002), (200), (020) monoclinic peaks (black).

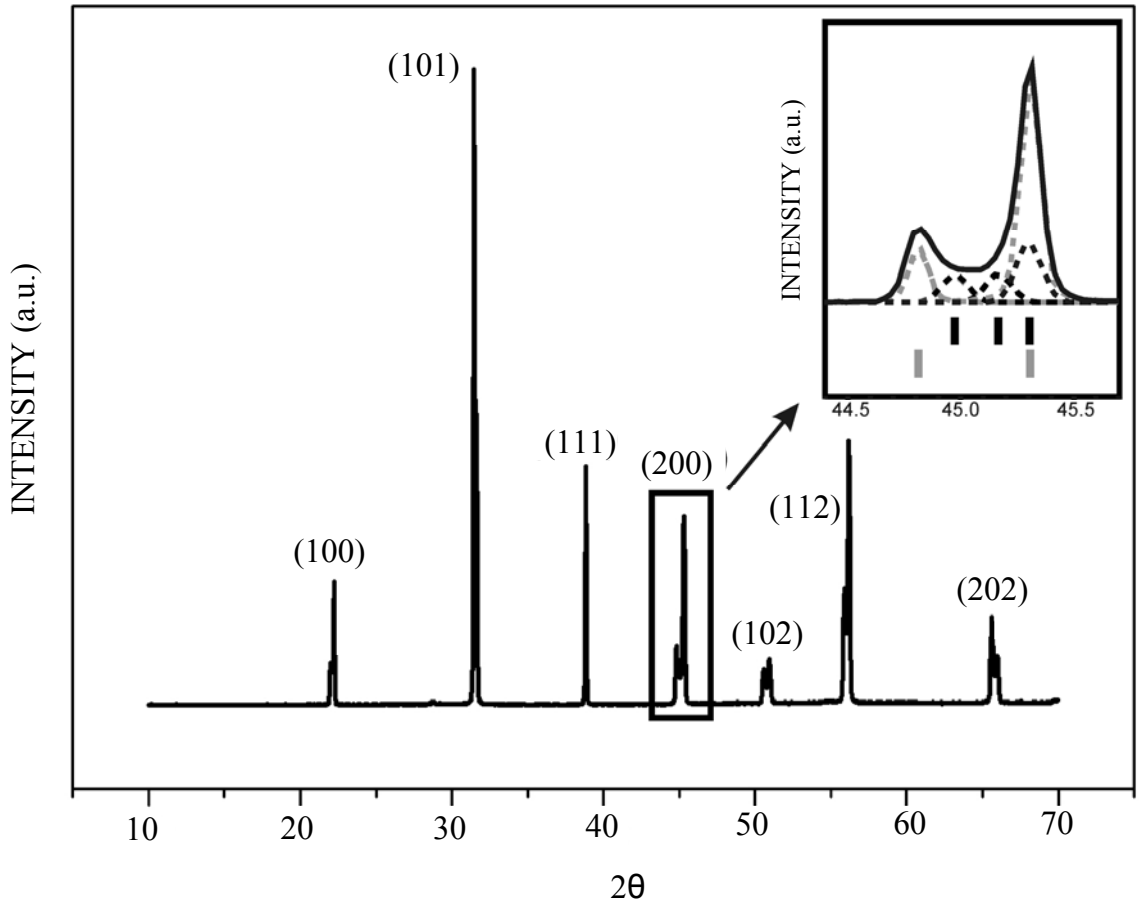

Figure 69: The X-ray diagram of the 0.65PMN–0.35PT film on the alumina substrate. The families of planes are given in brackets. The inset shows the refined Bragg peak positions of the (002), (200) tetragonal (grey) and the (002), (200), (020) monoclinic (black) phases.

The X-ray diffraction diagrams of the 0.65PMN–0.35PT films on the Al_2O_3, Pt, 0.65PMN–0.35PT and AlN substrates are different in spite of the same firing temperature and time. In Fig. 70 the X-ray diffraction diagrams of the 0.65PMN–0.35PT films on the Al_2O_3, Pt, 0.65PMN–0.35PT and AlN substrates in the range from $2\theta = 44.4°$ to $2\theta = 45.7°$ are shown. Rietveld refinement confirmed the coexistence of the tetragonal P4mm and monoclinic phases Pm in the 0.65PMN–0.35PT thick films on alumina substrates at room temperatures. A percent ratio of 42% Pm and 58% of P4mm phases was determined. We also considered the possibility that the phase is tetragonal only, however the quality of the refinement was lower. For 0.65PMN–0.35PT thick films on Pt substrates the amount of monoclinic Pm and tetragonal P4mm phases was 81% and 19%, respectively. Taking into account the (001) partial preferential orientation for tetragonal phase improved the quality of the refinement. The ratio of the intensities $I_{(001)}/(I_{(100)}+ I_{(010)} + I_{(001)})$ for these films was 0.66, whereas for the non-oriented films it was 0.33. The measured, calculated and difference curves obtained from the Rietveld refinements of the samples are presented in Figs. 71 and 72. The top marks correspond to the tetragonal phase and the bottom ones to the monoclinic. The positions corresponding to the Pt electrode (denoted by arrows) were excluded from the refinement.

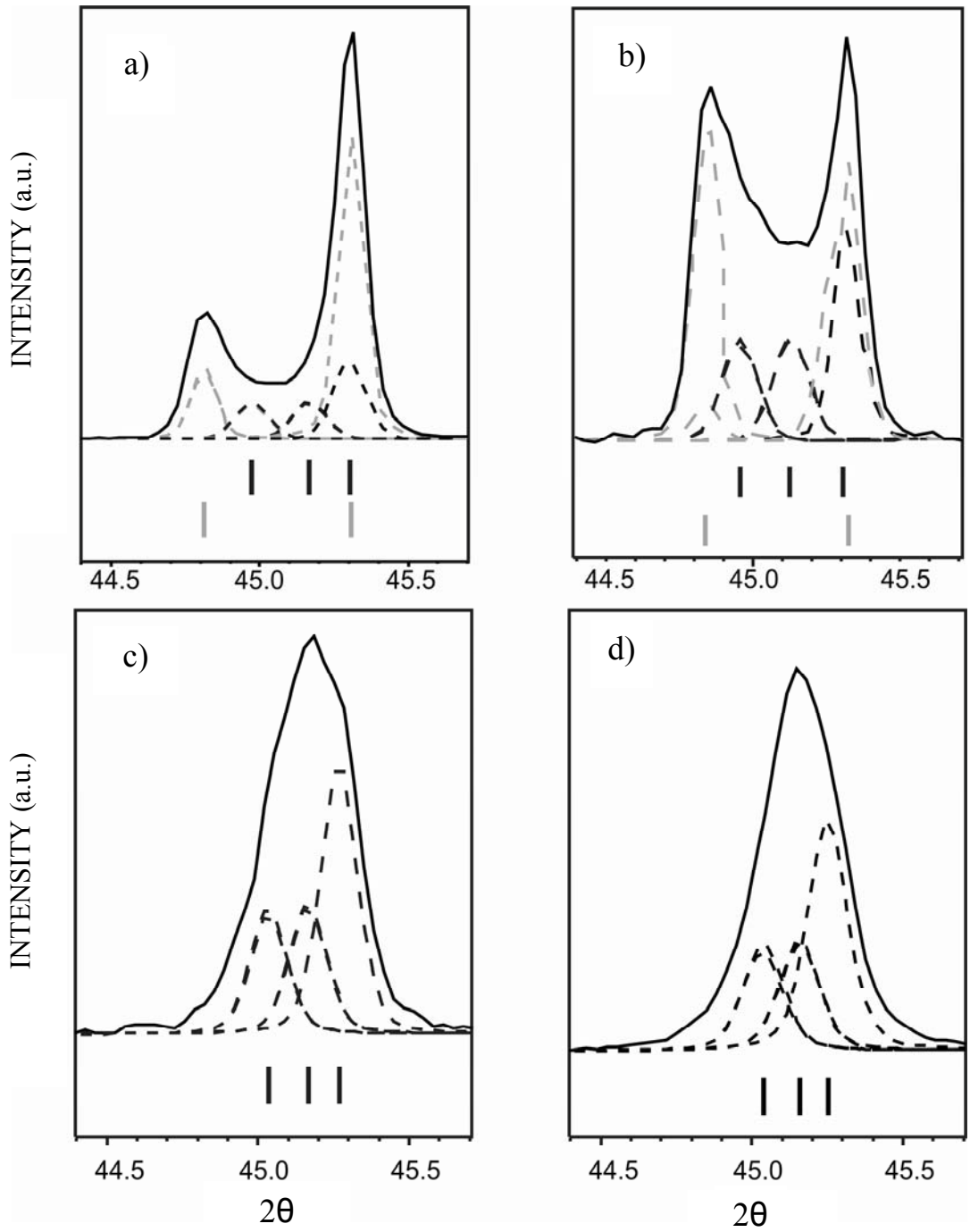

Figure 70: The X-ray diffraction diagrams of the 0.65PMN–0.35PT thick films on a) Al_2O_3, b) Pt, c) 0.65PMN–0.35PT and d) AlN substrates in the range from 2θ = 44.4° to 2θ = 45.7°. The refined peak positions of the (002), (200) tetragonal (grey) and the (002), (200), (020) monoclinic (black) phases are marked.

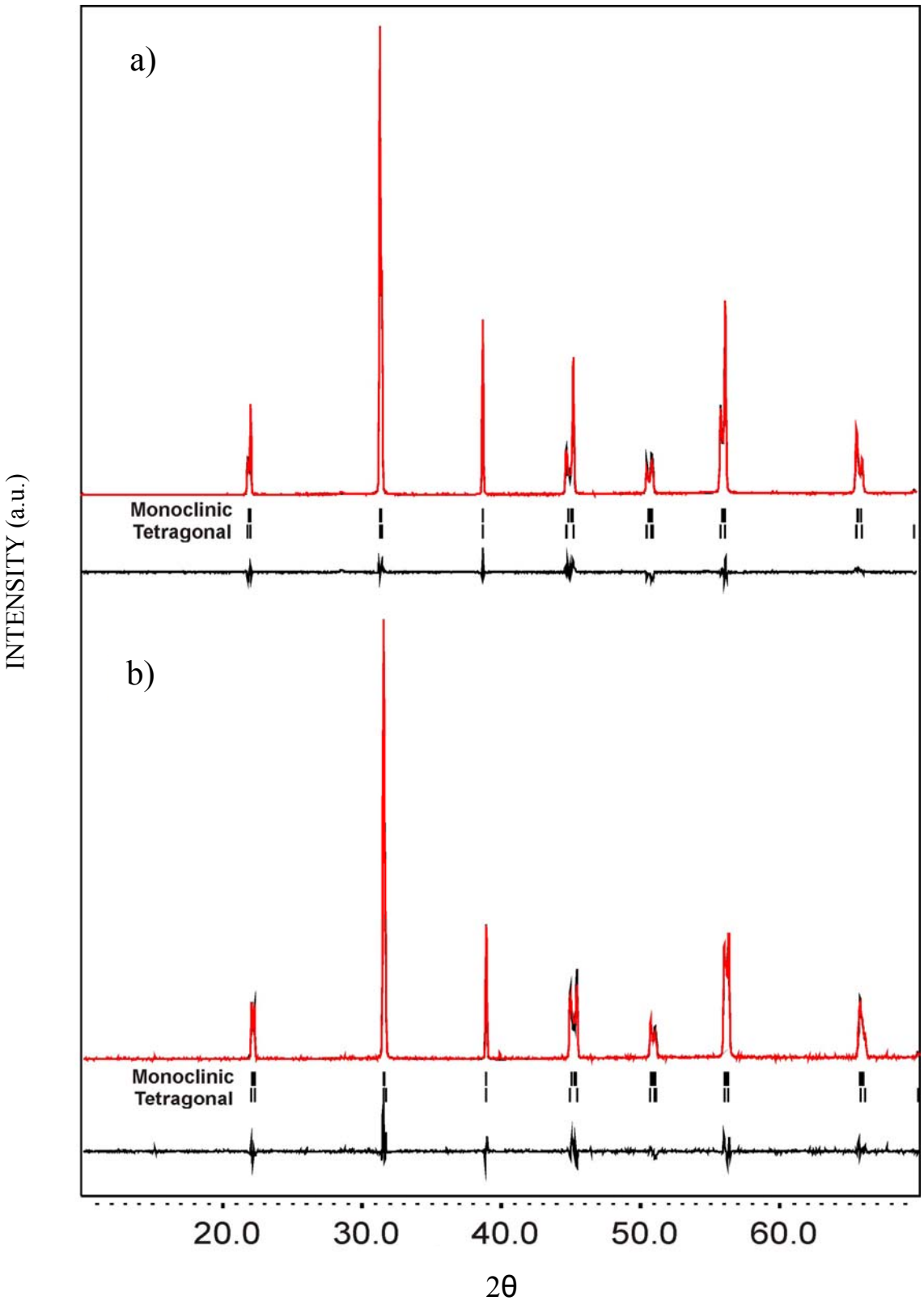

Figure 71: Final observed (red), calculated (black) and difference curves of the X-ray diffraction Rietveld refinement for films deposited on a) Al_2O_3 and b) Pt. The top black marks correspond to the tetragonal phase and the bottom ones to the monoclinic.

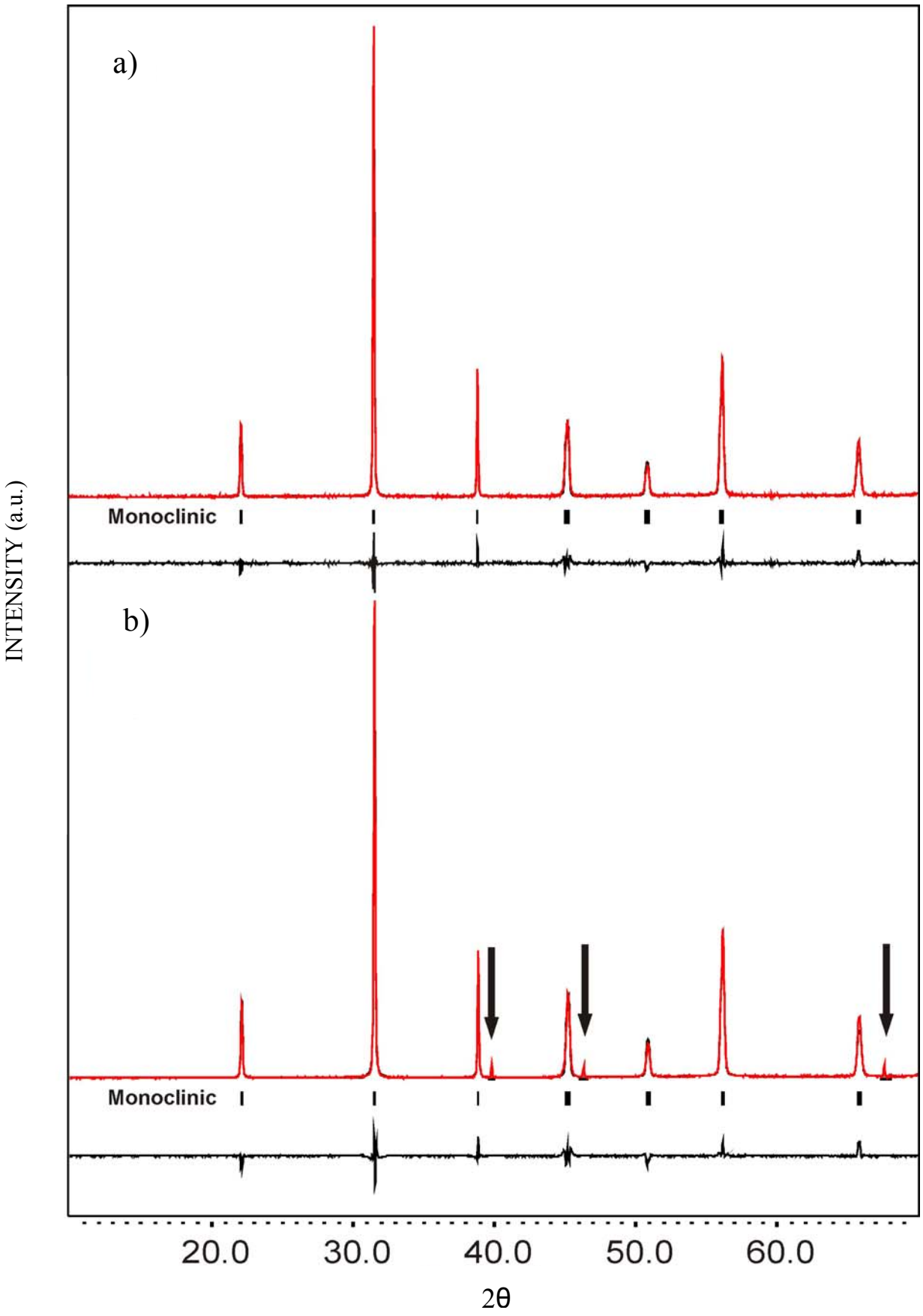

Figure 72: Final observed (red), calculated (black) and difference curves of the X-ray diffraction Rietveld refinement for films deposited on a) 0.65PMN–0.35PT and b) AlN. The black marks correspond to the monoclinic phase. The positions corresponding to Pt electrode (arrows) were excluded from the refinement.

In Table 13 the calculated phase ratio (monoclinic-to-tetragonal) in a percentage, the reliability factors R for the monoclinic and tetragonal phases, and the goodness of the fit for the profile, Gof, are collected for the 0.65PMN–0.35PT thick films on the Al_2O_3, Pt, 0.65PMN–0.35PT and AlN substrates. The values of the reliability factors and the goodness of fits are acceptable, taking into account the fixed atomic positions. The unit-cell parameters for the monoclinic Pm and the tetragonal P4mm phases for the 0.65PMN–0.35PT thick films on the Al_2O_3, Pt, 0.65PMN–0.35PT and AlN substrates are collected in Table 14. The major difference in the cell parameters of the films and bulk ceramics fired at 1200°C (section 4.2.1) is in the value of the monoclinic angle β. However, even this difference has no major influence on the volume of the unit-cell.

Table 13: Phase ratio, reliability factors R, for the monoclinic Pm (R_M) and the tetragonal P4mm (R_T) phases and goodness of fit (Gof), from the Rietveld analysis of the X-ray data measured at room temperature.

substrate	Phase ratio in percentage (%) (monoclinic Pm : tetragonal P4mm)	R_M	R_T	Gof
Al_2O_3	42 : 58	5.58	5.85	1.75
Pt	81 : 19	3.68	4.18	1.19
0.65PMN–0.35PT	100 : 0	4.31	/	1.10
AlN	100 : 0	5.49	/	1.89

Table 14: Unit-cell parameters for monoclinic Pm and tetragonal P4mm phases from the X-ray data of thick films measured at room temperature.

substrate	Unit-cell parameters for monoclinic Pm phase	Unit-cell parameters for tetragonal P4mm phase
Al_2O_3	a = 4.0135(2) Å, b = 4.0021(2) Å, c = 4.0299(2) Å, β = 90.00(7)°	a = 4.0016(1) Å, c = 4.04377(1) Å
Pt	a = 4.0204(3) Å, b = 4.0055(3) Å, c = 4.0350(3) Å, β = 90.00(6)°	a = 4.0039(2) Å, c = 4.0449(2) Å
0.65PMN–0.35PT	a = 4.0159(2) Å, b = 4.0072(2) Å, c = 4.0269(2) Å, β = 90.03(2)°	/
AlN	a = 4.0160(2) Å, b = 4.0081(2) Å, c = 4.0262(2) Å, β = 90.01(4)°	/

4.3.1.5 Phase composition of the 0.65PMN–0.35PT bulk ceramics fired at 950°C at room temperture

For the comparison with thick 0.65PMN–0.35PT films, the X-ray diffraction diagram of the bulk ceramics with the same composition and fired at the same temperature, i.e., 950°C was also measured and it is shown in Fig. 73. At first glance, the Bragg peaks appear single, but broad. Different phases were considered, however the best agreement factor and matching between the observed and calculated profiles is obtained with only a monoclinic Pm phase and the unit-cell parameters: a = 4.0160(1) Å, b = 4.0057(1) Å, c = 4.0271(2) Å and β = 90.091(3)°. The inset in Fig. 73 shows the family of (200) peaks. The refined peak positions (002), (200), (020) of the monoclinic Pm phase are marked.

Two regions, i.e., from 2θ = 38° to 2θ = 40° and from 2θ = 44.2° to 2θ = 46.4°, of the measured X-ray diffraction diagram and the Rietveld refinement for the monoclinic Pm phase are shown in Fig. 74. The Rietveld refinement for the cubic Pm-3m phase is also added for comparison (insets in Fig. 74). It is clearly evident that the calculation and the measurements are in better agreement for the monoclinic Pm phase than for the cubic Pm-3m phase.

We tried a mixture of the monoclinic Pm phase with the tetragonal P4mm one, but no improvement in the refinement was obtained. Therefore, the prepared bulk ceramics at 950°C are described by a monoclinic phase, while a small amount (not detected in our X-ray data) of tetragonal phase cannot be completely excluded.

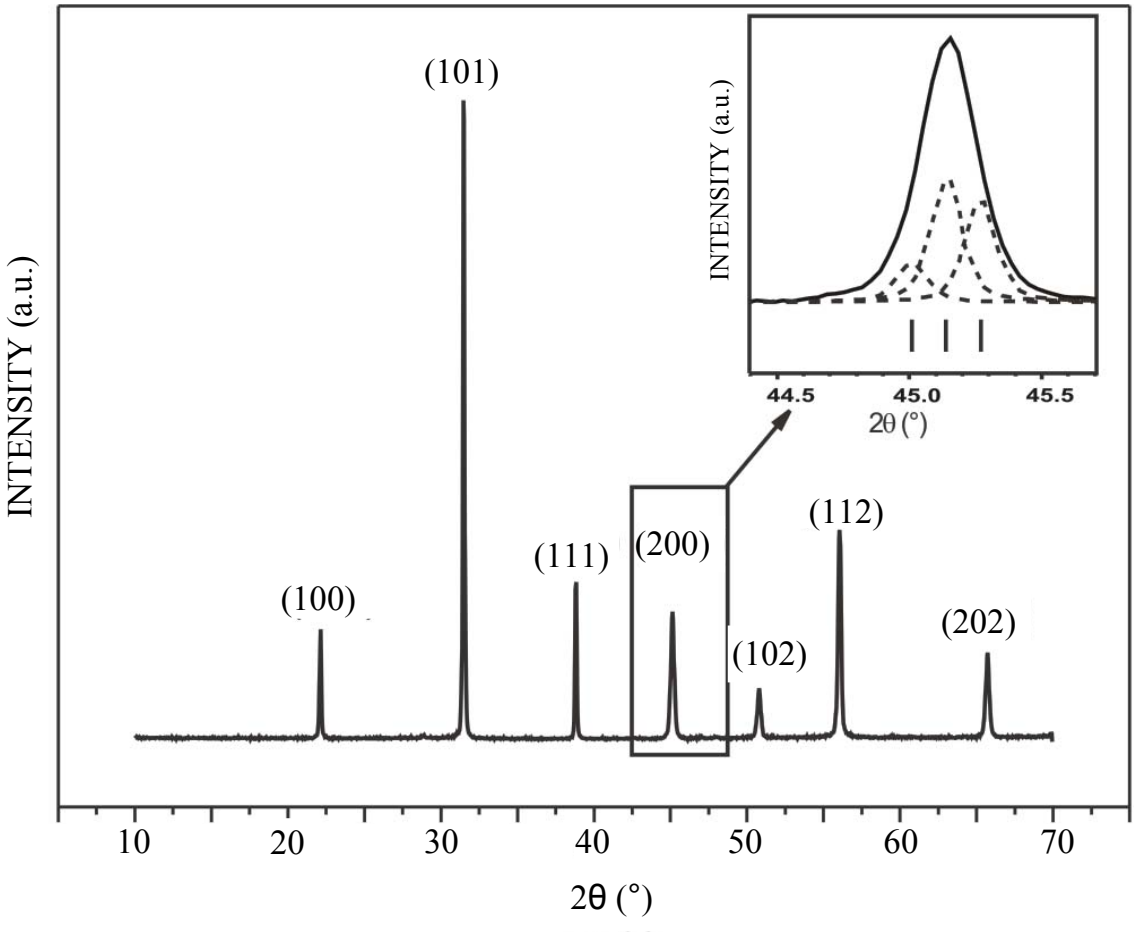

Figure 73: The X-ray diffraction diagram of 0.65PMN–0.35PT ceramics fired at 950°C. Inset shows the family of (200) peaks. The refined peak positions (002), (200), (020) of the monoclinic Pm phase are marked in the inset.

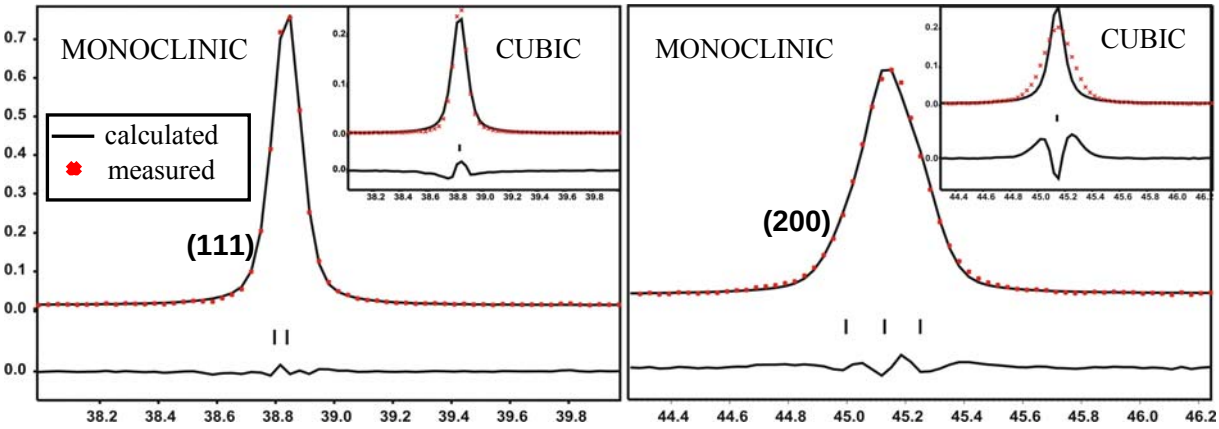

Figure 74: Two regions a) from 2θ = 38° to 2θ = 40° and b) from 2θ = 44.2° to 2θ = 46.4°, of measured X-ray diffraction diagram for the ceramics and the profile matching for the monoclinic Pm phase. Insets: the profile matching for the cubic Pm-3m phase is also added for comparison.

4.3.1.6. Temperature dependence of the phase composition of 0.65PMN–0.35PT films

To understand and clarify the co-existence of the monoclinic and tetragonal phases, the X-ray diffraction analysis of the 0.65PMN–0.35PT films were performed at different temperatures, i.e., from -173°C to 200°C. The X-ray diffraction patterns were measured within the interval from 2θ = 39.75° to 2θ = 41.25° using a step of 0.01°. The X-ray diagrams of the family of (200) peaks of 0.65PMN–0.35PT films on alumina substrates at different temperatures are shown in Fig. 75. The black arrow indicates the increasing temperatures.

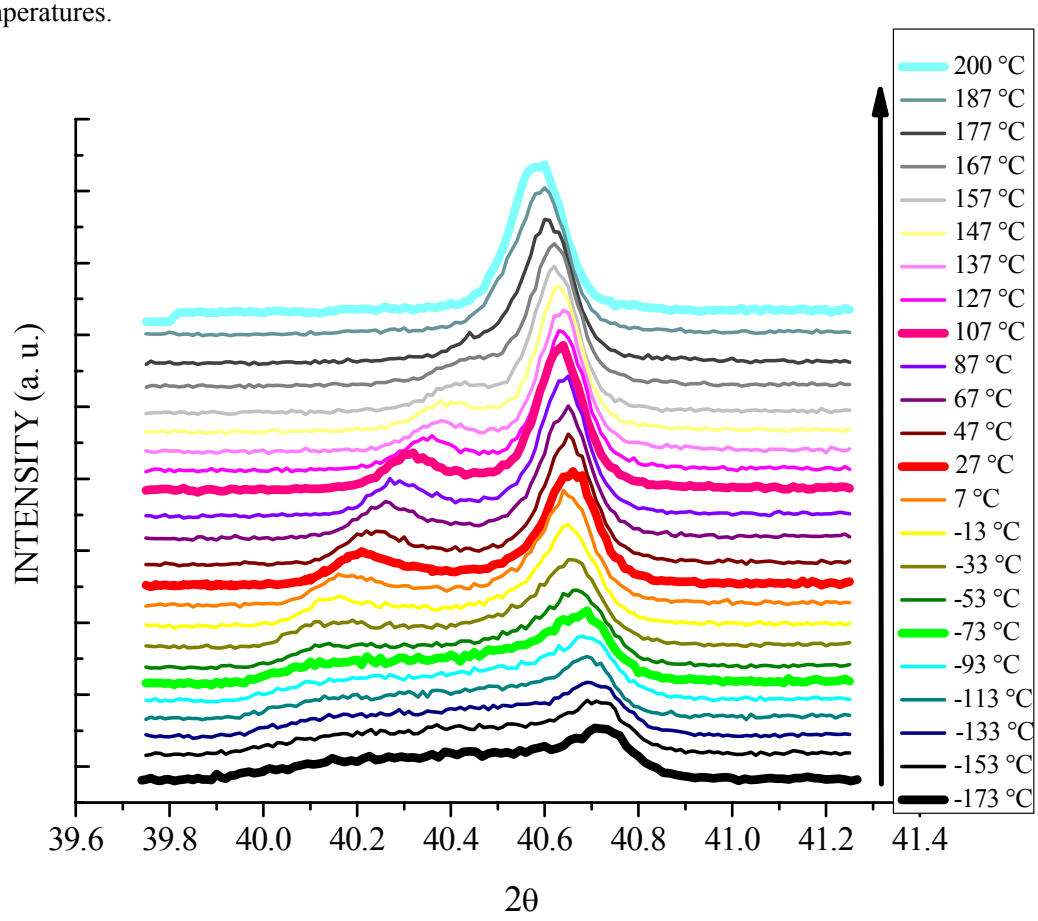

Figure 75: The X-ray diffraction diagram of the 0.65PMN–0.35PT films on the alumina substrates measured at different temperatures. The black arrow indicates the increasing temperatures.

At high temperatures of 187°C and 200°C, the diffraction pattern with single Bragg peaks is described by a cubic Pm-3m phase. At 177°C, a new peak on the left-hand side (at a lower angle) of the main Bragg peak appears, attesting to the occurrence of the tetragonal phase. The peak splitting is well understood by considering a tetragonal phase down to 107°C, but below that temperature an additional intensity is observed in between the two tetragonal Bragg peaks. This is an indication of the appearance of the monoclinic phase. As a result, at 27°C the phase ratio is 42% of monoclinic Pm phase and 58% of tetragonal P4mm phase, as was mentioned in the previous section. The coexisting phases are observed until –73°C, below which the phase has mainly a monoclinic symmetry. Fig. 76 shows the variations of the unit-cell parameters with temperature for both the monoclinic Pm and the tetragonal P4mm phases.

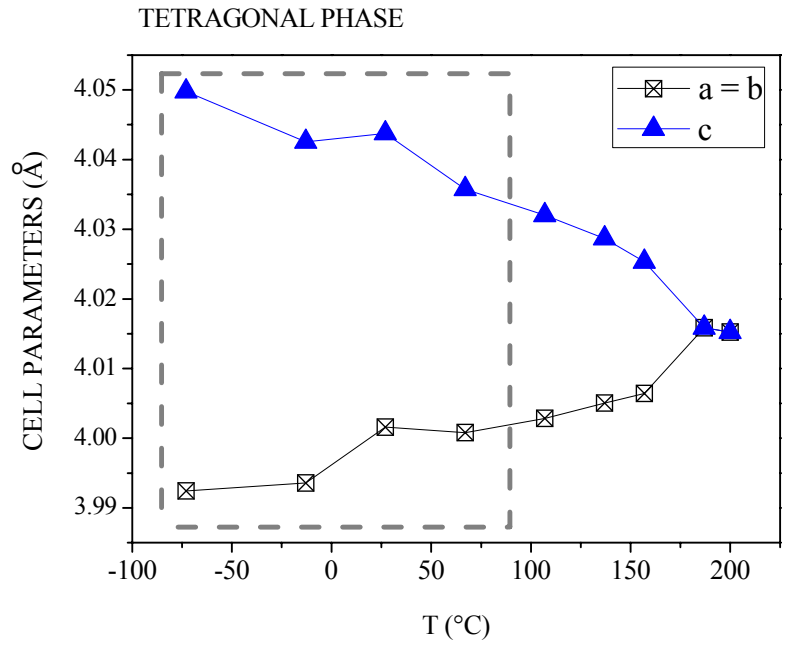

a)

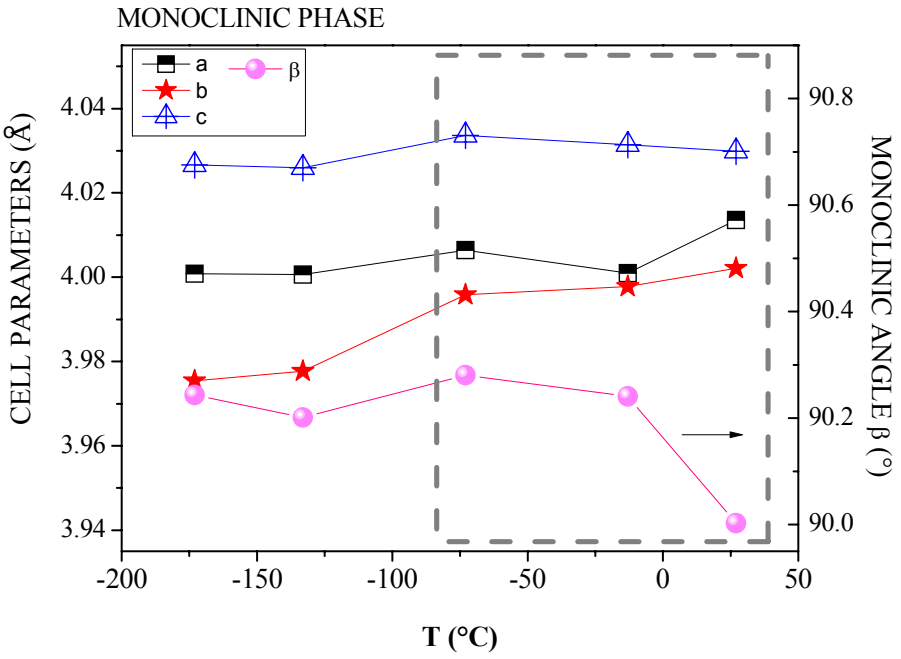

b)

Figure 76: Variations of cell parameters with temperature for a) the tetragonal P4mm and b) the monoclinic Pm phases of the 0.65PMN–0.35PT films on alumina substrates. The dashed rectangle shows the area of the coexistence of the tetragonal P4mm and monoclinic Pm phases. The lines between the measured values are just a guide to the eye.

With decreasing temperature the tetragonal *a*-parameter decreases, while the *c*-parameter increases describing the enhancement of the tetragonal strain, which reaches a value of ~1.4% at –73°C. The monoclinic unit-cell parameters decrease very weakly with the decreasing temperature. The beta monoclinic angle is relatively stable at 90.24° (±0.04°) until 27°C where it drops to a value close to 90°. In Fig. 76, the dashed rectangle shows the area of the coexistence of the tetragonal P4mm and the monoclinic Pm phases. Between 67°C and 87°C, a small amount of the monoclinic phase is detected, but due to the very weak intensity of its reflections, the positions cannot be refined.

The X-ray diagrams of the family of the (200) peaks for the 0.65PMN–0.35PT films on Pt substrate measured at different temperatures are shown in Fig. 77. The X-ray diffraction diagrams were measured within the interval from 2θ = 39.75° to 2θ = 41.25° using a step of 0.01°.

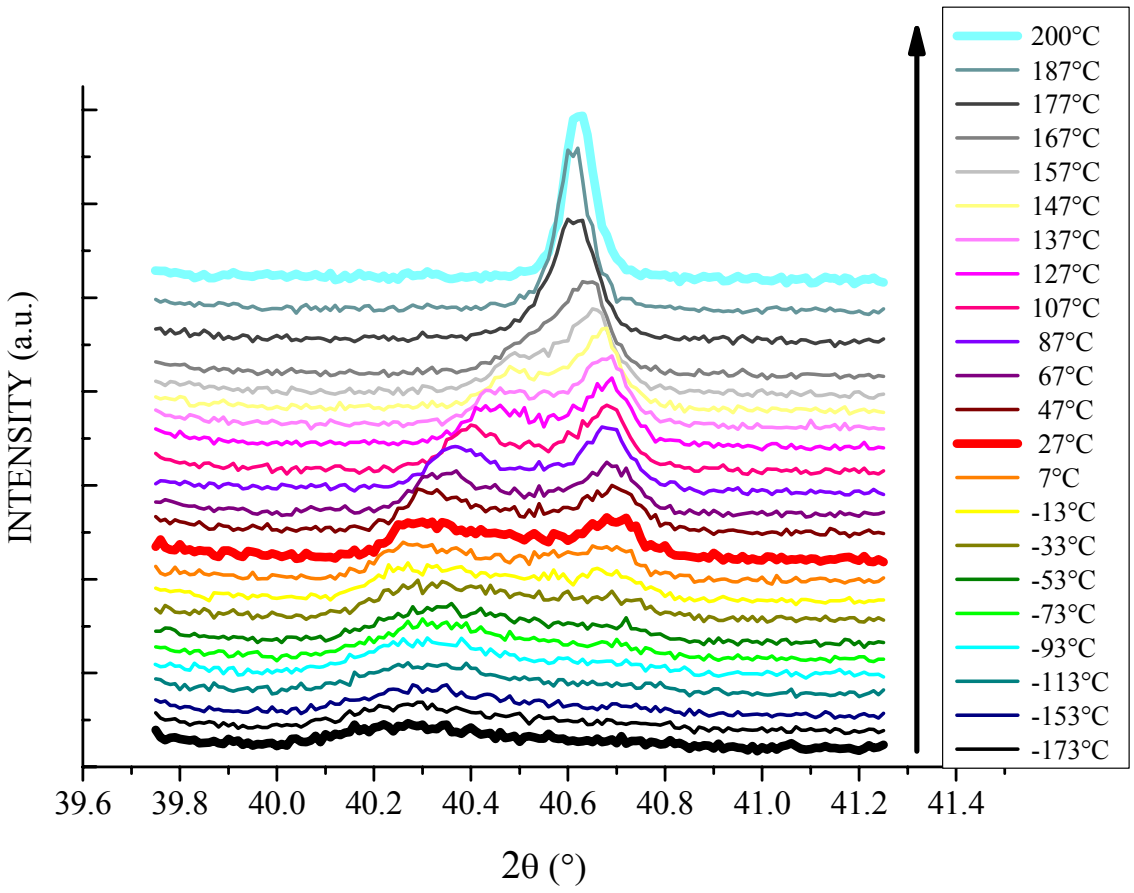

Figure 77: The X-ray diffraction diagram of the 0.65PMN–0.35PT films on the Pt substrates measured at different temperatures. The black arrow indicates an increase of the temperature.

For the 0.65PMN–0.35PT films on Pt substrates at low temperature, the monoclinic Pm phase is found as in the case of the film on the alumina substrate. The tetragonal phase is detected above –33°C, with a tetragonal strain of ~1.1%. At 27°C, as was already mentioned (Table 13), the phase ratio is 81% of the monoclinic Pm phase and 19% of the tetragonal P4mm phase. Above 177°C, the cubic Pm-3m phase appears. In Fig. 78 the temperature dependence of the cell parameters for the monoclinic Pm and the tetragonal P4mm phases are shown.

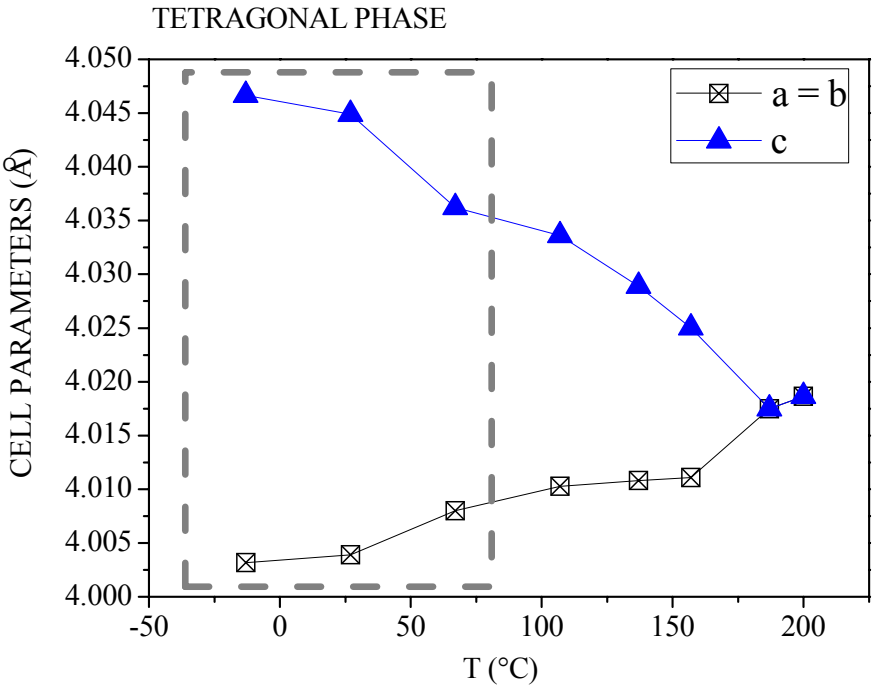

a)

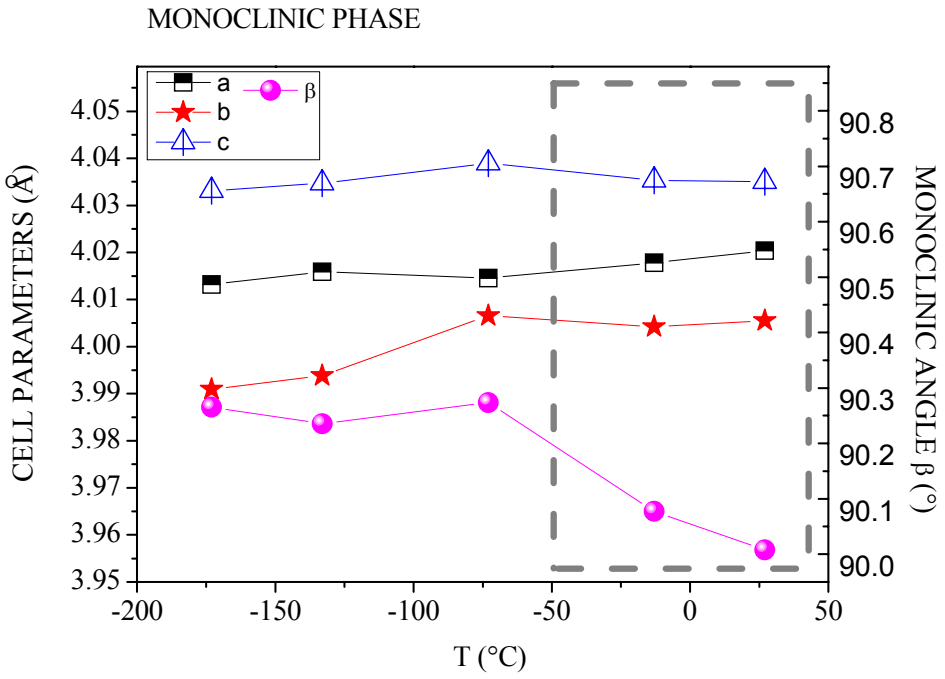

b)

Figure 78: Variation of the cell parameters with temperature for a) the tetragonal P4mm and b) the monoclinic Pm phases of 0.65PMN–0.35PT films on Pt substrates. The dashed rectangle shows the area of the coexistence of the tetragonal P4mm and the monoclinic Pm phases. The lines between the measured values are just a guide to the eye.

Like for films on the Al_2O_3 substrate, the monoclinic unit-cell parameters change very slowly with temperature. The monoclinic beta angle is relatively stable at 90.27° (±0.03°) until -13°C, after which it starts to decrease to reach a value close to 90° at 27°C. In Fig. 78 the dashed rectangle shows the area of the coexistence of the tetragonal P4mm and the monoclinic Pm phases.

The 0.65PMN–0.35PT films on the 0.65PMN–0.35PT and AlN substrates show the same tendency, i.e., they are both monoclinic at room temperature. The following results will be shown for films on the 0.65PMN–0.35PT substrate. The X-ray diagrams of the family of (200) peaks at different temperatures for films on the 0.65PMN–0.35PT substrate are shown in Fig. 79. The X-ray diffraction diagrams were measured within the interval from 2θ = 39.75° to 2θ = 41.25° using a step of 0.01°. The black arrow indicates increasing temperature.

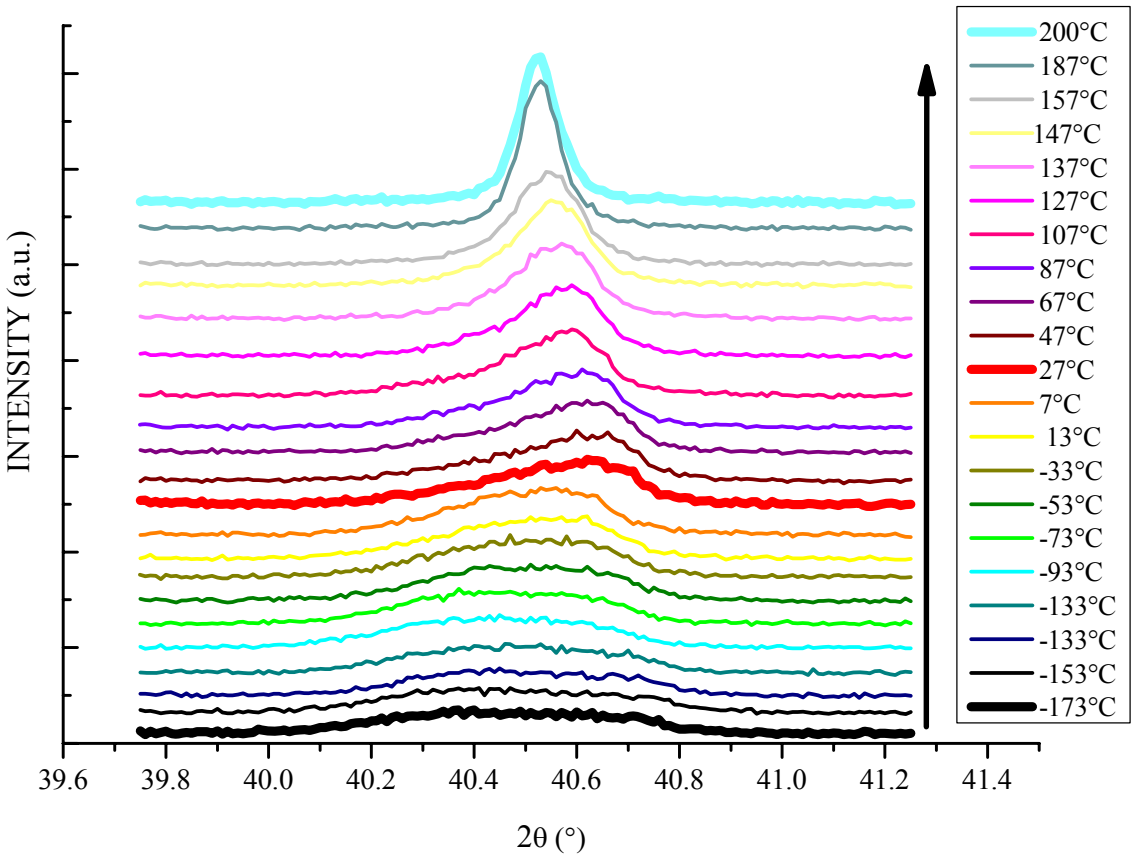

Figure 79: The X-ray diffraction diagram of 0.65PMN–0.35PT films on 0.65PMN–0.35PT substrates measured at different temperatures. The black arrow indicates the increasing temperature.

The Rietveld refinement showed that at -173°C the phase of the 0.65PMN–0.35PT films on the 0.65PMN–0.35PT substrates is the monoclinic Pm. The tetragonal phase was not detected up to the Curie temperature. It is possible that a very weak tetragonal phase also appears in these films, but the tetragonal distortion, if present, is too weak, which makes it difficult to distinguish it from the monoclinic phase in the refinement. At 187°C and higher temperatures the phase is cubic Pm-3m. In Fig. 80 the variation of the cell parameters with temperatures for the monoclinic Pm phase shows the direct transition from the monoclinic to cubic phase. The beta angle is decreasing with increasing temperature and reaches the value 90° after the transformation from the monoclinic to the cubic phase. It is worth noting that the beta angle shows two regions. Above 27°C, the value of the angle is almost constant with a typical value of 90.05°, which is very close to 90°. Below 27°C, the beta angle increases continuously reaching a value of 90.28° at –173°C. We observed a small shift off the general trend of the evolution of the cell parameters at low temperature. This shift is within the experimental error, around 0.005 Å, estimated from the error of the position of the detector at low temperatures.

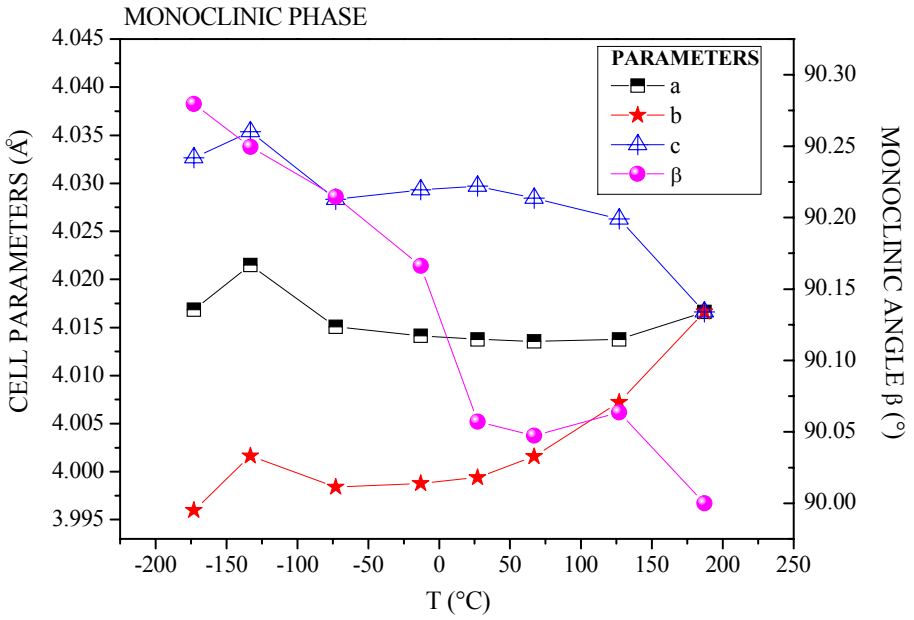

Figure 80: Variation of the cell parameters with temperature for the monoclinic Pm phase of the 0.65PMN–0.35PT films on the 0.65PMN–0.35PT substrates. The lines between the measured values are just a guide to the eye.

4.3.1. 7 Influence of the film thickness on the phase composition of the 0.65PMN–0.35PT films

To study the residual stresses in films, the influence of the film thickness vs. the phase composition of the 0.65PMN–0.35PT films was studied. The films on the alumina were chosen, because at room temperature the percent of the tetragonal phase is the highest. The films on the 0.65PMN–0.35PT were chosen, because at room temperature only the monoclinic phase is present. The X-ray diffraction diagrams of 20 µm, 35 µm, 65 µm and 100 µm thick 0.65PMN–0.35PT films on the alumina substrates are shown in Fig. 81a. The family of (200) peaks of these X-ray diagrams is shown in Fig. 81b. The black arrow indicates increasing film thickness. As we can see in Fig. 81, the X-ray diagram is slightly changing with thickness. In Fig. 81b the minimum between two peaks is increasing with increasing thickness. The phase ratio in percent for 20 µm thick film is 42% of the monoclinic Pm phase and 58% of the tetragonal P4mm phase (section 4.3.1.5). The phase ratio for the 100 µm thick film is 55% of the monoclinic Pm phase and 45% of the tetragonal P4mm phase. The percentage of the monoclinic Pm and the tetragonal P4mm phases for the thinnest and the thickest films are marked in Fig. 81b.

The difference in the phase ratio of 20 µm and 100 µm thick films on the alumina substrate could be due to the stress gradient in the films, which is developed during the sintering and the cooling procedure or due to the different grain sizes of the films as is reported in ref. [54] for bulk 0.65PMN-0.35PT ceramics. The microstructures of the surface of 20 µm and 100 µm thick films are shown in Figs. 82 and 83. The grain size of the 20 µm and 100 µm thick films is in agreement within the measurement error, i.e., 1.7 µm ± 0.5 µm and 1.8 µm ± 0.6 µm, respectively. The median grain sizes were determined from the SEM micrographs of the film surfaces.

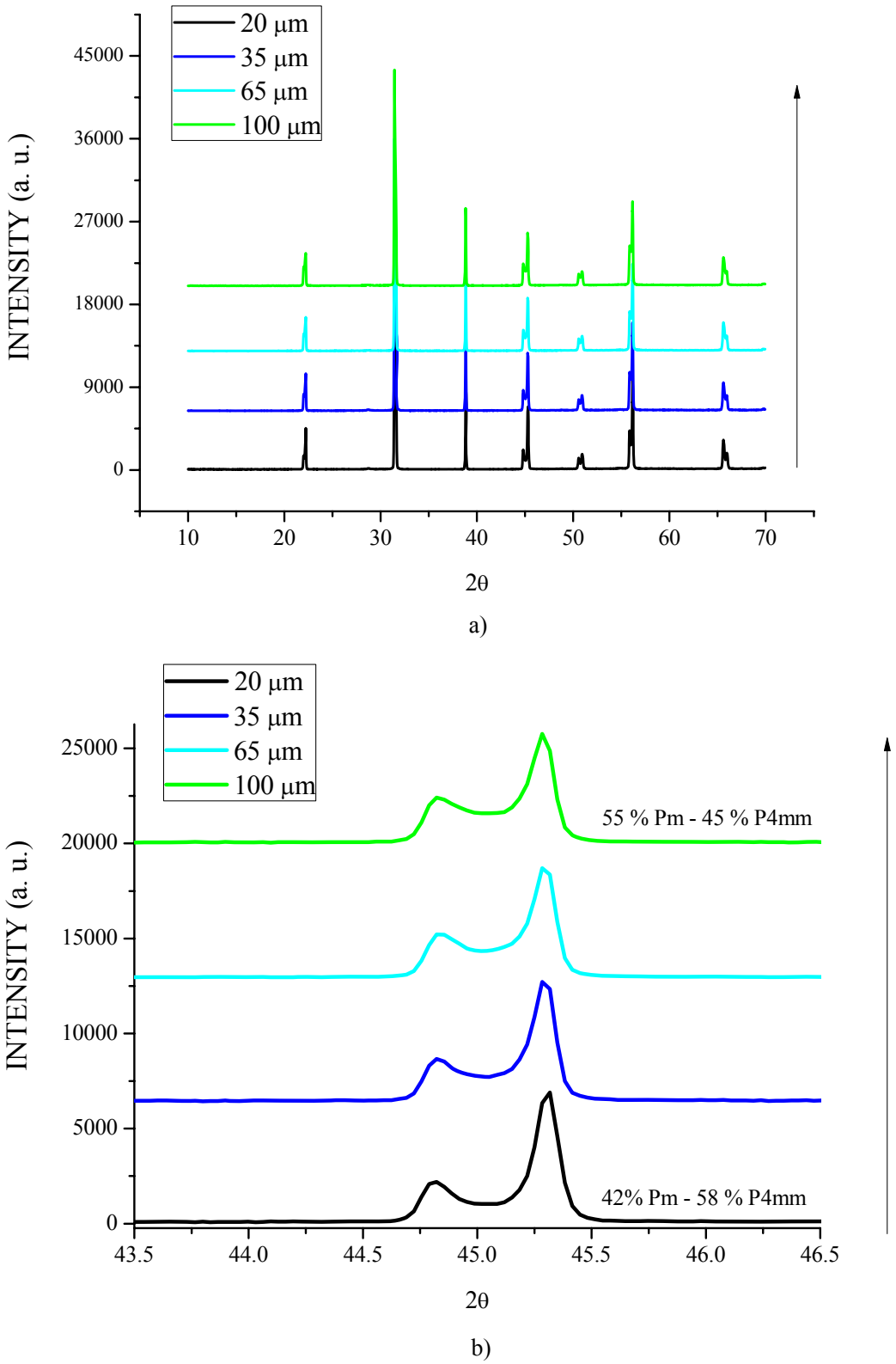

Figure 81: a) The X-ray diffraction diagram of the 20 µm, 35 µm, 65 µm and 100 µm thick 0.65PMN–0.35PT films on the alumina substrates. b) The family of (200) peaks for X-ray diagram of 20 µm, 35 µm, 65 µm and 100 µm thick 0.65PMN–0.35PT films on the alumina substrates. The percentage of the monoclinic Pm and the tetragonal P4mm phases for the thinnest and the thickest films are marked. The black arrow indicates the increasing film thickness.

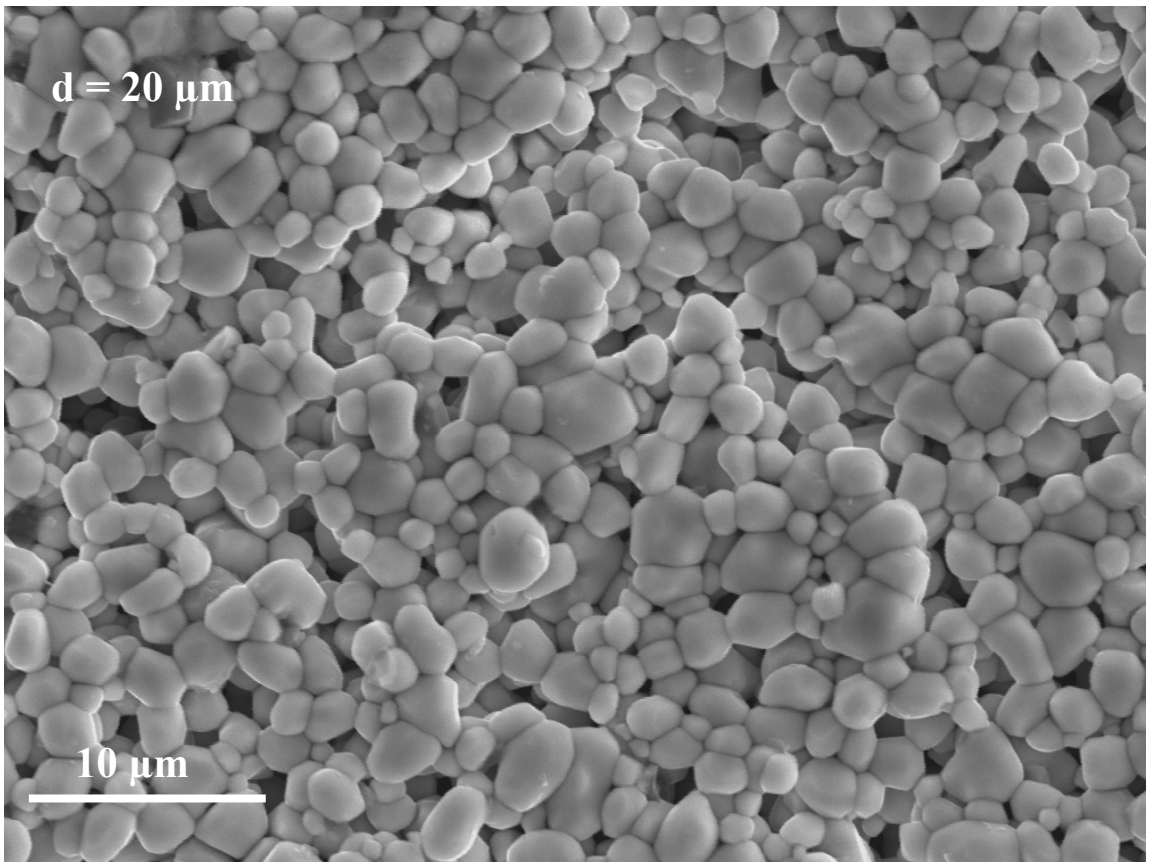

a)

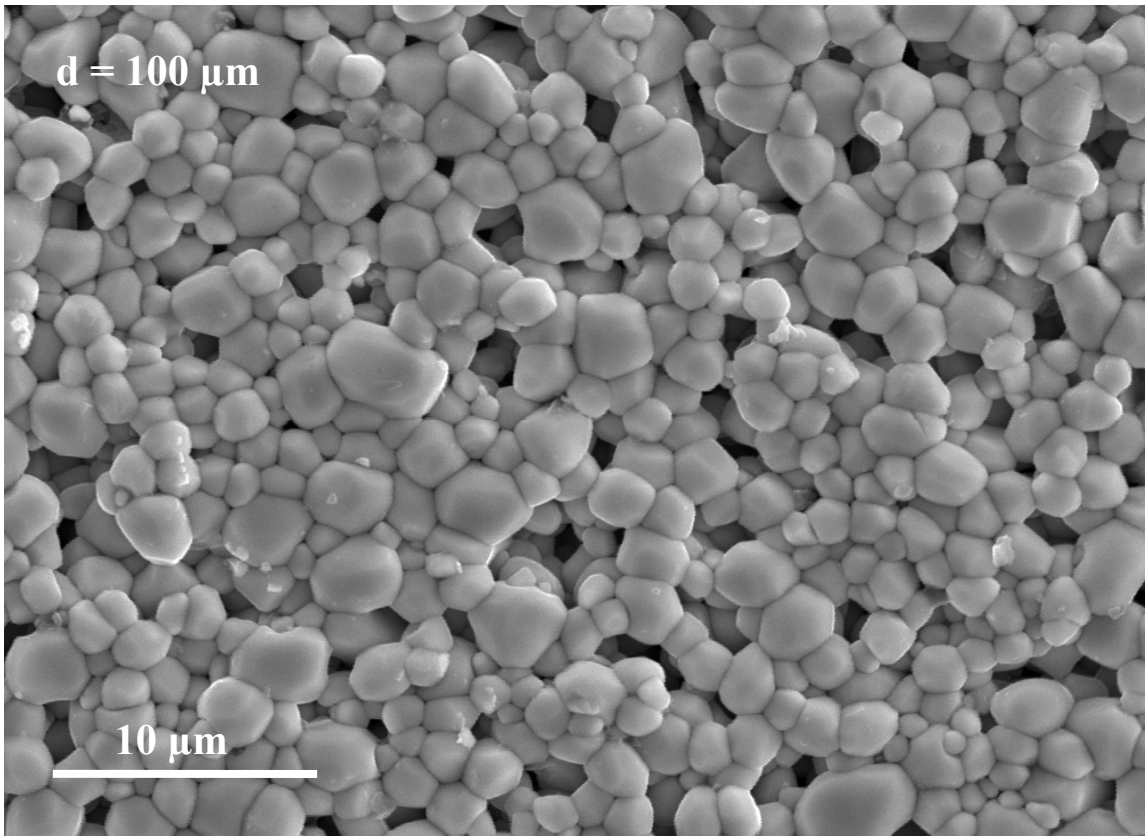

b)

Figure 82: The SEM micrographs of the surface of a) 20 µm and b) 100 µm thick 0.65PMN–0.35PT films on Al_2O_3 substrates (magnification 3000).

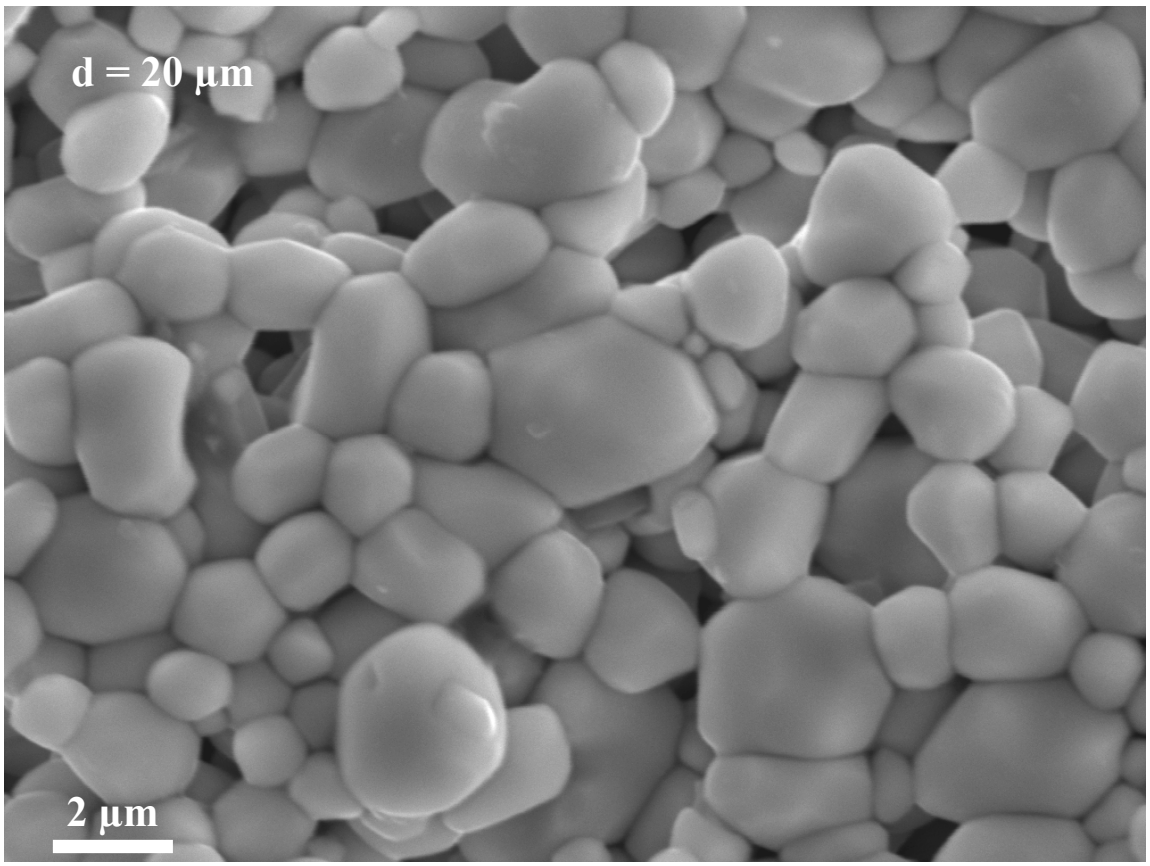

a)

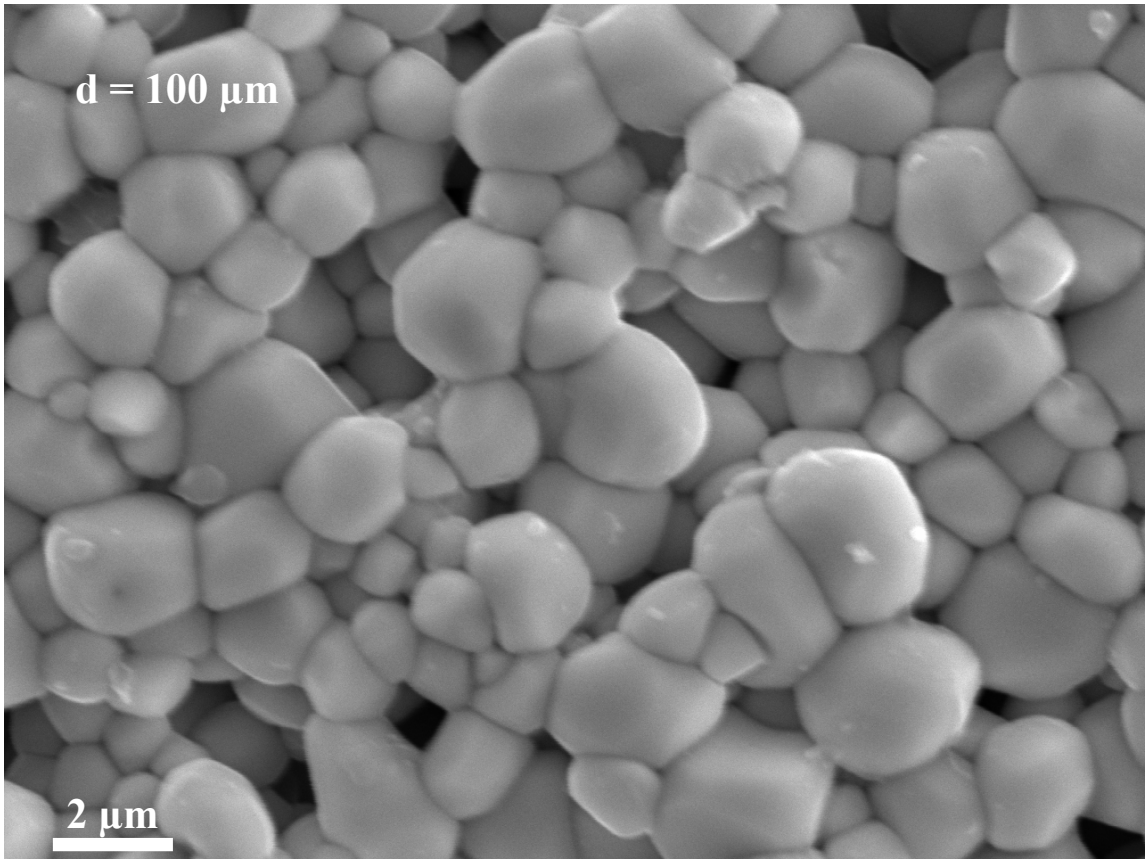

b)

Figure 83: The SEM micrographs of the surface of a) 20 µm and b) 100 µm thick 0.65PMN–0.35PT films on Al_2O_3 substrates (magnification 7000).

The X-ray diffraction diagrams of the 25 µm, 50 µm and 150 µm thick 0.65PMN–0.35PT films on 0.65PMN–0.35PT substrates are shown in Fig. 84a. The family of (200) peaks for these X-ray diagrams are shown in Fig. 84b. The black arrow indicates the increasing film thickness. No significant difference between the X-ray diagrams is observed. Only the monoclinic phase Pm was determined by the Rietveld analyses for all the films, regardless of the thickness.

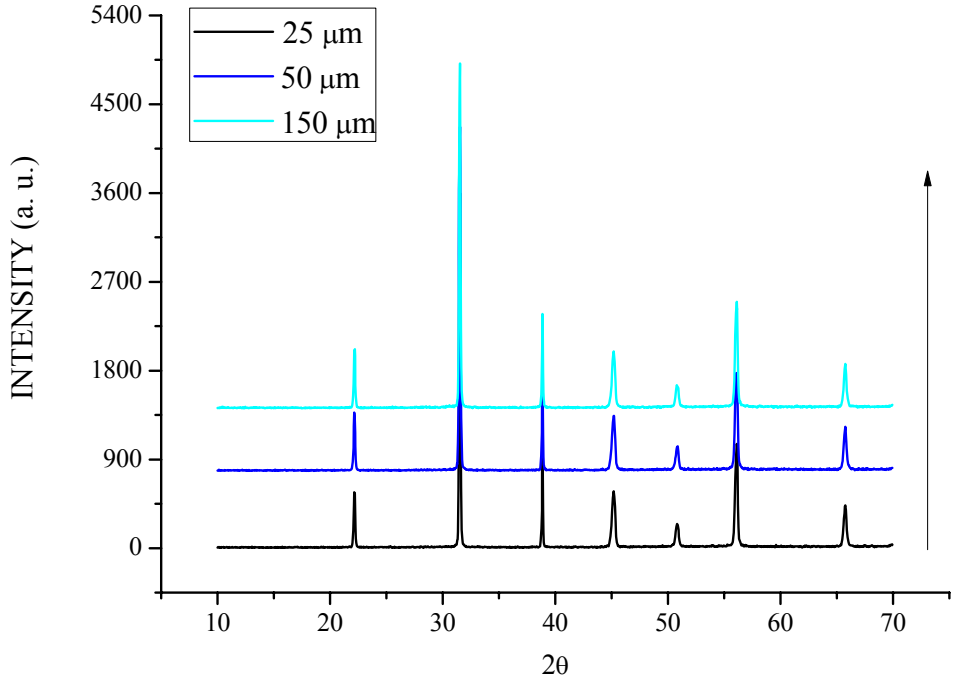

a)

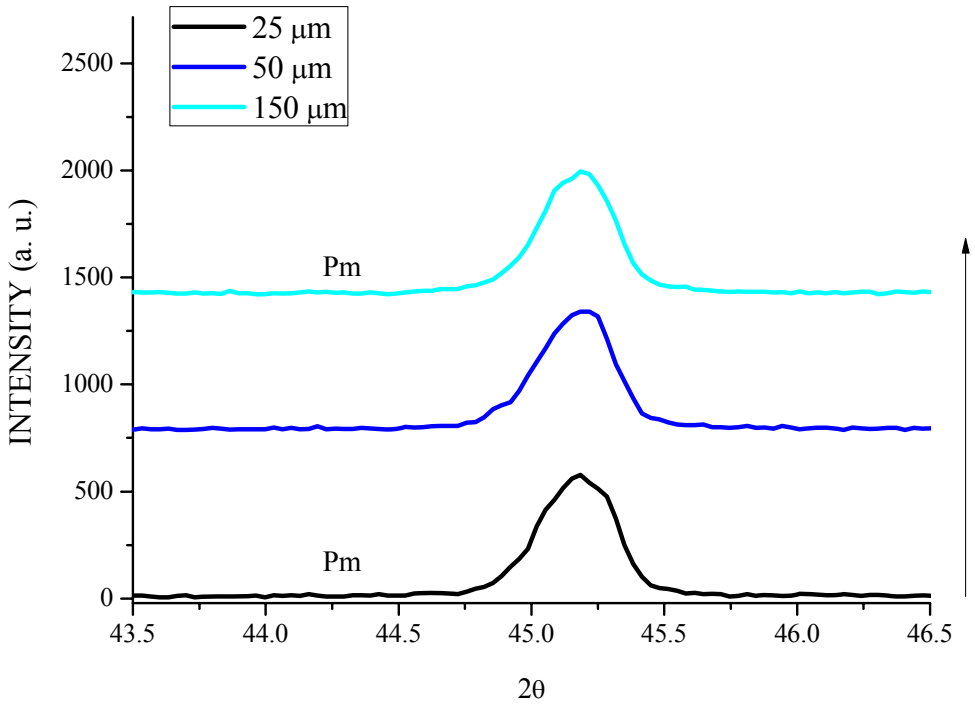

b)

Figure 84: a) The X-ray diffraction diagram of the 25 µm, 50 µm and 150 µm thick 0.65PMN–0.35PT films on 0.65PMN–0.35PT substrates. b) The family of (200) peaks for the X-ray diagram of 25 µm, 50 µm and 150 µm thick 0.65PMN–0.35PT films on 0.65PMN–0.35PT substrates. Only the monoclinic phase was detected. The black arrow indicates the increasing film thickness.

4.3.1.8. Young's modulus of the 0.65PMN–0.35PT film and bulk ceramics

The Young's moduli of the 0.65PMN–0.35PT films were measured by nano-indentation, as is explained in 3.2.2.1. The load-displacement curves F(h) of the 50 µm thick non-poled 0.65PMN–0.35PT film on the alumina substrate are shown in Fig. 85.

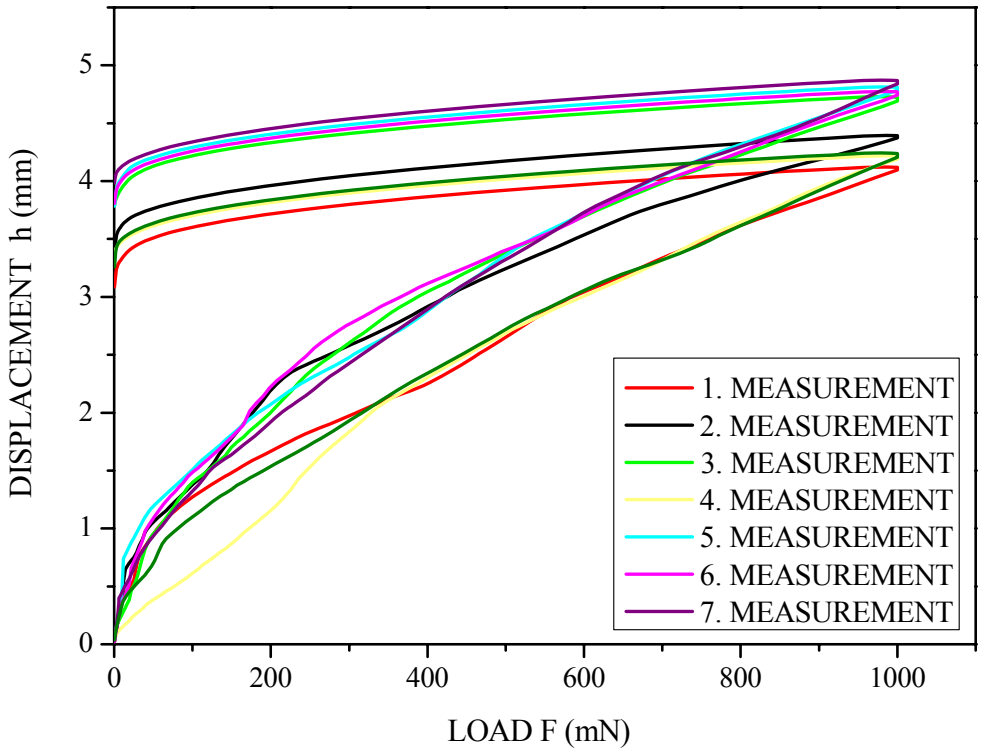

Figure 85: The load-displacement curves F(h) of the 0.65PMN–0.35PT film on the alumina substrate.

The determined Young's moduli of the 0.65PMN–0.35PT film on the alumina substrate are: Y_1 = 103 GPa, Y_2 = 92 GPa, Y_3 = 96 GPa, Y_4 = 103 GPa, Y_5 = 97 GPa, Y_6 = 87 GPa, Y_7 = 83 GPa with the average value: Y = 94 GPa ± 10 GPa. To see the difference among the measurements on the film without or with the top gold electrode, the same measurements were performed on the films with the top electrode. As expected, due to the small thicknesses of the sputtered electrodes (around 100 nm), the average Young's modulus is in agreement with the Young's modulus measured on the film without the top electrode within the measurement error. Measurements are collected in Table 15. The measurements were also performed on the poled 0.65PMN–0.35PT film on the alumina substrate. The optimal poling field for the 0.65PMN–0.35PT material was chosen, i.e., 2.5 kV/mm. Also in this case the average Young's modulus is in agreement with the Young's modulus of the non-poled film, i.e., Y = 89 GPa ± 10 GPa within the measurement error (Table 15). The results indicate that poling does not influence the values of the Young's moduli.

Table 15: The Young's moduli of the non-poled 0.65PMN–0.35PT film on the alumina substrate without or with the top electrode and of the poled 0.65PMN–0.35PT film on the alumina substrate measured on the top electrode.

Substrate	**Non-poled film (measured on the bare film) GPa**	**Non-poled film (measured on the electrode) GPa**	**Poled film -2.5 kV/mm (measured on the electrode) GPa**
Alumina	**94 ± 10**	**90 ± 10**	**89 ± 10**

The average Young's moduli of the 0.65PMN–0.35PT films on the Al_2O_3, Pt, 0.65PMN–0.35PT and AlN substrates and 0.65PMN–0.35PT bulk ceramics fired at 1200°C and 950°C are collected in Table 16.

Table 16: The Young's modulus of the non-poled 0.65PMN–0.35PT films on the Al_2O_3, Pt, 0.65PMN–0.35PT and AlN substrates and bulk 0.65PMN–0.35PT ceramics fired at 1200°C and 950°C.

Film on substrate or bulk	**Y (GPa)**
Al_2O_3	90 ± 10
Pt	90 ± 8
0.65PMN–0.35PT	30 ± 9
AlN	20 ± 2
bulk 1200°C	75 ± 12
bulk 950°C	20 ± 4

The highest values were obtained for the 0.65PMN–0.35PT film on the Al_2O_3 and Pt substrate. For the 0.65PMN–0.35PT bulk ceramics fired at 1200°C for 2 hours, the Young's modulus was 75 GPa. The significantly lower values were obtained for films on the AlN and 0.65PMN–0.35PT substrates and the bulk ceramics fired at 950°C, due to the high porosity of the samples.

The measured Young's modulus for the 0.65PMN–0.35PT bulk ceramics fired at 1200°C is in agreement with the reported values for the 0.7PMN–0.3PT bulk ceramics [104], i.e., 75 GPa. As is reported in ref. [102] the average Young's modulus of the 0.65PMN–0.35PT material prepared by tape casting depends on the grain size. In the measured areas of smaller grains the average Young's modulus was 70 GPa, however in the areas of the larger grains it was around 107 GPa. For the Young's modulus of the 0.65PMN–0.35PT thick films no data are reported. Zhong et al. reported Young's moduli for the 0.65PMN–0.35PT thin films on Si/SiO_2 and $LaAlO_3$ substrates to be 96 GPa and 92 GPa, respectively [105].

The measurements of the transverse Young's moduli Y_{13} of the 0.65PMN–0.35PT films were also performed. The measurements of Y_{33} and Y_{13} could be different in films due to the stresses in the films or due to the orientation, as described before for films on Pt substrates (section 4.3.1.4). The samples cross-sections were prepared and the indenter was pushed into the 0.65PMN–0.35PT film, as is schematically shown in Fig. 86. The z axis denoted 3 is perpendicular to the film surface. The measured value was around 60 GPa, however due to the influence of the substrate the measurements were not reliable. In Fig. 87 the photographs of the film cross-sections before and after the indentation are shown. The place of the indentation was close to the substrate, as is shown in Fig. 87b.

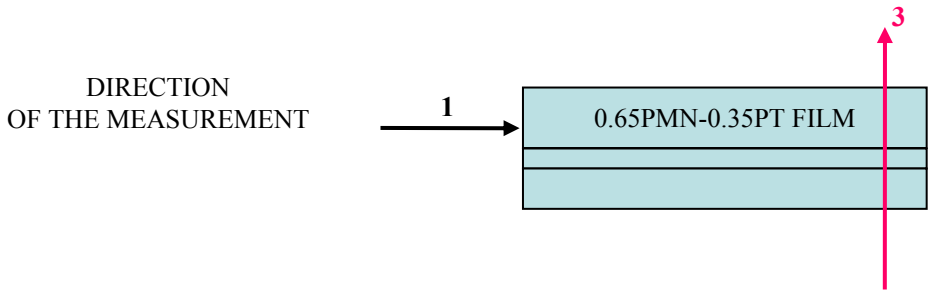

Figure 86: The measurements of the transverse Young's moduli Y_{13} of the 0.65PMN–0.35PT films on the Al_2O_3 substrate - schematically.

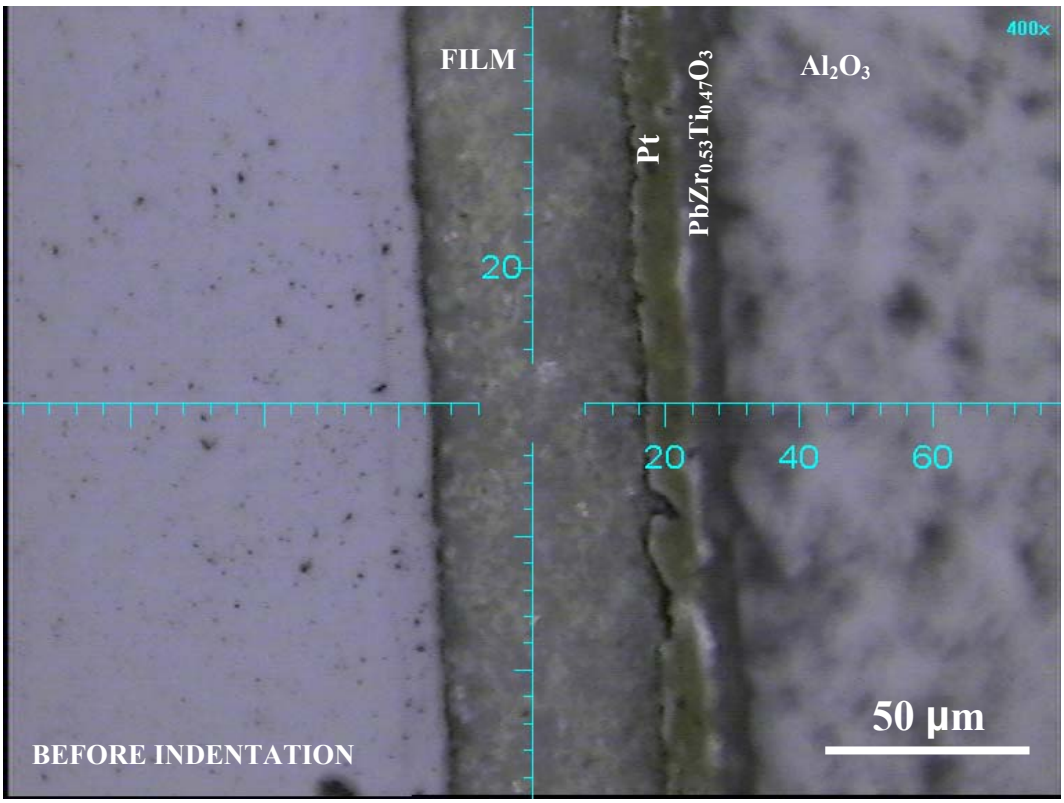

a)

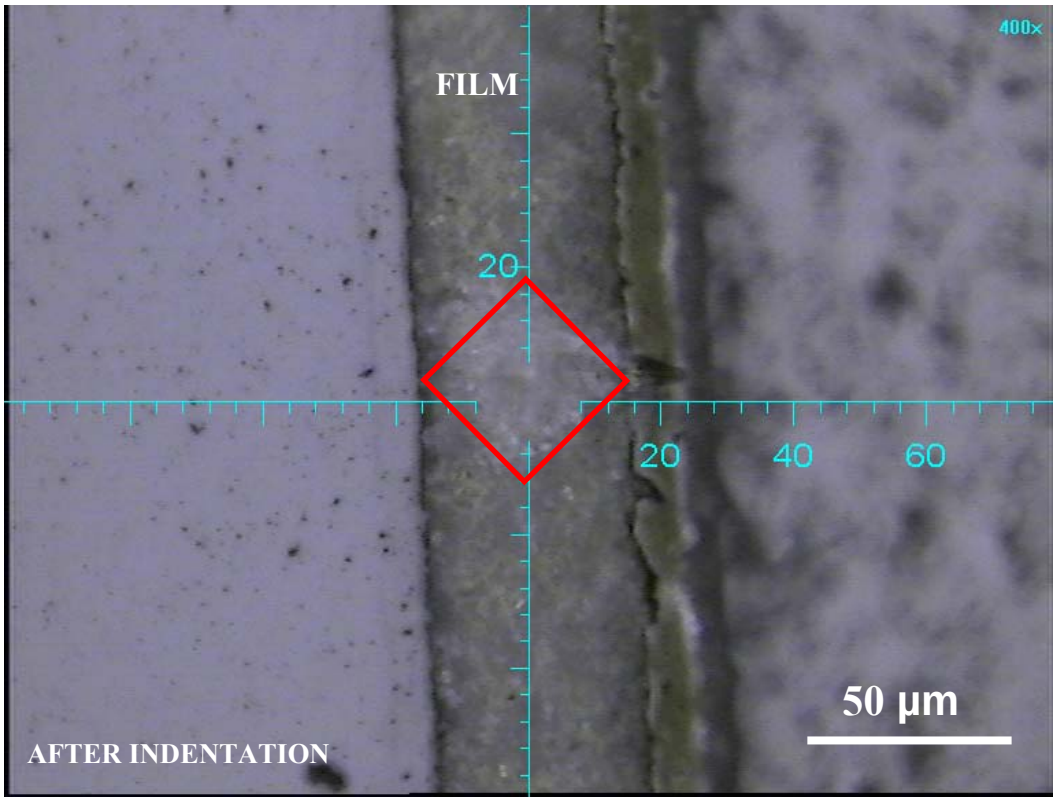

b)

Figure 87: The photograph of the indentation measurements of the transverse Young's moduli Y_{13} for the 0.65PMN–0.35PT film on the Al_2O_3 substrate: a) before the measurement and b) after the measurement. The place of the indentation is marked with the red square.

4.3.2 Influence of the substrate materials on the electrical properties of the 0.65PMN–0.35PT thick films

4.3.2.1 Dielectric properties of the 0.65PMN–0.35PT thick films

In Fig. 88 a), b), c) and d) the temperature dependences of the dielectric properties for films on Al_2O_3, Pt, 0.65PMN–0.35PT and AlN substrates with thicknesses of 21 µm, 20 µm, 26 µm and 34 µm are shown, respectively. Data were collected during ZFC. The measurement of the bulk ceramics sintered at 950°C is added for comparison.

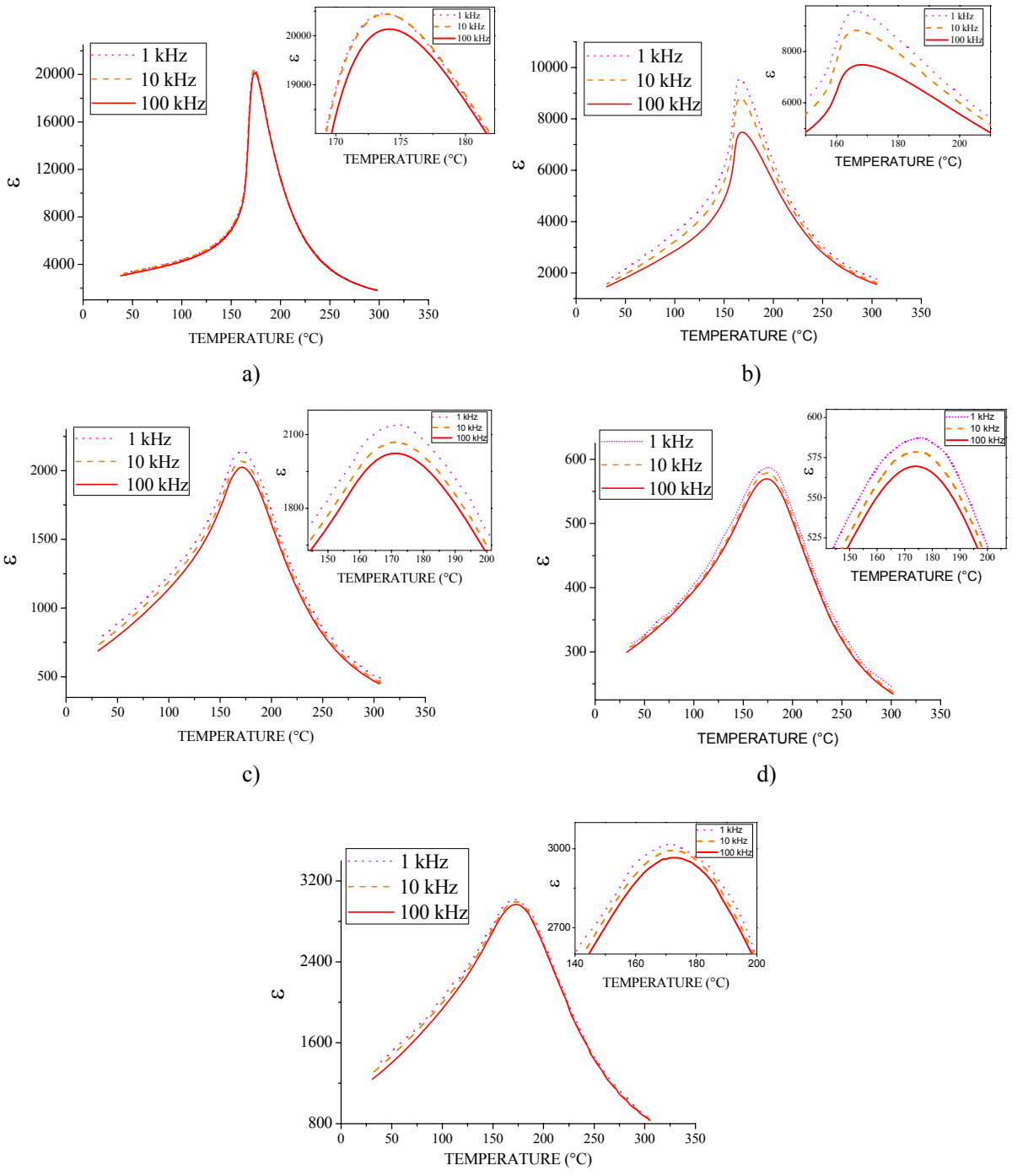

Figure 88: Dielectric constant ε measured as a function of the temperature at 1 kHz, 10 kHz and 100 kHz for films on a) Al_2O_3, b) Pt, c) 0.65PMN–0.35PT and d) AlN substrates. e) The measurements for bulk ceramics fired at the same temperature, i.e., 950°C are added. The insets show the detail of the peaks in the dielectric constants.

The highest ε at room temperature was obtained for the 0.65PMN–0.35PT films on the alumina substrates, i.e., around 3400 at 1 kHz, which is comparable with measurement made for dense bulk ceramics sintered at 1200°C, i.e., 3600 at 1 kHz (section 4.2.2). Also, the maximum value of the dielectric constant ε_{max} is high, i.e., approximately 21000. The ε of the films on the Pt substrates was below 2000. For the films on the 0.65PMN–0.35PT and AlN substrates low values were observed, i.e., ε = 700 and ε = 300, respectively. The reasons for the differences in the ε of thick 0.65PMN–0.35PT films on the different substrates are microstructures, as shown in section 4.3.1.3. The films on the 0.65PMN–0.35PT and AlN substrates are porous and consist of small grains, consequently the ε are low in comparison with the ε of 0.65PMN–0.35PT film on Al_2O_3.

The dielectric constants ε vs. temperature measured at 100 kHz in the extended temperature range (from approximately -120°C to 300°C) for films on Al_2O_3, Pt, 0.65PMN–0.35PT and AlN substrates with thicknesses of 21 µm, 20 µm, 26 µm and 34 µm are shown in Fig. 89. All the samples were sintered 2 hours at 950°C. The measurement ε(T) for the 0.65PMN–0.35PT bulk sintered at the same temperature and time is added for comparison.

The low-temperature (LT) phase-transition peaks from the monoclinic Pm to the tetragonal P4mm phases can be observed in the measurements ε(T) of the 0.65PMN–0.35PT films on the alumina and platinum substrates (insets in Fig. 89). Broad peaks of the low-temperature transition of monoclinic to tetragonal phase have maxima at around 50°C. The temperature of the phase-transition is in agreement with the data in the literature. Alguero et al. reported that the mechanical and electro-mechanical properties of 0.655PMN–0.345PT reflect the LT phase-transition at 40°C–70°C [91]. Xia et al. reported that ε vs. temperature measurements show that the LT phase-transition peak for the non-poled 0.65PMN–0.35PT ceramics is around 50–80°C [60]. The LT phase-transition peak is not observed for the bulk 0.65PMN–0.35PT samples and films on the 0.65PMN–0.35PT and AlN substrates, which indicate that the monoclinic Pm phase is stable up to the temperature of the transition into the cubic phase. These measurements are in agreement with the results of the X-ray analyses of the films at different temperatures.

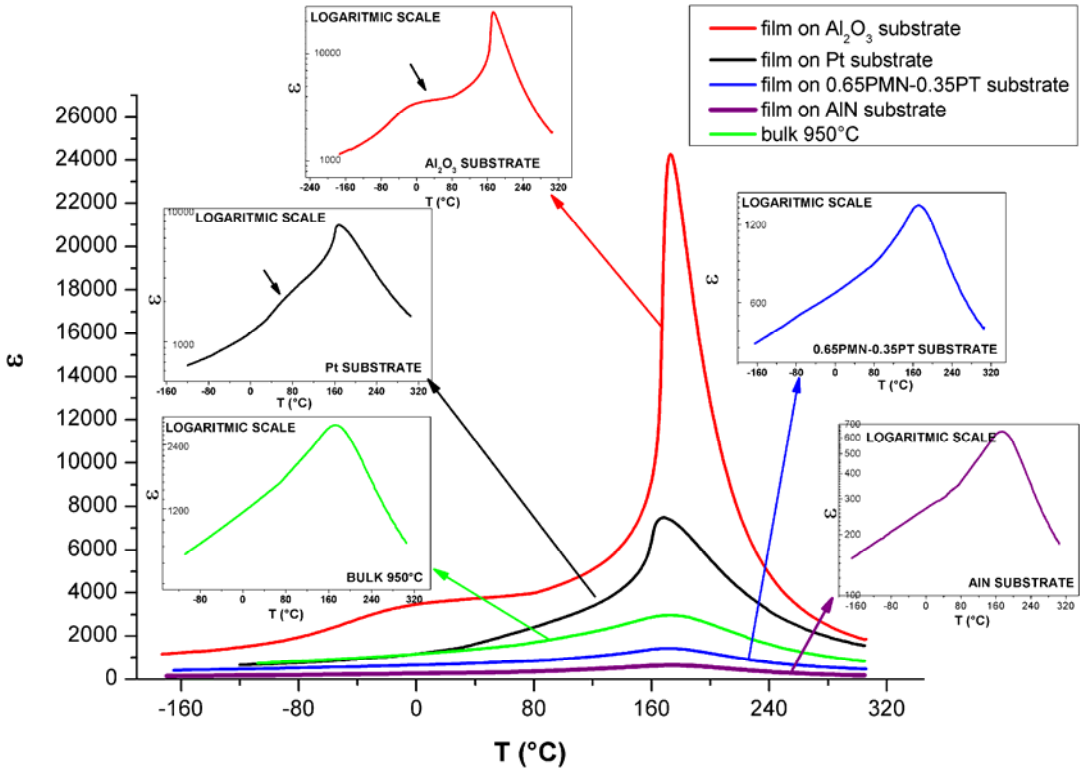

Figure 89: The dielectric constant ε vs. temperature at 100 kHz for the 0.65PMN–0.35PT films on the Al_2O_3, Pt, 0.65PMN–0.35PT, AlN substrates, and for the bulk ceramics. The insets show the same graphs on a logarithmic scale. The LT phase-transitions are marked with black arrows. All samples were fired at 950°C for 2 hours.

4.3.2.2 Piezoelectric properties of the 0.65PMN–0.35PT thick films

For the piezoelectric measurements samples were poled with the optimum poling conditions, i.e., 2.5 kV/mm (section 4.2.2.). The 50 μm thick 0.65PMN–0.35PT films on alumina substrates were measured by three different methods: by Photonic sensor, atomic force microscope AFM and Berlincourt piezometer, to examine the differences in obtained results. The 0.65PMN–0.35PT films on alumina substrates, the average displacement/voltage value measured by Photonic sensor was 185 pm/V ± 20 pm/V. The AFM measurement of displacement of the poled 0.65PMN–0.35PT thick film on the alumina substrate showed the values 190 pm/V ± 15 pm/V. The measurement error ± 15 pm/V is calculated from the noise-to-signal ratio of the AFM measurement. With the Berlincourt piezometer the average value d_{33}^{eff} of 180 pm/V ± 20 pm/V was obtained. All the measurements are summarized in Table 17.

Table 17: The piezoelectric coefficients d_{33}^{eff} of 50 μm thick 0.65PMN–0.35PT films on alumina substrates obtained by Photonic sensor, atomic force microscope AFM and Berlincourt piezometer.

d_{33}^{eff} (pm/V) Photonic sensor (1.1 Hz)	d_{33}^{eff} (pm/V) AFM (5 Hz)	d_{33}^{eff} (pC/N) Berlincourt piezometer (100 Hz)
185 ± 20	190 ± 15	180 ± 20

The measurements made by Photonic sensor, atomic force microscope AFM and Berlincourt piezometer are in agreement, within the measurement error. The average piezoelectric coefficient of the 0.65PMN–0.35PT film on the alumina substrate is 185 pm/V ± 20 pm/V, which is among the highest reported piezoelectric coefficients in [67, 68], as is shown in Table 2.

Due to the fact that the measurements for the piezoelectric coefficient d_{33}^{eff} of 0.65PMN–0.35PT films on Al_2O_3 substrates with all three methods are the same within the measurement error, we decided to measure the piezoelectric coefficients of the films on other substrates (Pt, 0.65PMN–0.35PT, AlN) with two methods, one based on the direct piezoelectric effect (Berlincourt piezometer method) and one based on the inverse piezoelectric effect (Photonic sensor method). The d_{33}^{eff} measurements of 50 μm thick films on Pt, 65 μm thick films 0.65PMN–0.35PT and 80 μm thick films AlN substrates are summarized in Table 18. From the equation (10) the estimation of the piezoelectric coefficient d_{33} of the unclamped 0.65PMN–0.35PT films can be made. The calculated d_{33} coefficients of the 0.65PMN–0.35PT films are added in Table 18. For the calculation the measurements of d_{33}^{eff} made by Berlincourt piezometer were used. The other parameters were taken from Refs. [83, 91, 104] for bulk material.

Table 18: The piezoelectric coefficient d_{33}^{eff} of the 0.65PMN–0.35PT film on Pt, 0.65PMN–0.35PT and AlN substrates.

Substrate	d_{33}^{eff} (pm/V) Photonic sensor (1.1 Hz)	d_{33}^{eff} (pC/N) Berlincourt piezometer (100 Hz)	Calculated d_{33} (pC/N)
Al_2O_3	185 ± 20	180 ± 20	280
Pt	110 ± 15	140 ± 15	240
0.65PMN–0.35PT	120 ± 10	105 ± 15	200
AlN	around 20 pC/N–30 pC/N (low value due to low density)		120

The highest value was obtained for the films on the alumina substrate, i.e., 185 pC/N. For films on the Pt and 0.65PMN–0.35PT substrates, lower d_{33}^{eff} values were obtained, i.e. 140–110 pC/N and 120–105 pC/N, respectively. The measured d_{33}^{eff} values for films on AlN were around 20 pC/N–30 pC/N, however the correct value of these films was not possible to determine as the error of the measurement was comparable with the measured value. These results can be explained with the high porosity of the films on AlN substrates.

The piezoelectric coefficients for densely sintered bulk materials are around 650 pC/N (Table 5). The measured piezoelectric coefficients d_{33}^{eff} for all the 0.65PMN–0.35PT films are below 200 pC/N. One of the reasons for the lower piezoelectric coefficient of films is that the films are clamped to the rigged substrates, which decreases the d_{33} for approximately 40% (as calculated by equation 10). One possible reason for the measured lower d_{33}values for the films in comparison with dense ceramics could be also that the polarized areas of film are surrounded by non-polarized material as the dimensions of the upper electrodes were 3 mm and the electrodes were separated by 2 mm. However for our samples this was not the case. The thick-film samples on alumina substrates were also prepared in the way that the top gold electrode covered the whole thick-film surface. Also in this case the measured d_{33} coefficient of 0.65PMN-0.35PT films on alumina substrates was 180 pC/N. For other reasons, which can contribute to the lower piezoelectric constant of film in comparison with bulk ceramics further investigation will be needed.

4.3.2.3 Ferroelectric properties of the 0.65PMN–0.35PT thick films

The ferroelectric hysteresis loops were measured for 0.65PMN–0.35PT films on Al_2O_3, Pt, 0.65PMN–0.35PT and AlN substrates with thicknesses of 50 µm, 50 µm, of 65 µm and of 80 µm, respectively. The hysteresis loops are shown in Fig. 90. The remanent polarization P_r and coercive fields E_c for 0.65PMN–0.35PT films on Al_2O_3, Pt, 0.65PMN–0.35PT and AlN substrates are summarized in Table 19.

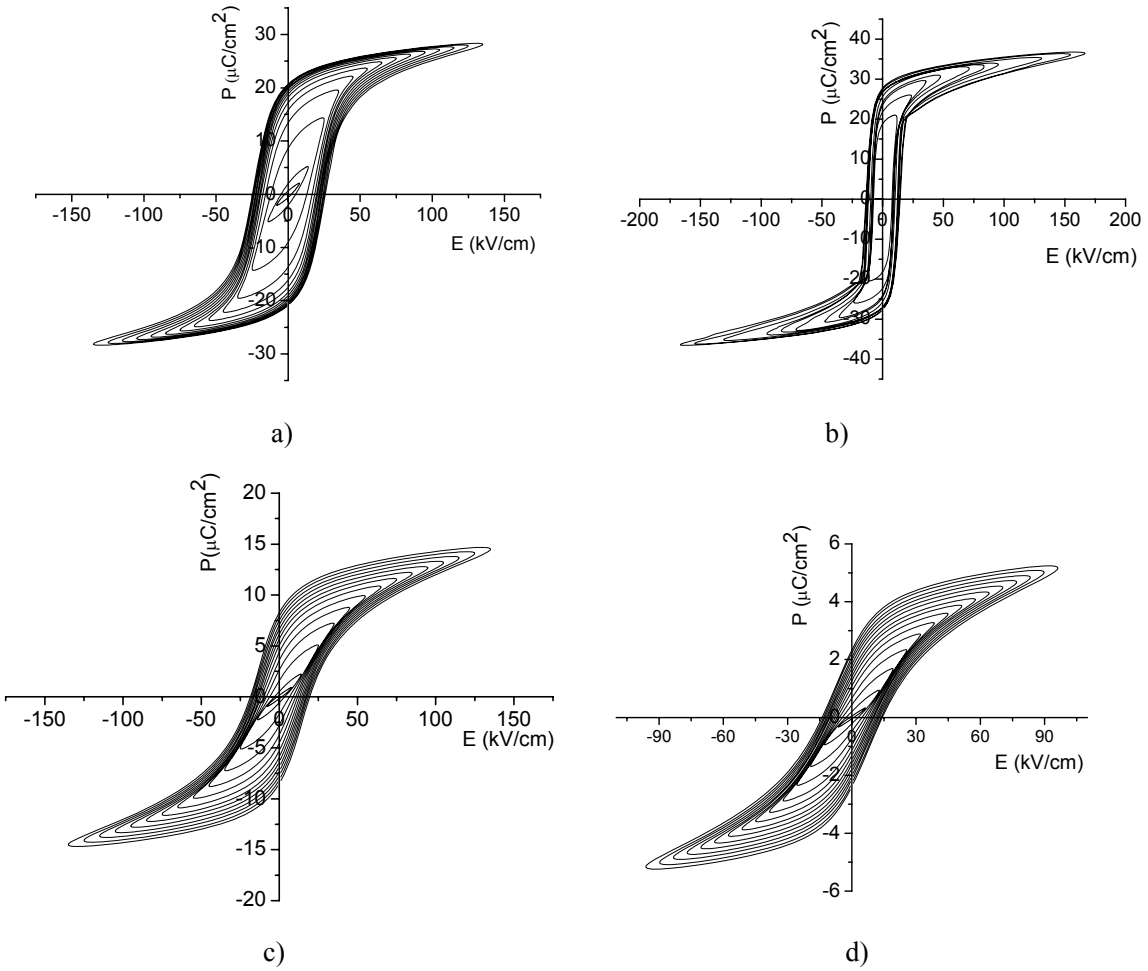

Figure 90: The ferroelectric hysteresis loops of 0.65PMN–0.35PT films on a) Al_2O_3, b) Pt, c) 0.65PMN–0.35PT and d) AlN substrates.

Table 19: The ferroelectric properties of 0.65PMN–0.35PT films on Al_2O_3, Pt, 0.65PMN–0.35PT and AlN substrates; remanent polarization P_r and coercive field E_c.

Substrate	P_r ($\mu C/cm^2$)	E_c (kV/cm)
Al_2O_3	22	24
Pt	27	14
0.65PMN–0.35PT	8	15
AlN	2.5	15

A high remanent polarization was obtained for films on Pt substrates, i.e., 27 $\mu C/cm^2$, which is comparable with the value obtained for 0.65PMN–0.35PT bulk ceramics fired at 1200°C, i.e., 33 $\mu C/cm^2$ (section 4.2.2). The remanent polarization is also high for films on Al_2O_3 substrates, i.e., 22 $\mu C/cm^2$. The lowest remanent polarization P_r was measured for 0.65PMN–0.35PT films on 0.65PMN–0.35PT and AlN substrates, due to the high porosity of the films and due to the small grain size.

4.3.3 Discussion on the influence of the substrate materials on the structural and electrical properties of the 0.65PMN–0.35PT films

The 0.65PMN–0.35PT thick films were prepared on different substrates to study the influence of the substrates on the properties of the films. Films on all substrates (Al_2O_3, Pt, 0.65PMN–0.35PT and AlN) were screen printed, fired and cooled under the same conditions, i.e., for 2 hours at 950°C and with a cooling rate of 3°C/min. For films on Al_2O_3 substrates the β-alumina crystals at the interface between the substrate and Pt electrode were observed. The formation of this phase is due to the reaction between the alumina and the PbO, which diffused from PMN–PT layers to the alumina substrates during firing. To prevent these interactions the $Pb(Zr_{0.53}Ti_{0.47})O_3$ barrier layer among bottom electrode and substrate were printed and fired.

The cross-sections of the films on different substrates were analyzed by EDXS analyses. The analyses showed that no difference in the chemical composition among the films on the different substrates can be observed within the measurement errors. According to EDXS analyses all the films were chemically homogenous through the thickness and interactions between the films and substrates were not detected with the exception of the films on alumina as described above and the formation of 30 nm thick Pb-Pt alloy layer at the interface of the film and the Pt substrate.

The films prepared under the same sintering conditions on different substrates have different microstructures. The films on Al_2O_3 and Pt substrates are dense with the median grain sizes of 1.7 μm and 1.2 μm, respectively, while the films on 0.65PMN−0.35PT and AlN substrates are porous and the median grain sizes of these films are 0.5 μm and 0.3 μm, respectively. The thicknesses of films printed two times on Al_2O_3, Pt, 0.65PMN-0.35PT and AlN substrates are 21 μm, 20 μm, 26 μm and 34 μm, respectively. The grain sizes of the films on Al_2O_3 and Pt substrates are comparable with the grain size of bulk ceramics fired at 1200°C, i.e., 1.1 μm, however the grain sizes of films on 0.65PMN−0.35PT and AlN substrates are comparable with the grain size of bulk ceramics fired at 950°C, i.e., 0.3 μm.

Thick-film structures on different substrates and the bulk ceramics fired at 950°C were analysed by the X-ray diffraction analyses. No extra diffraction peaks that might correspond to pyrochlore or PbO phases were detected. The phase composition of the films on Al_2O_3 and Pt substrates shows co-existence of the monoclinic Pm and the tetragonal P4mm phases. The co-existence of the monoclinic and tetragonal phases was also observed for 0.65PMN−0.35PT bulk ceramics fired at 1200°C. On the other hand, results showed that the films on the 0.65PMN–0.35PT and AlN substrates, and bulk ceramics fired at 950°C consist of monoclinic Pm. To understand and clarify the co-existence of monoclinic and tetragonal phases, the X-ray diffraction diagrams of the 0.65PMN–0.35PT films were measured at different temperatures. At low temperature, i.e., -173°C, the phase is monoclinic for all films. For the films on the Al_2O_3 and Pt substrates the co-existence of the monoclinic and the tetragonal phases was observed in wide temperature range around room temperature. At a temperature of 107°C and higher the phase is pure tetragonal and at 187°C and higher the phase is the cubic Pm-3m. For the films on the 0.65PMN–0.35PT and AlN substrates the phase stays monoclinic till the phase-transition into the cubic phase. The reason for the different phase compositions of the films on Al_2O_3, Pt, 0.65PMN−0.35PT and AlN substrates is the difference in the grain sizes. Data in the literature [54] show that the 0.65PMN−0.35PT bulk ceramics with small grains, i.e., 0.15 μm consist manly of monoclinic phase, while the ceramics with larger grains, i.e., 4 μm is a mixture of monoclinic and tetragonal phase. This is in agreement with our results.

In the measurements of dielectric constants vs. temperature for films on Al_2O_3 and Pt substrates and for bulk ceramics fired at 1200°C, besides a high-temperature transition from monoclinic to cubic phase, there is also a broad peak of the low-temperature transition of the monoclinic to tetragonal phase, with a maximum at around 50^oC. While for films on 0.65PMN–0.35PT and AlN substrates and for bulk ceramics fired at 950°C only the monoclinic-to-cubic transitions at the Curie temperature was observed. These results confirmed the results obtained by X-ray analyses.

The dielectric, piezoelectric and ferroelectric properties of the 0.65PMN–0.35PT films were measured. The highest dielectric constants ε at room temperature were obtained for the 0.65PMN–0.35PT

films on the alumina and platinum substrates, i.e., around 3400 and 2000, respectively. These two values are comparable with the dielectric constant of 0.65PMN–0.35PT ceramics densely sintered at 1200°C, which was 3400. For the films on the 0.65PMN–0.35PT and AlN substrates, low values for ε were measured, i.e., 700 and 300, respectively. The highest value for the piezoelectric coefficient d_{33}^{eff} was obtained for the films on the alumina substrate, i.e., 185 pC/N. For the films on the Pt and 0.65PMN–0.35PT substrates lower d_{33}^{eff} values were obtained, i.e. 140–110 pC/N and 120–105 pC/N, respectively. The measured d_{33}^{eff} values for the films on the AlN were around 20–30 pC/N, however the correct value of these films was not possible to determine as the error of the measurement was comparable with measured value. The largest difference between the properties of films and bulk ceramics sintered at 1200°C is shown in piezoelectric coefficients. Measured values for bulk ceramics fired at 1200°C and poled under the same conditions as films were 660 pC/N.

A high remanent polarization was obtained for the films on the Pt substrates, i.e., 27 μC/cm^2, which is comparable with the value obtained for densely sintered 0.65PMN–0.35PT bulk ceramics fired at 1200°C, i.e., 33 μC/cm^2. The remanent polarization is also high for the films on the Al_2O_3 substrates, i.e., 22 μC/cm^2. The lower remanent polarization was measured for the 0.65PMN–0.35PT films on the 0.65PMN–0.35PT and AlN substrates, i.e., 8 μC/cm^2 and 3 μC/cm^2, respectively.

As mentioned above the films on all the substrates were prepared under the same conditions, but the phase compositions, grain sizes and electrical properties are different. These results indicate that the choice of the substrate materials strongly influences the characteristics of the films. For example, if we compare films and bulk ceramics of the same composition and sintered at the same temperature, i.e., 950°C, we can conclude that the significant grain growth was observed for films on the Al_2O_3 and Pt substrate. The grain size for films on 0.65PMN–0.35PT and AlN as well for bulk ceramics fired at 950°C is similar to the grain size of the starting powder. Probably, the high porosity in the films inhibits the grain growth.

On the other hand, during the sintering and the cooling procedure, due to the difference in the thermal expansion coefficients (TECs) among the films and substrates, different residual stresses form and remain in the films. In the literature the values for the thermal expansion coefficient (TEC) of PMN–PT crystals with morphotropic phase boundary (MPB) compositions are reported, i.e., for the rhombohedral phase (latterly the rhombohedral phase was described in the open literature as monoclinic) $4 \cdot 10^{-6}$/K and for tetragonal phase $14 \cdot 10^{-6}$/K [106]. Our measurements of the TEC for the 0.65PMN–0.35PT bulk material with the composition of 86% monoclinic phase and 14% of tetragonal phase showed an average value $6.3 \cdot 10^{-6}$/K.

The TEC values of the alumina and platinum substrates are around $8 \cdot 10^{-6}$/K [107, 108] and $8.8 \cdot 10^{-6}$/K [109, 110], respectively and are higher than the TEC of the 0.65PMN–0.35PT material, while the TEC of AlN substrates is $4.5 \cdot 10^{-6}$/K [111, 112] and therefore lower than the TEC of the 0.65PMN–0.35PT. In Table 20, the TECs of the substrates, the differences in the TECs of the substrates and films ($\Delta TEC = TEC_{substrate} - TEC_{film}$), the compressive and tensile stresses and the phase compositions in the films are given. The data for the 0.65PMN–0.35PT bulk ceramics fired at 950°C are added for comparison.

Table 20: The TEC of the substrates, the differences in TEC of the substrates and films ($\Delta TEC = TEC_{substrate} - TEC_{film}$), the compressive and tensile stresses and the phase compositions in the films. The 0.65PMN–0.35PT bulk ceramics sintered at 950°C are added for comparison.

substrate	TEC (10^{-6}/K)	ΔTEC (10^{-6}/K)	Stress - compression or tension	Phase composition
Al_2O_3	8[107, 108]	1.7	compressive	coexistence Pm and P4mm
Pt	8.8[109, 110]	2.5	compressive	coexistence Pm and P4mm
0.65PMN–0.35PT	6.3	0	stress free*	Pm
AlN	4.5[111, 112]	-1.8	tensile**	Pm
Bulk ceramics	6.3	0	stress free	Pm

* Pt electrode is neglected, ** poorly sintered and porous

The 0.65PMN–0.35PT films on the alumna and platinum substrates are under a compressive stress, due to the positive differences in TECs of the films and the substrates (Table 20). As mentioned before the phase composition of the 0.65PMN–0.35PT films on the alumina and platinum substrates the tetragonal and the monoclinic phases co-exist.

In the case of the 0.65PMN–0.35PT films on the 0.65PMN–0.35PT substrates, if the Pt electrode, which is between the substrate and film, is neglected, the films are stress free, since the TEC of the substrate is the same as TEC of the film (ΔTEC = 0). The phase of the 0.65PMN–0.35PT film on the 0.65PMN–0.35PT substrate is the monoclinic Pm as in the case of 0.65PMN–0.35PT bulk ceramics fired at 950°C. The films on the AlN substrates ought to be under a tensile stresses as the TEC of the AlN is smaller than the TEC of the 0.65PMN–0.35PT. The phase in this case is also monoclinic. However, the material is poorly sintered and porous and the monoclinic phase is more likely due to the small grain size.

No literature was found on how the residual stress influences the phase composition of the 0.65PMN–0.35PT material. However, tentatively these results for the 0.65PMN–0.35PT films under a residual stress can be compared with thin PZT films from the literature. For the PZT system, according to the experimental results, the compressive residual stress in the PZT thin film shifts the MPB toward the Zr-rich composition, i.e., the rhombohedral phase [30–32], which strongly affects the measured electrical properties of the films [32]. Also, the thermodynamic formalism based on the Landau-Devonshire`s phenomenological theory predicts the enhanced thermodynamic stability of the tetragonal phase under a two dimensional compressive stress, where a calculation shows that a compressive stress shifts the MPB toward the rhombohedral phase and forces PZT films to be in the tetragonal phase [30, 33]. Here note that 0.65PMN–0.35PT films are thick in comparison with PZT thin films and that the phase diagrams for PMN–PT and PZT materials are not the same. However, the results for 0.65PMN–0.35PT thick films under a residual stress show the same tendency as in the PZT system, i.e., the compressive stresses enhanced the stability of the tetragonal phase.

To confirm the existence of the stresses in the films the influence of the thickness of the films vs. the phase composition for the 0.65PMN–0.35PT films on the Al_2O_3 substrates (compressive stress) and 0.65PMN–0.35PT substrates (if neglecting Pt electrode, the film is stress free) was studied by the X-ray diffraction analyses. Note that the penetration depth of X-rays in 0.65PMN−0.35PT material is around 10 μm and therefore the results show the composition of the upper layer of thick film. Due to the stress gradient through the film thickness, the material nearer to the substrate is under larger stress than the layers more distant from the substrate. The ratios of monoclinic and tetragonal phase for 20 μm and 100 μm thick films on Al_2O_3 substrates are 42% : 58% and 55% : 45%, respectively. However the microstructures of the surface of the films are similar with the same grain sizes. Therefore it could be concluded that the phase composition depends not only on the grain size but also on the stress. The thicker the film on the alumina substrate is, the more monoclinic Pm phase is observed with the X-ray diffraction and the composition is more similar to the composition of stress-free bulk ceramics fired at 950°C. On the other hand, the 0.65PMN-0.35PT films on 0.65PMN-0.35PT substrates are monoclinic, regardless of the film thickness.

Another conformation for stresses in the films we can obtain, if we compare the phase composition of bulk ceramics sintered at 1200°C with the composition of the films on Al_2O_3 and Pt substrates. The films and bulk ceramics are both dense, with a median grain size around 1-2 μm and the phase composition shows the coexistence of monoclinic and tetragonal phase. However, the films on alumina and platinum substrates contain higher amounts of tetragonal phase than bulk ceramics with the same composition and comparable grain sizes. This could be another conformation for residual stresses in the films, which influence the phase compositions. Here we can add that for films on Pt substrates a part of the stresses can presumably relax with the formation of the partial preferential orientation (001) observed by X-ray. These partial preferential orientation can also influence the electrical properties of these films in comparison with the electrical properties of films on Al_2O_3 substrates, however further work on this topic will be needed.

Differences in the dielectric, piezoelectric and ferroelectric properties of the films on different substrates are manly due to microstructure characteristics. Dielectric constants, piezoelectric coefficients and remanent polarizations are higher for the films on Al_2O_3 and Pt substrates and lower for the films on 0.65PMN–0.35PT and AlN substrates. As mentioned, the films on Al_2O_3 and Pt substrates are dense with median grain sizes comparable with the median grain size of bulk ceramics fired at 1200°C. Films on the 0.65PMN–0.35PT and AlN substrates are porous and consist of smaller grains. Median grain sizes are 0.5

μm and 0.3 μm for films on 0.65PMN–0.35PT and AlN substrates. Obviously, the choice of substrate with different TECs also influences the microstructures (grain size and porosity) of the films.

4.4 Realization of the 0.65PMN–0.35PT/Pt actuators

4.4.1 Electrostrictive effect in the 0.65PMN–0.35PT thick films

The electrostrictive effect of 50-µm-thick 0.65PMN–0.35PT films on the alumina substrates was measured with AFM. The measurements of the sample displacement versus time obtained by AFM at the applied force of 80 nN for the different voltage amplitudes at frequency 200 Hz is shown in Fig. 91. The frequency of the displacement was twice the frequency of the applied electric field, i.e., 200 Hz, which is indicative of the quadratic effect. To emphasize the double frequency of measured sample displacements, the applied external sinusoidal voltage curve with maximum amplitude of 50 V is added to Fig. 91.

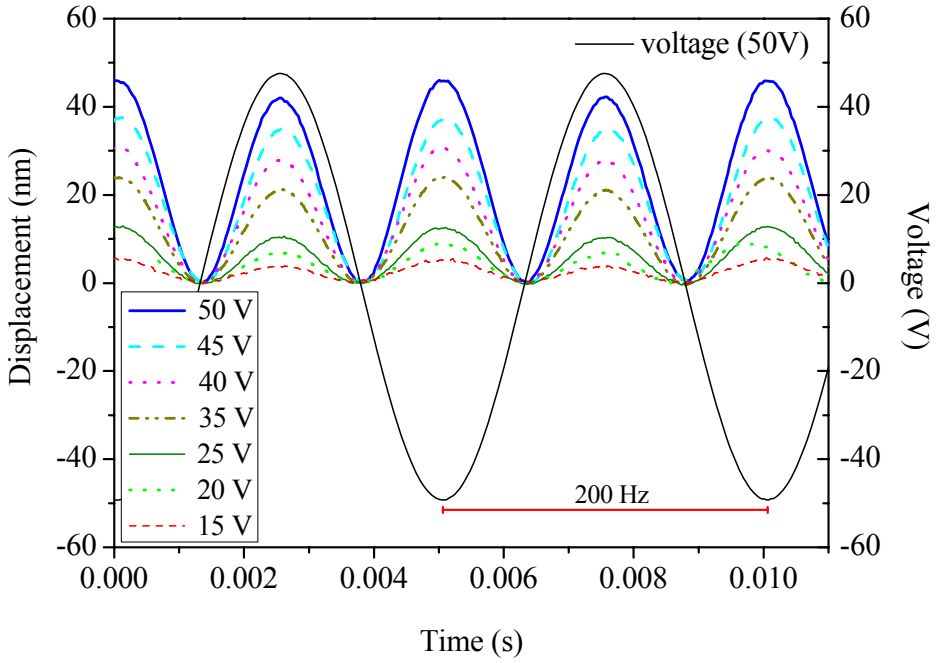

Figure 91: Measurements of displacement versus time at different voltage amplitudes and at a frequency of 200 Hz for the 0.65PMN–0.35PT thick film on the alumina substrate. The applied force was 80 nN. The applied external sinusoidal voltage curve with a maximum amplitude of 50 V is added to emphasize the double frequency of the measured sample displacements.

The measurements by AFM at sinusoidal electric voltage with the amplitude of 50 V were performed at applied forces of 80 nN, 200 nN and 300 nN to examine the force dependence of samples displacements. No dependence of the displacement versus the applied force between the tip and the sample was observed. Due to the stiffness of the thick alumina substrates, the bending of the substrate is negligible. The AFM measurements were performed locally from a direct contact on the bare surface of the film. Since the contact area of the AFM tip is around 20 nm, the contact areas between the AFM tip and the sample were smaller than a single 0.65PMN–0.35PT grain. However, due to the relatively large film thickness a few tens of grains were excited.

The displacement versus voltage amplitude for the 0.65PMN–0.35PT thick film on the alumina substrate is shown in Fig. 92. The dotted line between the measured values is just a guide to the eyes. Fig. 93 shows the relative strain versus the square of the electric field amplitude. The effective electrostrictive coefficient $M_{33} = 7.6 \cdot 10^{-16}$ m^2 /V^2 $\pm$ $0.8 \cdot 10^{-16}$ m^2/V^2 was determined from the slope of the linear-fit curve (Fig. 93). The uncertainty of $\pm$ $0.8 \cdot 10^{-16}$ m^2/V^2 is mainly due to the uncertainty in the measured thickness of the 0.65PMN–0.35PT film.

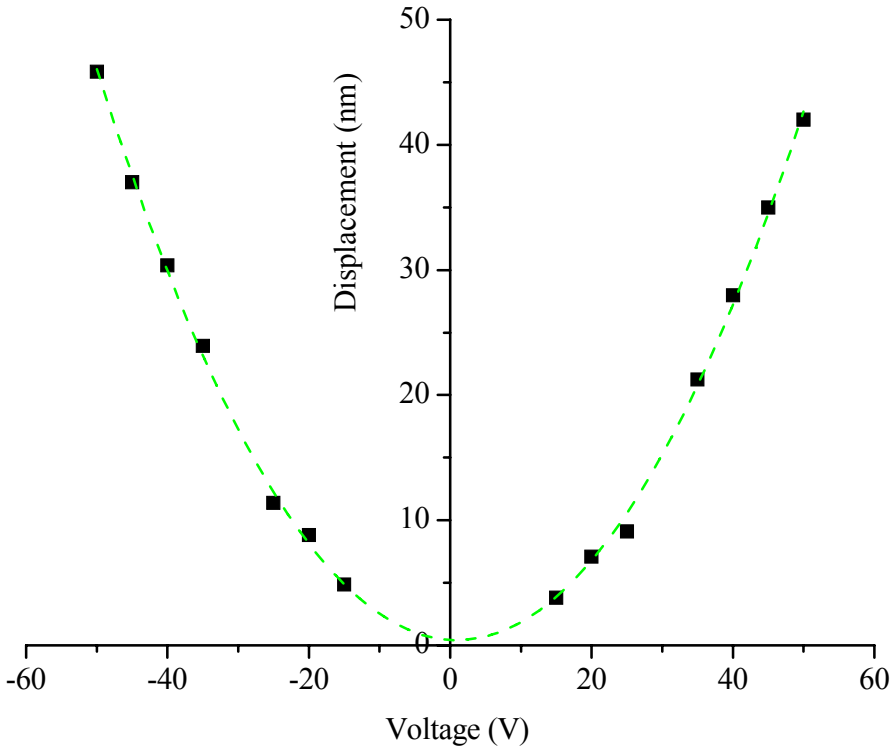

Figure 92: The displacement versus voltage amplitude for the 0.65PMN–0.35PT thick film on the alumina substrate. The dotted line between the measured values (quadratic fit) is just a guide to the eye.

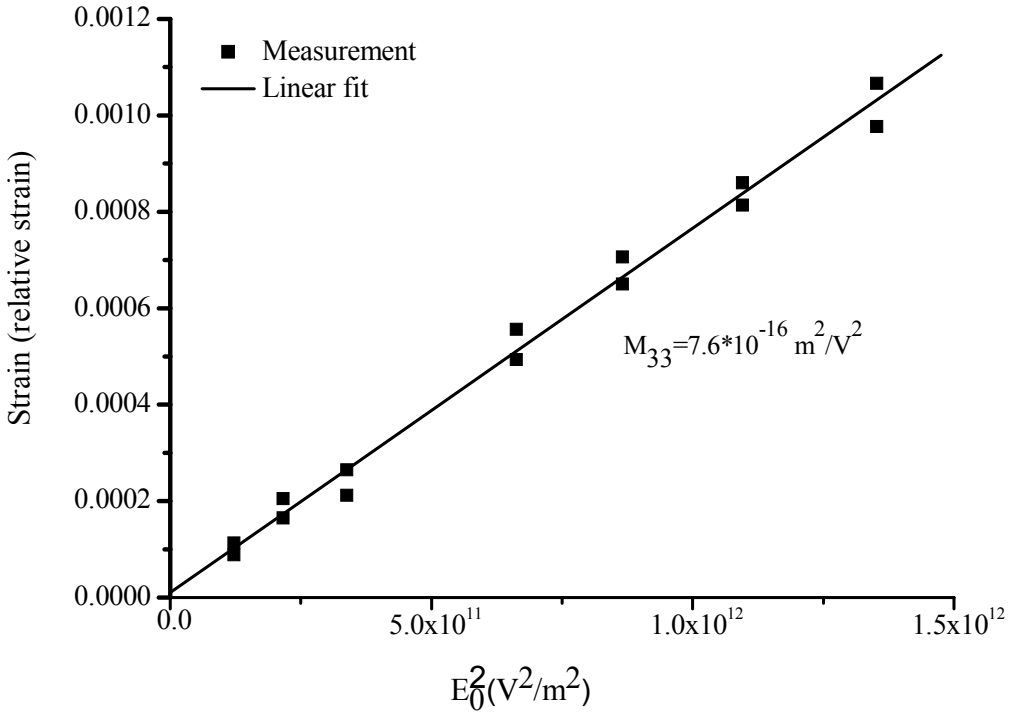

Figure 93: Relative strain versus the square of the electric field amplitude. The electrostrictive coefficient M_{33} was determined from the slope of the linear fit curve.

The electrostrictive effect in the xPMN– (1-x)PT material with the composition x = 0.0–0.1 has been previously studied, in single crystals [113], ceramics [114, 115], and thin films [116–117]. The measured M_{33} values for PMN (x = 0) bulk ceramics and for PMN (x = 0) thin films are $1.5 \cdot 10^{-16}$ m^2/V^2 [4] and $8.9 \cdot 10^{-17}$ m^2/V^2 [116], respectively. However, not much work was done on the composition 0.65PMN–0.35PT. Bokov and Ye [118] reported that the values of the electrostrictive coefficient M_{33} for the 0.65PMN–0.35PT single crystal are $M_{33} = 1.3 \cdot 10^{-15}$ m^2/V^2 – $4.0 \cdot 10^{-15}$ m^2/V^2. The electrostrictive coefficients for the 0.65PMN–0.35PT crystals are surprisingly high, because 0.65PMN–0.35PT crystals are usually considered to be a piezoelectric material. The high electrostrictive effect arises from intrinsic electrostriction and also extrinsic contributions, i.e., domain-wall switching [118], which is probably also the case for measured M_{33} of our 0.65PMN–0.35PT thick films. The measured electrostrictive coefficient of our 0.65PMN–0.35PT thick film is lower than electrostrictive coefficient for single crystals. Several parameters could reduce the electrostrictive coefficients of films, for example, clamping of the film to the substrate and a lower dielectric constant in the films compared to single crystals as reported for thin films in refs. [116, 117, 119].

The measured $M_{33} = 7.6 \cdot 10^{-16}$ m^2/V^2 of 0.65PMN–0.35PT thick films on alumina substrates is high in comparison with the values for PMN bulk ceramics, i.e., $M_{33} = 1.5 \cdot 10^{-16}$ m^2/V^2, which is one of the best known electrostrictive materials [4]. Due to these results, we decided to prepare the 0.65PMN–0.35PT thick-film actuators. To ensure a sufficient amount of bending, it is important to reduce the thickness of the substrate. For this reason we developed a new approach to prepare “substrate-free”, large-displacement actuators using the screen-printing method.

4.4.2 Preparation procedure and microstructures of the 0.65PMN–0.35PT/Pt actuators

The procedure for the preparation of the 0.65PMN–0.35PT/Pt actuators was possible to realize due to the bad adhesion between the platinum electrode and the alumina substrate (section 4.3.1.1). For this purpose the 0.65PMN–0.35PT films on the alumina substrates were prepared without a $PbZr_{0.53}Ti_{0.47}O_3$ barrier. The 0.65PMN–0.35PT/Pt actuators were prepared with a new approach, which is explained in section 3.1.3. As mentioned before the β-alumina crystals resulting from the reaction between PbO from the 0.65PMN–0.35PT and Al_2O_3 at the interface between the alumina substrate and the Pt electrode are formed. These crystals "pushed off" the 0.65PMN–0.35PT/Pt electrode structures.

A cross-section of the 0.65PMN–0.35PT/Pt actuator after peeling off of the alumina substrate is shown in Fig. 94. The thickness of the 0.65PMN–0.35PT layer is around 50 µm and the thickness of the Pt electrode is around 15 µm. The top gold electrode, deposited by sputtering, was too thin to be seen in Fig. 94. The measured porosity of the 0.65PMN–0.35PT film in Fig. 94 is 6.5%.

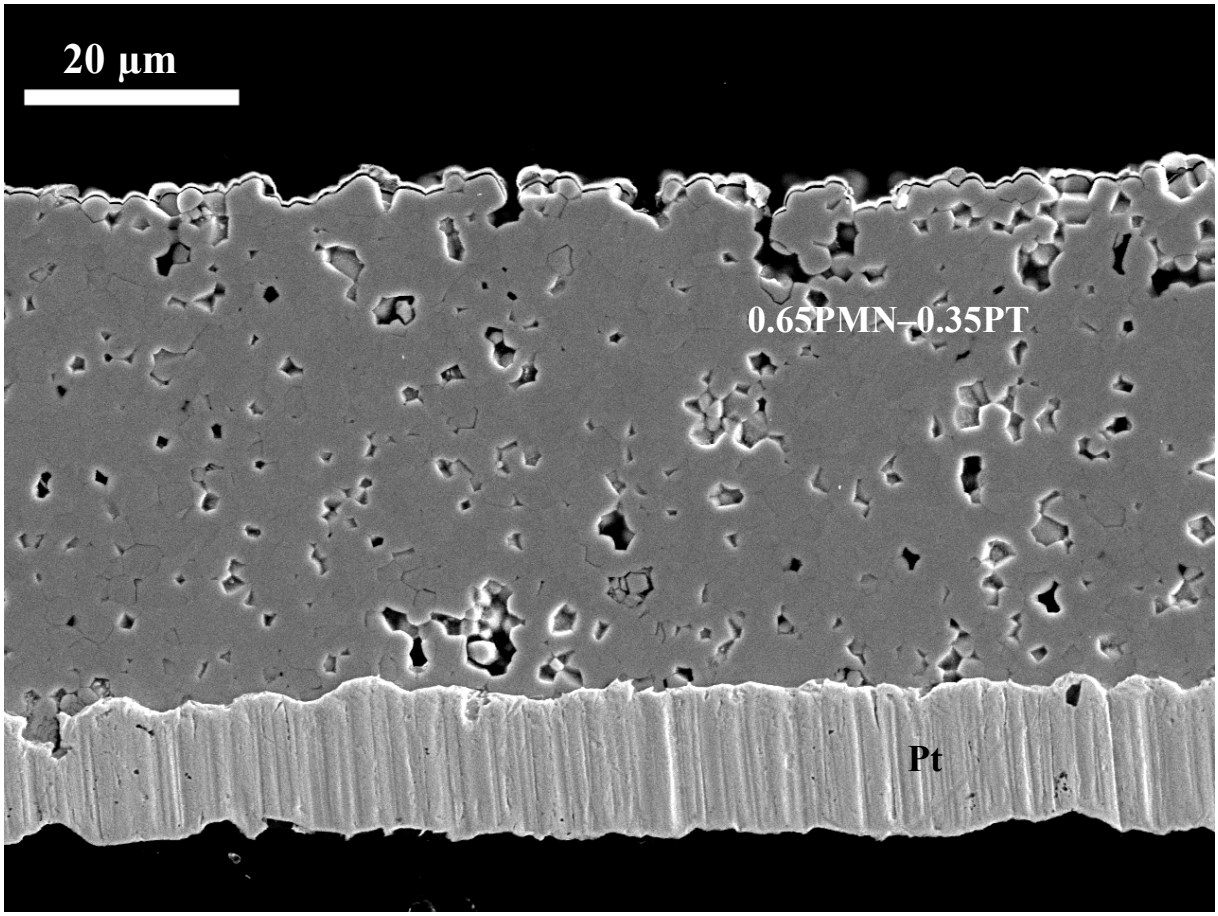

Figure 94: A cross-section of the 0.65PMN–0.35PT/Pt actuator.

4.4.3 Functional characterization of the 0.65PMN–0.35PT/Pt actuators

The 0.65PMN–0.35PT layer of the actuator was poled at 2.5 kV/mm. The 0.65PMN–0.35PT/Pt actuator's displacements normalized per unit length of the actuator vs. applied DC electric field for an actuator with dimensions of 1.8 cm × 2.5 mm × 65 μm (the thickness of the 0.65PMN–0.35PT layer is 50 μm and the thickness of the Pt layer is 15 μm) is shown in Fig. 95. The normalized displacement (the displacement per unit length of the actuator) is 55 μm/cm at the electric field of 3.6 kV/cm (voltage 18 V).

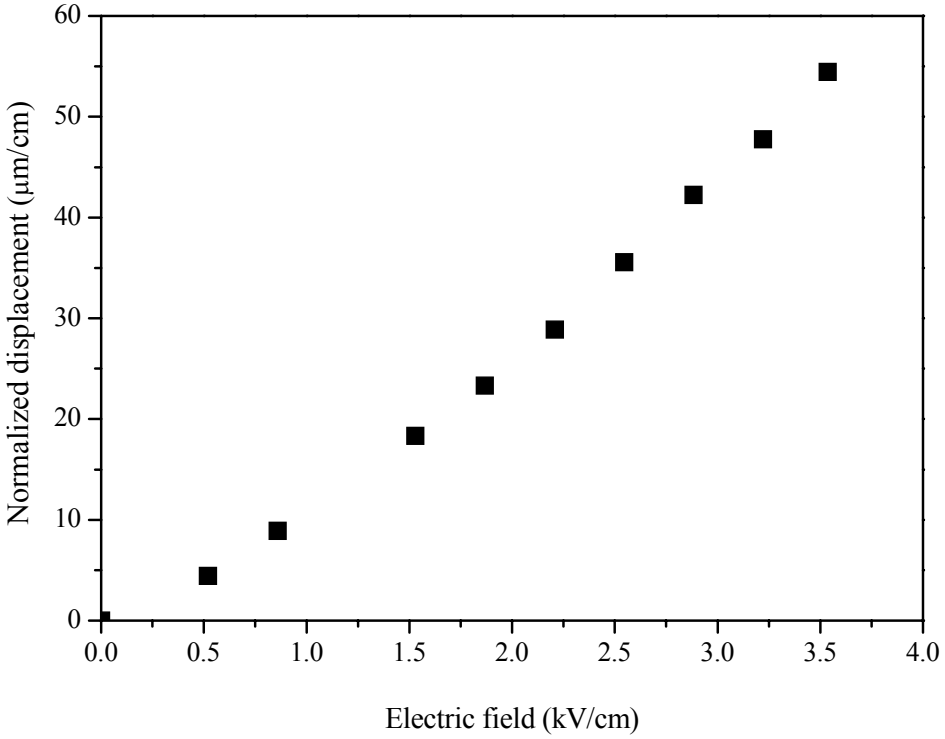

Figure 95: The bending displacement normalized per unit length of the actuator for the 0.65PMN–0.35PT/Pt actuator (with dimensions 1.8 cm × 2.5 mm × 50 μm of the active layer) versus applied electric field.

Hall et al. reported that for piezoelectric/electrostrictive PMN–PT monomorph actuators prepared by tape casting with dimensions of 2.6 cm × 11 mm × 2.3 mm the maximum tip displacement at 3 kV/cm was 11 μm [120] (the calculated normalized displacement was 4 μm/cm). The same authors also reported that the largest tip displacement of a piezoelectric 0.65PMN–0.35PT/electrostrictive 0.9PMN–0.1PT bilayer monomorph with dimensions of 3 cm × 8 mm × 1.2 mm was up to 40 μm at 5 kV/cm [121] (the calculated normalized displacement was 13 μm/cm). Zarnik et al. [122] and Belavic et al. [123] reported that for thick-film PZT actuators prepared by screen printing on the alumina substrates with dimensions of 1.2 cm × 4 mm × 0.25 mm (40-μm thick PZT layer), the maximum tip displacement in an electric field of 50 kV/cm (voltage 200 V) was 5 μm (the calculated normalized displacement was 4 μm/cm). The displacements of the 0.65PMN–0.35PT actuators described here were large in comparison to the data in the literature. A comparison between our normalized displacement and the normalized displacements in the literature is shown in Fig. 96 and in Table 21.

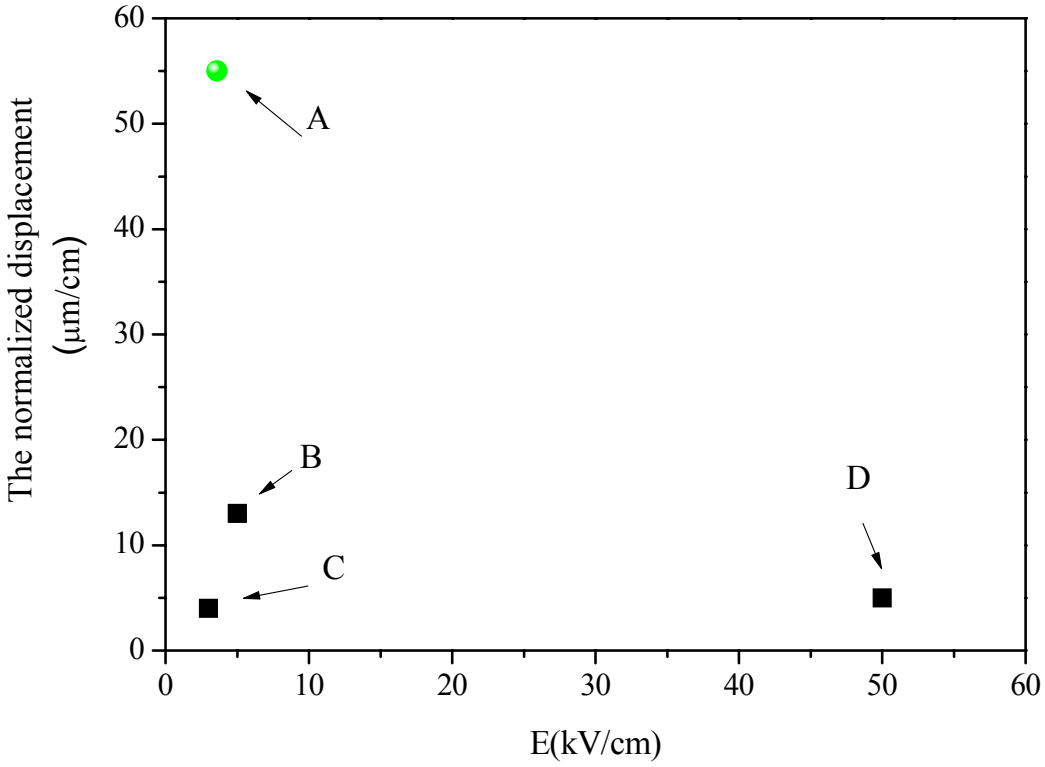

Figure 96: A comparison between our data (denoted A), i.e., the normalized displacement at an electric field of 3.6 kV/cm is 55 µm/cm, and the data from the literature; Ref. [120] (denoted B), Ref. [121] (denoted C) and Refs. [122, 123] (denoted D).

Table 21: The comparison between the measured data and the data from the literature.

Denoted in Fig. 96 (Literat.)	**Actuator**	**E (kV/cm)**	**Normalized displacement (µm/cm)**
A (This work)	**0.65PMN–0.35PT/Pt**	**3.6**	**55**
B (ref. [120])	**0.65PMN–0.35PT/0.9PMN–0.1PT**	**5**	**13**
C (ref. [121])	**0.65PMN–0.35PT/0.9PMN–0.1PT**	**3**	**4**
D (ref. [122])	**PZT thick-film actuators on alumina substrates**	**50**	**5**

4.4.4 The linear finite elements model of the actuator's displacement

As it is evident from the basic electromechanical equations, which describe linear material behaviour (Introduction, equations 5 and 6) a FE model of piezoelectric structures requires the elastic parameters s_{ij}, the piezoelectric coefficients d_{ij}, and the dielectric constants ε_{ij} to be entered in a form that the FE package expects for the piezoelectric material input. Which of the coefficients is non-zero depends on the symmetry. For poled ceramics, the elastic compliance matrix contains $s_{11,}$ $s_{33,}$ $s_{55,}$ s_{12}, s_{13} and s_{66}, the piezoelectric matrix contains d_{33}, d_{31} and d_{15} (while $d_{32} = d_{31}$ and $d_{24} = d_{15}$) and dielectric constant matrix ε_{33} and ε_{11} (while $\varepsilon_{22} = \varepsilon_{11}$) [1, 122].

The first initial FE model of the actuator was performed using material parameters of 0.655PMN–0.345PT bulk ceramics, i.e., $s_{11,}$ $s_{33,}$ $s_{55,}$ s_{12}, s_{13}, $s_{66,}$ d_{33}, d_{31}, d_{15} and ε_{33}, ε_{11} from the literature [91]. The parameters are collected in Table 22. For the Pt layer the elastic stiffness constants c_{11}, c_{12} and c_{66} were also taken from the literature [109]. The parameters used for Pt layer are collected in Table 23.

To improve the accuracy of the FE analysis prediction, we updated the FE model and we used material parameters for 0.65PMN–0.35PT thick films instead of parameters for bulk ceramics. For the updated model our measurements of dielectric constant ε_3, piezoelectric coefficient d_{33} and Young's modulus Y_{33} were used (values are summarized in Table 22). Because of the lack of experimental data for all electromechanical constants of 0.65PMN–0.35PT thick films a few assumptions, which were suggested in ref. [44], [122] for FE models of PZT thick films were made to obtained more accuracy with the FE analysis prediction. The assumptions were:

- For the updated FE model, the full elastic stiffness c_{ij} and the elastic compliance s_{ij} matrix were calculated from the experimentally measured Y_{33}, as it is explained in [122]. Due to the lack of experimental results for $Y_{MEASURED}$ in transverse direction (section 4.3.1.9) and with no data available in the literature for thick PMN–PT films, we presume the same ratio between the c_{ij} components for the thick films as for the bulk ceramics reported in the literature [91]. The full stiffness matrix was calculated from the experimentally obtained c_{33}. By transforming the c_{ij} components to s_{ij} (i.e. calculating the inverse of the c_{ij} matrix), all the elastic compliance parameters s_{ij} were calculated.

- The isotropic model for dielectric constant was taken, i.e., $\varepsilon_{33} = \varepsilon_{11}$.

- For the updated FE model the piezoelectric constant d_{31} = -100 pC/N was used, based on the assumption that the values of the piezoelectric coefficients for the 0.65PMN–0.35PT films are reduced by 50% from these for bulk ceramics as reported in ref. [122]. The same value was analytically calculated by using equations for the unimorph actuator from the literature [124], where measured displacement of actuator at 10 V, actuators dimensions and Young's modulus of 0.65PMN–0.35PT film ($Y_{0.65PMN\text{-}0.35PT}$ = 90 GPa) and Pt layer (Y_{Pt} = 168 GPa) [125, 126] were inserted.

- For the piezoelectric constant d_{15} a value of 554 pC/N was used in both the initial and the updated FE models. The reason for this was that the bending properties of the actuator are not strongly dependent on the value of the piezoelectric constant d_{15} and consequently the numerical calculations do not change dramatically, if the value for d_{15} is reduced by 50% or not.

The parameters used in the updated FE model for 0.65PMN–0.35PT films are also collected in Table 22. For the Pt layer the same parameters for updated FE model as for initial FE model were used.

Table 22: The material parameters specified in the initial and in the updated FE models.

Parameter	*Initial FE model*[a]	*Updated FE model*	Units
ε_{33}	4100	3000[b]	
ε_{11}	3700	3000[c]	
d_{31}	-223	-100[d]	pC/N
d_{33}	480	190[b]	pC/N
d_{15}	554	554	pC/N
s_{11}	13.5	23.1[e]	10^{-12} m^2/N
s_{33}	14.5	24.8[e]	10^{-12} m^2/N
s_{55}	31	53[e]	10^{-12} m^2/N
s_{12}	-4.8	-8.20[e]	10^{-12} m^2/N
s_{13}	-5.9	-10.1[e]	10^{-12} m^2/N
s_{66}	36.6	62.5[e]	10^{-12} m^2/N

[a] The constants are taken from the literature for $0.655Pb(Mg_{1/3}Nb_{2/3})O_3–0.345PbTiO_3$ ceramics [91].
[b] Measured values.
[c] The isotropic model for dielectric constant was taken.
[d] d_{31}= -100 pC/N was used on the assumption that the piezoelectric coefficients of the 0.65PMN–0.35PT films are reduced by 50% [122]. The same value was analytically calculated with equations from the literature [124].
[e] We kept the same ratio between the components c_{ij} and the experimentally obtained c_{33} as for bulk 0.65PMN–0.35PT ceramics from the literature [91]. The components s_{ij} for the updated FE model were calculated.

Table 23: The Pt material parameters specified in the initial and in the updated FE model [109].

Parameter	Stiffness constants (N/m^2) [109]
c_{11}	$3.47 \cdot 10^{11}$
c_{12}	$2.51 \cdot 10^{11}$
c_{66}	$7.65 \cdot 10^{10}$

A comparison of the simulation results obtained for the initial and the updated FE models of the actuator and the measured bending of the actuator is shown in Fig. 100. The initial model results in a discrepancy between the prediction and the real structure properties.

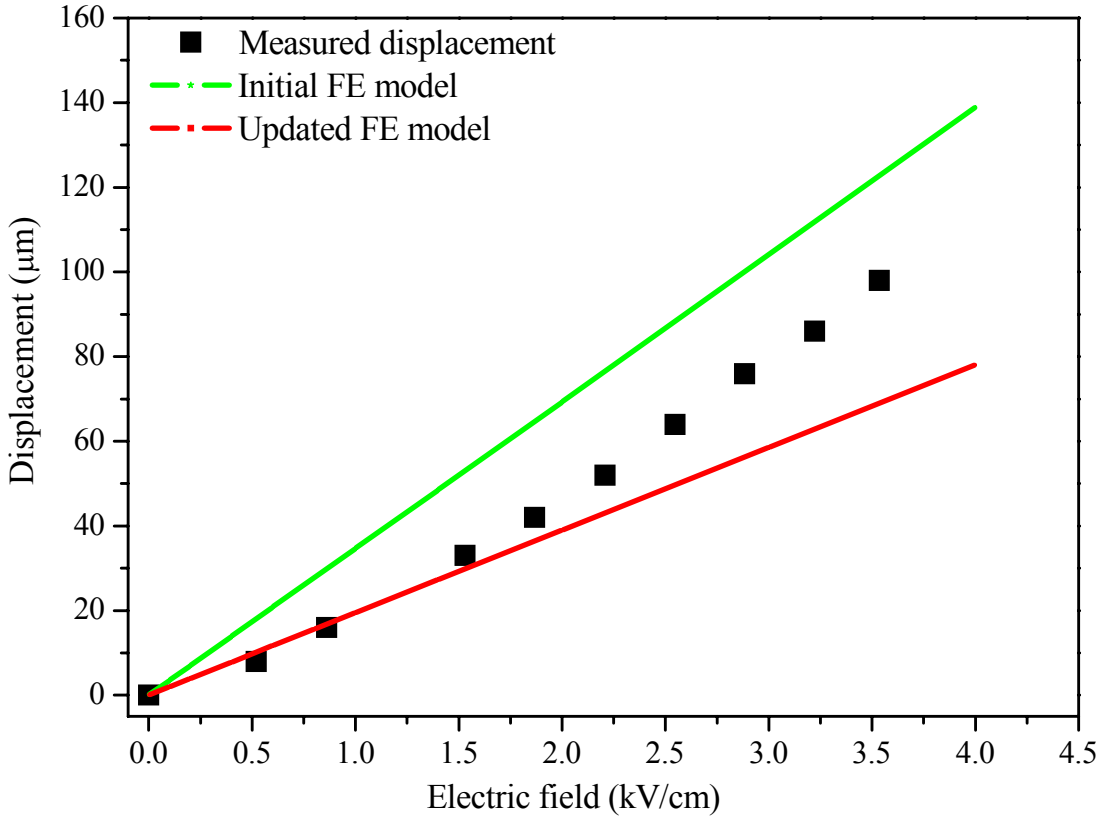

Figure 97: Comparison of the simulation results obtained from the initial FE model and the updated FE model with the measured displacement of the actuator.

As is evident from Fig. 100, when the electric field is low, i.e., from 0 kV/cm to 1-1.5 kV/cm, the experimental results are in relatively good agreement with the updated linear calculations. However, as the magnitude of the electric field strength increases the contribution of the second order prevails:

$$S_{ij} = d_{ijk}E_k + M_{ijmn}E_mE_n \quad (14)$$

where S_{ij} is the strain tensor, E_k, E_m and E_n (V/m) are the components of the electric field vector, d_{ijk} (pm/V) is a third-rank piezoelectric tensor and M_{ijmn} (m^2/V^2) is the fourth-rank-related electrostrictive tensor. Therefore, at higher electrical fields a difference between the measured results and the linear theoretical calculation is to be expected.

5 Conclusions

The purpose of this work was to compare the structural and electrical properties of the 0.65PMN–0.35PT films on different substrates, i.e., alumina (Al_2O_3), platinum (Pt), 0.65PMN–0.35PT and aluminium nitride (AlN), with a dense ceramic as well as with the ceramics processed under the same conditions as thick films, i.e., 950°C for 2 hours. The substrate materials were chosen according to thermal expansion coefficients (TEC) of these materials to obtain different stress conditions in the films after the heating and cooling treatment. The dense ceramics with the density of 98% of theoretical density were fired at 1200°C for 2 hours, while the ceramics fired at 950°C have a density of 71% of theoretical density.

The starting powder with the nominal composition of $0.65Pb(Mg_{1/3}Nb_{2/3})O_3–0.35PbTiO_3$ was prepared by the mechanochemical synthesis. It had narrow particle size distribution with the d_{50} equal to 0.32 μm. The X-ray analysis of powder confirmed the perovskite phase. Additional firing of powder at 700°C was performed to obtain fine particles and chemically homogeneous powder.

The microstructure of the ceramics fired at 1200°C was homogenous and the 98% of theoretical density was obtained after sintering. The median grain size was 1.1 μm. The Rietveld analysis of the X-ray data of this bulk ceramic shows the coexistence of the monoclinic Pm and the tetragonal P4mm phases. The determined monoclinic-to-tetragonal ratio was 86% of monoclinic Pm and 14% of tetragonal P4mm phases, which is in close agreement with previously reported results [54]. No extra diffraction peaks that might correspond to pyrochlore or PbO phases were detected after sintering. The ε at room temperature measured at 1 kHz was 3600, which is in agreement with results from ref. [60]. The maximum value of ε, measured at frequency of 100 kHz, was approximately $\varepsilon_{max} = 56.500$ at the temperature $T_{max} = 172°C$. These results for ε_{max} are higher than the values reported in [48, 58], which is presumably due to high chemical homogeneity. No dependence of T_{max} on the frequency was observed. The low temperature peak of the transition between the monoclinic and the tetragonal phases is clearly evident in the measurements of the dielectric constant vs. temperature. The LT phase-transition peak is broad, and the estimated peak transition temperature is between 50 and 80°C, which is in agreement with the data reported in the literature [60, 91]. The remanent polarization P_r and coercitive fields E_c of bulk ceramics fired at 1200°C for 2 hours are 33 $\mu C/cm^2$ and 6 kV/cm, respectively. This is in agreement with data from [58].

The Rietveld analyses of the X-ray diagram for the non-poled and poled 0.65PMN–0.35PT ceramics fired at 1200°C for 2 hours showed the coexistence of the monoclinic Pm and the tetragonal P4mm phases in different ratios. The monoclinic Pm to tetragonal P4mm ratio is changed with the application of the electric field, and it is strongly dependent on the electric field strength. The amount of the monoclinic phase is larger in the poled samples. The non-poled ceramics contains 86% of monoclinic Pm and 14% of tetragonal P4mm phases, while ceramics poled at 2.5 kV/mm contain 99% of monoclinic Pm and only 1% of tetragonal P4mm phases. Also, the poled 0.65PMN–0.35PT ceramics differ from the non-poled ones in terms of the presence of a slight (001) preferential orientation of the tetragonal crystallites. The highest piezoelectric coefficient d_{33} and coupling coefficients k_p and k_t were obtained with poling electric fields of 2 kV/mm to 3.5 kV/mm. The highest piezoelectric coefficient d_{33} is around 660 pC/N. The highest coupling coefficients k_p and k_t are 0.77 and 0.55, respectively, which are higher than the previously reported values [48]. The results showed that in 0.65PMN–0.35PT ceramics the poling electric field at which the highest piezoelectric and coupling coefficients d_{33}, k_p and k_t were obtained coincide with the poling electric fields at which the highest amount of monoclinic phase was confirmed from the X-ray diagram using Rietveld analyses.

The thick-film samples were fired on the alumina (Al_2O_3), platinum (Pt), 0.65PMN–0.35PT and aluminium nitride (AlN) substrates. All the films were processed under the same conditions, i.e., for 2 hours at 950°C and with cooling rate of 3°C/min. Among 0.65PMN–0.35PT film and Al_2O_3 substrate the $Pb(Zr_{0.53}Ti_{0.47})O_3$ barrier layer was printed to minimise the interactions between the film and the substrate and the formation of β-alumina crystals at the interface between the substrate and the platinum electrode.

For other substrates no significant interactions between films and substrate materials were observed. The cross-sections of the films on different substrates were analyzed by EDXS analysis. The results showed that no difference in chemical composition among the films on different substrates can be observed within the measurement errors. Also all films were chemically homogenous through the thickness.

The films on the alumina and platinum substrates are dense. Significant grain growth is observed. The median grain size is 1.7 μm for films on alumina substrates and 1.2 μm for films on platinum substrates. Microstructures of the films on the 0.65PMN–0.35PT and AlN substrates are porous and consist of small grains with dimensions below 0.5 μm. The grain sizes are similar to grain size of the starting powder. However, grains in the films on 0.65PMN–0.35PT and AlN substrates are sintered together and the grain boundaries can be observed. The thickness of 0.65PMN–0.35PT films with the same number of printed layers prepared at the same firing and cooling conditions differs with the choice of the substrates. The larger thicknesses of films on 0.65PMN–0.35PT and AlN substrates indicate more porous material. These results show that the choice of substrate strongly influences the sintering and microstructure characteristics.

Samples were studied by X-ray analysis and the phase compositions were determined with the Rietveld refinement. The phase composition of the films on the Al_2O_3 and Pt substrates is a mixture of the monoclinic and the tetragonal phases, similar to bulk ceramics sintered at 1200°C. The ratios between monoclinic and tetragonal phases are 42% : 58%, 81% : 19% and 86% : 14% for films on alumina and platinum substrates and for bulk ceramics, respectively. The films on alumina and platinum substrates contain higher amount of tetragonal phase than the bulk ceramics with the same composition and comparable grain sizes. The films on 0.65PMN–0.35PT and AlN substrates as well as bulk ceramics fired at 950°C are monoclinic.

The X-ray diffraction diagrams of the 0.65PMN–0.35PT films were measured at different temperatures. At low temperature, i.e., -173°C, the phase is monoclinic for films on all substrates. For the films on the 0.65PMN–0.35PT substrates the phase stays monoclinic till the phase-transition into the cubic phase. The films on the AlN substrates presumably show the same tendency as the films on the 0.65PMN–0.35PT substrates. For the films on the Al_2O_3 and Pt substrates the co-existence of the monoclinic and the tetragonal phases was observed over a wide temperature range around room temperature. At a temperature of 107°C and higher the phase is pure tetragonal and at 187°C and higher the phase is cubic Pm-3m.

Young's moduli were measured by the nanoindentation method. The highest values were obtained for the 0.65PMN–0.35PT film on the Al_2O_3 and Pt substrate, i.e., 90 GPa. For the 0.65PMN–0.35PT bulk ceramics fired at 1200°C for 2 hours, the Young's modulus was 75 GPa within measurements errors these two values are comparable. The significantly lower values between 20 GPa and 30 GPa were obtained for the films on the AlN and 0.65PMN–0.35PT substrates and bulk ceramics fired at 950°C, due to the high porosity of the samples.

The highest ε at room temperature, 3400, was obtained for the 0.65PMN–0.35PT films on the alumina substrates, which is comparable with the values obtained for bulk ceramics fired at 1200°C. The ε of films on the Pt substrates was below 2000. For the films on the 0.65PMN–0.35PT and AlN substrates low values were observed, i.e., $\varepsilon = 700$ and $\varepsilon = 300$, respectively. The main reason for the differences in ε of thick 0.65PMN–0.35PT films on different substrates are microstructures, i.e., the films on the 0.65PMN–0.35PT and AlN substrates are porous, consequently the ε are low in comparison with the ε of the better sintered 0.65PMN–0.35PT films on the Al_2O_3 and Pt.

For the piezoelectric measurements samples were previously poled with the optimum poling conditions, i.e., 2.5 kV/mm. The 0.65PMN–0.35PT films on the alumina substrates were measured by three different methods; Photonic sensor, atomic force microscope (AFM) and Berlincourt piezometer, to evaluate the possible differences of results depending on the used method. The average values of d_{33}^{eff} obtained by three methods were 185 pm/V ± 20 pm/V. The measurements made by Photonic sensor, AFM and Berlincourt piezometer are therefore in agreement within the measurement error.

The piezoelectric coefficients d_{33}^{eff} for all 0.65PMN–0.35PT films are below 200 pC/N. The highest value was obtained for the films on the alumina substrate, i.e., 185 pC/N. This is in agreement with data from the literature, which reports that PMN–PT ceramics with larger grains exhibit higher d_{33} [54]. For the films on the Pt and 0.65PMN–0.35PT substrates lower d_{33}^{eff} values were obtained, i.e. 140–110 pC/N and 120–105 pC/N, respectively. The measured d_{33}^{eff} values for the films on the AlN were around 30–20 pC/N.

However in this case the measurement error is comparable with measured value. The largest difference between the properties of films and bulk ceramics sintered at 1200°C is shown in piezoelectric coefficients. Measured values for the bulk ceramics fired at 1200°C and poled under the same conditions as films were 660 pC/N. One of the reasons for lower piezoelectric coefficient of films is that films are clamped to the rigged substrates, which decreases the d_{33}.

The high remanent polarization P_r was obtained for the 0.65PMN–0.35PT films on the Pt and Al_2O_3 substrates, i.e., 27 μC/cm^2 and 22 μC/cm^2, respectively, which is comparable with the value obtained for bulk ceramics fired at 1200°C. Much lower P_r was obtained for the films on the 0.65PMN–0.35PT (8 μC/cm^2) and AlN (3 μC/cm^2) substrates. This is attributed to the porosity of the films.

The 0.65PMN–0.35PT bulk ceramics fired at the same temperature and time as films, i.e., 950°C, 2 hours was studied for comparison. The structure shows grains with mainly sub-micron dimensions. The ceramics is porous as this firing temperature is low for sintering bulk 0.65PMN–0.35PT ceramics. The relative density of bulk samples fired at 950°C is low, i.e., around 70% of theoretical density. Due to this, the Young's modulus of bulk 0.65PMN–0.35PT ceramics fired at 950°C is low, i.e., 20 GPa. The X-ray diffraction diagram of bulk ceramics fired at 950°C was also measured. Only the monoclinic Pm phase was determined with the Rietveld analysis. As mentioned before the data in the literature showed that 0.65PMN–0.35PT material with small grain size consist mainly of the monoclinic phase [54].

The results show that the choice of the substrate materials strongly influences the characteristics of 0.65PMN–0.35PT films. For example, with the proper choice of the substrate materials we can obtain films with better structural and electrical properties than properties of bulk ceramics with the same composition and fired at the same temperature and time, i.e., 950°C, 2 hours, such as lower porosity, higher Young's moduli and dielectric constants. Therefore with the right choice of the substrate thick films with dielectric and ferroelectric characteristics comparable with densely sintered bulk ceramics can be prepared. However piezoelectric constants d_{33}^{eff} of films are lower compared to the densely sintered bulk ceramics. One of the reasons for lower measure piezoelectric coefficient of films is that films are clamped to the rigged substrates. Further investigation will be needed to find other reasons for lower piezoelectric constant in films in comparison to the bulk ceramics.

The proposed explanation for different characteristics of the films on Al_2O_3, Pt, 0.65PMN–0.35PT and AlN substrates is that during the sintering procedure, due to the difference in the thermal expansion coefficients (TEC) of the substrates and the 0.65PMN–0.35PT, residual stresses develop and remain in the films during cooling. The TECs of the alumina and platinum substrates are around $8\cdot10^{-6}$/K – $9\cdot10^{-6}$/K and are higher than the TEC of the 0.65PMN–0.35PT material, which is $6.3\cdot10^{-6}$/K. Due to this the 0.65PMN–0.35PT films on the alumna and platinum substrates are under compressive stresses after cooling.

The TEC of the AlN substrate is $4.5\cdot10^{-6}$/K and lower than TEC of the 0.65PMN–0.35PT material. Due to this it would be expected that the films are under tensile stresses. The films on 0.65PMN–0.35PT substrates are stress free, since the TEC of the substrate is the same as the TEC of the film. The phase composition of film on both AlN and 0.65PMN–0.35PT substrate is only the monoclinic Pm. The microstructures of films on both substrates are porous with grain sizes 0.3 μm and 0.5 μm, respectively. According to the literature [54] 0.65PMN–0.35PT ceramics with smaller grains, i.e., 0.15 μm tend to be monoclinic. Therefore we presume that the tensile stresses were relaxed during cooling and the structural and microstructural characteristics are therefore similar for films on AlN (potential tensile stress) as for films on 0.65PMN–0.35PT (stress free) substrates. For comparison the phase composition of the stress free bulk ceramics fired at 950°C is monoclinic Pm and the grain size is also below 0.5 μm.

No data on how the residual stress influences the phase composition of the 0.65PMN–0.35PT material was found in the open literature. However, thermodynamic formalism based on the Landau-Devonshire's phenomenological theory predicts and also the measurements made on thin PZT films on different substrates state that thermodynamic stability of the tetragonal phase under a compressive stress is enhanced. The stresses influence the position of the morphotropic phase boundary (MPB) and therefore the phase composition. This is in accordance with our results, which shows that compressive stress increases the amount of the tetragonal phase in the 0.65PMN–0.35PT thick films.

The influence of the film thickness vs. the phase composition of the 0.65PMN–0.35PT films were studied

for the films on the Al_2O_3 and 0.65PMN–0.35PT substrates. The films on the alumina were chosen, because at room temperature the percent of the tetragonal phase is the highest. The X-ray diagrams are different for the films of different thicknesses. The phase ratios of 20 μm and 100 μm thick films are 42% and 55% of the monoclinic Pm phase, respectively. The rest is the tetragonal P4mm phase. Due to the stress gradient through the film thickness, the material nearer to the substrate is under larger stress than the layers more distant from the substrate and therefore contain larger amount of tetragonal phase. The microstructures of the surface of the films are similar with the same grain sizes and therefore it could be concluded that compressive stress increases the tetragonal-monoclinic phase ratio. For the films on the 0.65PMN–0.35PT substrates only the monoclinic phase is present. In this case, no significant difference between the X-ray diagrams is observed, regardless of thickness of the films.

Another conformation for stresses can be obtained with a comparison of bulk ceramics sintered at 1200°C with the films on Al_2O_3 and Pt substrates. The films and bulk ceramics are both dense with median grain size around 1-2 μm and the phase composition shows the coexistence of monoclinic and tetragonal phase. However, the films on alumina and platinum substrates contain a larger amount of tetragonal phase than the bulk ceramics with the same composition and comparable grain sizes. This could be another conformation for residual stresses in the films, which influence the phase compositions. Here we can add that for films on Pt substrates a part of stresses can presumably relax with the formation of the partial preferential orientation (001) observed by X-ray. This partial preferential orientation can also influence electrical properties of these films. Presumably lower dielectric constant of the films on Pt substrate, i.e., 2000 in comparison with films on Al_2O_3 substrate, i.e., 3600 could be the consequence of preferential orientations in the films on Pt substrate as it is reported in ref. [8] for $BaTiO_3$ crystals, PZN and 0.2PZN-0.8PT crystals in ref. [127] and 0.62PMN-0.38PT crystals in ref. [128]. As reported in ref. [128] also higher remanent polarization P_r for films on Pt substrates in comparison with films on Al_2O_3 substrates could be the consequence of preferential orientations (001).

The measured electrostrictive coefficient of the 0.65PMN–0.35PT films on the alumina substrates was high in comparison with the PMN bulk ceramics, which is one of the most known electrostrictive materials, therefore it was decided to prepare the 0.65PMN–0.35PT thick-film actuators with large displacement. To ensure a sufficient amount of bending, a new approach to prepare “substrate-free” large-displacement actuators using the screen printing method was developed. This approach was possible due to the bad adhesion in the 0.65PMN–0.35PT structures among the platinum electrode and the alumina substrate. This is due to the formation of β-alumina crystals on the interface between the Pt electrode and the Al_2O_3 substrate resulting from the reaction between the PbO from the film and the Al_2O_3. The result of the new preparation procedure is the 0.65PMN–0.35PT/Pt actuator, which shows a large displacement.

The normalized measured displacement (the displacement per unit length of the actuator) for the actuators with the dimensions of 1.8 cm × 2.5 mm × 65 μm is 55 μm/cm at an electric field of 3.6 kV/cm (voltage 18 V), which is a few times higher than the normalized displacement for bulk PMN–PT and thick-film PZT actuators on the substrates reported in the open literature. The measurements of displacement vs. the applied field indicate that two contributions from the electromechanical coupling are present, i.e., the piezoelectric linear effect (important at fields below 1 – 1.5 kV/cm) and the quadratic effect, which prevail at higher electric fields. The linear finite-element analysis of the actuator was performed using material parameters from the literature as well as experimentally obtained data. The models were used to calculate the bending vs. the applied electric field, and the results of the calculations were in good agreement with the measured data for low electric fields.

Acknowledgements

I would like to thank, most sincerely, all the people who contributed to the realisation of this research work:

Most of all I would like thank my supervisor Prof. Dr. Marija Kosec, co-supervisor Asst. Prof. Dr. Marko Hrovat and Dr. Janez Holc for continual and valuable guidance during this work and for encouragements, support, help and supervision of my thesis. Thank you.

I would like to thank all my colleagues from the Electronic Ceramics Department (K5), especially:
Silvo Drnovšek and Miha Skalar for sample preparation,
Dr. Jenny Tellier for help in Rietveld refinements,
Dr. Marina Santo Zarnik for help in finite-element modelling,
Asst. Prof. Dr. Andreja Benčan, Dr. Elena Tchernychova, Sebastjan Glinšek, Jena Cilenšek and Brigita Kužnik for help in transmission electron microscopy, field-emission scanning electron microscopy and related sample preparation,
and Srečo Maček for help in measurements of the actuators' displacements.

I would like to thank co-workers from the Department for Condensed Matter (F5) and the Department of Thin Films and Surfaces (F3), especially to Asst. Prof. Dr. Miha Škarabot for help in atomic force microscopy, Asst. Prof. Dr. Vid Bobnar for fruitful discussions on dielectric spectroscopy measurements and Matjaž Panjan for help with the nano-indentation measurements.

I would like to thank Dr. Miguel Alguero (Materials Science Institute of Madrid) for interesting and fruitful discussions during his visit to the Jožef Stefan Institute, Prof. Dr. Brahim Dkhil (Ecole Centrale Paris) and Dr. Nicolas Guiblin (Ecole Centrale Paris) for help with the Rietveld refinements during a 14-day scientific exchange, Prof. Dr. Dragan Damjanovič (Laboratory, EPFL, Lausanne), for help in piezoelectric measurements during a one-month scientific exchange (EC FP6 Network of Excellence MIND), Dr. Markys Cain (National Physical Laboratory, London) for basic research by atomic force microscopy during three-month scientific exchange (EC FP6 Network of Excellence MIND) and Prof. Dr. Hisao Suzuki (Shizuoka University, Hamamatsu, Japan) for an interesting three-month scientific visit to his laboratory at Shizuoka University.

Thanks also to my fellow students, especially Grega Trefalt for help with the figure design. Finally, thanks go to my mother and father, for support during my education, to my friends and especially to my husband Miha Nemevšek for encouragement and understanding during the writing of this thesis.

The financial support of the Slovenian Research Agency is gratefully acknowledged.

Thank you all!

References

[1] Damjanovic, D. Ferroelecric, dielectric and piezoelectric properties of ferroelectric thin films and ceramics. *Rep. Prog. Phys*. **61**, 1267 (1998).

[2] Nye, J. F. *Physical properties of crystals* (Oxford University Press, 2000).

[3] Henderson, I. R. *Piezoelectric Ceramics: Principles and Applications* (APC International Ltd., 2002).

[4] Sundar, V.; Newnham, R. E. *Electrostriction*, *2nd ed.* (IEEE, New York, 1997).

[5] Bobnar, V.; Malic, B.; Holc, J.; Kosec, M. Electrostrictive effect in lead-free relaxor $K_{0.5}Na_{0.5}NbO_3$–$SrTiO_3$ ceramic system*, J. Appl. Phys.* **98**, 024113 (2005).

[6] Haertling, G. H. Ferroelectric Ceramics: History and Technology. *J. Am. Ceram. Soc.* **82**, 797 (1999).

[7] Safari, A.; Panda, R. K.; Janas, V. F. Ferroelectric Ceramics: Processing, Properties and Applications, Department of Ceramic Science and Engineering, http://www.rci.rutgers.edu/~ecerg/projects/ferroelectric.html

[8] Jaffe, B.; Cook, W. R.; Jaffe, H. *Piezoelectric Ceramics* (Academic Press inc., London, 1971).

[9] Krempl, P.; Schleinzer, G.; Wallnofer, W. Gallium phosphate, $GaPO_4$: a new piezoelectric crystal material for high-temperature sensorics, *Sensors and Actuator* **A61**, 361 (1997).

[10] Bobnar, V. *Raziskave faznih prehodov v relaksorjih z dielektrično spektroskopijo: doktorska disertacija., P.h.D thesis,* 7 (Ljubljana, 2000).

[11] http://www.khulsey.com/jewelry/crystalline_structures.html

[12] Setter, N. *Piezoelectric Materials in Devices* (published by Ceramics Laboratory EPFL Swiss Federal Institute of Technology, Lausanne 1015, Switzerland, 2002).

[13] Pitt, K. E. G. *Handbook of thick film technology* (Electrochemical Publication Ltd 2005).

[14] Harper, C.A: *Handbook of thick film hybrid microelectronics* (McGraw-Hill, Inc. USA 1974).

[15] Holc, J.; Hrovat, M; Kosec, M. Interactions between alumina and PLZT thick films, *Materials Research Bulletin* **34**, 2271 (1999).

[16] Kosec, M.; Holc, J.; Malic, B.; Bobnar, V. Processing of high performance lead lanthanum zirconate titanate thick films*, J. Eur. Ceram. Soc.* **19**, 949 (1999).

[17] Kosec, M.; Jenko, D.; Holc, J.; Malic, B.; Čeh, M., Hauke, T.; Beige, H.Low-temperature processing of (Pb, La)(Zr, Ti)O_3 thick films on alumina substrate:dedicated to Professor Dr. Drago Kolar in memory of this brilliant scientist and teacher, *Z. Met.kd.*, **92**, 97 (2001).

[18] Uršič, H.; Hrovat, M.; Belavič, D.; Cilenšek, J.; Drnovšek, S.; Holc, J.; Zarnik, M. S.; Kosec, M. Microstructural and electrical characterisation of PZT thick films on LTCC substrates. *J. Eur. Ceram. Soc.* **28**, 1839 (2008).

[19] Ohring, M. *The material science of thin films* (Academic Press, San Diego, 1992).

[20] http://en.wikipedia.org/wiki/Residual_stress

[21] Lu, S.; Zuo, C.; Zeng, H.; Wen, H.; Ji, H. Residual stress and structure characteristics in PZT ferroelectric thin films annealed at differnet ramp rates. *Materials Letters* **60**, 255 (2006).

[22] Panjan, P.: Čekada M. *Zaščita orodij s trdimi PVD-prevlekami* (SYNCOMP, d.o.o. 2005).

[23] Šimunov, K.; Franz, M.; Marić, G. Investigation and estimation of residual stress in flame sprayed and fused NiCrBSi coatings, *Metalurgija* 47, 93.97 (2008).

[24] Lefki, K.; Dormans, G. J. M. Measurement of piezoelectric coefficients of ferroelectric thin films. *J. Appl. Phys.* **76**, 1764 + (1994).

[25] Setter, N.; Damjanovič, D.; Eng, L.; Fox, G.; Gevorgian, S.; Hong, S.; Kingon, A.; Kohlstedt, H.; Prak, N. Y.; Stephenson, G. B.; Stolitchnov, I.; Taganstev, A. K.; Taylor, D. V.; Yamada, T.; Streiffer, S. Ferroelectric thin films: Review of materials, properties, and applications. *J. Appl. Phys.* **100**, 051606 (2006).

[26] Dawber, M.; Rabe, K. M.; Scott, J. F. Physics of thin-film ferroelectric oxides. *Reviews of Modern Physics* **77**, 1083 (2005).

[27] Choi, K. J.; Biegalski, M.; Li Y. L.; Sharan, A.; Schubert, J.; Uecker, R.; Reiche, P.; Chen, Y. B.; Pan, X. Q.; Gopalan, V.; Chen, L. – Q.; Schlom, D. G.; Eom, C. B. Enhanced of ferroelectricity in strained $BaTiO_3$ thin films. *Science* **306**, 1005 (2004).

[28] Torah, R. N.; Beeby, S. P.; White, N. M. Experimental investigation into the effect of substrate clamping on the piezoelectric behaviour of the thick-film PZT elements. *J. Phys. D: Appl. Phys.* **37**, 1074 (2004).

[29] Uršič, H.; Lowe, M.; Stewart, M.; Hrovat, M.; Belavič, D.; Holc, J.; Zarnik, M. S.; Kosec, M.; Cain, M. PZT thick films on different ceramic substrates; piezoelectric measurements. *J. Electroceram* **20**, 11 (2008).

[30] Oh, S. H.; Jang, H. M. Enhanced thermodynamic stability of tetragonal-phase field in epitaxial Pb(Zr, Ti)O_3 thin films under a two-dimensional compressive stress, *Appl. Phys. Lett.* **72**, 1457 (1998).

[31] Lee, K.; Baik, S. Morphotropic phase boundary in epitaxial Pb(Zr, Ti)O_3 thin films: Two-dimensional planar size effect, *Applied Physics Letters* **86**, 202901 (2005).

[32] Sakamaki, Y.; Fukazawa, H.; Wakiya, N.; Suzuki, H.; Shinozaki, K.; Ohno, T.; Kosec, M. Effect of film thickness on electrical properties of chemical solution deposition-derived $Pb(Zr_xTi_{1-x})O_3/LaNiO_3$/Si. *J. J. Appl. Phys.* **46**, 6925 (2007).

[33] Oh, H. S.; Jang, H. M. Two-dimensional thermodynamic theory of epitaxial Pb(Zr,Ti)O_3 thin films. *Physical Review B*, **62**, 14757 (2000).

[34] Oh, H. S.; Jang, H. M. Epitaxial Pb(Zr,Ti)O_3 thin films with coexisting tetragonal and rhombohedral phases, *Physical Review B* **62**, 132101/1 (2001).

[35] Richerson, D. *The Magic of Ceramics* (The American Ceramic Society, 2000).

[36] http://en.wikipedia.org/wiki/Thick_film_technology

[37] Ahn, B.G.; Lee, D.K.; Han, D.Y.; Kang, C.Y.; Choi, J.W.; Kim, H.J.; Yoon, S.J. Bender typed piezoelectric multilayer actuator, *J. Korean Ceram. Soc.* **40**, 225 (2003).

[38] Allahverdi, M.; Hall, A.; Brennan, R.; Ebrahimi, M.E.; Marandian, H. N.; Safari A. An overview of rapidly prototyped piezoelectric actuators and grain-oriented ceramics, *J. Electroceram.* **8**, 129 (2002).

[39] Hall, A.; Akdogan, E.K.; Safari, A. Fatigue properties of piezoelectric-electrostrictive $Pb(Mg_{1/3}, Nb_{2/3})O_3$–$PbTiO_3$ monolithic bilayer composites, *J.Appl. Phys.* **100**, 094105 (2006).

[40] Takagi, H.; Sakata, K.; Takenaka, T. Electrostrictive properties of $Pb(Mg_{1/3}Nb_{2/3})O_3$-based relaxor ferroelectric ceramics, *Jpn. J. Appl. Phys.* **32**, 4280 (1993).

[41] Arbogast, D. J.; Calkins, F. T. Electrical system for electrostrictive bimorph actuator, Patent US 6,888,291 B2.

[42] Wu, T.; Ro, P.I.; Kingston, A.I.; Mulling, J.F. Piezoelectric resonating structures for microelectronic cooling, EUROSIME (2002).

[43] Tanuma, C. A parallel-bimorph-type piezoelectric actuator for high-resolution imager, *Jpn. J. Appl. Phys.* **38**, 5603–5607 (1999).

[44] Zarnik, M. S; Belavič, D.; Uršič, H.; Maček, S. Numerical modelling of ceramic mems structures with piezoceramic thick films, *J. Electroceram* **20**, 3 (2008).

[45] Alguero, M. Perovskite, relaxor-based MPB ceramic materials structured at different (levels and) scales, Seminar at IJS, Ljubljana, January 24th (2008).

[46] Ye, Z. – G.; Dong, M. Morphotropic domain structures and phase transitions in relaxor-based piezo-/ferroelectric (1-x)$Pb(Mg_{1/3}Nb_{2/3})O_3$-x$PbTiO_3$ single crystals. *J. Appl. Phys.* **87**, 2312 (2000).

[47] Noblanc, O.; Gaucher, P; Calvarin, G. Structural and dielectric studies of $Pb(Mg_{1/3}Nb_{2/3})O_3$-$PbTiO_3$ ferroelectric solid solutions around the morphotropic boundary. *J. Appl. Phys.* **79**, 4291 (1996).

[48] Kelly, J.; Leonard, M.; Tantigate, C.; Safari, A. Effect of composition on the electromechanical properties of (1-x)$Pb(Mg_{1/3}\ Nb_{2/3})O_3$– x$PbTiO_3$ ceramics. *J. Am. Ceram. Soc.* **80**, 957 (1997).

[49] Singh, A. K.; Pandey, D. Structure and the location of the morphotropic phase boundary region in (1 − *x*)[$Pb(Mg_{1/3}Nb_{2/3})O_3$]–*x*$PbTiO_3$. *J. Phys.: Condens. Matter* **13,** L931 (2001).

[50] Kiat, J. M.; Uesu, Y.; Dkhil, B.; Matsuda, M.; Malibert, C.; Calvarin, G. Monoclinic structure of unpoled morphotropic high piezoelectric PMN–PT and PZN–PT compounds. *Phys. Rev. B* **65**, 064106 (2002).

[51] Noheda, B.; Cox, D. E.; Shirane, G.; Gao, J.; Ye Z.-G. Phase diagram of the ferroelectric relaxor (1-x)$PbMg_{1/3}Nb_{2/3}O_3$-x$PbTiO_3$. *Phys. Rev. B* **66**, 054104 (2002).

[52] Ye, Z.-G.; Noheda, B.; Dong, M.; Cox, D.; Shirane, G. Monoclinic phase in the relaxor-based piezoelectric/ferroelectric $Pb(Mg_{1/3}Nb_{2/3})O_3$–$PbTiO_3$ system. *Phys. Rev. B* **64**, 184114 (2001).

[53] Singh, A. K.; Pandey, D. Evidence for M_B and M_C phases in the morphotropic phase boundary region of (1-x)[$Pb(Mg_{1/3}Nb_{2/3})O_3$] –x$PbTiO_3$: A rietveld study. *Phys. Rev. B* **67**, 064102 (2003).

[54] Alguero, M.; Ricote, J.; Jimenez, R. Size effect in morphotropic phase boundary $Pb(Mg_{1/3}Nb_{2/3})O_3$–$PbTiO_3$. *Appl. Phys. Lett.* **91**, 112905 (2007).

[55] Alguero, M.; Jimenez, R; Pardo, L. Transition between the relaxor and ferroelectric states for (1-x)[$Pb(Mg_{1/3}Nb_{2/3})O_3$]–x$PbTiO_3$ with x=0.2 and 0.3 polycrystalline aggregates, *Appl. Phys. Lett.* 87, 082910 (2005).

[56] Bokov, A. A.; Luo, H.; Ye, Z.-G. Polar nanodomains and relaxor behaviour in (1-x)[$Pb(Mg_{1/3}Nb_{2/3})O_3$]–x$PbTiO_3$ crystals with x = 0.3 - 0.5, *Materials Science and Engineering B* **120,** 206 (2005).

[57] Alguero, M.; Moure, A.; Pardo, L.; Holc, J.; Kosec, M. Processing by mechanosynthesis and properties of piezoelectric $Pb(Mg_{1/3}Nb_{2/3})O_3$–$PbTiO_3$ with different compositions. *Acta Materialia* **54**, 501 (2006).

[58] Leite, E. R.; Scotch, A. M.; Khan, A.; Chan H.; Harmer M. P. Chemical heterogeneity in PMN–35PT ceramics in effects on dielectric and piezoelectric properties, *J. Am. Ceram. Soc.*, 85, 3018 (2002).

[59] Koo, T. Y.; Cheong, S. W. Dielectric and piezoelectric enhancement due to 90° domain rotation in the tetragonal phase of $Pb(Mg_{1/3}Nb_{2/3})O_3$–$PbTiO_3$. *Appl. Phys. Lett.* **80**, 4205 (2002).

[60] Xia, Z.; Wang, L.; Yan, W.; Li, Q.; Zhang, Y. Comparative investigation of structure and dielectric properties of $Pb(Mg_{1/3}Nb_{2/3})O_3$–$PbTiO_3$ (65/35) and 10% $PbZrO_3$-doped $Pb(Mg_{1/3}Nb_{2/3})O_3$–$PbTiO_3$ (65/35) ceramics prepared by a modified precursor method. *Materials Research Bulletin* **42**, 1715 (2007).

[61] Cross, L. E. Relaxor ferroelectrics. *Ferroelectrics* **76**, 241(1987).

[62] Swartz, S. L.; Shrout, T. R.; Schulze, W. A.; Cross, L. E. Dielectric Properties of Lead-Mganesium Niobate Ceramics. *J. Am. Ceram. Soc.* **67**, 311 (1984).

[63] Swartz, S. L.; Shrout, T. R. Fabrication of perovskite lead magnesium niobate. *Mat. Res. Bull.* **17**, 1245 (1982).

[64] Carreaud, J.; Gemeiner, P.; Kiat, J. M.; Dkhil, B.; Bogicevic, C.; Rojac, T.; Malic B. Size-driven relaxation and polar states in $PbMg_{1/3}Nb_{2/3}O_3$-based system. *Phys. Rev. B* **72**, 174115 (2005).

[65] Carreaud, J.; Kiat, J. M.; Dkhil, B.; Alguero, M.; Ricote, J.; Jimenez, R.; Holc, J.; Kosec, M. Monoclinic morphotropic phase and grain size-induced polarization rotation in $Pb(Mg_{1/3}Nb_{2/3})O_3$-$PbTiO_3$, *Appl. Phys. Lett.* **89**, 252906 (2006).

[66] Jaeger, R. E.; Egerton, L. Hot Pressing of Potassium-Sodium Niobates. *J. A m. Ceram. Soc.* **45**, 209 (1962).

[67] Kosec, M.; Holc, J.; Kuščer, D.; Drnovšek, S. $Pb(Mg_{1/3}Nb_{2/3})O_3$–$PbTiO_3$ thick films from mechanochemically synthesized powder. *J. Eur. Ceram. Soc.* **27**, 3775 (2007).

[68] Gentile, S.; Damjanovic, D.; Setter, N. $Pb(Mg_{1/3}Nb_{2/3})O_3$ and (1-x)$Pb(Mg_{1/3}Nb_{2/3})O_3$–x$PbTiO_3$ relaxor ferroelectric thick films:processing and electrical characterization. *J. Electroceramics* **12**, 151 (2004).

[69] Gentile, S.; Damjanovic, D.; Setter, N. Development of relaxor ferroelectric materials for screen-printing on alumina and silicon substrates. *J. Eur. Ceram. Soc.* **25**, 2125 (2005).

[70] Kuščer, D., Skalar, M., Holc, J., Kosec, M. Processing and properties of 0.65 $Pb(Mg_{1/3}Nb_{2/3})O_3$ – 0.35 $PbTiO_3$ thick films. *J. Eur. Ceram. Soc.* **29**, 105 (2009).

[71] Thi, M. P.; March, G.; Colomban, P. Phase diagram and Raman imaging of grain growth mechanisms in highly textured $Pb(Mg_{1/3}Nb_{2/3})O_3$–$PbTiO_3$ piezoelectric ceramics. *Journal of European Ceramic Society* **25**, 3335 (2005).

[72] Saha, D.; Sen, A.; Maiti, H. S. Low temperature liquid phase sintering of lead magnesium niobate. *Ceramics International*, **25**, 145 (1999).

[73] Kuščer, D.; Holc, J.; Kosec, M. The formation of 0.65 $Pb(Mg_{1/3}Nb_{2/3})O_3$–0.35 $PbTiO_3$ using a high-energy milling process, *J. Am. Ceram. Soc.* **90**, 29 (2007).

[74] personal communication with Silvo Drnovšek, Jožef Stefan Institute

[75] Petricek, V.; Dusek, M.; Palatinus, L.(2006) Jana2006. The crystallographic computing system, Institute of Physics, Praha, Czech Republic.

[76] Rietveld, H.M. Line profiles of neutron powder diffraction peaks for structure refinement. *Acta Crystallographica* **22**, 151 (1967).

[77] Rietveld, H.M. A profile refinement method for nuclear and magnetic structures. *Journal of Applied Crystallography* **2**, 65 (1969).

[78] UTHSCSA Image Tool Version 3.00, 2002

[79] Panjan, M.; Čekada, M. Merjenje mikrotrdote trdnih PVD-prevlek z nanoindenterjem (2. del). *Vakuumist* **25**(4), 8-17 (2005).

[80] Zarnik, M. S.; Belavič, D.; Maček, S. Simulation and experimental testing of a thick-film PZT bending actuator. Proceeding of the 4th EMPS, Terme Čatež, Slovenia (2006).

[81] An European standard EN ISO 14577-1 (October 2002): Metallic materials – Instrumented indentation test for hardness and materials parameters-Part1: Test method (ISO 14577-1:2002).

[82] Kunert, M. *Mechanical properties on nanometer scale and their relations to composition and mechrostructure*, P.h.D. thesis, Fakultat Chemie der Universitat Stuttgard (2000).

[83] Catalan, G.; Corbett, M. H.; Bowman, R. M.; Gregg, J. M., Effect of thermal expansion mismatch on the dielectric peak temperature of thin film relaxors, *J. Appl. Phys.* **91**, 2295 (2002).

[84] An American National Standard, *IEEE Standard on Piezoelectricity* (The Institute of Electrical and Electronics Engineering Inc., 1988).

[85] Take Control Piezometer, Manual for Piezometer System PM10.

[86] Davis, M. (EPFL, P.h.D Thesis No. 3513, 2006).

[87] ANSYS release 9.0 documentation.

[88] Kuščer, D.; Tchernychova Šturm, E.; Kovač, J.; Kosec, M. "Characterization of the amorphous phase and the nanosized crystallites in high-energy-milled lead magnesium-niobate powder", *J. Am. Ceram. Soc.* **92**, 1224 (2009).

[89] Nunes, A.C.; Lin, O.' Effects of surface relaxation on powder diffraction patterns of very fine particles, *J. Appl. Crystl.* **28**, 274 (1995).

[90] PCPDFWin Version 2.2 PDF-ICDD. June 2001. International Center for Diffraction Data, (2002).

[91] Alguero, M.; Alemany, C.; Pardo, L.; Thi, M. P. Piezoelectric resonances, linear coefficients and losses of morphotropic phase boundary $Pb(Mg_{1/3}Nb_{2/3})O_3$–$PbTiO_3$ ceramics, *J. Am. Ceram. Soc.* **00**, 1 (2005).

[92] Zhao, X.; Wang, J.; Chan, H. L. W.; Choy, C. L.; Luo H. Effect of bias field on the dielectric properties of $0.7Pb(Mg_{1/3}Nb_{2/3})O_3$–$0.3PbTiO_3$ single crystals with different orientations, *Applied Physics A*, **80**, 653 (2005).

[93] Sehirlioglu, A.; Payne, D. A.; Han, P. Effect of poling on dielectric anomalies at phase transitions for lead magnesium niobate-lead titanate crystals in the morphotropic phase boundary region, *J. Appl. Phys.*, **99**, 064101 (2006).

[94] Guo, Y.; Luo, H.; Chen, K.; Xu, H.; Zhang, X.; Yin, Z. Effect of composition and poling field on the properties and ferroelectric phase-stability of $Pb(Mg_{1/3}Nb_{2/3})O_3$–$PbTiO_3$ crystals, *J. Appl. Phys.* **92**, 6134 (2002).

[95] Lu, Y.; Jeong, D.Y.; Cheng, Z. Y; Zhang, Q. M.; Luo, H. S.; Yin, Z. W.; Viehland D. Phase transitional behaviour and piezoelectric properties of the orthorhombic phase of $Pb(Mg_{1/3}Nb_{2/3})O_3$–$PbTiO_3$ single crystals, *Appl. Phys. Lett.* **78**, 3109 (2001).

[96] Guo, Y.; Luo, H.; He, T.; Xu, H.; Yin, Z. Domain configuration and ferroelectric related properties of the $(110)_{cub}$ cuts of relaxor-based $Pb(Mg_{1/3}Nb_{2/3})O_3$–$PbTiO_3$ single crystals, *J. J. Appl. Phys.* **41**, 1451 (2002).

[97] Chen, K. P.; Zhang, X. W.; Luo, H. S. Electric-field-induced phase transition in <001>–oriented $Pb(Mg_{1/3}Nb_{2/3})O_3$–$PbTiO_3$ single crystals, *J. Phys.: Condens. Matter* **14**, L571 (2002).

[98] Davis M., Damjanovič D., Setter N. Electric-field-, temperature-, and stress-induced phase transitions in relaxor ferroelectric single crystals, *Phys. Rev. B* **73**, 014115 (2006).

[99] Wan Q., Chen C., Shen Y. P.: Effects of stress and electric field on the electromechanical properties of $Pb(Mg_{1/3}Nb_{2/3})O_3$-$0.32PbTiO_3$ single crystals, *J. Appl. Phys.* **98**, 024103 (2005).

[100] Lu, Y.; Jeong, D. Y.; Cheng, Z. Y.; Shrout, T.; Zhang, Q. M., Phase stabilities of "morphotropic" phases in $Pb(Zn_{1/3}Nb_{2/3})O_3$–$PbTiO_3$ single crystals, *Appl. Phys. Lett.* **80,** 1918 (2002).

[101] Fu, H.; Cohen, R. E. Polarization rotation mechanism for ultrahigh electromechanical response in single-crystal piezoelectrcs, *Nature* **403**, 281 (2000).

[102] Luo, H. *Colloidal Processing of PMN–PT Thick Films for Piezoelectric Sensor Applications* (Doctoral disertation, Drexel University, Pennsylvania 2005).

[103] Mandeljc, M; *Študij kristalizacije tankih plasti na osnovi Pb(Zr,Ti)O_3* (Doktorska disertacija, Ljubljana, 2006).

[104] Viehland, D.; Li, J. F. Young's modulus and hysteretic losses of $0.7Pb(Mg_{1/3}Nb_{2/3})O_3$–$0.3PbTiO_3$: single versus polycrystalline forms, *J. Appl. Phys.* **94**, 7719 (2003).

[105] Zhong, X. L.; Lu, L.; Ali, M.O. Growth of highly orientated $0.65Pb(Mg_{1/3}Nb_{2/3})O_3$–$0.35PbTiO_3$ films by pulsed laser deposition, *Surface & Coatings Technology* **198,** 400 (2005).

[106] Sehirlioglu, A.; Payne, D. A.; Han, P. Thermal expansion of phase transformations in (1-x)$Pb(Mg_{1/3}Nb_{2/3})O_3$–$xPbTiO_3$: evidence for preferred domain alignment in one of the <001> directions for melt-grown crystals, *Phys. Rev. B* **72**, 214110 (2005).

[107] http://www.marketech-alumina.com/

[108] http://emtoolbox.nist.gov/Temperature/Slide14.asp

[109] Lide, D. R. *Handbook of Chemistry and Physics* (86^{TH} Edition, Press Taylor&Francis Group, Broken Sound Parkway NW, Suite 30, USA, 2005-2006).

[110] http://en.wikipedia.org/wiki/Coefficient_of_thermal_expansion

[111] Li, J.; Wei, P.; Qiliang, H.; Chen, J.; Zhang, Z. Mechanism of titanium deposition on AlN surface by molten salt reaction, *Materials Letters* **57**, 1369– 1373 (2003).

[112] Zhu, S.; Wlosinski, W. Joining of AlN ceramic to metals using sputtered Al or Ti film, *Journal of Materials Processing Technology* **109**, 277-282 (2001).

[113] Uchino, K.; Nomura, S.; Cross, L.E; Jang, S. J.; Newnham, R. E. Electrostrictive effect in lead magnesium niobate single crystals, *J. Appl. Phys.* **51**, 1142 (1980).

[114] Zhao, J.; Zhang, Q. M; Kim, N.; Shrout, T. Electromechanical properties of relaxor ferroelectric lead magnesium niobate-lead titanate ceramics, *Jpn. J. Appl. Phys.* **34**, 5658 (1995).

[115] Vikhnin, V.S.; Blinc, R.; Pirc R. Mechanisms of electrostriction and giant piezoelectric effect in relaxor ferroelectrics, *J. Appl. Phys*. **93**, 5649 (2003).

[116] Kighelman, Z.; Damjanovic, D.; Setter N. Dielectric and electromechanical properties of ferroelectric-relaxor $0.9Pb(Mg_{1/3}Nb_{2/3})O_3–0.1PbTiO_3$, *J. Appl. Phys*. **90**, 1393 (2001).

[117] Donnelly, N. J.; Catalan, G.; Morros, C.; Bowman, R. M.; Gregg J. M. Electromechanical properties of $Pb(Mg_{1/3}Nb_{2/3})O_3–7\%PbTiO_3$ thin films made by pulsed laser deposition, J. Appl. Phys. **91**, 6200 (2002).

[118] Bokov, A. A.; Ye, Z.-G. The giant electrostriction and stretched exponential electromechanical relaxation in $0.65Pb(Mg_{1/3}Nb_{2/3})O_3–0.35PbTiO_3$, *J. Appl. Phys.* **91,** 6656 (2002).

[119] Kholkin, A. L.; Akdogan, E. K.; Safari, A.; Chauvy, P.-F.; Setter, N. Characterization of the effective electrostriction coefficients in ferroelectric thin films, *J. Appl. Phys.* **89**, 9947 (2001).

[120] Hall, A.; Akdogan, E. K.; Safari, A. Fatigue properties of piezoelectricelectrostrictive $Pb(Mg_{1/3}, Nb_{2/3})O_3–PbTiO_3$ monolithic bilayer composites, *J. Appl. Phys.* **100,** 094105 (2006).

[121] Hall, A.; Allahverdi, M.; Akdogan, E. K.; Safari, A. Piezoelectric/electrostrictive multimaterial PMN–PT monomorph actuators, *J. Eur. Ceram. Soc.* **25**, 2991 (2005).

[122] Zarnik, M. S.; Belavič, D.; Maček S. Evolution of the constitutive material parameters for the numerical modeling of structures with lead–zirconate–titanate thick films, Sens. Actuators A **13**, 618 (2007).

[123] Belavič, D.; Zarnik, M.S.; Holc, J.; Hrovat, M.; Kosec, M.; Drnovšek, S.; Cilenšek, J.; Maček, S. Properties of lead zirconate titanate thick-film piezoelectric actuators on ceramic substrates, *Int. J. Appl. Ceram. Technol.* **3,** 448 (2006).

[124] Wang, Q. M.; Zhang, Q.; Xu, B.; Liu, R.; Cross, L. E. Nonlinear piezoelectric behavior of ceramic bending mode actuators under strong electric fields, *J. Appl. Phys.* **86**, 3352 (1999).

[125] http://en.wikipedia.org/wiki/Platinum

[126] http://www.webelements.com/platinum/physics.html

[127] Park, S. E.; Thomas R. S. Ultrahigh strain and piezoelectric behaviour in relaxor based ferroelectric single crystals, *J. Appl. Phys.* **82**, 1804 (1997).

[128] Feng, Z.; Zhao, X.;Luo, H.; Electric field effects on the domain structures and the phase transition of $0.62[Pb(Mg_{1/3}Nb_{2/3})O_3] –0.38PbTiO_3$ single crystals with different orientations, *J. Phys.: Condens. Matter* **16**, 3769 (2004).

Index of Figures

Figure 1: The direct piezoelectric effect (a) and the inverse piezoelectric effect (b).

Figure 2: Coordinate system used in the thesis. The direction of polarization is marked [3]. Numbers 4, 5 and 6 represents directions of shear stresses.

Figure 3: Illustration of the changes in the dielectric constant ε of a ferroelectric material, which transform from a paraelectric cubic phase into a ferroelectric tetragonal phase, versus temperature T. The arrows show possible directions of the spontaneous polarization (the unit-cell is represented by a square in the cubic phase and rectangle in the tetragonal phase) [1].

Figure 4: Temperature dependence of dielectric constant **ε** measured at different frequencies for the relaxor $Pb(Mg_{1/3}Nb_{2/3})O_3$ (PMN) crystal [10].

Figure 5: An example of perovskite crystal structure: a) cubic lattice, symmetric arrangement of positive and negative charges, temperature above Curie point, b) tetragonal lattice, crystal has electrical dipole, temperature below Curie point [3].

Figure 6: Perovskite unit-cells of a) cubic, b) rombohedral, c) tetragonal, d) orthorhombic and e) monoclinic phases.

Figure 7: Poling of piezoelectric ceramics: a) The unpoled ceramics. Each grain contains a number of domains and the net polarization is zero. b) After poling the domains are oriented with a net polarization along the direction of the applied field [12].

Figure 8: Hysteresis curve of ferroelectric ceramics [3].

Figure 9: The scheme of the screen printing procedure.

Figure 10: Cooling stresses in the substrate-film system: ΔS is difference in deformation between substrate and film, Δα is difference in TEC of substrate and film, ΔT is a difference in temperature [19, 23].

Figure 11: Film under a) compressive and b) tensile residual stress [19].

Figure 12: Illustration of the film on the substrate and a rectangular system of 1, 2, and 3-axes. The direction of polarization coincides with axis 3.

Figure 13: The computed phase diagram of $PbZrO_3$–$PbTiO_3$ (PZ–PT) system, showing the effect of two-dimensional compressive stress on the shift of the MPB [30].

Figure 14: Varity of piezoelectric bulk parts [35].

Figure 15: Example of the versatility of thick-film technology: the hybrid integrated circuits, sensors and actuators produced at Institute Jožef Stefan, Electronic Ceramics Department.

Figure 16: a) Schematic view, b) photograph [44] and c) picture of computational simulation of bending [44] for PZT bimorph bender actuator.

Figure 17: Phase diagram of PMN–PT material [45].

Figure 18: a) The molar fractions of different phases versus the composition for PMN–PT ceramics and b) lattice parameters for the majority phases versus composition of PMN–PT ceramics [53].

Figure 19: The dielectric constant ε versus temperature for 0.65PMN–0.35PT ceramics with the average grain size of a) 4 μm and b) 0.15 μm [54].

Figure 20: The hysteresis loop measured at 0.1 Hz for 0.65PMN–0.35PT ceramics with the average grain size of 4 μm and 0.15 μm [54].

Figure 21: The X-ray diagram of 0.65PMN–0.35PT films on alumina substrates sintered at a) 850°C, 900°C, 950°C [67] and b) 1184°C [68].

Figure 22: Photograph of the manual screen printer in laboratory.

Figure 23: The sintering vessels and the arrangement of packing powder during sintering of the 0.65PMN–0.35PT films.

Figure 24: The schemes of the cross-sections of the 0.65PMN–0.35PT films on a) Al_2O_3, b) Pt, c) 0.65PMN–0.35PT and d) AlN substrates.

Figure 25: The 0.65PMN–0.35PT films on a) Al_2O_3, b) Pt, c) 0.65PMN–0.35PT and d) AlN substrates.

Figure 26: a) The arrangement for sintering of the 0.65PMN–0.35PT bulk ceramics and b) the photograph of the 0.65PMN–0.35PT ceramics after cutting, polishing and after deposition of the electrodes. Thickness of the pellets and diameter of the pellets are 0.6 mm and 6 mm, respectively.

Figure 27: Microstructure of the surface of the alumina substrate after the peeling off of the 0.65PMN–0.35PT/Pt composite. Inset shows the photograph of the alumina substrate after peeling off of the 0.65PMN–0.35PT/Pt composite. The yellow colour of the substrates shown in the inset is due to the reaction between PbO from the film and alumina substrates.

Figure 28: EDXS analysis of the white crystals on the surface of Al_2O_3 substrate, beside strong peaks of Al, peaks of Pb are also detected.

Figure 29: Microstructure of the surface of the alumina substrate after firing the 0.65PMN–0.35PT film at 950°C for 2 hours. The lighter hexagonal grains are PbO-stabilised β-alumina on the surface of darker alumina substrates.

Figure 30: The scheme of the cross-section of the 0.65PMN–0.35PT films on alumina substrates prepared for the 0.65PMN–0.35PT/Pt bimorph actuator realization. Inset: Microstructure of the surface of the alumina substrate after the peeling off of the 0.65PMN–0.35PT/Pt composite. β-alumina crystals are visible.

Figure 31: A schematic view of the actuator's realization in four steps.

Figure 32: a) The scheme of the cross-section and b) the photograph of the top view of the 0.65PMN–0.35PT/Pt bimorph actuators.

Figure 33: a) The setup for measuring ferroelectric hysteresis loops; an Aixact TF Analyser 2000, high voltage amplifier TREK 609E-6 and computer. b) Micro manipulator stage with the thick-film sample.

Figure 34: a) The poling setup; high voltage supply KEITHLEY MODEL 248. b) 0.65PMN–0.35P thick-film sample placed on the poling stage between contact tips.

Figure 35: a) The resonance measurement setup; BODE 100 Omicron Lab device and the micro manipulator stage and the sample holder. b) Micro manipulators, contact tips and the 0.65PMN–0.35PT bulk ceramic sample.

Figure 36: a) The Berlincourt Take Controle Piezometer PM10. b) 0.65PMN–0.35PT thick film on alumina substrate placed in the force head of piezometer during measurements of d_{33}.

Figure 37: The measurement setup for measuring the displacements of the 0.65PMN–0.35PT/Pt actuators vs. the applied electric field with the Viking optical profiler system (Solarius Development). b) The actuator during measurement. The external electric field was applied between the top and bottom electrodes. The 3 mm long bottom part of the actuator was placed on the conductive step. The top electrode was connected with the contact tip. The measurements were performed at the end of the actuator's cantilever.

Figure 38: Top view of 0.65PMN–0.35PT layer geometry (half symmetry) used in FE models.

Figure 39: The geometry of the actuator and the boundary conditions (fixed point and fixed area) used in the FE model are shown.

Figure 40: The particle size distribution of the 0.65PMN–0.35PT powder. The green line is the cumulative curve.

Figure 41: The FE-SEM micrographs of the a) submicron particles and b) particles larger than 1 μm.

Figure 42: The X-ray diagram of the 0.65PMN–0.35PT powder.

Figure 43: The measured (dot), calculated (line) and difference (bottom) curve of the 0.65PMN–0.35PT powder. The regions from $2\theta = 36°$ to $2\theta = 48°$ of measured X-ray diffraction for the 0.65PMN–0.35PT powder and profile matching for a) monoclinic Pm, b) tetragonal P4mm and c) cubic Pm-3m phases. Peaks correspond to the families of planes (111) at around $2\theta = 38°$ and (200) at around $2\theta = 45°$. The thick marks correspond to the positions of the peaks for (111) and (200) families of planes.

Figure 44: The SEM micrographs of polished cross-section for the bulk 0.65PMN–0.35PT ceramics fired at 1200°C for 2 hours.

Figure 45: The SEM micrographs of thermally etched cross-section for the bulk 0.65PMN–0.35PT ceramics fired at 1200°C for 2 hours.

Figure 46: The X-ray diagram of the non-poled 0.65PMN–0.35PT ceramics fired at 1200°C for 2 hours. The families of planes are given in brackets. The inset shows the convolution of the (002) and (200) tetragonal peaks and the (002), (200), (020) monoclinic peaks. The approximate peak positions of the tetragonal (grey) and monoclinic (black) phases are marked with dashed lines.

Figure 47: Dielectric constant ε and dielectric losses tg δ vs. temperature at frequencies of 1 kHz, 10 kHz and 100 kHz for non-poled 0.65PMN–0.35PT bulk ceramics fired at 1200°C.

Figure 48: The ferroelectric hysteresis loops of the 0.65PMN–0.35PT ceramics fired at 1200°C for 2 hours.

Figure 49: The measurement of impedance, i.e., amplitude (red) and phase (blue) vs. frequency of applied el. field for 0.65PMN–0.35PT ceramics poled with 4 kV/mm. Antiresonance f_a and resonance f_r frequencies are marked. The crossed dotted lines show the position of determined f_r.

Figure 50: The piezoelectric coefficient d_{33} and the coupling coefficients k_p and k_t vs. poling field. The rectangle shows the area of the optimum poling conditions. The line between the measured values is just a guide to the eye.

Figure 51: The X-ray diffraction diagram of the family of (200) peaks for the poled 0.65PMN–0.35PT ceramics. The X-ray diagram of the non-poled material is added for comparison. The black arrow indicates the increase in the poling electric field from 0 kV/mm to 4.5 kV/mm in steps of 0.5 kV/mm.

Figure 52: Final observed, calculated and difference plots of the X-ray diffraction Rietveld refinement for a) a non-poled sample and samples poled at b) 2.5 kV/mm and c) 4.5 kV/mm. The top mark corresponds to the tetragonal phase and the bottom ones to the monoclinic. The positions corresponding to the gold (the grey shadows) were excluded from the refinement.

Figure 53: The dielectric constant ε vs. temperature at 100 kHz for the non-poled and poled 0.65PMN–0.35PT ceramics. The inset shows the data obtained for the non-poled sample on a logarithmic scale.

Figure 54: The thickness of the 0.65PMN–0.35PT films on alumina substrates after firing vs. number of screen printed layers. The line between the measured values is just a guide to the eye.

Figure 55: The thickness of the 0.65PMN–0.35PT films on Al_2O_3, Pt, 0.65PMN–0.35PT and AlN after firing. Two layers of 0.65PMN–0.35PT paste were printed in all cases.

Figure 56: The micrograph of the surface of a 0.65PMN–0.35PT thick film that was screen printed, dried and heated to 500°C.

Figure 57: The SEM micrographs of the surface of 0.65PMN–0.35PT thick films on a) Al_2O_3, b) Pt substrates.

Figure 58: a) The SEM micrographs of the surface of 0.65PMN–0.35PT thick films on 0.65PMN–0.35PT and b) the FE-SEM micrographs of the surface of 0.65PMN–0.35PT thick films on AlN substrates.

Figure 59: The FE- SEM micrographs of fracture for bulk 0.65PMN–0.35PT ceramics fired at 950°C.

Figure 60: SEM micrographs of the cross-section of the 0.65PMN–0.35PT thick films on a) Al_2O_3 and b) Pt substrates.

Figure 61: SEM micrographs of the cross-section of the 0.65PMN–0.35PT thick films on a) 0.65PMN–0.35PT and b) AlN substrates.

Figure 62: The cross-section of the 0.65PMN–0.35PT thick film on the Pt substrate. The positions of EDXS area analyses (area 7 μm x 7 μm) on the 0.65PMN–0.35PT thick-film cross-section.

Figure 63: The microstructure of the 0.65PMN–0.35PT film – Pt substrate junction. The EDXS analyses were performed in the "points" marked with the numbers 1 and 2.

Figure 64: EDXS analysis of the point marked in Fig. 63 with number 1.

Figure 65: EDXS analysis of the point marked in Fig. 63 with number 2.

Figure 66: The cross-section of the 0.65PMN–0.35PT thick film on the alumina substrate. The positions of EDXS area analyses (window 7 μm x 7 μm) on the 0.65PMN–0.35PT thick-film cross-section are marked with the black squares and numbers from 1 to 5.

Figure 67: The cross-section of the 0.65PMN–0.35PT thick film on the 0.65PMN–0.35PT substrate. The positions of the EDXS area analyses (window 7 μm x 7 μm) on the 0.65PMN–0.35PT thick-film cross-section are marked with the black squares and numbers from 1 to 5.

Figure 68: The cross-section of the 0.65PMN–0.35PT thick film on the AlN substrate. The positions of EDXS area analyses (window 7 μm x 7 μm) on the 0.65PMN–0.35PT thick-film cross-section are marked with the black squares and numbers from 1 to 5.

Figure 69: The X-ray diagram of the 0.65PMN–0.35PT film on the alumina substrate. The families of planes are given in brackets. The inset shows the refined Bragg peak positions of the (002), (200) tetragonal (grey) and the (002), (200), (020) monoclinic (black) phases.

Figure 70: The X-ray diffraction diagrams of the 0.65PMN–0.35PT thick films on a) Al_2O_3, b) Pt, c) 0.65PMN–0.35PT and d) AlN substrates in the range from $2\theta = 44.4°$ to $2\theta = 45.7°$. The refined peak positions of the (002), (200) tetragonal (grey) and the (002), (200), (020) monoclinic (black) phases are marked.

Figure 71: Final observed (red), calculated (black) and difference curves of the X-ray diffraction Rietveld refinement for films deposited on a) Al_2O_3 and b) Pt. The top black marks correspond to the tetragonal phase and the bottom ones to the monoclinic.

Figure 72: Final observed (red), calculated (black) and difference curves of the X-ray diffraction Rietveld refinement for films deposited on a) 0.65PMN–0.35PT and b) AlN. The black marks correspond to the monoclinic phase. The positions corresponding to Pt electrode (arrows) were excluded from the refinement.

Figure 73: The X-ray diffraction diagram of 0.65PMN–0.35PT ceramics fired at 950°C. Inset shows the family of (200) peaks. The refined peak positions (002), (200), (020) of the monoclinic Pm phase are marked in the inset.

Figure 74: Two regions a) from 2θ = 38° to 2θ = 40° and b) from 2θ = 44.2° to 2θ = 46.4°, of measured X-ray diffraction diagram for the ceramics and the profile matching for the monoclinic Pm phase. Insets: the profile matching for the cubic Pm-3m phase is also added for comparison.

Figure 75: The X-ray diffraction diagram of the 0.65PMN–0.35PT films on the alumina substrates measured at different temperatures. The black arrow indicates the increasing temperatures.

Figure 76: Variations of cell parameters with temperature for a) the tetragonal P4mm and b) the monoclinic Pm phases of the 0.65PMN–0.35PT films on alumina substrates. The dashed rectangle shows the area of the coexistence of the tetragonal P4mm and monoclinic Pm phases. The lines between the measured values are just a guide to the eye.

Figure 77: The X-ray diffraction diagram of the 0.65PMN–0.35PT films on the Pt substrates measured at different temperatures. The black arrow indicates an increase of the temperature.

Figure 78: Variation of the cell parameters with temperature for a) the tetragonal P4mm and b) the monoclinic Pm phases of 0.65PMN–0.35PT films on Pt substrates. The dashed rectangle shows the area of the coexistence of the tetragonal P4mm and the monoclinic Pm phases. The lines between the measured values are just a guide to the eye.

Figure 79: The X-ray diffraction diagram of 0.65PMN–0.35PT films on 0.65PMN–0.35PT substrates measured at different temperatures. The black arrow indicates the increasing temperature.

Figure 80: Variation of the cell parameters with temperature for the monoclinic Pm phase of the 0.65PMN–0.35PT films on the 0.65PMN–0.35PT substrates. The lines between the measured values are just a guide to the eye.

Figure 81: a) The X-ray diffraction diagram of the 20 μm, 35 μm, 65 μm and 100 μm thick 0.65PMN–0.35PT films on the alumina substrates. b) The family of (200) peaks for X-ray diagram of 20 μm, 35 μm, 65 μm and 100 μm thick 0.65PMN–0.35PT films on the alumina substrates. The percentage of the monoclinic Pm and the tetragonal P4mm phases for the thinnest and the thickest films are marked. The black arrow indicates increasing film thickness.

Figure 82: The SEM micrographs of the surface of a) 20 μm and b) 100 μm thick 0.65PMN–0.35PT films on Al_2O_3 substrates (magnification 3000).

Figure 83: The SEM micrographs of the surface of a) 20 μm and b) 100 μm thick 0.65PMN–0.35PT films on Al_2O_3 substrates (magnification 7000).

Figure 84: a) The X-ray diffraction diagram of the 25 μm, 50 μm and 150 μm thick 0.65PMN–0.35PT films on 0.65PMN–0.35PT substrates. b) The family of (200) peaks for the X-ray diagram of 25 μm, 50 μm and 150 μm thick 0.65PMN–0.35PT films on 0.65PMN–0.35PT substrates. Only the monoclinic phase was detected. The black arrow indicates the increasing film thickness.

Figure 85: The load-displacement curves F(h) of the 0.65PMN–0.35PT film on the alumina substrate.

Figure 86: The measurements of the transverse Young's moduli Y_{13} of the 0.65PMN–0.35PT films on the Al_2O_3 substrate - schematically.

Figure 87: The photograph of the indentation measurements of the transverse Young's moduli Y_{13} for the 0.65PMN–0.35PT film on the Al_2O_3 substrate: a) before the measurement and b) after the measurement. The place of the indentation is marked with the red square.

Figure 88: Dielectric constant ε measured as a function of the temperature at 1 kHz, 10 kHz and 100 kHz for films on a) Al_2O_3, b) Pt, c) 0.65PMN–0.35PT and d) AlN substrates. e) The measurements for bulk ceramics fired at the same temperature, i.e., 950°C are added. The insets show the detail of the peaks in the dielectric

constants.

Figure 89: The dielectric constant ε vs. temperature at 100 kHz for the 0.65PMN–0.35PT films on the Al_2O_3, Pt, 0.65PMN–0.35PT, AlN substrates, and for the bulk ceramics. The insets show the same graphs on a logarithmic scale. The LT phase-transitions are marked with black arrows. All samples were fired at 950°C for 2 hours.

Figure 90: The ferroelectric hysteresis loops of 0.65PMN–0.35PT films on a) Al_2O_3, b) Pt, c) 0.65PMN–0.35PT and d) AlN substrates.

Figure 91: Measurements of displacement versus time at different voltage amplitudes and at a frequency of 200 Hz for the 0.65PMN–0.35PT thick film on the alumina substrate. The applied force was 80 nN. The applied external sinusoidal voltage curve with a maximum amplitude of 50 V is added to emphasize the double frequency of the measured sample displacements.

Figure 92: The displacement versus voltage amplitude for the 0.65PMN–0.35PT thick film on the alumina substrate. The dotted line between the measured values (quadratic fit) is just a guide to the eye.

Figure 93: Relative strain versus the square of the electric field amplitude. The electrostrictive coefficient M_{33} was determined from the slope of the linear fit curve.

Figure 94: A cross-section of the 0.65PMN–0.35PT/Pt actuator.

Figure 95: The bending displacement normalized per unit length of the actuator for the 0.65PMN–0.35PT/Pt actuator (with dimensions 1.8 cm × 2.5 mm × 50 μm of the active layer) versus applied electric field.

Figure 96: A comparison between our data (denoted A), i.e., the normalized displacement at an electric field of 3.6 kV/cm is 55 μm/cm, and the data from the literature; Ref. [120] (denoted B), Ref. [121] (denoted C) and Refs. [122, 123] (denoted D).

Figure 97: Comparison of the simulation results obtained from the initial FE model and the updated FE model with the measured displacement of the actuator.

Index of Tables

Table 1: The processing conditions, dielectric, piezoelectric, ferroelectric properties and coupling coefficients of 0.65PMN–0.35 PT ceramics obtained by different authors. Notation: ε-dielectric constant, d_{33}-piezoelectric coefficient P_r remanent polarization, E_c coercitive field and k_p, k_t coupling coefficients.

Table 2: Dielectric, piezoelectric, ferroelectric properties of 0.65PMN–0.35 PT thick films obtained by different authors. Notation: ε dielectric constant, d_{33}^{eff} piezoelectric coefficient, P_r remanent polarization and E_c coercitive field.

Table 3: The thickness, shape, dimensions and producer of the Al_2O_3, Pt, 0.65PMN–0.35PT and AlN substrates.

Table 4: The average EDXS "point" analysis made in 23 spots (atomic percents), the standard deviation and the maximum and minimum determined values of the 0.65PMN–0.35PT bulk ceramic fired at 1200°C for 2 hours.

Table 5: The piezoelectric coefficient d_{33} and the coupling coefficients k_p and k_t measured for the 0.65PMN–0.35PT ceramics poled at different poling fields.

Table 6: Phase ratio in percentage, reliability factors R, for the monoclinic Pm (R_M) and tetragonal P4mm (R_T) phases and the goodness of the fit for the profile Gof, of the Rietveld analyses for the X-ray data of the non-poled and poled 0.65PMN–0.35PT ceramics. The calculated uncertainty for the percentage of phases is less than 1%.

Table 7: The average EDXS "point" analysis made in 23 spots (atomic percents), the standard deviation and the maximum and minimum determined values of the 0.65PMN–0.35PT thick film on the Pt substrate in comparison with the 0.65PMN–0.35PT bulk ceramic fired at 1200°C for 2 hours.

Table 8: The EDXS average "point" analysis made for the bottom, the middle and the top layers (atomic percents), standard deviation and the maximum and the minimum determined values.

Table 9: Area EDXS analyses for the 0.65PMN–0.35PT thick film on the Pt substrate cross-section (atomic percents) shown in Fig. 62.

Table 10: Area EDXS analyses for the 0.65PMN–0.35PT thick film on the alumina substrate cross-section (atomic percents) shown in Fig. 66.

Table 11: Area EDXS analyses for the 0.65PMN–0.35PT thick film on the 0.65PMN–0.35PT substrates cross-section (atomic percents) shown in Fig. 67.

Table 12: Area EDXS analyses for the 0.65PMN–0.35PT thick film on the AlN substrates cross-section (atomic percents) shown in Fig. 68.

Table 13: Phase ratio, reliability factors R, for the monoclinic Pm (R_M) and the tetragonal P4mm (R_T) phases and goodness of fit (Gof), from the Rietveld analysis of the X-ray data measured at room temperature.

Table 14: Unit-cell parameters for monoclinic Pm and tetragonal P4mm phases from the X-ray data of thick films measured at room temperature.

Table 15: The Young's moduli of the non-poled 0.65PMN–0.35PT film on the alumina substrate without or with the top electrode and of the poled 0.65PMN–0.35PT film on the alumina substrate measured on the top

electrode.

Table 16: The Young's modulus of the non-poled 0.65PMN–0.35PT films on the Al_2O_3, Pt, 0.65PMN–0.35PT and AlN substrates and bulk 0.65PMN–0.35PT ceramics fired at 1200°C and 950°C.

Table 17: The piezoelectric coefficients d_{33}^{eff} of 50 µm thick 0.65PMN–0.35PT films on alumina substrates obtained by Photonic sensor, atomic force microscope AFM and Berlincourt piezometer.

Table 18: The piezoelectric coefficient d_{33}^{eff} of the 0.65PMN–0.35PT film on Pt, 0.65PMN–0.35PT and AlN substrates.

Table 19: The ferroelectric properties of 0.65PMN–0.35PT films on Al_2O_3, Pt, 0.65PMN–0.35PT and AlN substrates; remanent polarization P_r and coercive field E_c.

Table 20: The TEC of the substrates, the differences in TEC of the substrates and films ($\Delta TEC = TEC_{substrate} - TEC_{film}$), the compressive and tensile stresses and the phase compositions in the films. The 0.65PMN–0.35PT bulk ceramics sintered at 950°C are added for comparison.

Table 21: The comparison between the measured data and the data from the literature.

Table 22: The material parameters specified in the initial and in the updated FE models.

Table 23: The Pt material parameters specified in the initial and in the updated FE model [109].

Publications from the Disertation

Scientific articles (first author)

- Uršič, H.; Škarabot, M.; Hrovat, M.; Holc, J.; Skalar, M.; Bobnar, V.; Kosec, M.; Muševič, I. "The electrostrictive effect in ferroelectric 0.65Pb($Mg_{1/3}Nb_{2/3}$–0.35$PbTiO_3$ thick films", *J. Appl. Phys.* **103**, 124101-1 (2008).

- Uršič, H.; Hrovat, M.; Holc, D.; Zarnik, M. S.; Drnovšek, S.; Maček, S.; Kosec, M. "A large-displacement 65Pb($Mg_{1/3}Nb_{2/3}$)O_3–35$PbTiO_3$/Pt bimorph actuator prepared by screen printing", *Sensors and Actuators B Chem.* **133**, 699 (2008).

- Uršič, H.; Hrovat, M.; Belavič, D.; Cilenšek, J.; Drnovšek, S.; Holc, J.; Zarnik, M. S.; Kosec, M. "Microstructural and electrical characterisation of PZT thick films on LTCC substrates", *J. Eur. Ceram. Soc.* **28**, 1839 (2008).

- Uršič, H.; Lowe, M.; Stewart, M.; Hrovat, M.; Belavič, D.; Holc, J.; Zarnik, M. S.; Kosec, M.; Cain, M. "PZT thick films on different ceramic substrates; piezoelectric measurements", *J. Electroceram* **20**, 11 (2008).

- Uršič, H.; Benčan. A., Škarabot, M.; Godec, M.; Kosec, M.; "Dielectric, ferroelectric, piezoelectric and electrostrictive properties of $K_{0.5}Na_{0.5}NbO_3$ single crystals", *J. Appl. Phys.* **107**, 033705 (2010).

- Uršič, H.; Tellier, J.; Hrovat, M.; Holc, J.; Drnovšek, S.; Bobnar, V.; Alguero, M.; Kosec, M.; "The effect of poling on the properties of 0.65Pb($Mg_{1/3}Nb_{2/3}$)O_3–0.35$PbTiO_3$ ceramics", *J. Appl. Phys.* submitted.

- Uršič, H.; Hrovat, M.; Holc, J.; Tellier., J.; Drnovšek, S.; Guiblin, N.; Dkhil; B., Kosec, M.; "Influence of the substrate on the phase composition and electrical properties of 0.65PMN–0.35PT thick films", *J. Eur. Ceram. Soc.,* submitted.

Scientific articles (co-author)

- Zarnik, M. S.; Belavič, D.; Uršič, H.; Maček, S. "Numerical modelling of ceramic mems structures with piezoceramic thick films", *J. Electroceram* **20**, 3 (2008).

- Rojac, T.; Benčan, A.; Uršič, H.; Malič, B.; Kosec, M. "Synthesis of a Li- and Ta- modified (K,Na)NbO_3 solid solution by mechanochemical activation", *J. Am. Ceram. Soc.* **91**, 3789 (2008).

- Kosec, M; Uršič H.; Holc, J; Hrovat, M.; Kuščer D.; Malič B. "High performing PMN–PT thick films", Transaction on Ultrasonics, Ferroelectrics, and Frequency control, submitted.

COBISS

COBISS Co-operative Online Bibliographic system & services COBISS

HANA URŠIČ NEMEVŠEK [26468]
Personal bibliography for the period
2005-2009

ARTICLES AND OTHER COMPONENT PARTS

1.01 Original scientific article

1. ELLABBAN, M. A., FALLY, M., URŠIČ, Hana, DREVENŠEK OLENIK, Irena. Holographic scattering in photopolymer-dispersed liquid crystals. *Appl. phys. lett.*, 2005, 87, str. 151101-1-151101-3. [COBISS.SI-ID 1865060]

2. ELLABBAN, Mostafa A., DREVENŠEK OLENIK, Irena, FALLY, Martin, URŠIČ, Hana. Effect of electric field and temperature on holographic scattering from holographic polymer-dispersed liquid crystals. *Opt. mater. (Amst.)*. [Print ed.], 2007, 29, str. 1416-1422. [COBISS.SI-ID 1988964]

3. URŠIČ, Hana, ŠKARABOT, Miha, HROVAT, Marko, HOLC, Janez, SKALAR, Miha, BOBNAR, Vid, KOSEC, Marija, MUŠEVIČ, Igor. The electrostrictive effect in ferroelectric 0,65Pb(Mg[sub](1/3)Nb[sub](2/3)-0,35PbTiO[sub]3 thick films. *J. appl. physi.*, 2008, vol. 103, no. 12, str. 124101-1-124101-4. [COBISS.SI-ID 21792039]

4. SANTO-ZARNIK, Marina, BELAVIČ, Darko, URŠIČ, Hana, MAČEK, Srečo. Numerical modelling of ceramic MEMS structures with piezoceramic thick films. *Journal of electroceramics*, 2008, vol. 20, no. 1, str. 3-9. http://dx.doi.org/10.1007/s10832-007-9329-6. [COBISS.SI-ID 21287719]
tipologija 1.08 -> 1.01

5. URŠIČ, Hana, LOWE, Martin, STEWART, Marc, HROVAT, Marko, BELAVIČ, Darko, HOLC, Janez, SANTO-ZARNIK, Marina, KOSEC, Marija, CAIN, Markys. PZT thick films on different ceramic substrates: piezoelectric measurements. *Journal of electroceramics*, 2008, vol. 20, no. 1, str. 11-16. http://dx.doi.org/0.1007/s10832-007-9327-8. [COBISS.SI-ID 21319975]
tipologija 1.08 -> 1.01

6. ROJAC, Tadej, BENČAN, Andreja, URŠIČ, Hana, MALIČ, Barbara, KOSEC, Marija. Synthesis of a Li- and Ta- modified (K, Na)NbO[sub]3 solid solution by mechanochemical activation. *J. Am. Ceram. Soc.*, 2008, vol. 91, no. 11, str. 3789-3791. [COBISS.SI-ID 22179879]

7. URŠIČ, Hana, HROVAT, Marko, BELAVIČ, Darko, CILENŠEK, Jena, DRNOVŠEK, Silvo, HOLC, Janez, SANTO-ZARNIK, Marina, KOSEC, Marija. Microstructural and electrical characterisation of PZT thick films on LTCC substrates. *J. Eur. Ceram. Soc.*. [Print ed.], 2008, vol. 28, no. 9, str. 1839-1844. [COBISS.SI-ID 21623847]

8. URŠIČ, Hana, HROVAT, Marko, HOLC, Janez, SANTO-ZARNIK, Marina, DRNOVŠEK, Silvo, MAČEK, Srečo, KOSEC, Marija. A large-displacement 65Pb(Mg[sub](1/3)Nb[sub](2/3))O[sub]3-35PbTiO[sub]]3/Pt bimorph actuator prepared by screen printing. *Sens. actuators, B, Chem.*. [Print ed.], 2008, vol. 133, no. 2, str. 699-704. [COBISS.SI-ID 21679143]

1.05 Popular article

9. URŠIČ, Hana, TREFALT, Gregor, GLINŠEK, Sebastjan. Obisk podiplomskih študentov z ameriške univerze Brown, Rhode Island. *Novice - IJS (Tisk. izd.)*. [Tiskana izd.], št. 30-34, str. 30-34. [COBISS.SI-ID 22636071]

1.06 Published scientific conference contribution (invited lecture)

10. BELAVIČ, Darko, SANTO-ZARNIK, Marina, HROVAT, Marko, HOLC, Janez, KOSEC, Marija, MAČEK, Srečo, JERLAH, Mitja, BERNARD, Janez, PAVLIN, Marko, URŠIČ, Hana. An investigation of thick-film technology for sensors and actuators in C-MEMS. V: ZARASKA, Wiesław (ur.), CICHOCKI, Andrzej (ur.), SZAWAGIERCZAK, Dorota (ur.). XXX International Conference of IMAPS Poland Chapter, Kraków, 24-27 September, 2006. *Proceedings*. Kraków: Institute of Electron Technology, Cracow Division, 2006, str. 21-28. [COBISS.SI-ID 20238375]

1.08 Published scientific conference contribution

11. URŠIČ, Hana, HROVAT, Marko, BELAVIČ, Darko, CILENŠEK, Jena, DRNOVŠEK, Silvo, HOLC, Janez, SANTO-ZARNIK, Marina, KOSEC, Marija. PZT thick-films on LTCC substrates. V: VRTAČNIK, Danilo (ur.), ŠORLI, Iztok (ur.). 42th International Conference on Microelectronics, Devices and Materials and the Workshop on MEMS and NEMS, September, 13. - September 15, 2006, Strunjan, Slovenia. *Proceedings*. Ljubljana: MIDEM - Society for Microelectronics, Electronic Components and Materials, cop. 2006, str. 133-138. [COBISS.SI-ID 20186919]

12. BELAVIČ, Darko, SANTO-ZARNIK, Marina, HROVAT, Marko, HOLC, Janez, KOSEC, Marija, MAČEK, Srečo, URŠIČ, Hana. Study of piezoelectrical actuators for use in micro- and mezo-electro-mechanical system applications. V: VRTAČNIK, Danilo (ur.), ŠORLI, Iztok (ur.). 42th International Conference on Microelectronics, Devices and Materials and the Workshop on MEMS and NEMS, September, 13. - September 15, 2006, Strunjan, Slovenia. *Proceedings*. Ljubljana: MIDEM - Society for Microelectronics, Electronic Components and Materials, cop. 2006, str. 277-282. [COBISS.SI-ID 20188967]

13. BELAVIČ, Darko, HROVAT, Marko, URŠIČ, Hana, DRNOVŠEK, Silvo, JERLAH, Mitja, CILENŠEK, Jena, HOLC, Janez, SANTO-ZARNIK, Marina, KOSEC, Marija. Structural and electrical investigation of PZT films on different substrates. V: EMPC 2007, The 16th European Microelectronics and Packaging Conference & Exhibition, June 17-20, 2007, Oulu, Finland. *Proceedings*. [Washington]: IMAPS, 2007. [COBISS.SI-ID 20872487]

14. HROVAT, Marko, BELAVIČ, Darko, URŠIČ, Hana, KITA, Jarosław, HOLC, Janez, DRNOVŠEK, Silvo, CILENŠEK, Jena, GOLONKA, Leszek, DZIEDZIC, Andrzej, KOSEC, Marija. Thick-film sensors / actuators for LTCC based MEMS : a characterization and evaluation. V: *MicroTech 2008 : Beaumont House, Windsor, UK, June 10-11, 2008 : proceedings*. [S. l.]: IMAPS-UK, 2008, 8 str. [COBISS.SI-ID 21793831]

15. HROVAT, Marko, BELAVIČ, Darko, URŠIČ, Hana, KITA, Jarosław, HOLC, Janez, DRNOVŠEK, Silvo, CILENŠEK, Jena, KOSEC, Marija, MOOS, Ralf. An investigation of thick-film materials for temperature and pressure sensors on self-constrained LTCC substrates. V: [ESTC 2008], 2nd Electronics Systemintegration Technology Conference, Greenwich, UK. *Proceedings*. Piscataway: Institute of Electrical and Electronics Engineers, 2008, zv. 1, str. 339-345. [COBISS.SI-ID 22023207]

16. BELAVIČ, Darko, HROVAT, Marko, SANTO-ZARNIK, Marina, HOLC, Janez, CILENŠEK, Jena, JERLAH, Mitja, MAČEK, Srečo, URŠIČ, Hana, KOSEC, Marija. PZT thick films for pressure sensors : characterisation of materials and devices. V: [ESTC 2008], 2nd Electronics Systemintegration Technology Conference, Greenwich, UK. *Proceedings*. Piscataway: Institute of Electrical and Electronics Engineers, 2008, zv. 2, str. 989-994. [COBISS.SI-ID 22023463]

17. HROVAT, Marko, BELAVIČ, Darko, URŠIČ, Hana, KITA, Jarosław, HOLC, Janez, DRNOVŠEK, Silvo, CILENŠEK, Jena, SANTO-ZARNIK, Marina, KOSEC, Marija. Thick-film pressure/force sensors on different LTCC substrates : a characterization and evaluation. V: 2009 IMAPS/ACerS, 5th International Conference and Exhibition on Ceramic Interconnect and Ceramic Microsystems Technologies (CICMT), April 21-23, 2009, Denver, Colorado. *Proceedings*. Washington: International Microelectronics and Packaging Society, 2009, str. 149-156. [COBISS.SI-ID 22677799]

1.12 Published scientific conference contribution abstract

18. URŠIČ, Hana, DREVENŠEK OLENIK, Irena, ELLABBAN, M. A., FALLY, M. Electrooptic properties of thick H-PDLC gratings. V: 8th European Conference on Liquid Crystals, February 27 - March 4, 2005, Sesto(BZ), Italy. *Book of abstracts*. [S. l.: s. n.], 2005, str. P35. [COBISS.SI-ID 18876967]

19. ELLABBAN, M. A., URŠIČ, Hana, DREVENŠEK OLENIK, Irena, FALLY, M. Holographic scattering from polymer dispersed liquid crystals. V: 8th European Conference on Liquid Crystals, February 27 - March 4, 2005, Sesto(BZ), Italy. *Book of abstracts*. [S. l.: s. n.], 2005, str. P36. [COBISS.SI-ID 18907431]

20. ELLABBAN, M. A., FALLY, M., URŠIČ, Hana, DREVENŠEK OLENIK, Irena, ČOPIČ, Martin. Holographic scattering in H-PDLCs. V: 11th International Topical Meeting on Optics of Liquid Crystals, October 2-7, 2-7, 2005, Sand Key, Florida, USA. *OLC 2005 : book of abstracts*. [S.l.: s.n.], 2005, str. 35. [COBISS.SI-ID 19371303]

21. DREVENŠEK OLENIK, Irena, URŠIČ, Hana, ELLABBAN, M. A., PRANZAS, P. Klaus, VOLLBRANDT, Jürgen, ČOPIČ, Martin. Photo-neutronrefractive effect in holographic polymer dispersed liquid crystals. V: ILCC-06, 21st International Liquid Crystal Conference, Keystone, Colorado, July 2-7, 2006. *Abstracts*. Boulder: The Liquid Crystal Materials Research Center, University of Colorado, 2006, str. 520. [COBISS.SI-ID 20037415]

22. FALLY, Martin, DREVENŠEK OLENIK, Irena, ELLABBAN, M. A., URŠIČ, Hana. Strongly overmodulated diffraction gratings in holographic polymer-dispersed liquid cryslats. V: International Workshop on Liquid Crystals for Photonics, April 26-28, 2006, Gent. *Book of abstracts*. Gent: Universiteit Gent, 2006, str. O-11-O-12. [COBISS.SI-ID 1920356]

23. URŠIČ, Hana, LOWE, Martin, STEWART, Marc, HROVAT, Marko, BELAVIČ, Darko, CILENŠEK, Jena, DRNOVŠEK, Silvo, HOLC, Janez, SANTO-ZARNIK, Marina, KOSEC, Marija, CAIN, Markys. Piezoelectric measurements of thick film PZT structures on ceramic substrates. V: *Piezoelectricity for end users III : POLECER conference, February 7-9, 2005, Liberec, Czech Republic : program & abstracts*. Liberec: Technical University of Liberec, 2007, str. 69. [COBISS.SI-ID 20562471]

24. SANTO-ZARNIK, Marina, BELAVIČ, Darko, URŠIČ, Hana, MAČEK, Srečo. Finite element modelling of the ceramic MEMS with the piezo thick films. V: *Piezoelectricity for end users III : POLECER conference, February 7-9, 2005, Liberec, Czech Republic : program & abstracts*. Liberec: Technical University of Liberec, 2007, str. 109. [COBISS.SI-ID 20620071]

25. BELAVIČ, Darko, HROVAT, Marko, SANTO-ZARNIK, Marina, HOLC, Janez, CILENŠEK, Jena, JERLAH, Mitja, MAČEK, Srečo, URŠIČ, Hana, KOSEC, Marija. An investigation of thick PZT films for sensor applications. V: ICE 2007, International Conference on Electroceramics, 31 July - 3 August 2007, Ngurdoto Mountain Lodge, Arusha, Tanzania. *Program & abstracts*. [S. l.: s. n.], 2007, str. 96. [COBISS.SI-ID 21308455]

26. BENČAN, Andreja, URŠIČ, Hana, KOSEC, Marija. Characterization of single crystals of (K,Na)NbO[sub]3 and (K,Na,Li)(Nb,Ta)O[sub]3 for use as lead-free piezoelectric. V: ZALAR, Boštjan (ur.), MALIČ, Barbara (ur.), BOBNAR, Vid (ur.). EMF-2007 - 11th European Meeting on Ferroelectricity, September 3-7 2007, Bled, Slovenia. *Programme and book of abstracts*. Ljubljana: J. Stefan Institute, 2007, str. 52. [COBISS.SI-ID 21053223]

27. URŠIČ, Hana, HROVAT, Marko, HOLC, Janez, DRNOVŠEK, Silvo, KOSEC, Marija. Properties of PMN-PT (65/35) thick films on different substrates. V: ZALAR, Boštjan (ur.), MALIČ, Barbara (ur.), BOBNAR, Vid (ur.). EMF-2007 - 11th European Meeting on Ferroelectricity, September 3-7 2007, Bled, Slovenia. *Programme and book of abstracts*. Ljubljana: J. Stefan Institute, 2007, str. 219. [COBISS.SI-ID 21049383]

28. URŠIČ, Hana, HROVAT, Marko, HOLC, Janez, SANTO-ZARNIK, Marina. Electrical and structural parameters of 0.65PMN-0.35PT thick films on different substrates. V: 47th Symposium on Basic Science

of Ceramic, 8-9 January, 2009, Osaka, Japan. *Abstract book*. [S. l.]: The Ceramic Society of Japan, 2009, str. 42-43. [COBISS.SI-ID 22388263]

29. URŠIČ, Hana, ŠKARABOT, Miha, HROVAT, Marko, HOLC, Janez, SKALAR, Miha. Electrostriction in 0.65Pb(Mg[sub](1/3)Mb[sub](2/3)O[sub]3-0.35PbTiO[sub]3 thick films on alumina substrates. V: ECAPDIX, 9th European Conference on Applications of Polar Dielectrics, Roma, Italy, August 25-29,2008. *Abstract booklet*. Roma: Sapienza Università di Roma, Facoltà di Ingegneria, 2008, str. 284. [COBISS.SI-ID 21936679]

30. ROJAC, Tadej, BENČAN, Andreja, KOSEC, Marija, MALIČ, Barbara, URŠIČ, Hana. Li- and Ta-modified (K, Na)NbO[sub]3 solid solution : comparison between synthesis methods. V: Electroceramics XI, August 31 - September 4,2008, Manchester, UK. *Abstracts and CD proceedings*. [S. l.: s. n.], 2008. [COBISS.SI-ID 21948967]

31. BENČAN, Andreja, URŠIČ, Hana, FISHER, John Gerard, TCHERNYCHOVA, Elena, KOSEC, Marija. Properties of alkaline niobate single crystals prepared by solid state crystal growth. V: Electroceramics XI, August 31 - September 4,2008, Manchester, UK. *Abstracts and CD proceedings*. [S. l.: s. n.], 2008. [COBISS.SI-ID 21948711]

32. URŠIČ, Hana, OHNO, Tomoya, NUKINA, Takerou, WAKIYA, Naoki, SAKAMOTO, Naonori, SUZUKI, Hisao, MALIČ, Barbara, KOSEC, Marija. Effect of processing for CSD-derived LNO seeding later on electrical properties of PZT thin film. V: IUMRS-ICA 2008, The IUMRS International Conference in Asia 2008, December 9-13, 2008, Nagoya, Japan. *Abstracts*. [S. l.]: The Materails Research Society of Japan, 2008. [COBISS.SI-ID 22362919]

33. URŠIČ, Hana, HROVAT, Marko, KOSEC, Marija, HOLC, Janez, SANTO-ZARNIK, Marina, OHNO, Tomoya. Strukturna in električna karakterizacija debelih plasti 65/35 PMN-PT na različnih podlagah. V: PONIKVAR-SVET, Maja (ur.). Ljubljana, 15. 2. 2008. *Prispevki*. Ljubljana: Institut "Jožef Stefan", 2008. [COBISS.SI-ID 21890343]

34. URŠIČ, Hana. Piezokeramični materiali spreminjajo naše življenje. V: TORKAR, Matjaž (ur.). *Promocija študija in raziskav materialov : program in povzetki predavanj, Poslovni center Slovenijales, Dunajska 22, Ljubljana, 6. 12. 2007*. Ljubljana: Slovensko društvo za materiale, 2008, str. 13. [COBISS.SI-ID 21889831]

35. KOSEC, Marija, URŠIČ, Hana, HOLC, Janez, KUŠČER, Danjela. High performing piezoelectric thick films by designing of powder and texture : [invited talk]. V: IMF-ISAF-2009, 12th International Meeting on Ferroelectricity, (IMF-12) & 18th IEEE International Symposium on the Applications of Ferroelectrics, (ISAF-18), August 23-27, 2009, Xi'an, China. *Abstract CD*. Xi'an: Xi'an Jiaoton University, Electronic Materials Research Laboratory, 2009. [COBISS.SI-ID 22898983]

36. URŠIČ, Hana, HROVAT, Marko, HOLC, Janez, DRNOVŠEK, Silvo, SANTO-ZARNIK, Marina, KOSEC, Marija. Strukturne in električne lastnosti debelih plasti 0.65PMN-0.35PT na korundu, na platini in na 0.65PMN-0.35PT podlagi. V: ISKRA, Jernej (ur.), MILOŠEV, Ingrid (ur.). *Dan mladih raziskovalcev 2009*. Ljubljana: Institut "Jožef Stefan", 2009, 1 str. [COBISS.SI-ID 22442023]

37. ROJAC, Tadej, BENČAN, Andreja, KOSEC, Marija, MALIČ, Barbara, URŠIČ, Hana. Synthesis of (K,Na, Li)(Nb, Ta)O[sub]3 lead-free piezoceramics using mechanochamical activation. V: *Piezo 2009 : Electroceramics for end-users IV, 1-4 March 2009, Zakopane, Poland*. [S. l.]: Piezo Institute, 2009, str. 23. [COBISS.SI-ID 22492967]

38. RINGGAARD, Erling, ZAWADA, Tomasz, DAMJANOVIĆ, Dragan, DOREY, Robert A., URŠIČ, Hana. Changes in permittivity during the poling process. V: *Piezo 2009 : Electroceramics for end-users IV, 1-4 March 2009, Zakopane, Poland*. [S. l.]: Piezo Institute, 2009, str. 53. [COBISS.SI-ID 22493991]

39. URŠIČ, Hana, HROVAT, Marko, HOLC, Janez, SANTO-ZARNIK, Marina, KOSEC, Marija. 0.65Pb(Mg[sub](1/3)Nb[sub](2/3))O[sub]3-0.35PbTiO[sub]3 thick film actuators on thin Pt supports. V: JENKO, Monika (ur.). 17. konferenca o materialih in tehnologijah, 16.-18. november 2009, Portorož,

Slovenija = 17. konferenca o materialih in tehnologijah, 16.-18. november 2009, Portorož, Slovenija. *Program in knjiga povzetkov*. Ljubljana: Inštitut za kovinske materiale in tehnologije, 2009, str. 35. [COBISS.SI-ID 23126055]

40. URŠIČ, Hana. Piezoelektrični debeloplastni aktuator z velikim odmikom. V: ŠETINA, Barbara (ur.), JUNKAR, Ita (ur.), KALUŽA, Boštjan (ur.), ELERŠIČ, Kristina (ur.). 1. študentska konferenca Mednarodne podiplomske šole Jožefa Stefana, 19. - 20. maj 2009, Ljubljana, Slovenija = 1st Jožef Stefan International Postgraduate School Student's Conference, 19th - 20th May 2009, Ljubljana, Slovenia. *Zbornik prispevkov*. Ljubljana: Mednarodna podiplomska šola Jožefa Stefana, 2009, str. 58-59. [COBISS.SI-ID 22635815]

MONOGRAPHS AND OTHER COMPLETED WORKS

2.11 Undergraduate thesis

41. URŠIČ, Hana. *Optične holografske mrežice na osnovi polimerov in tekočih kristalov : diplomsko delo*. Ljubljana: [H. Uršič], 2005. 63 str., graf. prikazi. [COBISS.SI-ID 1857380]

2.13 Treatise, preliminary study, study

42. URŠIČ, Hana, HROVAT, Marko, MALIČ, Barbara, KOSEC, Marija. *Piezoelectric measurements of thick an thin PZT films on different substrates*, (IJS delovno poročilo, 9495). 2006. [COBISS.SI-ID 20379687]

43. BELAVIČ, Darko, RADEŽ, Roman, URŠIČ, Hana, HROVAT, Marko. *Substrati za debeloplastno tehnologija : primerjalna analiza*, (IJS delovno poročilo, 9284). 2006; [S.l.: s.n.]. [COBISS.SI-ID 19608359]

44. URŠIČ, Hana, HROVAT, Marko, BENČAN, Andreja, DAMJANOVIĆ, Dragan, KLEIN, Naama, HOLC, Janez, DRNOVŠEK, Silvo, FISHER, John Gerard, BERNARD, Janez, KOSEC, Marija. *Dielectric and piezoelectric properties of bulk KNLNT ceramics, KNN single crystals and PMN-PT thick films*, (IJS delovno poročilo, 9631). 2007. [COBISS.SI-ID 20885543]

45. URŠIČ, Hana, DURCZYNSKI, Pawel, HROVAT, Marko, BELAVIČ, Darko. *Aging process in PZT thick films on alumina and LTCC substrates*, (IJS delovno poročilo, 10230). 2009. [COBISS.SI-ID 22702119]

46. KUTNJAK, Zdravko, ROŽIČ, Brigita, MALIČ, Barbara, URŠIČ, Hana, HOLC, Janez, KOSEC, Marija. *Elektrokalorični pojav : literaturni pregled in stanje v Sloveniji*, (IJS delovno poročilo, 10307, zaupno). 2009. [COBISS.SI-ID 22994471]

47. URŠIČ, Hana, HOLC, Janez, BELAVIČ, Darko, SANTO-ZARNIK, Marina, KOSEC, Marija. *Piezoelektrični senzorji*, (IJS delovno poročilo, 10231). 2009. [COBISS.SI-ID 22702375]

PERFORMED WORKS (EVENTS)

3.14 Invited lecture at foreign university

48. URŠIČ, Hana. *0.65PMN-0.35PT thick films : (electrical and structural characterization)*. Hamamatsu: Department of Material Science of Technology, Shizuoka University, 21 Nov. 2008. [COBISS.SI-ID 22377767]

49. URŠIČ, Hana. *0.65PMN-0.35PT thick films on different substrates : invited talk*. Hamamatsu: Department of Materials Science and Technology, Shizuoka University, 17 Oct. 2008. [COBISS.SI-ID 22398503]

3.15 Unpublished conference contribution

50. URŠIČ, Hana, BENČAN, Andreja. *Dielectric properties of pure KNN single crystals and dielectric and piezoelectric properties of doped KNN ceramics : presented at Structural phenomena in the framework of MIND project, 4-5 June 2007, Bedford, GB*. 2007. [COBISS.SI-ID 22397735]

51. URŠIČ, Hana, HROVAT, Marko, HOLC, Janez, SANTO-ZARNIK, Marina, DRNOVŠEK, Silvo, MAČEK, Srečo, KOSEC, Marija. *0.65PMN-0.35PT bimorph actuators with large displacement : presented at Workshop on Nanostructured Materials and Membrane Modelling and Simulation, June 18-27, 2008, Patras, Greece*. 2008. [COBISS.SI-ID 22397479]

52. URŠIČ, Hana, HROVAT, Marko, HOLC, Janez, OHNO, Tomoya, DRNOVŠEK, Silvo, KOSEC, Marija, SUZUKI, Hisao. *0.65PMN-0.35PT thick films : electrical and structural characterization : presented at 3rd Meeting of the Processing Research Group Association, 20 December 2008, Tokyo*. 2008. [COBISS.SI-ID 22378023]

53. URŠIČ, Hana. *Phase composition and electrical properties of 0.65PMN-0.35PT thick films : Workshop on thick film and their applications, 21 January 2009, Orbassano, Italy*. 2008. [COBISS.SI-ID 22398247]

54. URŠIČ, Hana. *Structural and electrical characterization of PMM-PT thick films on different substrates : presented at MIND International Seminar on "Functional characterisation of piezoelectric materials", 22 January 2008, Blois, France*. 2008. [COBISS.SI-ID 22397991]

55. URŠIČ, Hana. *Films in planar geometrics : presented at project meeting MULTICERAL, Multifunctional ceramic layers with high electromagnetoelastic coupling in complex geometrics, 27 June 2009, Aveiro, Portugal*. 2009. [COBISS.SI-ID 22746919]

3.16 Unpublished invited conference lecture

56. URŠIČ, Hana. *Elektronska keramika : Dan znanosti in raziskovanja na šoli, OŠ dr. Vita Kraigherja, 21. oktober 2009, Ljubljana, Slovenija*. 2009. [COBISS.SI-ID 23047719]

Request for bibliography sent from: 193.2.4.4
Selected format of bibliographic unit: ISO 690

Source of bibliographic records: shared data base COBISS.SI/COBI